UNIVERSITY OF BIRMINGHAM

ADDITIVE MANUFACTURING OF NICKEL BASED SUPERALLOYS FOR AEROSPACE APPLICATIONS

By

Lakshmi Lavanya Parimi

A thesis submitted to

The University of Birmingham

for the degree of

DOCTOR OF PHILOSOPHY

Metallurgy and Materials
School of Engineering
The University of Birmingham
April 2014

Abstract

Additive Manufacturing (AM) is a near net-shape technique where the final component is produced directly from a CAD model without dies or substantial machining as in conventional routes. This can lead to improved material utilisation, increased flexibility in engineering design, reduced time to market and lower cost. Among the several AM routes Direct Laser Fabrication (DLF) is of growing interest within the aerospace industry for repairing applications as well as in the hybrid manufacturing routes, where features are deposited on an existing part avoiding the machining of expensive material. However, the repeated heating and cooling cycles lead to non-uniform expansion and contraction of the material and hence distortion and residual stresses while the solidification conditions in this process lead to undesirable microstructures. Due to the large number of variables in this process it is difficult to predict the microstructure and residual stresses in the build and currently there is a limited knowledge regarding the influence of these process parameters on the build structural integrity, microstructure and residual stresses.

The aim of the work presented in this thesis is to establish the influence of the many process variables on the microstructure and the nature of internal stress in samples produced directly from powder using direct laser fabrication. The alloy that has been studied is IN718 while the process variables that have been studied include, specimen geometry, laser power, laser traverse speed, the detailed laser path and powder feed rate. It has been found that the microstructure is strongly influenced by all of these variables with the propensity for the production of equiaxed or columnar grains being strongly influenced by laser power. The texture is correspondingly strongly influenced by changes in processing conditions. The extent of precipitation of the various phases expected in IN718 was also found to be influenced by the process conditions. Pores were present in the final build for all conditions investigated and the minimum pore density obtained was about 0.2%. The level and nature of the residual stress in the sample and in the substrate have been determined for a wide range of experimental conditions and using neutron diffraction it has been found that the level of these stresses could be reduced to a minimum value of about 300 MPa, but could not be eliminated. A simple 3D thermo-mechanical model was developed to understand the residual stress distribution, which agreed closely with the experimental measurements. It is suggested that either Hot Isostatic Pressing could be used to remove the residual stresses, or on-line control of the process variables could be developed in a future study.

The Thesis is dedicated to my parents

Dr. P. Uma Devi and Prof. P. Atchuta Ramaiah

Who are my strength and inspiration in my life..

Acknowledgements

I would like to express my love and gratitude to my parents **Prof. P. Atchuta Ramaiah** and **Dr. P. Uma Devi**, for their affection, blessings, continuous support and encouragement in every moment of my life. I would also like to thank both my sisters for their love and encouragement.

I avail this unique opportunity to thank **Prof. Xinhua Wu** and **Prof. Roger. C. Reed** for offering me the PhD position and supervising me at the beginning of my PhD. I express my profound sense of gratitude and indebtedness to **Dr. Moataz. M. Attallah,** who kindly agreed to be my supervisor upon Prof. Wu and Prof. Reed's departure, for his efficacious advice and perpetual encouragement throughout the project. Without his guidance and great patience this work could not have been accomplished.

I am grateful to the Engineering and Physical Sciences Research Council (EPSRC) of the United Kingdom and to Rolls-Royce plc for sponsorship of this work and financial support, via a **Dorothy Hodgkin Postgraduate Award (DHPA).** Thanks are due to my industrial supervisor **Dr. Daniel Clark** for his helpful discussions during my PhD.

Special thanks must go to the following individuals: **Prof. Michael Loretto,** for his helpful advice and technical discussions. His enthusiasm and hard-working really impressed me, which will be an inspiration throughout my future life. To **Dr. Alphons A. Antonysamy**, Materials Lead at GKN aerospace, who encouraged me right from the beginning of taking the decision to do a PhD abroad to finishing the thesis successfully. I am in debt for his never ending support and technical advice in every aspect of the work, especially for his patience to give me some wisdom on the solidification theories and microstructures. I am also thankful for his continuous moral support which made my stay in UK wonderful. To **Dr Jean-Christophe Gebelin**, former member of Partnership for Research in the Simulation and Manufacturing and Materials Group (PRISM2), for his considerable help and guidance to carry out the modelling work. To **Dr. Khamis Essa**, Lecturer at School of Mechanical engineering, University of Birmingham, UK, who showed great interest in my work and for his willingness for technical discussion, who also made my life more enjoyable during this work. To **Dr. Ravi G.A** and **Mr. John Shurvinton** at University of Birmingham for their help with the Quantum laser machine operation and transferring all their knowledge on the machine.

I would like to thank former and present members of the AMPlab and PRISM^2 and CASiM group, especially to Dr. Jianglin Huang, Dr. Hector Basoalto, Dr. Luke Carter, Dr. Noriko Read, Mr. Matteo Villa and Mr. Christopher Karl for their helping hand in the experimentation as well as for being a pleasant company in the very difficult times. I would also like to thank all the technical staff at the School of Metallurgy and Materials for their time and expertise in assisting me in my practical work.

Finally, I thank God Almighty for giving me the strength and patience to face the challenges encountered during this period.

List of Publications and Presentations

Parts of this dissertation have been published in the following journals and presented in international conferences listed below:

Journal Publications:

- Lakshmi L. Parimi, Ravi G. A., Daniel Clark, and Moataz M. Attallah, *Microstructural and texture development in direct laser fabricated IN718,* **Materials Characterization, Vol** 89, Pages 102-111, March 2014.
- Lakshmi Lavanya Parimi, Moataz M Attallah, Jean-Christophe Gebelin, and Roger C Reed, *Direct Laser Fabrication of INCONEL-718: Effects on Distortion and Microstructure,* **in the Proceedings of Superalloys 2012**, Warrendale, USA.

Presentations:

- Lakshmi L. Parimi, Moataz M. Attallah and Daniel Clark, *Influence of Direct Laser Fabrication Process Parameters on the Microstructural Development in IN718,* **EuroMat 2011**, at Montpellier, France.
- Lakshmi Lavanya Parimi, Moataz M Attallah, Jean-Christophe Gebelin, and Roger C Reed, *Direct Laser Fabrication of INCONEL-718: Effects on Distortion and Microstructure,* in **Superalloys 2012**, Warrendale, USA.
- Lakshmi L. Parimi, Moataz M. Attallah and Daniel Clark, *Effect of Process Parameters on the Build Quality, Porosity, Microstructure and Hardness of Direct Laser Fabricated Inconel 718,* in **Fifth edition of International Symposium for Research Scholars (2012),** IIT Madras, India**. (Won the Best Paper award).**

Intentionally left blank

Table of Contents

List of Figures……VII

List of Tables……...XXV

Nomenclature……..……..…..XXVII

Chapter one 1

1 Introduction 1

1.1 Metallic Additive Manufacturing 1

1.2 Advantages and Applications of AM Metallic Structures 2

1.3 Limitations and Issues with AM 4

1.3.1 Issues with Metallic AM 4

1.4 Aim and Objectives of the Project 5

1.5 Thesis Outline 7

Chapter Two 9

2 Literature Review 9

2.1 Metallurgy of Nickel-based Superalloys 9

2.1.1 Introduction 9
2.1.2 Influence of alloying additions in Ni and Ni-Fe based superalloys 11
2.1.3 Phases in the superalloys 13

2.2 Metallurgy of IN718 21

2.2.1 Introduction 21
2.2.2 Precipitation in IN718 23
2.2.3 Heat Treatment of IN718 32

2.3 General Solidification Theory 33

2.3.1 Nucleation and growth behaviour 34
2.3.2 Columnar to equiaxed transition (CET) in Ni-based superalloys 36
2.3.3 Factors controlling the melt-pool solidification behaviour 36

2.4 Residual Stresses Characterisation Techniques 41

2.4.1 Measuring Techniques 42

2.5 Direct Laser Fabrication 49

2.5.1 Introduction 49
2.5.2 Build Geometry and Quality 50
2.5.3 Microstructure 58
2.5.3.1 Dendrite Morphology of laser deposits: 59
2.5.4 Post Deposition Treatment in DLF 68
2.5.5 Mechanical Properties in DLF 70
2.5.6 Distortion and Residual Stresses in DLF 75
2.5.7 Thermo-Mechanical Modelling of DLF 80
2.6 Summary of literature: Key findings and areas on investigation 91
2.6.1 Potential for further study 94
Chapter Three 96
3 Materials and Experimental Methods 96
3.1 Introduction 96
3.2 Materials 96
3.3 Direct Laser Fabrication (DLF) Experimental setup 97
3.4 IN718 Builds 98
3.4.1 Stage I: Thin Wall samples 98
3.4.2 Stage II: Thick Wall Samples 102
3.4.3 Stage III: Solid Blocks 104
3.5 Thermocouple measurements 109
3.5.1 Thermocouple measurements for FE model Validation 109
3.5.2 Correlation of distortion with corresponding cooling rates 110
3.6 Microstructural Characterisation 111
3.6.1 Sample preparation 111
3.6.2 Image analysis 113
3.6.3 Optical Microscopy 113
3.6.4 Scanning Electron Microscopy (SEM) 114
3.6.5 Electron Backscattered Diffraction (EBSD) 115
3.7 Distortion Measurements 115
3.8 Residual Stress Characterisation using Neutron Diffraction 116
3.9 Hardness 118
3.10 Heat Treatment 119
Chapter Four 120

4 Process Window development for DLF of IN718 120

4.1 Introduction 120

4.2 Powder Characterisation 120

4.2.1 Morphology and Size Distribution of Powders 121

4.3 Parametric Study for Thin Walled builds (stage I) 123

4.3.1 Effect of build parameters on thickness and height 125
4.3.2 Validation of Statistical Model on Thick Walled builds (Stage II) 130
4.3.3 Porosity 131

4.4 Solid Blocks (stage III) 133

4.5 Summary 137

Chapter Five 139

5 Thermal and Thermo-Mechanical Modelling of DLF: Model and Validation 139

5.1 Introduction 139

5.2 Modelling Strategy 140

5.3 Thermal and Thermo-Mechanical Model Set-up 141

5.3.1 Governing Equations 141
5.3.2 Geometry, mesh, boundary conditions and simplifying assumptions 145
5.3.3 Model calibration for η and efforts for reduction in computational time 150
5.3.4 Material Properties 155

5.4 Thermal and Thermo-Mechanical Analysis and Validation 157

5.4.1 Thermal Predictions 157
5.4.2 Thermo-Mechanical Model 158
5.4.3 Results and Validation 158
5.4.4 Discussion 166

5.5 Summary 181

Chapter Six 182

6 Microstructure and texture evolution in DLF 182

6.1 Introduction 182

6.2 Effect of Process Parameters on the Grain Structure and Texture: Thin-walled builds (stage I) 183

6.2.1 Effect of Deposition Path 183
6.2.2 Effect of Laser Power 193
6.2.3 Summary 201

6.3 Effect of Scan Strategy on Grain Structure: Thick Walled build (Stage II) 201

6.4 Microstructural Development in DLFed Solid Blocks (Stage III) 205

6.4.1 Bead Morphology: 206
6.4.2 Grain Size 210
6.4.3 Grain Selection and Texture: Influence of substrate texture 212

6.5 Precipitation in DLF of IN718 216

6.6 Effect of Heat Treatment on grain structure: Study on Thick Wall Samples (stage II) 226

6.7 Summary 227

Chapter Seven 230

7 Distortion and Residual stress Development due to Hybrid Manufacturing using DLF (stage III) 230

7.1 Introduction 230

7.1.1 Distortion 231
7.1.2 Correlation of Distortion with Cooling Rates 234

7.2 Residual stress (stage III) 239

7.3 Final Scale-up of deposition with optimum process conditions 246

7.4 Summary 250

Chapter Eight 252

8 Overall Conclusion and Future Work 252

8.1 Parametric study 252

8.2 Development of the transient thermo-mechanical model and validation 253

8.3 Microstructure and texture evolution in DLF 253

8.4 Distortion and Residual stress Development due to Hybrid Manufacturing 254

8.5 Recommendations for DLF of IN718 255

8.6 Proposed Future Work 257

9 References: 259

Appendix A: Engineering Drawings for Various Deposits 275

Appendix B: Temperature dependent Thermo-Physical properties for IN718 278

List of Figures

Figure 1-1: Examples of components produced via AM for aerospace application (a) Gear box spider (Courtesy: Red Bull), (b) Dual Wall Exhaust Duct for a military turbine engine through LENS (Laser Engineered net shaping) route (Courtesy: RPM & Associates Inc.) (c) Housing (Courtesy of Sandia National Laboratory) for defence applications, (d) Gas Thruster in Ti 6-4 (Courtesy: Bell Helicopter Inc.)[2] 3

Figure 1-2: Examples of repairs made by AM on: (a) an IN718 Compressor Seal repaired (Courtesy of RPM & Associates), (b) an IN718blisk airfoil repaired by laser powder deposition with the adaptive deposition path method, and (c) repair, post finishing for T700 Engine.[8] 3

Figure 1-3: The Overview of the Thesis. 8

Figure 2-1: Illustration of material usage in the Trent 800 engine. Note the Ni-based alloys are all in the combustor and turbine (Courtesy of Rolls-Royce [30]). 10

Figure 2-2: Influence of the alloying elements on the Ni-superalloys microstructure. Cross-hatching refers to beneficial minority elements, while horizontal hatching indicates detrimental tramp elements [26]. 11

Figure 2-3: Effect of various alloying additions to Ni-based superalloys with corresponding micrographs of the phases and precipitates [31] 13

Figure 2-4: The unit cell of the face-centred cubic (FCC) crystal structure, which is displayed by nickel [27]. 14

Figure 2-5: Crystal structure of the γ' - $Ni_3(Ti, Al)$ with Ni atoms at the face centres and Al atoms at the corners, Ti can take the place of Al in this phase [31]. 15

Figure 2-6: Superimposed ternary phase diagrams Ni–Al–X [35], illustrating the effect of alloying elements on the extent of the γ' phase field. 15

Figure 2-7: Transmission electron micrograph showing a large fraction of cuboidal γ' particles in a γ matrix of a Ni-based superalloy with composition Ni-9.7Al-1.7Ti-17.1Cr-6.3Co-2.3W at% (Courtesy of Hillier, Ph.D. Thesis, University of Cambridge, 1984; picture taken from [31]).....16

Figure 2-8: Crystal structure of the γ ″ (Ni_3Nb) phase with black circles denoting Nb atoms and white circles denoting Ni atoms [37].....17

Figure 2-9: Ni - Nb binary phase diagram. (Courtesy ASM International from[38]).....18

Figure 2-10: SEM of RR1000 showing extensive precipitation of the σ phase at γ grain boundaries, after a heat treatment of 5000 h at 750 ˚C [45].....20

Figure 2-11: SEM micrographs showing carbide phases in Ni-based superalloys (a) Ta-rich MC type carbide formed in an experimental nickel-based single-crystal superalloy [49] (b) $M_{23}C_6$ type carbide seen at the grain boundaries in Nimonic 80 alloy at a magnification of 6000 × [26].....21

Figure 2-12: Diagram showing the potential sequence of events leading to SAC [26].....22

Figure 2-13: Effect of Al and Ti content on susceptibility to strain-age cracking in Ni-base superalloys [51].....23

Figure 2-14: Curve showing the SAC behaviour for Waspaloy and IN 718 showing much greater tolerance for PWHT cracking for IN 718 due to slower aging rate [51].....23

Figure 2-15: Scanning electron micrograph showing the δ phase plates, γ″ discs and γ' spheroids in IN718 treated isothermally at 850˚C/24h [52].....24

Figure 2-16: Dark field TEM micrographs of IN718 aged at 800°C for 100 h showing γ′ (circular) and γ″(lens-shaped) precipitates in <100> direction; a) g = 100; b) g = 010; c) g = 110 [37].....26

Figure 2-17: DTA curves showing the different phase evolution in Inconel 718 for (a) cast and (b)wrought products [56] (The samples were heated and cooled at a rate of 40°C/min through melting/solidification range). 27
Figure 2-18: δ needles after prolonged exposure at 621 C for 5000 h in IN 718 alloy [57]. 28
Figure 2-19: Creep behaviour of IN718 as a function of the δ phase content showing excess delta precipitate leading to decreased creep resistance [60]. 29
Figure 2-20: The morphology of Niobium carbides in a sample quenched from 1243°C [66]. 30
Figure 2-21: Typical eutectic(left) and globular (right) type Laves phases that are seen in an as cast IN718 alloy [70]. 31
Figure 2-22: Time-Temperature-Transformation (TTT) curve of IN718 [71]. 31
Figure 2-23: Room and elevated temperature tensile results for wrought Inconel718 with various amounts of Laves [72]. 32
Figure 2-24: Morphologies of directionally solidified nickel based superalloys marked on log R (solidification rate) and log G (thermal Gradient) graph [77]. 35
Figure 2-25: Non-planar solidification structures in alloys (a) transverse section of a cellularly solidified Pb–Sn alloy (b) columnar dendrites in a Ni alloy (c) equiaxed dendrites of a Mg–Zn alloy (d) three-dimensional view of dendrites in a Ni-base superalloy [73, 78]. 35
Figure 2-26: Solidification map for IN 718 alloy [79]. 36
Figure 2-27: Schematic diagram showing the relationships between the heat source rate or travelling speed and the solidification front growth rate [3]. 37

Figure 2-28: Diagram showing variation of thermal gradient G_L and growth rate R_S along solidification front for different travelling speed (a) elliptical shape (low and moderate speed) (b) tear drop shaped (high speed) [73]. 39
Figure 2-29: Variation of pool shape and growth rate as function of welding speed for arc welded stainless steel [73]. 39
Figure 2-30: Schematic diagrams illustrating the effect of welding speed on the grain structure in welds: a) axial grains at low welding speeds b) stray grains for low to intermediate welding speeds and c) equiaxed grain structure for faster welding speeds [84]. 40
Figure 2-31: Schematic drawing of structural variation of weld microstructure across fusion zone[73]. 41
Figure 2-32: Illustration of different types of macro and micro residual stress [88].....42
Figure 2-33: Schematic Illustration of the capabilities of the various techniques. The destructive techniques are shaded [89]. 43
Figure 2-34: Dataset collected for stress in shot peened Ni-based alloy using hole drilling, showing a suitable arrangement of the strain gauges [90].....44
Figure 2-35: The principle of the neutron diffraction technique, for residual stress characterisation, showing the scattering vector for a Bragg reflection from the crystal planes, d [93]. 45
Figure 2-36: Table summarising the various methods for determining stress free d_0 values [94]. 47
Figure 2-37: 2D schematic of the contour method showing various steps involved in residual stress measurement and residual stresses calculated around the weld bead [98]. .48
Figure 2-38: Schematic of direct laser fabrication system layout[1].....50

Figure 2-39: Schematic showing the a) laser stand-off distance [101] and b) line overlap / hatch spacing between layers [102] in a DLF system. 51
Figure 2-40: Figure showing the effect of Z-overlap on inter-run porosity in a Ni-based superalloy Nimonic 80A: a) schematic showing the Z overlap distance, b) micrograph inter-layer porosity due to large Z overlap distance, c) micrograph showing no visible inter layer porosity after reducing the Z overlap distance by 50 % [105]. 52
Figure 2-41: Effect of the initial porosity in the build quality in DLFed IN 718 builds: a & b) showing the cross section of gas atomised (GA) and plasma rotating electrode process (PREP) powder, c & d) showing the corresponding laser builds with different porosity levels [22]. 53
Figure 2-42: Effect of scan speed on the: a)build height and b) porosity at different laser powers in DLFed Ti-6Al-4V alloy [9]. 54
Figure 2-43: Effect of powder flow rate on the porosity of the DLFed H13 tool steel builds at different laser powers [108].....55
Figure 2-44: The Variation in porosity and penetration depth of laser with varying powder flow rate and scan speed at 1400W laser power and 40% overlap between layers [101]. ..56
Figure 2-45: Process window showing the effect of laser power, travel speed in wire deposited IN 625 [115]. 57
Figure 2-46: Effect of linear energy and powder type on porosity in DLFed IN718 builds [22]. 57
Figure 2-47: Variation of Layer thickness with % overlap between laser passes[118]. 58
Figure 2-48: Optical micrographs of DLFed IN718 showing a) layered type morphology and b) magnified image showing fine dendrites [16]. 59

Figure 2-49: Optical micrographs of laser deposited Inconel 625 thin walls showing the effect of deposition direction on the dendrite orientation: a) bi-directional and b) uni-directional [17]. 61
Figure 2-50: Micrograph showing banded grain structure in DLFed IN718 [23].....61
Figure 2-51: The process map showing the regions for columnar and equiaxed grain zones in laser deposited CMSX-4: (a) showing the process map for different laser power (P) and G/R ratios (b) processing map for different laser power (P) and beam scanning speed (V); at different pre-heating temperatures (T_0) [82].....63
Figure 2-52: Grain width as a function of (a) scan speed/ travel speed at various laser powers and (b) incident energy for different build sizes in DLFed Ti-6Al-4V [9].....64
Figure 2-53: SEM micrograph showing the laves phases in DLFed IN718 [21].....65
Figure 2-54: Effect of heat treatment on the precipitation in DLFed IN718: (a) Laves phase transformed to δ needles after solution + aging treatment; (b) Considerable grain growth after Homogenisation+ solution + aging treatment [22] with occasional δ phase at the grain boundaries. 66
Figure 2-55: Schematic diagram of the sample cross-section geometry and texture measurement location (white rectangle box) for (a) the longitudinal direction, and (b) the transverse direction, (c) the definition of the <001> plane tilt with respect to the geometry and, d) a pole figure showing fibre texture tilted by 43.5˚ from Nz due to the unidirectional movement of the heat source along X: taken from Moat *el al*. [126] for laser deposited Waspaloy. 67
Figure 2-56: Effect of deposition direction on texture: (a) schematic of uni-directional scanning (b) Schematic of bi-directional scanning patterns; (100) pole figure of builds for c) uni-direction and d) bi-directional deposition patterns [18].....68

Figure 2-57: The microstructures of the laser deposited Inconel 625 sample annealed at different temperatures showing (a) No effect heat treatment on grain structure at 1000 C (b) Start of recrystallisation at the layer boundaries at 1100 C (c) Complete recrystallisation and grain growth at 1200 C[17]. 69
Figure 2-58: Tensile properties of DLFed IN718 samples in comparison to wrought and cast products (a) Showing the effect of heat treatment on the tensile, elongation and yield (b) fracture surfaces of the tensile samples at different heat treatments [22]. 72
Figure 2-59: Effect of aging temperature on hardness in laser deposited IN718 [18]. 73
Figure 2-60: Stress strain curves at different locations on a IN718 deposits in longitudinal and transverse deposition directions [11]. 74
Figure 2-61: Temperature and stress field around a welding heat source [137]. 75
Figure 2-62: The three components (X,Y parallel to the motion of melt-pool and Z- along the growth direction) of stress in rectangular samples as function of position along the growth direction for different rastering/deposition directions showing negligible stresses in X and Y directions and compressive stresses along growth direction [24]. 78
Figure 2-63: Residual stress contours in 5 mm thick Waspaloy deposits characterised by contour method a) longitudinal i.e. along the melt-pool moving direction and b) along build growth i.e. perpendicular to the substrate [25]. 78
Figure 2-64: Principal stress distribution along the length of thin stainless steel base plate of 60 mm long and 12 mm thick due to 3 layer wire arc deposition of size 5 mm wide and 2mm thick: (a) Stress in longitudinal direction (along 60 mm) distribution in the plate (b) Stresses in the three directions in the base plate along the length (along dotted lines in figure a) [137]. 79
Figure 2-65: Reflectivity of some materials as a function of wavelength (inner table showing the reflectivity values for 1.06μm radiation) [156]. 81

Figure 2-66: Temperature at the surface of the substrate laser powder : (a) laser beam attenuation by a 1ms^{-1} TA6V powder flow at 2 g min−1 and (b) temperature distribution of the powder stream just before dissolving in the melt pool [150, 162]. 85

Figure 3-1 : a) DLF system at UoB showing: a) The CO_2 laser, b) powder feeder, c) glove box with a 3-axis head, and d) a four nozzle assembly showing the powder focus. 98

Figure 3-2: Deposition modes (movement of the head) in a) Unidirectional (as in B1) and b) Bidirectional (as in B2) paths. 100

Figure 3-3: a) Thick wall build sample and b) different deposition paths used in stage II. 102

Figure 3-4: The hatched type laser deposition path employed for solid blocks, showing the infill deposition path in X and Y directions, with a contour scan after each layer. 105

Figure 3-5: schematic illustration of solid blocks deposited on the curved substrates (with a radius of curvature of ~ 495 mm) showing deposits: a) parallel to X-direction, and b) perpendicular to X direction. 106

Figure 3-6: The various deposition paths that were used in depositing rectangular blocks on the curved substrates : a) long, b) short, and c) hatched; d) and e) show how a deposition path is laid for short and long deposition paths. 107

Figure 3-7: The different deposition paths employed for stage III distortion studies. 108

Figure 3-8: Solid block of size 30 mm×30 mm×10 mm on a curved IN718substrate. 109

Figure 3-9: Schematic showing thermocouple locations for thick walls (the white dots representing the thermocouple location). 110

Figure 3-10: a) Back side of the substrate showing the location of thermocouples and b) Long type of deposition path on the substrate. 111

Figure 3-11: Diagram (not to scale) illustrating the investigated planes in the builds (red: X-Y (top) plane, black: X-Z (side) plane). 112

Figure 3-12: (a) Neutron diffraction setup at SALSA, ILL Grenoble for measuring the stresses in thick walls (b) schematic of neutron diffraction. 118
Figure 3-13: Post DLF heat treatment cycle for IN718 routine used in the current investigation based on [22].....119
Figure 4-1: Powder size distribution of gas atomised IN718powders.....121
Figure 4-2: SEM micrograph of gas atomised IN718 powder particles, with an insert micrograph showing the surface of a large particle.....122
Figure 4-3: BSe micrographs for the cross section of the powder showing a) inherent porosity, b) dendrite morphology inside powder particle. 122
Figure 4-4: Various problem encountered in the builds: (a) to (f) show thin wall builds with different process conditions as shown in the figure where P stands for laser power in watts, S is the scan speed in mm/min and PFR is the powder flow rate in g/min.....124
Figure 4-5: Variation of height and thickness of the samples at different scan speeds and powder flow rates for Unidirectional and bidirectional builds.....124
Figure 4-6: The model fit showing the predicted and actual values for: a) build thickness and b) build height.....128
Figure 4-7: Effect of individual process parameters on the thickness of the build. 128
Figure 4-8: Effect of individual process parameters on the height of the build. 130
Figure 4-9: Graph showing the interaction between laser power and powder flow rate at a scan speed of 400 mm/min. 130
Figure 4-10: Comparison of height and thickness of one bead for the thick wall builds with the model derived from DoE. 131
Figure 4-11: Porosity in the thin wall samples: a) Unidirectional build, b) bidirectional deposited with 390W laser power, 200 mm/min scan speed and, 18 g/min powder flow rate, and c) enlarged image of a pore.....132

Figure 4-12: Variation in porosity with laser power at a scan speed of 200 mm/min and a powder flow rate of 18 g/min. 132
Figure 4-13: Optical micrograph of polished thick walled build (P390_SS300_PFR18_L). 133
Figure 4-14: Locations in the solid blocks where the images were captured for porosity measurements. 135
Figure 4-15: Spatial variation in porosity (a) along the height of the build (b) across the length/width of the build. 137
Figure 5-1: Schematic illustration of a melt-pool showing the heat input and losses. 144
Figure 5-2: Meshing of the thermal model for a thick walled sample (stage II) showing the build, substrate and clamping. 146
Figure 5-3: (a) Geometry of the thick walled deposits used for thermo-mechanical modelling, and (b) mesh of thick walled section, showing the clamped surface at the base (dotted in red). 150
Figure 5-4: Temperature on the substrate at five different locations during DLF for deposition with a pre-scan and 8 layers (Laser power: 390W, scan speed: 400 mm/min, deposition path: short+ long). 151
Figure 5-5: Thermal reading on location TC1 for simulation run with different efficiencies (dotted line showing the actual thermocouple data for pre-scan). 153
Figure 5-6: Element and mesh optimisation, showing (a) the variation in temperature with mesh size (temperature taken at 1 mm below the deposit) and the (b) variation in temperature with multiple element activation (temperature taken at 3 mm below deposit). 155
Figure 5-7: Comparison of thermocouple and predicted data. (a) At all the 5 thermocouple locations (TC) for pre-scan and (b) at location TC5 showing pre-scan+6 layers. 157

Figure 5-8: FEA model showing the Von Mises stress distribution in the build due to DLF in the short deposition direction with process parameters of laser power: 390W, scan speed 300 mm/min and powder flow rate of 18.46 g/min. 160

Figure 5-9: Model results showing the temperature distribution at various layers of deposition during DLF with process parameters of laser power: 390W, scan speed 300 mm/min, powder flow rate of 18.46 g/min, and short deposition path (a) during pre-scan (b) 1^{st} layer (c-d) 4^{th} layer with beam in the middle and edge (e-f) 14^{th} layer when the beam is in the middle and edge (g-h) 19^{th} layer when the beam is in the middle and edge (The upper figures show the enlarged view of the bead, grey area showing the temperature which is above the melting point of IN718 of 1336°C). 162

Figure 5-10: FEA model results, showing the residual stresses in the three different directions of the deposit. (a) S11 (b) S22 (c) S33 (The process parameters are: laser power of 390W, scan speed 300 mm/min, powder flow rate of 18.46 g/min and short deposition path). 164

Figure 5-11: Residual stresses in all the three directions plotted across the deposit (along the dotted lines in Figure 5-8). The points represent the stresses characterised by neutron diffraction experiments. 166

Figure 5-12: Schematic diagram showing the tensile and compressive stresses generated near a melt-pool. 167

Figure 5-13: Stress in S11 direction during deposition of (a)pre-scan (b)1^{st} layer (c)4^{th} layer (d)14^{th} layer (e)19^{th} layer (f) after cooling down to room temperature.(The process parameters are: laser power of 390W, scan speed 300mm/min, powder flow rate of 18.46 g/min and short deposition path). 170

Figure 5-14: Residual stresses in the S11 (σ_x) directions plotted across the build (along the dotted lines in Figure 5-8) at different layers of the build. 171

Figure 5-15: Von-mises stresses distribution with various deposition paths (a) Short (S) (b) Long (L) and (c) Mixed (M). (The process parameters are: laser power of 390W, scan speed 300 mm/min, powder flow rate of 18.46 g/min). 172

Figure 5-16: Stress distribution in S11 (σ_x) and S33 (σ_z) direction for long, short and mixed deposition paths at the mid-section of the deposit (dotted region in Figure 5-8)...173

Figure 5-17: Temperature histories experienced by the substrate during various deposition paths (model results).....173

Figure 5-18: Model results showing the temperature distribution at various layers of deposition during DLF with process parameters of laser power: 390W, scan speed 300 mm/min, powder flow rate of 18.46 g/min and short with delay deposition path (a) 1st layer (b) 4th layer (c)9th layer d) 14th layer and e)19th layer (The upper figures show the enlarged view of the bead, grey area showing the temperature which is above the melting point of IN718 of 1336°C). 177

Figure 5-19: Temperature histories experienced by the substrate during various scan strategies. 178

Figure 5-20: Von-Mises stresses distribution with various deposition strategies: a) Short (S), b) short + delay (SD) and c) short + post scan (SP). (The process parameters are: laser power of 390W, scan speed 300 mm/min, powder flow rate of 18.46 g/min). 179

Figure 5-21: Stress distribution for short, short+deay and short+post scan strategies at the mid-section of the deposit (dotted region in Figure 5-8) in: a) S11 (σ_x) and b) S33 (σ_x) directions. 180

Figure 6-1: Optical micrographs showing the dendrites orientation and layer demarcation in (a) B1, (b) B2 and (c) schematic illustrations of the heat flux directions (not to scale). 185

Figure 6-2: The grain structure development due to DLF, showing the grain structure in (a) B1 with the equiaxed grain region between the layers and (b) in B2 showing the absence of a similar region. EBSD-IPF map of (c) B1 and (d) B2, also showing the same features..187
Figure 6-3: Grain Size distribution in B1 and B2 (a and b); Aspect ratio of B1 and B2 (c and d); Grain size and aspect ratio of fine grain zone between layers in B1 (e and f). 189
Figure 6-4: A Schematic illustration showing the dendrite orientations in B1 and B2 based on the microstructural observation of entire builds (not to scale). The dotted box represents the areas from which large EBSD maps were plotted (Figure 6-5).....190
Figure 6-5: EBSD maps for Unidirectional (a), bidirectional deposits (b). The dotted boxes show the equiaxed grain regions. 192
Figure 6-6: {100} pole figures plotted parallel to the Z direction, on one layer of a) B1 and b) B2 depositions, and of the entire map for c) B1 and d) B2 (bottom picture shows the schematic of the build with directions).....193
Figure 6-7: a) Optical micrograph showing the dendrite orientations in B3 and (b) a schematic illustration of the heat flux directions (not to scale). 194
Figure 6-8: BSE micrographs showing the influence of laser power on the grain morphology and size at a constant scan speed of 200 mm/min in bi-directional laser deposits: a) 390W, b) 474W, c) 580W, d) 693W (all at a powder flow rate of 18 g/min), e) 910W at 12 g/min, and f) 910W at 5 g/min (B3). 196
Figure 6-9:(a-c) Variation in grain size with laser power at 390, 580, and 910 W (12 g/min) and the aspect ratio for the corresponding grain sizes (d-f).....196
Figure 6-10:a) IPF coloured EBSD map showing large columnar grains in B1 b) A schematic diagram of the grain/ dendrite orientation of the entire build (not to scale) with the dotted box showing the region mapped by EBSD, and c) {100} pole figure plotted parallel to Z (growth direction). 200

Figure 6-11: EBSD maps (2 mm × 5 mm area from bottom to top) in the XZ plane of the thick walled samples, showing the grain distribution in different scan strategies a) long b) long+ delay c) long+ post scan (with other process parameters constant). 203
Figure 6-12: {100} nickel pole figures plotted as seen from the top of the build for a) long b) long+ delay c) long+ post scan strategy for the maps in Figure 6-11. 204
Figure 6-13: Optical micrographs for the solid block structure showing (a) the XZ plane (showing beads from bottom to 5 mm) and (b) the XY plane (taken at a plane 5 mm from the substrate) ; schematic showing the locations from which the micrographs were taken. 206
Figure 6-14: Microstructure of DLF IN718 solid block in the XZ plane, showing (a) an optical micrograph for the bead morphology showing the dendrites (white bands) protruding from the bead boundary to the centre, (b) BSE SEM micrograph of a bead showing columnar grains from the bead boundary to centre, and (c) IPF, map of the bead showing the grain morphology with different regions marked as A, B and C. 207
Figure 6-15: (a) Inverse pole figure (IPF) map showing the XY, XZ and YZ planes of the build, (b) Schematic showing 3D bead morphology. 209
Figure 6-16: IPF map of the XY plane (top view) of the build showing the overlap of two passes, and the corresponding pole figure for the two layers. 210
Figure 6-17: (a) Grain size distribution in a 1 mm × 1 mm area at the centre of the build, and (b) grain size variation from the bottom to the top of the build.....211
Figure 6-18: EBSD map from the bottom to the top of the XZ plane of the build. 213
Figure 6-19: Pole figures plotted at different layers of the build as marked in Figure 6-18. 214
Figure 6-20: Optical micrograph of B1 sample etched with Kelling's reagent showing different regions of the build: a) bottom b) middle and c) side. 217

Figure 6-21: BSE micrographs showing the dendrite morphology at the a) bottom, and b) middle of the builds for the sample in Figure 6-20. 217
Figure 6-22: Hardness contours in the thin-walled samples (B2 sample). 218
Figure 6-23: Hardness development due to DLF, showing: a) hardness traces (from bottom to top) in B1 and B2 samples b) Variation in hardness with laser power keeping the other process parameters constant (measures at the centre of the build taken from an average of 10 points). 218
Figure 6-24: BSE SEM micrographs showing the intermetallic precipitates in (a) B2 (lower inset shows the γ′ and Laves phases at higher magnification) and (b) B3 (lower inset shows the δ needles at Laves phases and carbides at higher magnification). 220
Figure 6-25: (a) BSE SEM micrograph of sample B2 showing a number of EDS point scans, and their respective chemical compositions of the various precipitates (b) EDS of sample B2 showing the composition of line scans of γ′ phase. 221
Figure 6-26: The precipitation in DLF solid blocks with inner figures showing carbides and γ′ phases. 223
Figure 6-27: Variation in hardness in the deposition and substrate for thick walled samples before and after heat treatment. 224
Figure 6-28: (a)Precipitates after solution and ageing heat treatment showing γ′ at the grain centre and δ and carbides at the grain boundaries (inner figures showing the enlarged images of the precipitates; (b) γ′ (c) carbide and (d) δ needles). 225
Figure 6-29:EBSD map showing the grain distribution of the build and the substrate in the (a) as deposited condition and (b) after solutionising and ageing heat treatment at 1093°C (with process parameters as in Figure 6-11.a). 227

Figure 7-1: Effect of the deposition path on the distortion on a curved substrate (stage III): a) along the X-axis b) along the Y-axis. The vertical lines show the location of the build and the dotted curve shows the substrate profile before deposition. 232
Figure 7-2: Distortion in the curved substrate along X-axis: a) showing the effect of laser power and b) showing the effect of the build orientation to the substrate on the distortion. The dotted curve shows the substrate profile before deposition. A hatched type deposition path is used. 234
Figure 7-3: Thermal cycles at different thermocouple locations (see the location in Figure 3-10) for different deposition paths (stage III): a) long b) short and c) mixed. Thermocouple 1 and 8 are at the extreme ends of the substrate without deposition on the top. 237
Figure 7-4: Distortion contours of the substrate in a) long b) short and c) mixed deposition paths (as represented in stage III). 238
Figure 7-5: The correlation between a) distortion and b) the corresponding cooling rates in the substrate along the centre line near the 8 thermocouple locations. 239
Figure 7-6: Effect of laser power on residual stress distribution in the substrate: a) σ_x stress along X axis, b) σ_y stress along X axis, c) σ_x stress along Y axis, and d) σ_y stress along Y axis.....243
Figure 7-7: Effect of deposition path on residual stress distribution in the substrate: a) σ_x stress along X axis, b) σ_y stress along X axis, c) σ_x stress along Y axis, and d) σ_y stress along Y axis. 244
Figure 7-8: Effect of build orientation on residual stress distribution in the substrate: a) σ_x stress along X axis, b) σ_y stress along X axis, c) σ_x stress along Y axis, and d) σ_y stress along Y axis. 245

Figure 7-9: Stress distribution on the substrate due to DLF of solid block showing the variation of stress along the X axis.....247
Figure 7-10: Contour maps for residual stress distribution in XZ plane of solid block on a thin substrate a) schematic showing the area where the stress contours were plotted b-d) residual stress contours in σx, σy and σz directions. 249

Table of Contents

Table 2-1: Summary of the general effect of various alloying elements on phase stability in Ni - base alloys (Courtesy ASM International [28]). 12

Table 2-2: Chemical composition of IN718 (Wt. %)[27] 22

Table 2-3: Three standard heat treatment methods employed for IN718according to Aerospace Material Specifications (AMS)[21]. 33

Table 2-4: Young's modulus for different IN718 sample states and lattice planes determined by neutron diffraction compared with diffraction elastic constants for pure nickel calculated with a computer software based on the Kröner model [95]. 47

Table 2-5: Mechanical properties of as-deposited IN718 AM parts in comparison with wrought and as-cast products. 70

Table 2-6: Normal, spectral absorption of materials at important laser wavelengths [156]82

Table 3-1: Chemical composition of the IN718 powder batch (provided by the supplier) showing the weight % of the alloying elements. 96

Table 3-2 : Various deposit parameters with constant power of 390 W. 99

Table 3-3: Process factors and corresponding levels in the DoE study.....100

Table 3-4: Parameters with varying laser power and powder flow rate. 101

Table 3-5: Various deposition paths and strategies employed for thick wall samples.....103

Table 3-6: Process factors and corresponding levels.....104

Table 3-7: Process parameters for the deposits on the curved substrates, with a scan speed of 500 mm/min at the first few layers and 400 mm/min in the rest of the build. Powder flow rate was kept at 25.5 g/min.....107

Table 4-1: Oxygen pick-up in the build during laser deposition in controlled Ar atmosphere and air at two laser powers keeping scan speed at 200 mm/min and powder flow rate at 18.6 grams/min. 125

Table 4-2: Central composite DoE running conditions and the corresponding bead width and height measured using a screw gauge (±0.05 mm).....126
Table 4-3: Process parameters and corresponding P-value with significant factors highlighted.....128
Table 4-4: Coefficient values corresponding to process parameter. 129
Table 4-5: Central composite DoE running conditions and the corresponding porosity. .134
Table 5-1: Deposition paths and scan strategies used in the simulations (laser power: 390W, scan speed 300 mm/min and powder flow rate of 18.46 g/min). 150
Table 5-2: Various input parameters used in the model.....153
Table 5-3: Temperature dependent density, heat capacity an thermal conductivity of IN718 (* melting range) [194].....156
Table 6-1: Composition of various phases in laser deposited IN718.....226

Nomenclature

Symbol

Item	Units	Description
α	K^{-1}	Coefficient of thermal expansion
γ	-	Absorption rate
ε	-	Emissivity
ε_e	-	Elastic strain
ε_P	-	Plastic strain
ε_T	-	Thermal strain
ε_{hkl}	-	Elastic strain normal to the hkl plane
η	-	Efficiency of laser process
λ	$W\ m^{-1}\ K^{-1}$	Thermal conductivity
ρ	Kg/m^3	Density of the material
σ	$5.67 \times 10^{-8}\ W/m^2.K^4$	Stefan-Boltzmann constant
σ_x/S11	$Kg\ m^{-1}s^{-2}$	Stress in the direction of the moving melt pool in X
σ_y/S22	$Kg\ m^{-1}s^{-2}$	Stress in the direction of the moving melt pool in Y
σ_z/S33	$Kg\ m^{-1}s^{-2}$	Stress along the deposit growth direction
Γ	m^2	Laser beam spot size
C_p	$JK^{-1}Kg^{-1}$	Specific heat capacity
h	W/m^2	Convection coefficient
P	$kg{\cdot}m^2/s^3$	Laser Power
Q_{flux}	J/Kg	Heat flux
q_x	J/Kg	Horizontal heat flux i.e. flux along melt-pool moving direction
q_z	J/Kg	Vertical heat flux i.e. flux along deposition growth direction
q_r	J/Kg	Resultant of horizontal and vertical heat flux
PFR	Kgs^{-1}	Powder Flow Rate
SS	Ms^{-1}	Scan speed
T	K	Temperature

Acronyms

Item	Description
AM	Additive Manufacturing
ANOVA	Analysis of Variance
B1	Sample deposited in Unidirectional deposition path
B2	Sample deposited in Bidirectional deposition path
B3	Sample deposited in Bidirectional deposition path at high laser power (910W)
BSE	Back-scattered electrons
d^0	Stress-free d-spacing
DAS	Dendrite Arm Spacing
DLF/ DLD	Direct Laser Fabrication/ deposition
DoE	Design of Experiments
DSC	Differential Scanning Calorimetry
EBSD	Electron backscattered diffraction
EDM	Electric Discharge Machining
F_{max}	feret max
FCC	Face centred cubic
FEM	finite element models
HAZ	Heat Affected Zone
HIP	Hot Isostatic Pressing
HSTA	homogenisation, solution and ageing heat treatment
IN718	Inconel 718
L	Long deposition path
M/H	Mixed/ hatched type deposition paths
NNS	Near-net Shape Manufacturing
PFR	Powder Flow Rate
S	Short deposition path
SD	Short deposition path with a delay
SEM	Scanning Electron Microscopy
SP	Short deposition path with post laser scan
UoB	University of Birmingham

Chapter one

1 Introduction

Near-net shape manufacturing (NNS) through Additive Manufacturing (AM) has gained considerable attention in the aerospace industry due to its many potential benefits, including shortened lead time, reduction in process steps, and more design freedom. Over past years, there has been an increasing demand for industrial use of AM. Thus, it is important to develop a better scientific understanding of the process capabilities and limitations.

1.1 Metallic Additive Manufacturing

Metallic AM is a manufacturing approach whereby solid components can be produced by consolidating metal powders or wire using a focused heat source. The heat source can be laser, electron beam, plasma or electric welding arc. A 3D geometry is formed by depositing-up a stack of 2D profiles layer-by-layer, by local melting [1]. Direct Laser Fabrication/ deposition (DLF/ DLD) or Laser Engineered Net Shaping (LENS®, developed at Sandia National Laboratory, USA), is an AM technique which uses a laser as a heat source to melt the powder which is blown in a controlled manner. DLF is used for overhaul, repair, near net-shape component manufacture, and hybrid manufacturing [2]. The term hybrid manufacturing in this thesis refers to adding a feature in the existing part. Other than DLF there are other AM techniques, including powder bed (using laser or electron beam heat sources) used to produce intricate shapes. Additionally process techniques such as, arc plus wire deposition, are being developed to achieve higher deposition rates [3-4].

1.2 Advantages and Applications of AM Metallic Structures

The following main factors outline the potential benefits for AM in the aerospace manufacturing industry:

i. AM is a NNS manufacturing route, that results in a reduction in the extent of machining and finishing operations required to produce the final component, hence reducing the buy to fly ratio. Figure 1-1.a shows a "Gearbox Spider" produced through AM route, which took 1h for deposition, considerably reducing the material waste and production time compared to conventional casting and machining route which takes 10h for machining wasting up to 98% of material.

ii. Complex or bespoke shapes can be manufactured in short times without the need for tooling as in forging or casting, which typically requires several months of design and manufacture. Figure 1-1.b-d; show a few examples where the final parts were produced after several design changes during manufacturing, reducing the final cost of production by 65%.

iii. Functionally graded materials can be produced through this route [5-6], which allows the chance to rapidly explore new alloys.

iv. The buy-to-fly ratio of components produced through AM approaches 1.5:1 when compared to 20:1 for the normal ingot cast-roll-forging and machining routes [2, 7]. AM uses 90% less raw materials than traditional methods [3, 7].

v. Other than manufacturing of structural components AM, in particular DLF is also useful in repairing existing parts. AM has the potential to compete with existing repair methods and to enable previously impossible repairs in certain circumstances. In this case, the cost and restoration of mechanical performance are the key factors. Blown powder AM has been used to repair advanced turbine engine compressor or blisk airfoils, in addition to the manufacture of structural components [2, 8]. Figure 1-2

shows examples of repairs carried out using AM for IN718 compressor seals and blisk airfoil components [2, 8].

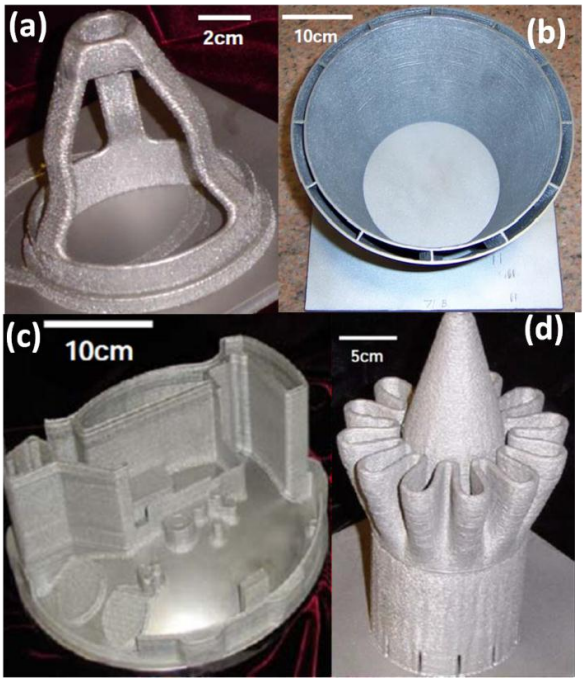

Figure 1-1: Examples of components produced via AM for aerospace application (a) Gear box spider (Courtesy: Red Bull), (b) Dual Wall Exhaust Duct for a military turbine engine through LENS (Laser Engineered net shaping) route (Courtesy: RPM & Associates Inc.) (c) Housing (Courtesy of Sandia National Laboratory) for defence applications, (d) Gas Thruster in Ti 6-4 (Courtesy: Bell Helicopter Inc.)[2]

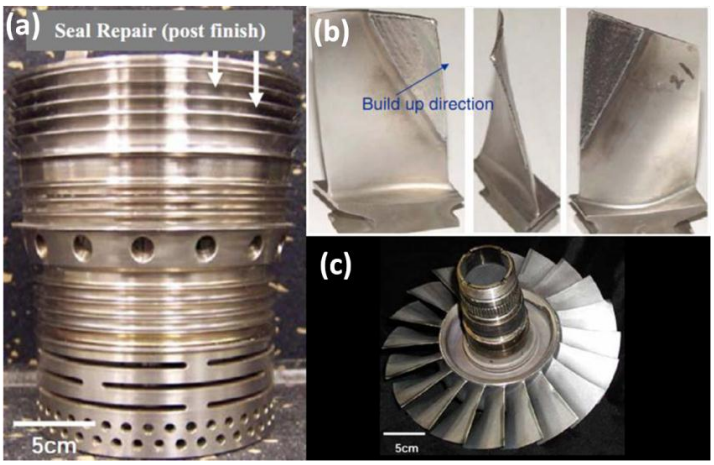

Figure 1-2: Examples of repairs made by AM on: (a) an IN718 Compressor Seal repaired (Courtesy of RPM & Associates), (b) an IN718blisk airfoil repaired by laser powder deposition with the adaptive deposition path method, and (c) repair, post finishing for T700 Engine.[8]

1.3 Limitations and Issues with AM

There are some obvious limitations for AM, the most relevant of which include:

i. The process has relatively low deposition rates and low deposit volumes in the case of powder bed methods.
ii. High capital investments are required to set up the machine.
iii. It is difficult to detect and control the defect formation during the process.
iv. Repeatability and reproducibility of the parts has to be established for each component and there are no reliable standards for this method developed yet.

1.3.1 Issues with Metallic AM

The build geometry and microstructure of components of AM products are affected by several process parameters including laser power, scan speed, powder flow rate, spot size, deposition direction, overlap between layers and other parameters. The microstructure of the AMed products is also highly dependent on the substrate microstructure. In addition, the number of possible variations in raw materials (powder type), deposition systems, and part-specific geometric variables complicate the development of transferable process maps and appropriate process control procedures [9-12]. This can also result in a degree of microstructural in-homogeneity within the single part, leading to difficulties in characterising and predicting structural performance in designing parts for aircraft assemblies [13-14]. In AM, the majority of these characteristics are directly related to either transport phenomena (e.g. fluid flow, heat transfer, and diffusion) or to metallurgical phenomena (e.g. melting, solidification, solid-state phase transformations, and solid-state deformation). There is therefore a need to understand the relationship between the process parameters and the microstructure-property development to identify the critical process parameters that influence the microstructure in the final component.

1.3.1.1 Issues with IN718

IN718 is a good weldable alloy and consequently it does not form cracks during DLF, however, the microstructure of DLFed IN718 shows a banded microstructure with coarse columnar grains as well as fine grains at the layer interface [15-16] due to the cooling rates associated with the process. This banded microstructure would result in non-uniform mechanical properties at different locations of the build. In addition, the orientation of the grains is dependent on the sense of movement of the heat source [17-18] which would also lead to further non-uniformity in the mechanical properties of the build [19].

IN718 is an alloy strengthened by precipitates that are formed during the ageing heat treatment. Due to the high temperatures associated with the process the usual strengthening phases are not precipitated on cooling. Instead segregation of heavy elements, like Nb, occurs during solidification which in turn results in the formation of Laves phase. This phase is brittle and is detrimental to the mechanical properties.

1.4 Aim and Objectives of the Project

The overall aim of this project is to study the process-material interaction in DLF, focusing on the influence of the process variables that affect the build quality, microstructural inhomogeneity, and development of residual stresses in the build as well as in the substrate of DLF IN718 alloy. Although DLF is reasonably established in terms of obtaining defined geometry by optimising the process parameters [8-9, 20] limited work is available on the control of the deposited microstructure. The research showed that the laser process parameters and the type of powder chosen have a profound effect on porosity content. Still, there is a need to understand the variation in porosity. It is known that that the microstructure of DLFed Ni-based superalloys shows a banded microstructure with coarse columnar grains [15-16]. In addition, the orientation of the grains is dependent on the sense of movement of

the heat source [17-18]. Limited information is available on the microstructural and texture development at each layer, and the effect of substrate texture on the build. It is also important to obtain key process parameters in order to attain the desired microstructure (columnar or equiaxed). DLF In718 leads to the formation of the detrimental Laves phase, which has a strong influence on the mechanical properties. Laves can generally be dissolved with heat treatment [21-22], but it will be useful to understand the impact of the process parameters on size, shape and morphology of these precipitates. This could potentially lead to a change in the mechanical properties of the final components, or may avoid the need for post DLF heat treatment.

DLF is also used in repair applications in the aerospace industry. For DLF repair applications it is useful to understand the influence of the process parameters on the properties of the part being repaired especially the distortion, microstructure, and residual stress development in the deposit and the original structure. In the previous studies residual stress characterisation was performed in the build to understand the stress distribution across the build [23-25] with various process parameters. Limited work is available on the residual stress development in the substrate (or the component being repaired). It is important to understand the effect of deposition path and the related thermal fields in the build to obtain optimum deposition strategy for minimum distortion and residual stresses. This will also be of interest in the potential use of DLF for hybrid manufacturing applications.

The current project has focussed on DLF IN718 specimens. These specimens were studied to address the following key objectives,

i. To optimise DLF process parameters for IN718 to build sound structures of various geometries (thin walls, thick walls and solid blocks). To identify the key process

parameters that affect the build geometry (i.e. height and thickness of build) and build quality (like porosity, bonding defects etc.).

ii. To characterise the texture development due to DLF of IN718, and its variation with deposition strategies and laser power.

iii. To characterise how the microstructure reacts to geometrical changes (build size) by studying the microstructure in thin walls, thick walls and solid blocks.

iv. To characterise the deposited layer forms, and the influence of subsequent thermal cycling during each following deposition pass and to understand the effect of the prior substrate texture on the deposit texture.

v. To assess the influence of the deposition strategies and laser parameters on the distortion and residual stress development and correlate these with the cooling rates.

vi. To investigate the benefits of novel deposition strategies to modify the grain structure to obtain fine grained structures and control the residual stresses development.

vii. To develop simple thermal and thermo-mechanical DLF models to understand the development of stresses in the substrate due to DLF and validate the models using experimental techniques for residual stress measurement (neutron diffraction).

1.5 Thesis Outline

The thesis is divided into 6 chapters with a literature review, an experimental section and, 3 results and discussion chapters. The literature review discusses the metallurgy of Ni-based superalloys, and in particular IN718, the field of AM, and the solidification and precipitation kinetics of relevance to the AM process. The history of production of metallic components by DLF is also discussed alongside the relevant and recent literature available on the DLF process. The following chapter on experimental and characterisation techniques describes the experimental procedures used to carry out all of the investigations in this work and, the

methods of metallographic preparation and analysis used to characterise the IN718 samples. In the results and discussion chapter initially a simple thermo mechanical model was developed to understand the temperature distribution in the deposit and substrate and the resulting residual stresses during DLF of IN718 walls used in repair applications. Later process optimisation was done to obtain geometrically sound builds. Microstructure evolution, precipitate morphology and texture are then discussed for various process conditions and build geometries and other novel modifications in the processes. Finally the distortion residual stresses were characterised on a curved substrate, representing hybrid manufacturing, due to laser deposition. The key conclusions and suggestions for further study as a result of this present investigation are presented at the end of the thesis. The outline of the thesis can be schematically drawn as shown in Figure 1-3.

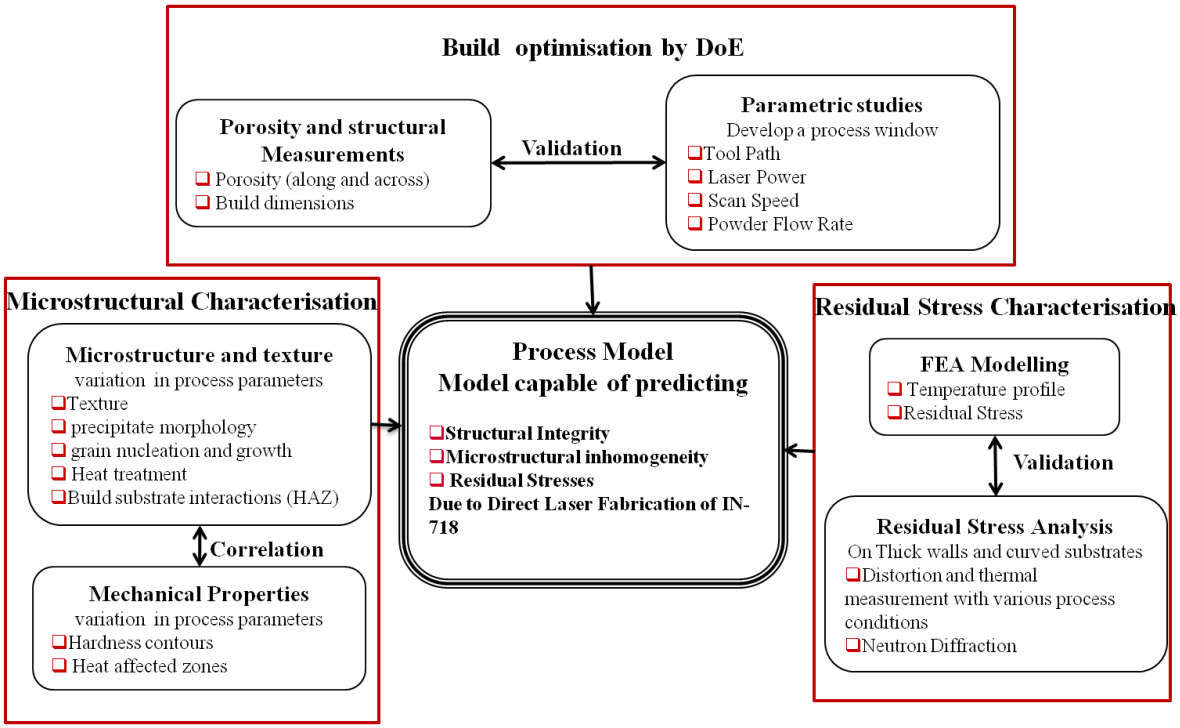

Figure 1-3: The Overview of the Thesis.

Chapter Two

2 Literature Review

This chapter reviews the published literature on the metallurgy of Ni-based superalloys, focusing on its solidification behaviour of AM, in particular using DLF. The reviews on DLF of Ni-based superalloys focus on the mechanical properties, microstructural, and residual stress development, alongside the thermal and thermo-mechanical modelling of DLF. Emphasis is given to Ni-Fe-based superalloys (IN718), which is the alloy used in the current study.

2.1 Metallurgy of Nickel-based Superalloys

2.1.1 Introduction

Superalloys can be traditionally categorised into one of three main classes. The first to be developed are known as Ni-Fe-based superalloys. These alloys contain high wt. % Fe which acts as a joint base material with Ni [26] . Most of these alloys display a solid-solution strengthening mechanism similar to Ni-based superalloys yet show a spherical rather than cuboidal precipitation of the strengthening γ′ phase [26] and are typically used as wrought rather than cast materials[27-28]. The second category is Ni-base superalloys, which contain the majority of currently used blade alloys and can themselves be subcategorised depending on microstructure (i.e. strengthening mechanism) and composition. The final category is Co-based superalloys which use cobalt as the base material. These alloys typically rely on strengthening by elements within solid-solution and the formation of carbides for their high temperature properties[26].

Ni-based superalloys are considered for high temperature applications (about 1370 ºC) whereas Ni-Fe-based superalloys such as the popular alloy IN718 are used at lower temperatures (up to 650 ºC). At lower temperatures, and dependent on the type of strength needs for an application, Ni-Fe-based superalloys find more use than Co- or Ni-based superalloys because they are economical due to less expensive alloy additions when compared to Ni-based superalloys [26].

The vast majority of use by tonnage of these alloys is found in turbines, both for aerospace applications and for land-based power generation. Ni-based superalloys are used primarily in turbine blades, turbine disks, combustion casings, and vanes in modern engines. Figure 2-1 illustrates the materials used in the Trent 800 engine, which is the Rolls-Royce engine used in the Boeing 777. Ni-base superalloys currently constitute over 50 % of the weight of advanced engines [27]. The combination of strength and toughness at high temperature, makes Ni-based superalloys the material of choice for high performance high temperature applications [29].

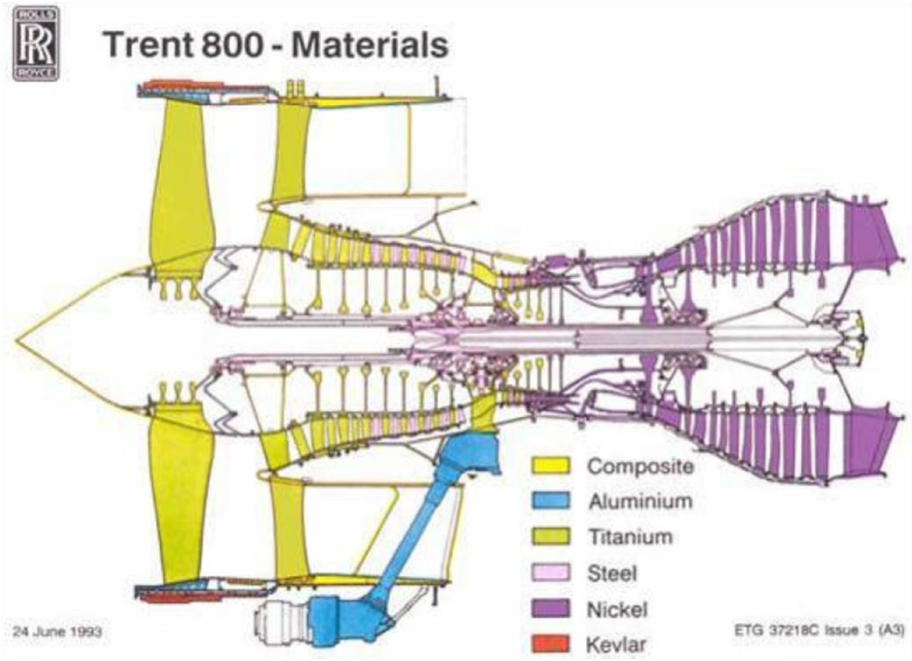

Figure 2-1: Illustration of material usage in the Trent 800 engine. Note the Ni-based alloys are all in the combustor and turbine (Courtesy of Rolls-Royce [30]).

2.1.2 Influence of alloying additions in Ni and Ni-Fe based superalloys

The austenitic FCC matrices of Ni-Fe- and Ni-based superalloys have extended solubility for some alloying additions, excellent ductility, and favourable characteristics for precipitation of uniquely effective strengthening phases. Ni is capable of dissolving high concentrations of alloying elements compared to other metals. The major alloying additions for Ni-based superalloys and their influence on the properties and microstructure are shown in Figure 2-2 and Table 2-1 summarises the influence of various alloying elements on the phase stability in Ni-based superalloys.

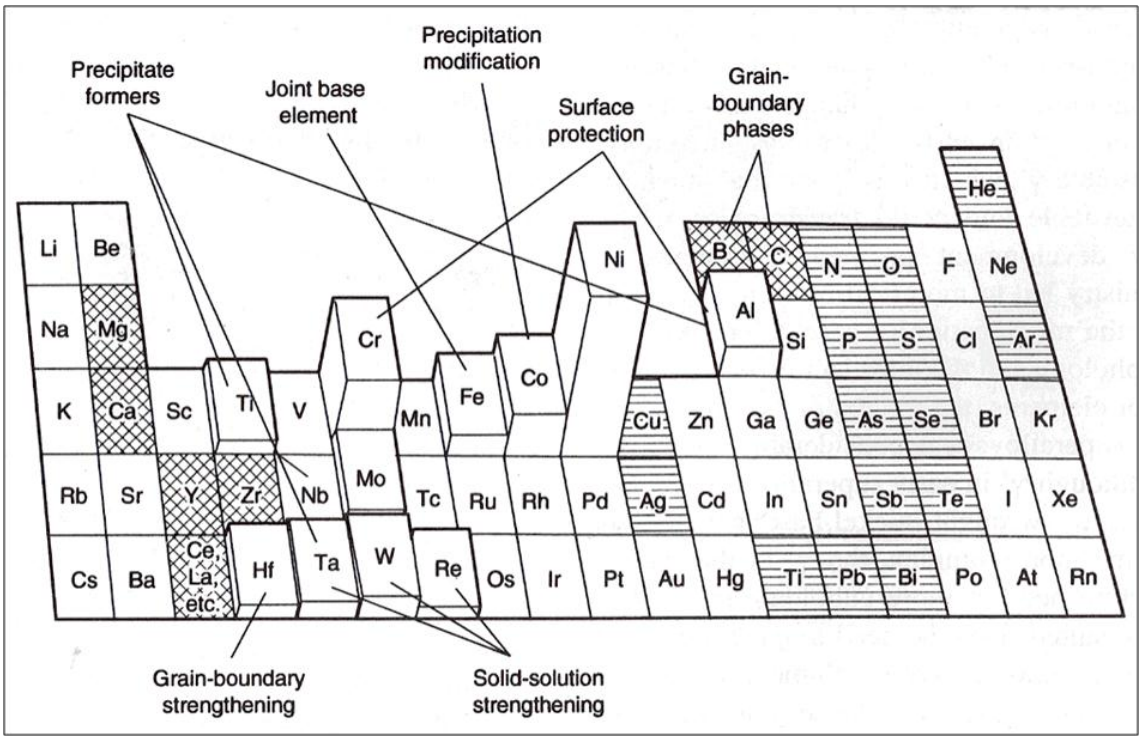

Figure 2-2: Influence of the alloying elements on the Ni-superalloys microstructure. Cross-hatching refers to beneficial minority elements, while horizontal hatching indicates detrimental tramp elements [26].

Table 2-1: Summary of the general effect of various alloying elements on phase stability in Ni - base alloys (Courtesy ASM International [28]).

Effect	Element
Solid Solution Strengthener	Co, Cr, Fe, Mo, W, Ta
γ'-$Ni_3(Al,Ti)$ Former	Al, Ti
Solid Solution Strengthening of γ'	Cr, Mo, Ti, Si, Nb
γ''-Ni_3Nb Former	Nb
Carbide Formers:	
MC and M(C,N)	W, Ta, Ti, Mo, Nb
M_7C_3	Cr
$M_{23}C_6$	Cr, Mo, W
M_6C	Mo, W
TCP Phase (σ, P, μ, Laves)	Ti, V, Zr, Nb, Ta, Al, Si
Surface Oxide (Cr_2O_3/Al_2O_3) Fromer	Cr, Al

Figure 2-3 shows the phases and precipitates that are formed due to various alloying additions to Ni-based superalloys. Elements that exhibit atomic radii, electronic structure, and crystal structure relatively similar to Ni are most likely to remain in solid solution. The ability of a dissolved element to increase strength by solid - solution hardening can be assessed by its atomic size difference compared to that of Nickel. Co, Cr, Fe, Mo, and Ta are generally used as solid solution strengtheners. Although Ti and Al can be effective solid-solution strengtheners due to their atomic radii mismatch and appreciable solubility, they typically improve strength by precipitation of the γ' - Ni_3 (Ti, Al) phase in Ni base superalloys. Niobium is also an effective strengthener and is used for both solid-solution strengthening and for its ability to strengthen by promoting precipitation of the γ'' - Ni_3Nb phase.

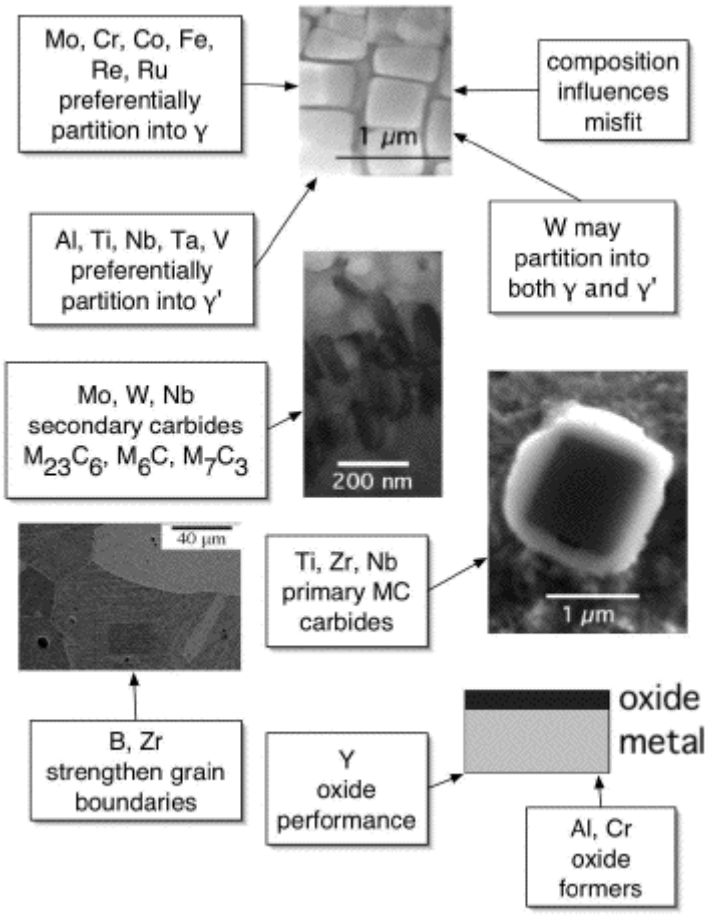

Figure 2-3: Effect of various alloying additions to Ni-based superalloys with corresponding micrographs of the phases and precipitates [31].

2.1.3 Phases in the superalloys

2.1.3.1 The gamma phase (γ)

The FCC γ phase in nearly all cases, forms a continuous matrix phase in which the other phases reside. It contains significant concentrations of elements such as cobalt, chromium, molybdenum, ruthenium and rhenium, where these are present, since these prefer to reside in this phase. Being FCC, the γ phase displays the lowest diffusivity relative to its melting point and the highest normalised activation energy(Q/RT) for diffusion among the various crystal classes of transition metals [32]. These two properties make FCC γ phase display better creep properties than other crystal structures such as HCP and BCC [33].

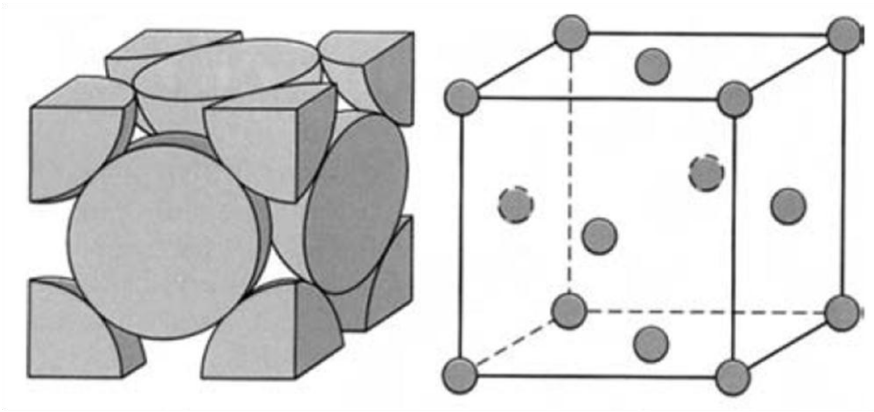

Figure 2-4: The unit cell of the face-centred cubic (FCC) crystal structure, which is displayed by nickel [27].

2.1.3.2 The gamma prime phase (γ')

The Ni–Al system exhibits a number of solid phases other than the FCC. The Ni–Al bonding is preferred over the Ni–Ni or Al–Al bonds. A strong degree of chemical ordering is displayed by these phases. The chemical formulae of these phases are Ni_3Al, NiAl, Ni_2Al_3, $NiAl_3$ and Ni_2Al_9. Among these phases, the γ′ phase (Ni_3Al) displays the primitive cubic, $L1_2$, crystal structure (see Figure 2-5), with Al atoms at the cube corners and Ni atoms at the centres of the faces. The various alloying additions have an influence on the formation of the γ' phase. The ternary phase diagram Ni-Al-X (Figure 2-6), where X can be Cr, Co, Ti, Ta, etc. illustrates the effect of alloying addition on γ' phase where elements like Co and Pt promote this phase, whereas elements like Ti and Ta replace Al.

The γ′ precipitates in a cube-cube orientation relationship with the γ phase [27] and its cell edges are exactly parallel to corresponding edges of the γ phase. As the γ' is an atomically ordered structure, the dislocations find it difficult to penetrate into this phase thereby strengthening the alloy. The dislocation movement depends on the size of these precipitates, where in small precipitates the ½<110> dislocation pairs would cut through and in large γ' precipitates they bypass by Orowan looping [34]. A large fraction of γ′ (typically in excess of

0.6) is used in aeroengine applications in turbine blades where the temperatures exceed 1000°C. Figure 2-7 shows the characteristic cuboidal γ′ structure within the nickel-base superalloy.

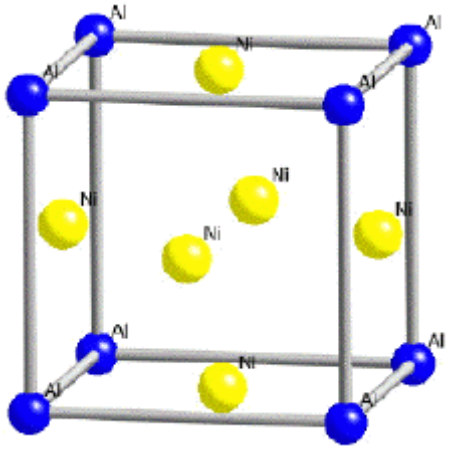

Figure 2-5: Crystal structure of the γ ′ - Ni_3(Ti, Al) with Ni atoms at the face centres and Al atoms at the corners, Ti can take the place of Al in this phase [31].

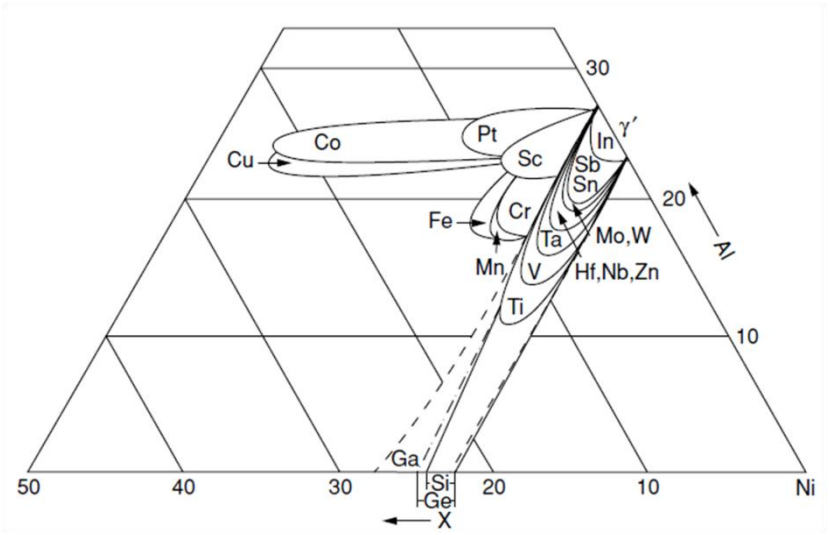

Figure 2-6: Superimposed ternary phase diagrams Ni–Al–X [35], illustrating the effect of alloying elements on the extent of the γ' phase field.

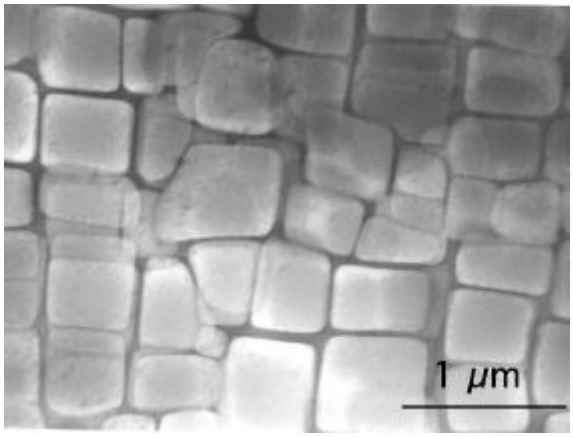

Figure 2-7: Transmission electron micrograph showing a large fraction of cuboidal γ' particles in a γ matrix of a Ni-based superalloy with composition Ni-9.7Al-1.7Ti-17.1Cr-6.3Co-2.3W at% (Courtesy of Hillier, Ph.D. Thesis, University of Cambridge, 1984; picture taken from [31]).

2.1.3.3 The gamma double prime phase (γ'')

In Ni-Fe-based superalloys (e.g. IN718 and IN706), which contain quantities of niobium, a coherent body-centred tetragonal (BCT) ordered compound (Ni_3Nb) with $D0_{22}$ crystal structure (Figure 2-8) is formed as primary strengthening phase instead of γ′ [36]. The Ni - Nb binary phase diagram is shown in Figure 2-9. The γ″ phase (Ni_3Nb) follows a simple eutectic reaction involving γ and Ni_3Nb at 22.5 wt% Nb. The γ phase exhibits a maximum solubility of 18.2 wt. % for Nb, which increases by 50% with addition of Cr and Fe.

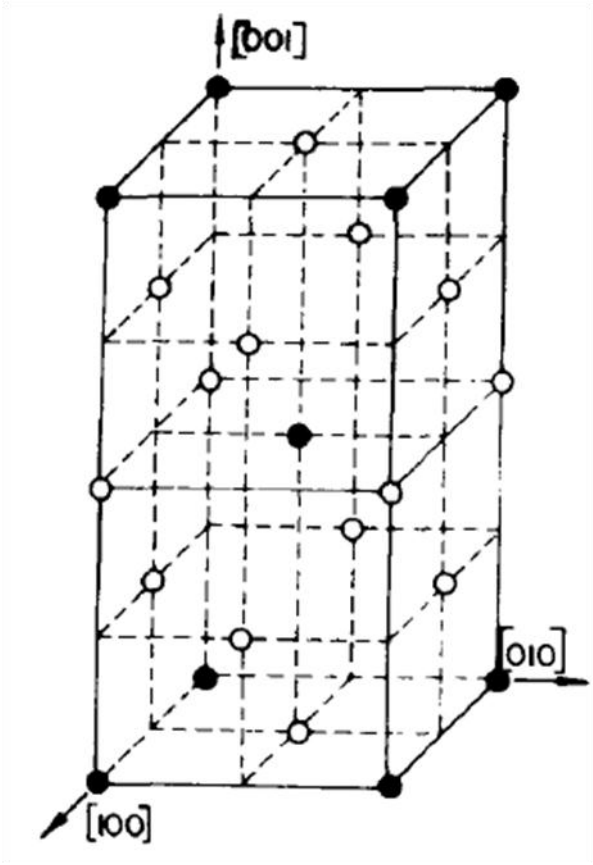

Figure 2-8: Crystal structure of the γ ″ (Ni_3Nb) phase with black circles denoting Nb atoms and white circles denoting Ni atoms [37].

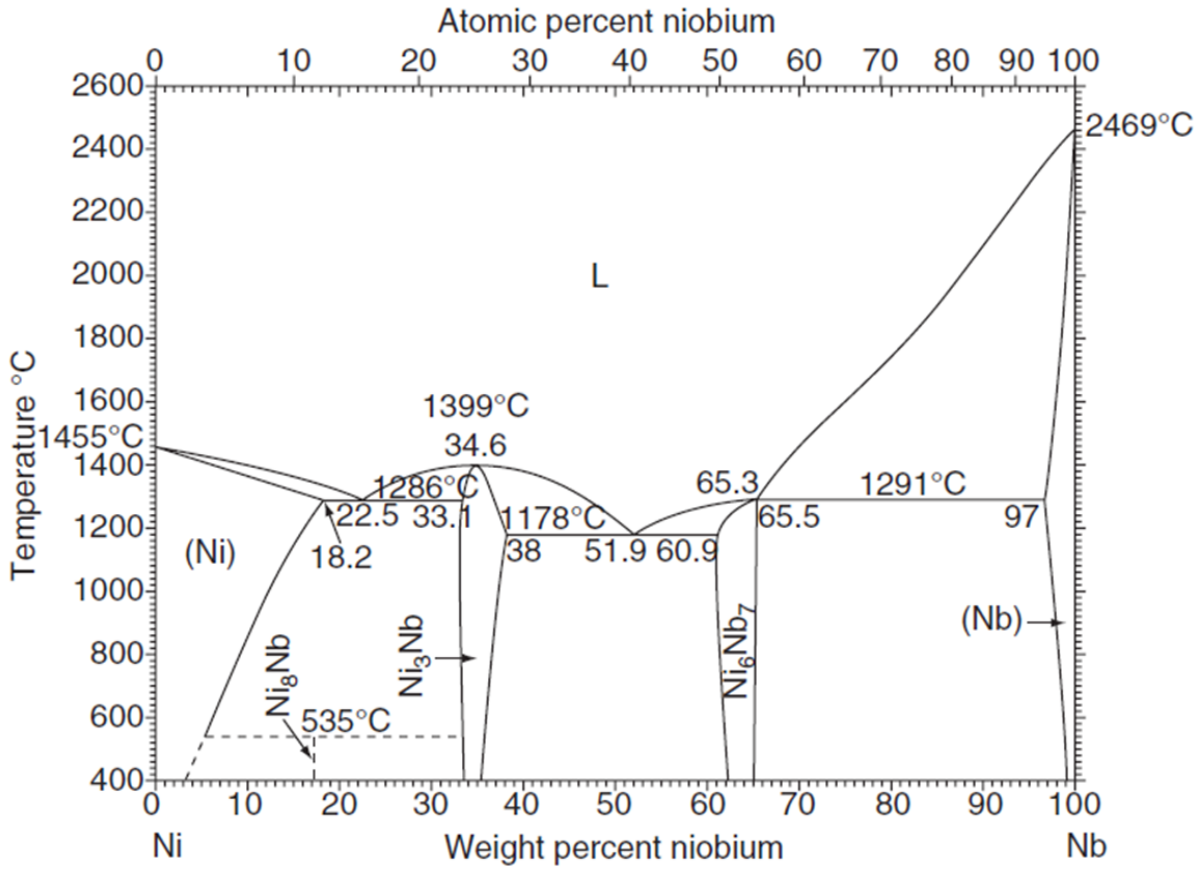

Figure 2-9: Ni - Nb binary phase diagram. (Courtesy ASM International from[38]).

The γ″ displays a disc-shaped morphology, with a thickness often as small as 10 nm and a diameter about 50 nm [39]. It exhibits a large lattice misfit, the mismatch between the γ and γ″ lattice parameters, along the tetragonal (c) axis with the alloy matrix [40]. Only a small amount of γ″-precipitates is enough to attain the required strength due to the large coherency strain associated with formation of γ″. The γ″ plates are sheared by the a/2<110> dislocation and the energy of the antiphase boundary created thus is sufficient to couple the dislocation into pairs, and even quadruples. The latter has been observed for small γ″ particle sizes [41]. Four dislocations are required to restore full order to the γ″ plates on the three {110, habit planes. Furthermore, the precipitation kinetics of γ″ are slow, thereby making the alloy weldable due to its resistance to strain age cracking (SAC) during post-weld heat treatment

[40, 42] . γ″ strengthened Ni-Fe-based superalloys are susceptible to the formation of an orthorhombic δ phase in the over aged condition [39]. This phase is incoherent with γ and therefore does not confer strength even when present in significant quantities. Many Nb-bearing alloys (e.g. IN718) are prone to Laves phase formation instead of γ″ (further details of these phases are discussed in metallurgy of IN718 section).

2.1.3.4 TCP phases

Excessive quantities of Cr, Mo, W and Re promote the precipitation of intermetallic phases [43] with a complex crystal structure whereby the structure is built up of distinct tessellated layers consisting of arrays of hexagons, pentagons and triangles, hence the name topologically close-packed (TCP) phases [44]. These phases are usually detrimental to mechanical properties [45]. They may appear as thin linear plates, which generally nucleate on grain boundary carbides. σ, μ and Laves are some of the phases that belong to this group.

Ni-based superalloys are generally prone to the formation of σ and μ phases, whereas Ni-Fe-based superalloys are prone to Laves phases. These phases can cause lowered rupture strength and ductility [26]. Figure 2-10 shows the σ phase at the grain boundaries of Ni-based superalloy RR1000 after prolonged heat treatment. The formula for σ is $(Fe, Mo)_x$ $(Ni, Co)_y$, where x and y can vary from 1 to 7. σ phase formation depletes the refractory metals in the γ matrix, causing loss of strength of the matrix [46]. Little is known about the detrimental effects of plate-like μ phase. A general formula for μ is $(Fe, Co)_7(Mo, W)_6$ [45]. Finally, Laves phase has a hexagonal crystal structure with a composition of AB_2 type. Typical examples include Fe_2Ti, Fe_2Nb, and Fe_2Mo. A more general formula is $(Fe, Cr, Mn, Si)_2$ (Mo, Ti, Nb). Excessive amounts of this phase will impair room-temperature tensile ductility and creep properties. More details about the formation of Laves phase will be discussed in later sections.

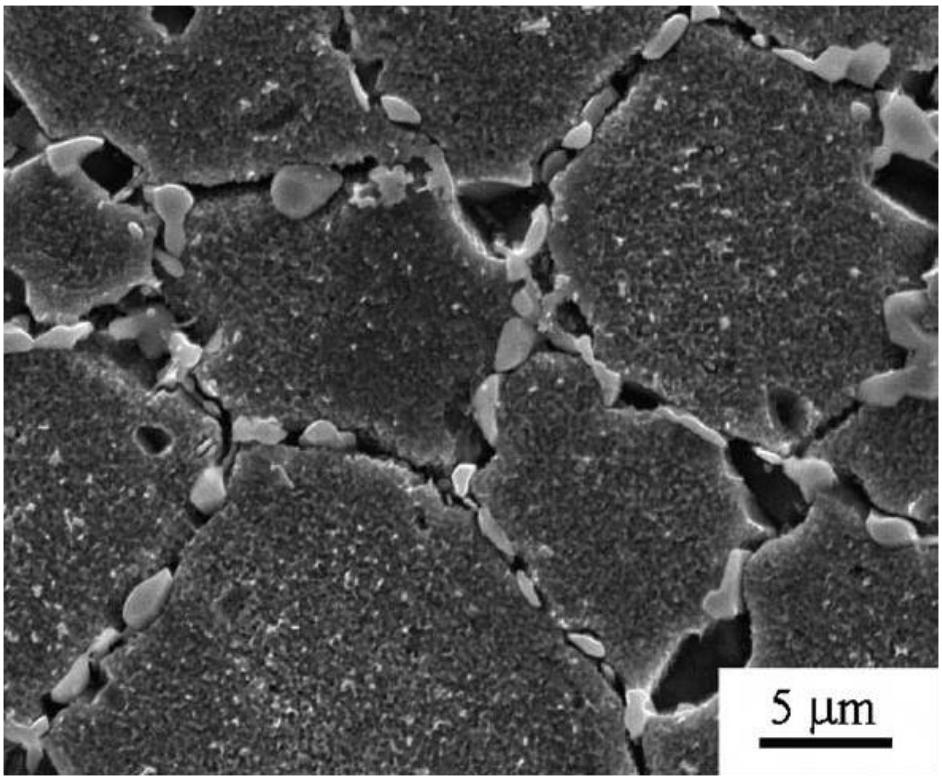

Figure 2-10: SEM of RR1000 showing extensive precipitation of the σ phase at γ grain boundaries, after a heat treatment of 5000 h at 750 ˚C [45].

2.1.3.5 *Carbides*

Ni-based superalloys (with appreciable carbon levels) can form various types of carbides, depending on the alloy composition, processing route, and service history. Some of the more important types include MC, M_6C, $M_{23}C_6$ and M_7C_3, where M stands for Cr, Mo, Ti, Ta or Hf. Figure 2-11 shows the different type of carbides in Ni-based superalloys. MC type carbides, which are usually rich in Ti, Ta and Hf, precipitate at high temperatures (in excess of 1038°C [26]) from the liquid phase, thus they are often found at interdendritic regions, with no distinct orientation relationship to the γ matrix. Conversely, the $M_{23}C_6$ forms due to the breakdown of the MC carbides at around 750°C (favoured at 750 - 810°C) during prolonged service exposure [47-48] in the following sequence.

$$MC + \gamma \rightarrow M_{23}C_6 + \gamma'$$

These carbides are usually seen in Cr-rich alloys and they form at the grain boundaries[26].

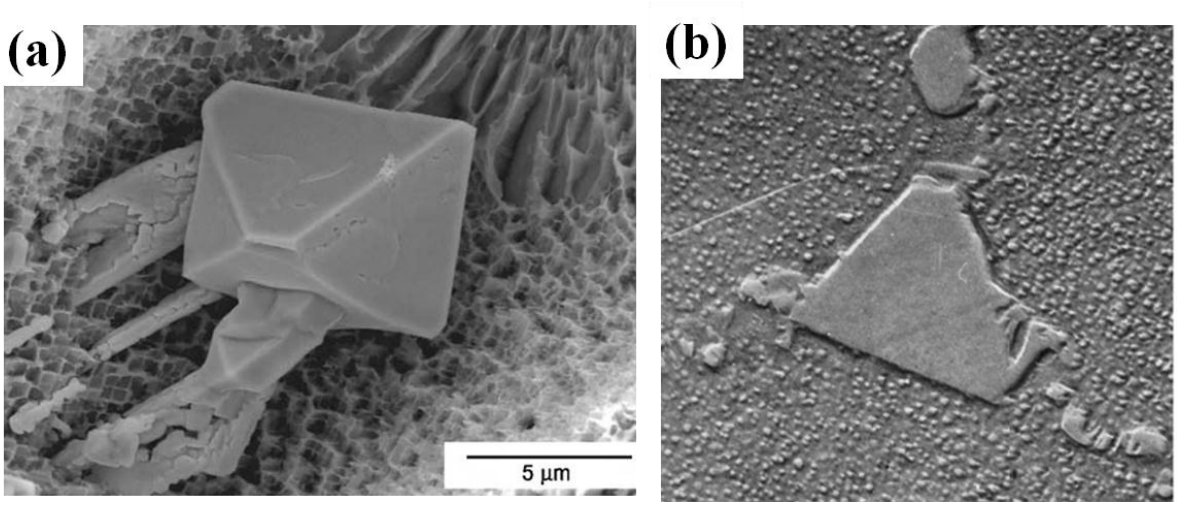

Figure 2-11: SEM micrographs showing carbide phases in Ni-based superalloys (a) Ta-rich MC type carbide formed in an experimental nickel-based single-crystal superalloy [49] (b) $M_{23}C_6$ type carbide seen at the grain boundaries in Nimonic 80 alloy at a magnification of 6000 × [26].

2.2 Metallurgy of IN718

2.2.1 Introduction

IN718 is a γ′+ γ″ strengthened precipitation hardenenable alloy. It was designed in an effort to improve weldability and reduce Strain Age Cracking (SAC)[26]. The chemical composition (wt. %) of the alloy is given Table 2-2. This alloy is extensively used in aeroengine applications, for gas turbine shafting and pressure containment, up to a temperature range of 700˚C. It is considered the workhorse for large structural castings, due to its excellent resistance to SAC [40]. The alloy is less susceptible to SAC due to sluggish γ" precipitation kinetics. SAC is associated with post-weld heat-treatment (PWHT) of γ′ precipitation hardenable Ni-base superalloys. Relaxation of residual stresses and precipitation of γ′ phase takes place simultaneously while heat treating the welds. The precipitation of γ′ phase would improve the strength of the material while reducing the ductility [26]. The residual stresses, which will be relaxing at a slower rate, when combined with the reduced

ductility can exceed the material strength causing the cracks to open. Figure 2-12 showing the sequence of event that could occur during SAC [26]. The SAC in Ni-based superalloys depends on the Al + Ti content in the alloy [50], as shown in Figure 2-13, IN718 is resistant to SAC which follows a C-curve behaviour (demonstrated by Duvall and Owzarski [51]) due to the sluggish γ" precipitation rate, Figure 2-14.

Table 2-2: Chemical composition of IN718 (Wt. %)[28]

Alloy	%	Ni	Cr	Fe	Mo	Nb	Co	C	Mn	Si	S	Cu	Al	Ti	O
718	Min	50	17	balance	2.8	4.75							0.2	0.7	0.002
	Max	55	21		3.3	5.5	1	0.08	0.35	0.35	0.01	0.3	0.8	1.15	0.05

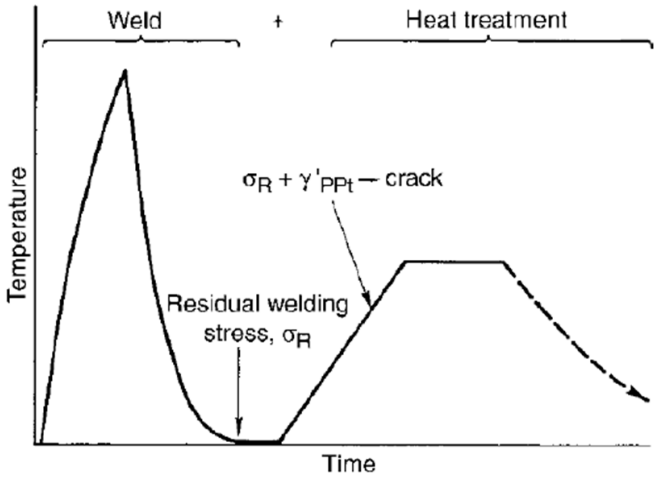

Figure 2-12: Diagram showing the potential sequence of events leading to SAC [26].

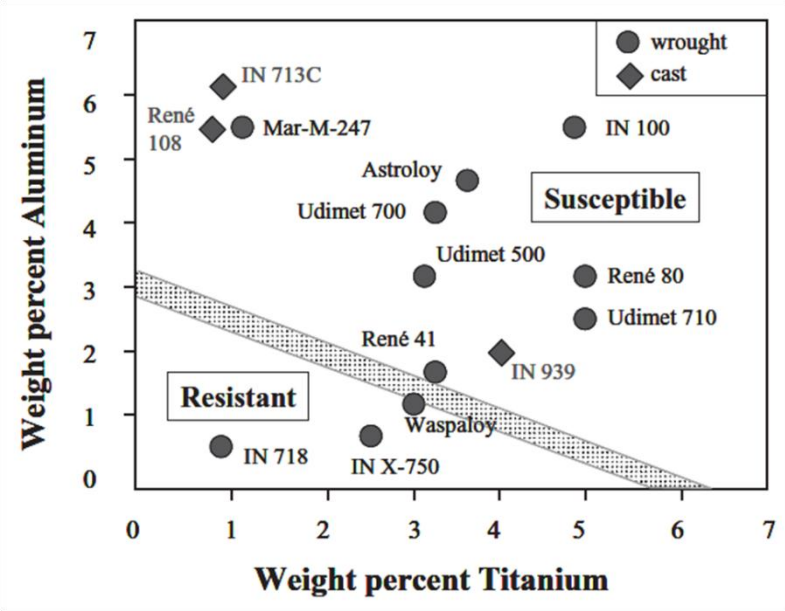

Figure 2-13: Effect of Al and Ti content on susceptibility to strain-age cracking in Ni-base superalloys [51].

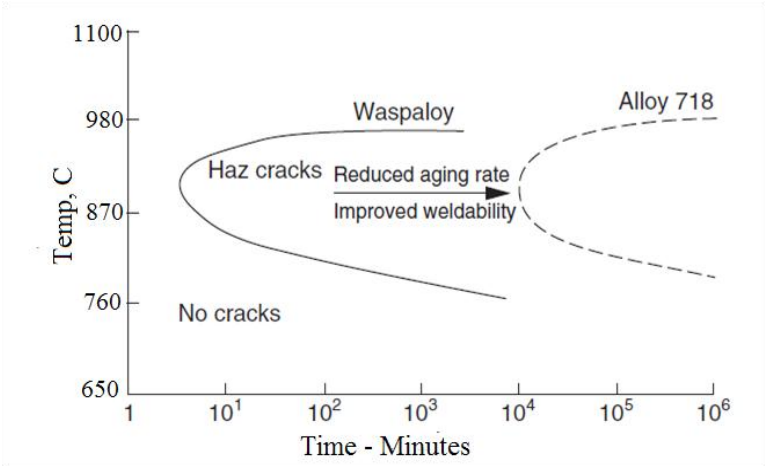

Figure 2-14: Curve showing the SAC behaviour for Waspaloy and IN 718 showing much greater tolerance for PWHT cracking for IN 718 due to slower aging rate [51].

2.2.2 Precipitation in IN718

IN718 features various phases that form during solidification, which including strengthening phases likeγ',γ'', δ and detrimental phases like Laves. The precipitation kinetics of IN718 has been reported extensively in the literature, and will be discussed in the following sections.

The three main precipitate strengthening phases, γ′, γ′′ and δ simultaneously precipitate during heat treatment of solution treated microstructure, within temperature range of 600-900˚C, Figure 2-15 [52].

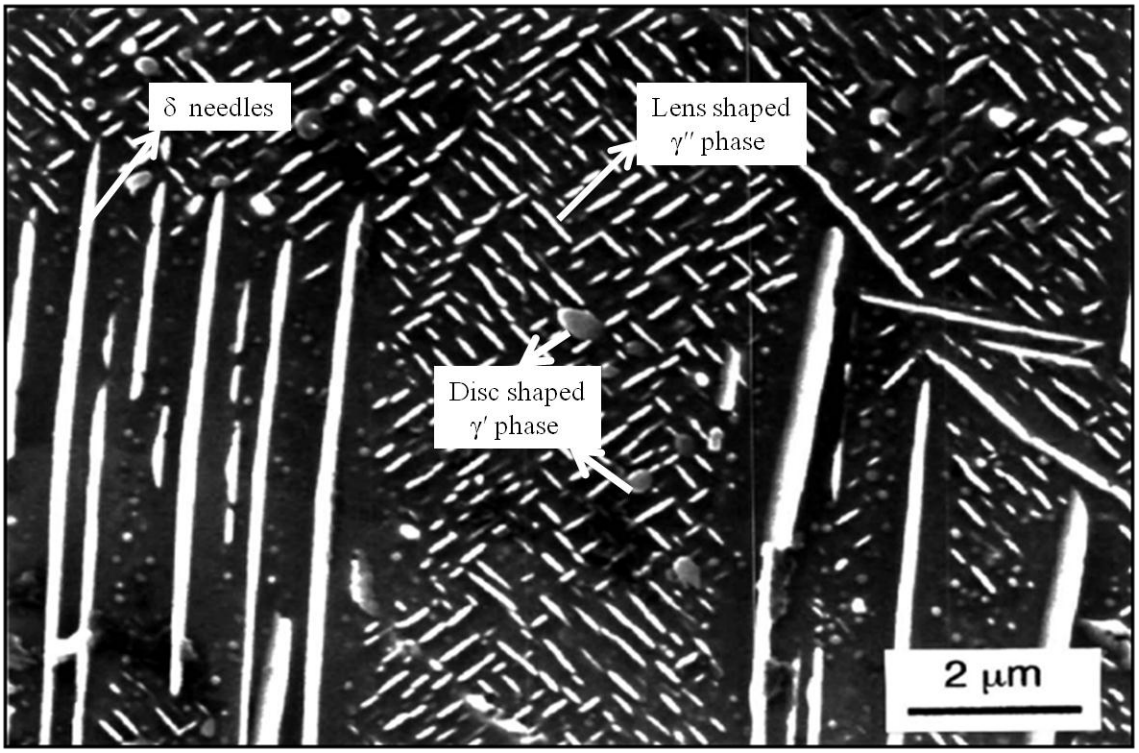

Figure 2-15: Scanning electron micrograph showing the δ phase plates, γ′′ discs and γ' spheroids in IN718 treated isothermally at 850˚C/24h [52].

2.2.2.1 The γ′ and γ′′ precipitation:

Both γ′ and γ′′ phases precipitate homogeneously within the γ-grains. The γ′ forms as small spheres of size around 200 Å [53], and can be observed only through transmission electron microscopy (TEM), whereas γ′′ precipitates, are disc-shaped which can grow up to 1 μm thick, and can be easily detected [52]. The γ′′ forms in the presence of Fe in Nb-rich superalloys. The morphology of both γ′ and γ′′ precipitates are shown in Figure 2-15. These phases can be seen more clearly under a TEM (Figure 2-16). Both phases start to precipitate at around 620˚C, making it very difficult to distinguish which type precipitates first [52]. The

order of precipitation depends on the (Ti+Al)/Nb ratio in the alloy. If this ratio is greater than 0.8 , then γ′-precipitation precedes γ′′ precipitation [39]. The γ′ phase dissolves at around 640-670°C followed by the γ′′ phase at around 840°C (The evolution of various phases can be seen in Figure 2-17). γ′′ precipitates are generally unstable, converting to the δ phase on prolonged ageing. Figure 2-18 shows the δ needles that started nucleating after prolonged aging of 5000 h at 621°C. In general, both the precipitates grow separately. However, at 750˚C, both types grow together, whereby γ′′ tends to grow on the flat face of γ′ as hemispherical particles due to the difficulty in nucleating separately at this temperature [36, 39] .The fraction of these precipitates depends on the heat treatment, as well as the amount of Nb present in the material. γ′ forms with less than 4% wt. Nb, whereas for γ′′ the Nb should be more than 4% wt. [53-54]. Pre-treatment and heat treatment have no influence on the relative fraction of γ′′ and γ′ phases in IN718. In fact, the ratio of γ′′ to γ′ is approximately the same under different pre-treatment conditions and can be taken as a constant equal to 3 [55].

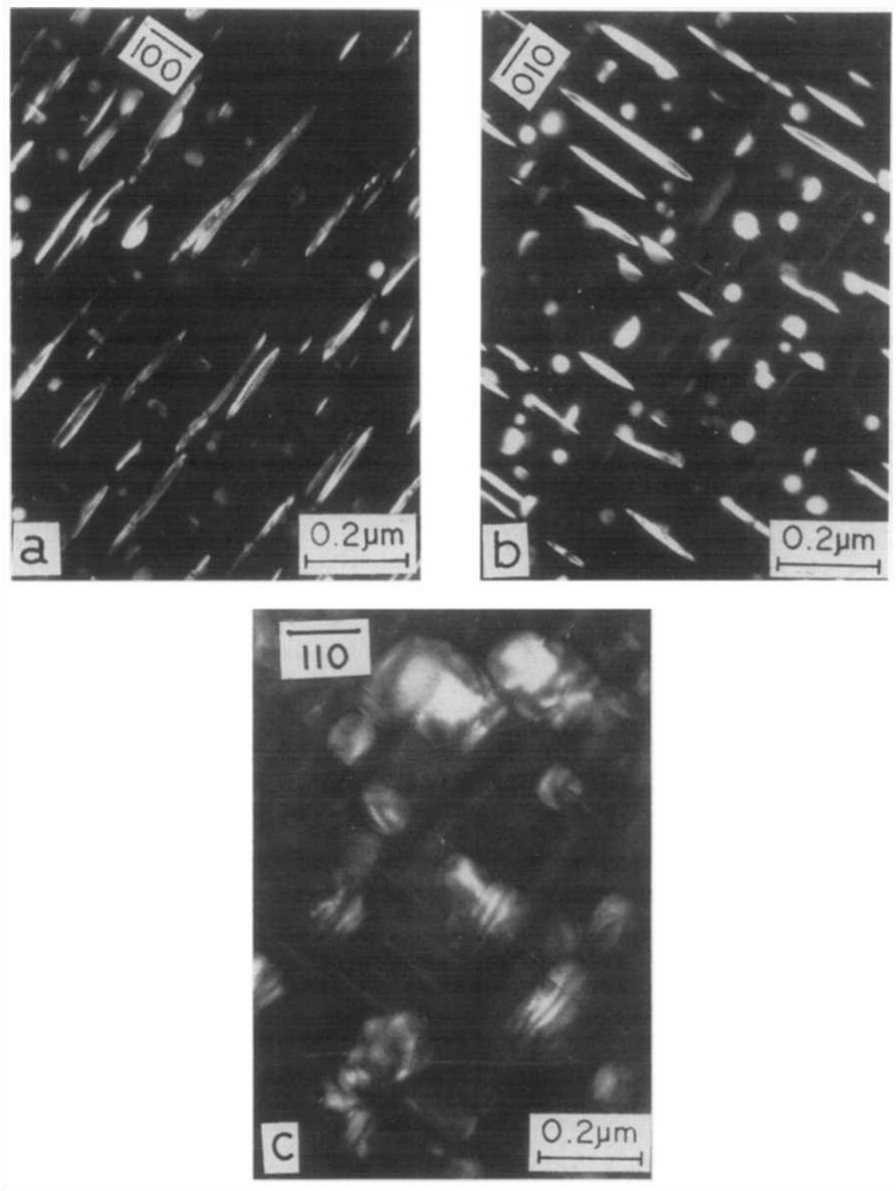

Figure 2-16: Dark field TEM micrographs of IN718 aged at 800°C for 100 h showing γ′ (circular) and γ′′(lens-shaped) precipitates in <100> direction; a) g = 100; b) g = 010; c) g = 110 [37].

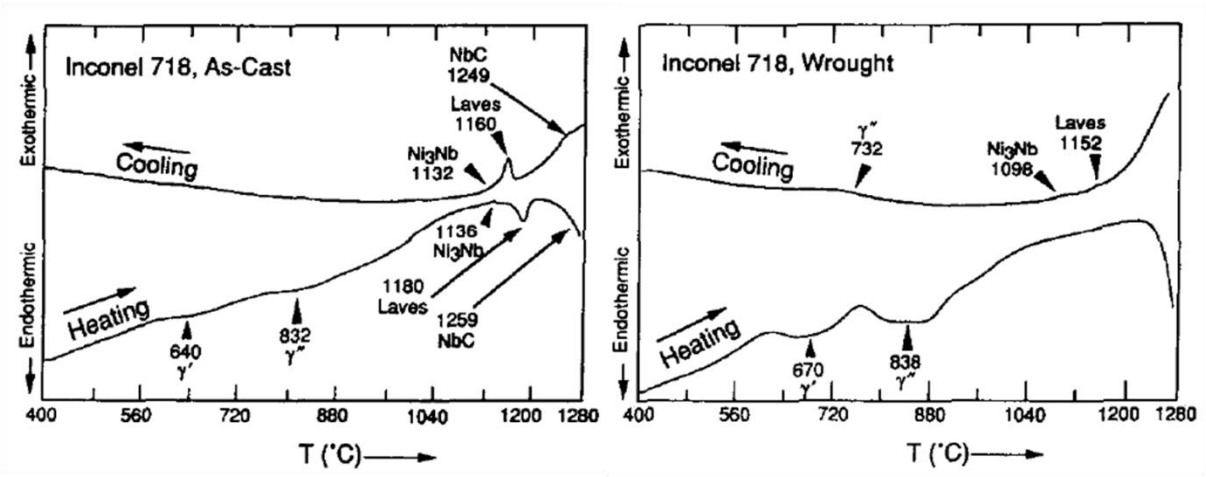

Figure 2-17: DTA curves showing the different phase evolution in Inconel 718 for (a) cast and (b)wrought products [56] (The samples were heated and cooled at a rate of 40°C/min through melting/solidification range).

2.2.2.2 The delta phase (δ)

The δ-phase has a composition of Ni_3Nb, with an orthorhombic crystal structure which is incoherent with the matrix with 6-8 wt. % Nb. It precipitates between 700 and 1000˚C, with the highest precipitation rate at 900˚C. The precipitation can be intergranular, where the nucleation starts at the stacking faults of the γ″ phase [52]. The δ-phase is more stable than the γ″ phase, but the formation is slow below 900˚C because of the preferential formation of γ″. Both the phases are formed due to Nb, but the δ-phase forms by the loss of the γ″ phase up to 900˚C, and once the γ″ precipitation stops the δ-phase formation peaks.

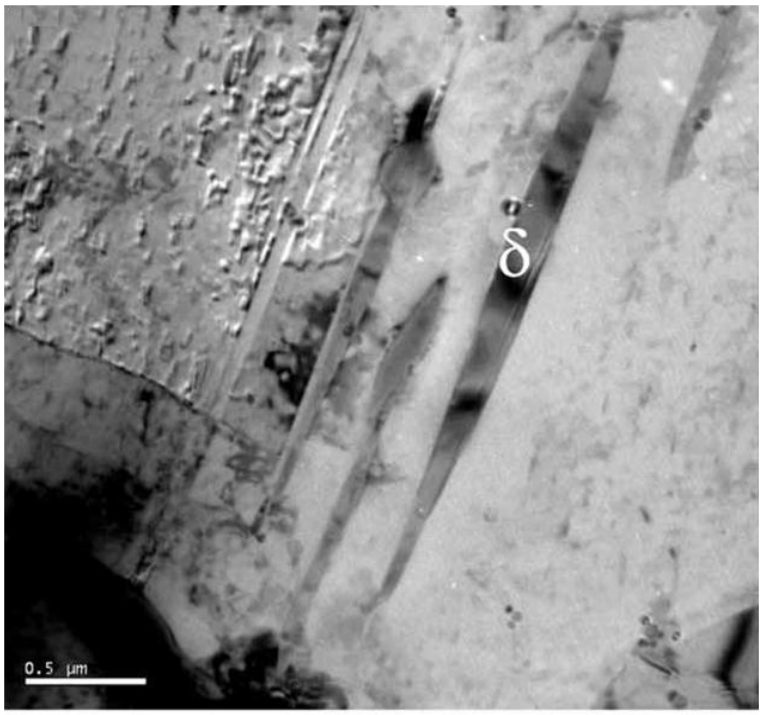

Figure 2-18: δ needles after prolonged exposure at 621 C for 5000 h in IN 718 alloy [57].

The presence of the δ-phase is detrimental to the material properties due to its morphology where the creep properties of the material decrease with an increase in the amount of this phase (Figure 2-19). In addition, its formation causes the depletion of the major strengthening phase, γ″. As this phase forms at the γ-grain boundaries, it will inhibit grain growth during heat treatment [58]. The δ-phase also improves the creep properties of the material provided that an appropriate morphology at the boundaries is achieved [59]. This phase can be completely dissolved in the matrix at a temperature of 1025˚C.

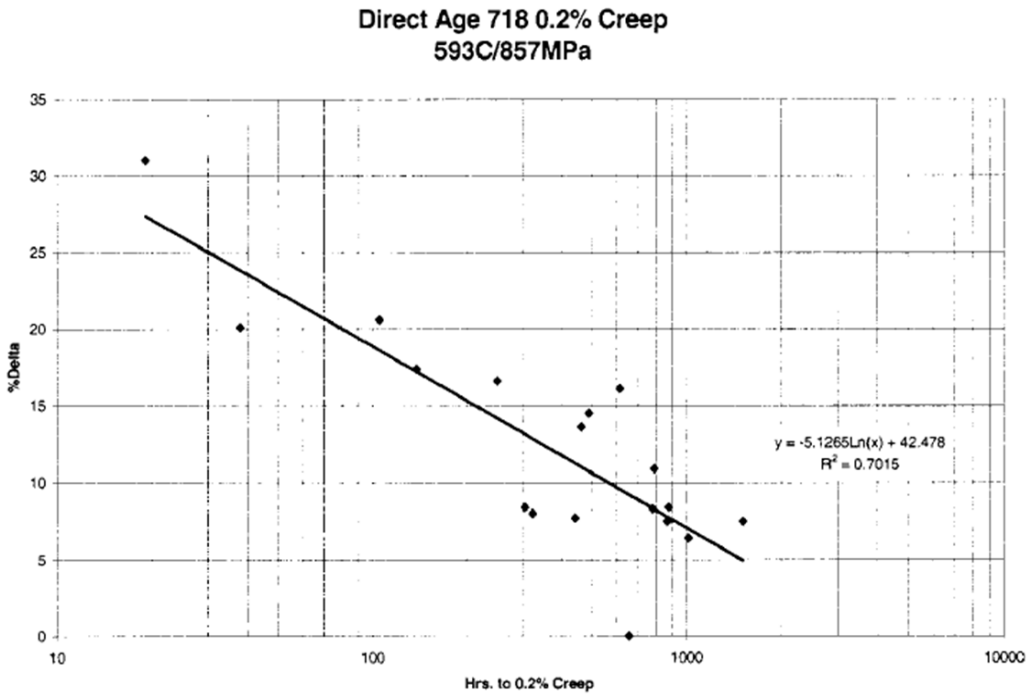

Figure 2-19: Creep behaviour of IN718 as a function of the δ phase content showing excess delta precipitate leading to decreased creep resistance [60].

2.2.2.3 The Carbides

The only major carbide type reported in IN718 is the MC type with minor amounts of M_6C type [61-62]. The MC carbides which contain predominantly Nb and Ti are located both on grain boundaries and in the matrix. The morphology of carbides can be seen in Figure 2-20. The NbC is formed at ~1250 ˚C during solidification and they are the last phases dissolved during heat treatment (Figure 2-17). The size and shape of carbides depend on the cooling rate where slow cooling rate results in large carbides. δ phase has been observed emanating from NbC particles, apparently providing the Nb required for its formation [63]. The carbides are generally not considered to be important in determining the mechanical properties of IN718 but a study by Rao *et al.* [64] on hot isostatically pressed (HIP) IN718 suggested that carbides would cause intergranular failure reducing the ductility of the material, however this effect is not prominent at low oxygen levels of around 140 ppm [65].

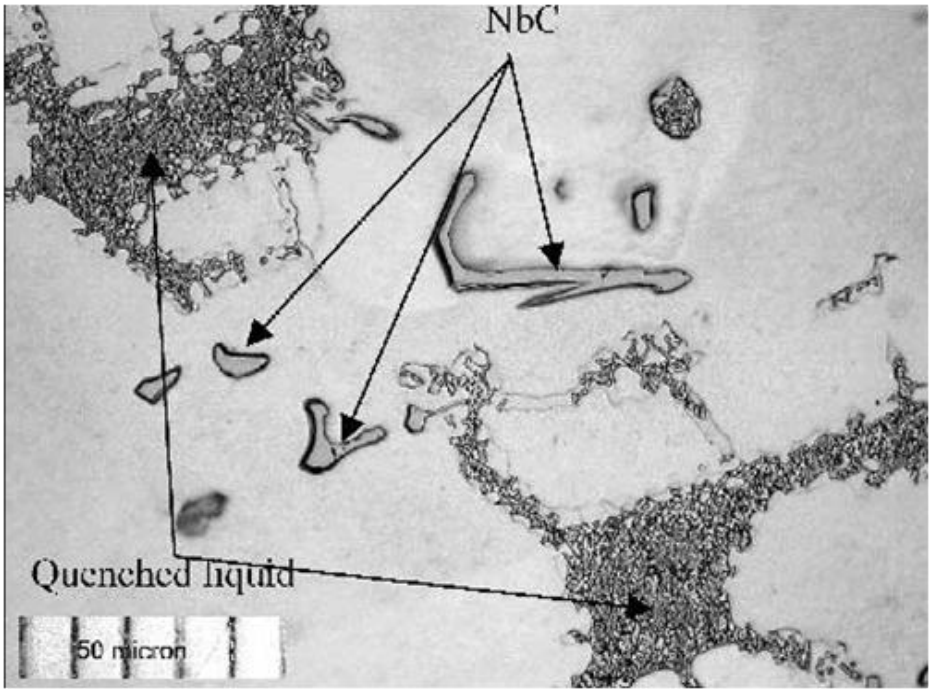

Figure 2-20: The morphology of Niobium carbides in a sample quenched from 1243°C [66].

2.2.2.4 *Laves phases:*

Other than the strengthening phases, which form during ageing, detrimental phases like Laves are formed during slow cooling. They are frequently observed in cast and welded microstructures. Laves phases appear as islands and are found in various shapes and sizes depending on the cooling rates associated in the process. These phases are irregular in shape. The typical morphology of these phases can be seen in Figure 2-21. The formation of Laves phases is strongly dependent on the heat input during the manufacturing process (e.g in welding) and the cooling rate. The processes with high cooling rate typically produce less Laves phase [67]. Figure 2-22 shows the time temperature transformation diagrams for IN718, which clearly shows the range of temperature and time where the Laves phases are expected to form. Laves is formed in two steps during solidification which starts with primary liquid→ γ reaction, and proceeds causing enrichment of interdendritic liquid in Nb, Mo, Ti, and C until an eutectic reaction L→(γ + Laves) occurs, terminating the solidification process [68-69].

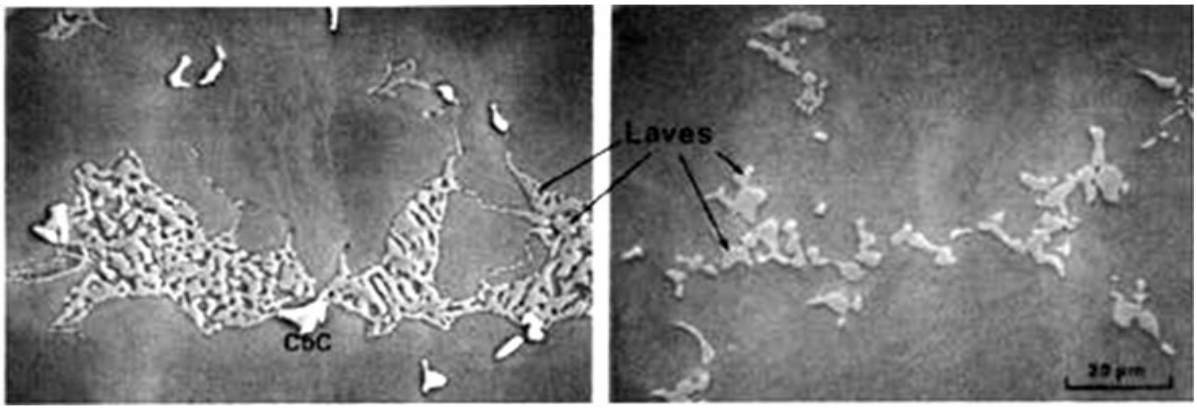

Figure 2-21: Typical eutectic(left) and globular (right) type Laves phases that are seen in an as cast IN718 alloy [70].

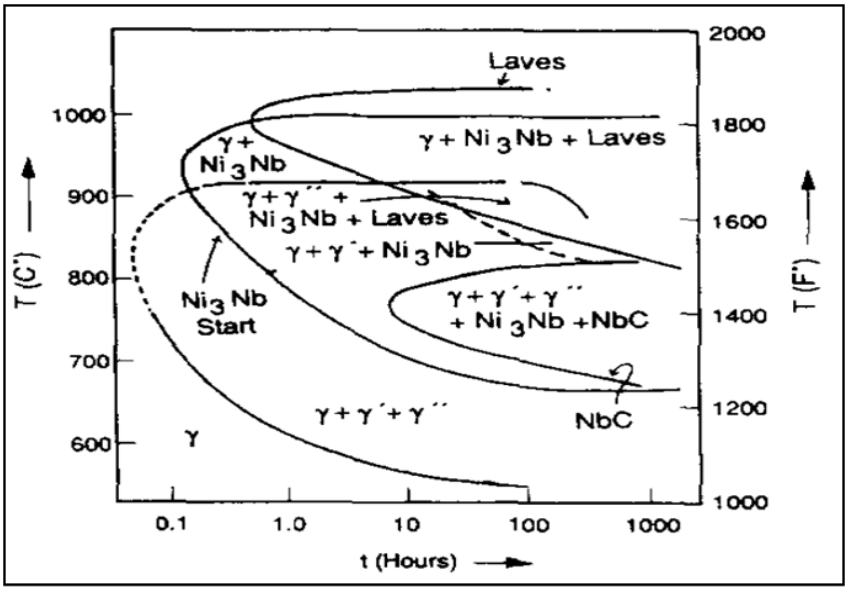

Figure 2-22: Time-Temperature-Transformation (TTT) curve of IN718 [71].

Laves phases are detrimental to the mechanical properties and increase in the amount of Laves would reduce the elongation and ultimate tensile strength of the material at room and elevated temperatures (Figure 2-23). Laves phases are also detrimental to the low cycle fatigue life as they act as crack initiation sites [53]. Laves phases can be dissolved at 1180˚C, which can be essential to improve the mechanical properties.

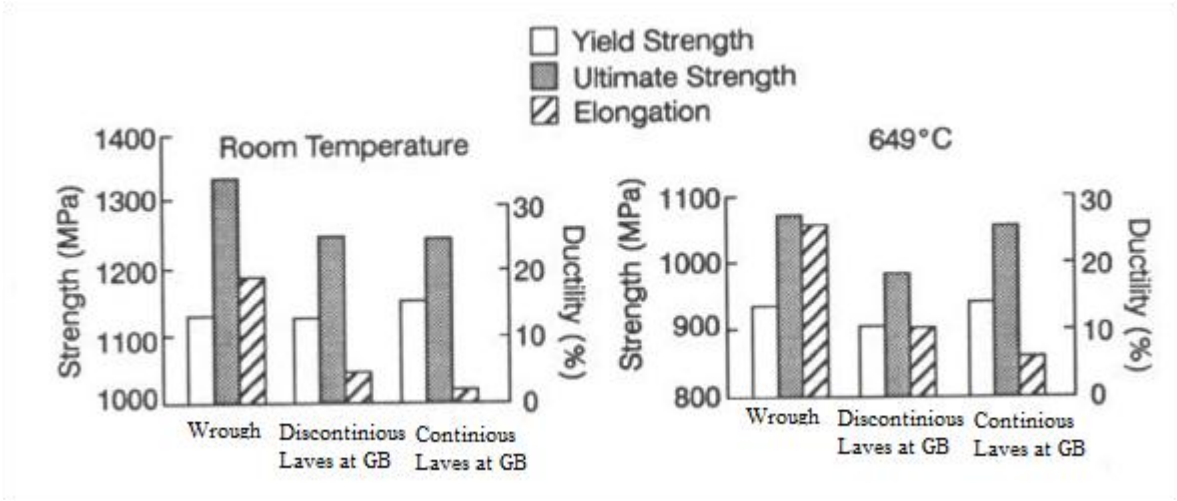

Figure 2-23: Room and elevated temperature tensile results for wrought Inconel718 with various amounts of Laves [72].

2.2.3 Heat Treatment of IN718

IN718 is typically heat treated after casting or welding for several reasons: to reduce residual stresses, to achieve the required strength by dissolving detrimental Laves and/ or δ phases to allow the precipitation of the strengthening phases (γ' and γ'') and to obtain a uniform grain size. The major strengthening phases in IN718 (γ'') forms after solution treatment at around 980°C followed by aging in the range of about 704 to 899 ºC. The γ'' solvus is about 910 ºC. The δ phase (depending on exposure time) precipitates in the vicinity of about 871 ºC, and has a solvus temperature of about 1010 ºC. Typically IN718 can be worked and heat-treated above the δ solvus, or at a temperature between the δ solvus and the γ'' solvus for grain-size control, which is an important aspect of current high-strength IN718 production [26]. The detrimental Laves phases can be completely dissolved into the γ matrix at 1180ºC [53] whereas the carbides can only be dissolved above 1270ºC [61]. The three heat treatment methods conforming to Aerospace Material Specifications (AMS) are shown in Table 2-3. They include direct ageing, solution treatment and ageing (STA), which is performed on forged parts, and homogenisation followed by STA, which is used for castings.

Table 2-3: Three standard heat treatment methods employed for IN718according to Aerospace Material Specifications (AMS)[22].

Homogenized STA* (Steps 1 + 2 + 3)	STA** (Steps 2 + 3)	Direct Aging (Step 3)
Step 1 homogenization	heat to 1093 °C ± 14, hold for 1 to 2 h, air cool or faster	
Step 2 solution	heat to 954 to 982 °C, hold for >1 h, air cool or faster	
Step 3 aging	heat to 718 °C ± 8, hold for 8 h, furnace cool to 621 °C ± 8, hold for 10 h, air cool or faster	

*According to AMS-5383D for cast IN718.
**According to AMS-5662M for forged IN718.

2.3 General Solidification Theory

Either in casting process or translated melt pool process (e.g. welding or AM), solidification behaviour controls the size and morphology of the grains, the extent of micro and macro segregation, the distribution of inclusions, the extent of defects such as porosity and hot cracks, and ultimately the properties. Thus, it is important to understand the development of the solidification microstructure by considering the nucleation and solid phase growth stages as a result of the variations in the solidification parameters, including temperature-gradient, growth rate, superheat and undercooling. As AM involves solidification within a moving melt pool it has many similarities to welding. Hence, the solidification behaviour will be reviewed in this context. A key reference in this regard is the excellent review by David and Vitek [73], as well as a book on Welding metallurgy by DuPont and Lippold [74].

2.3.1 Nucleation and growth behaviour

2.3.1.1 Nucleation

There are two types of nucleation phenomena, homogeneous nucleation which happens at large undercooling when no nucleation site is present, and the more practical heterogeneous nucleation where solidification starts from a solid impurity or the liquid container which only needs undercooling of 1 K. Nucleation in welding melt pools is typically observed to take place with an undercooling of 1-2 K [75-76].

2.3.1.2 Growth:

After nucleation, growth of the solid occurs by the addition of atoms (diffusion) from the liquid to the solid at the pre-existing solid/liquid (S/L) interface. A key factor that determines the nature of the S/L interface is the heat flow and the associated thermal gradients in the melt pool. Mass flows associated with compositional gradients are also crucial in establishing the shape of the stable solidification front. The interaction between the thermal gradient (G) with the growth rate (R) and the other solidification conditions determines the final microstructure of the primary phase during solidification. Based on the steady state microscopic shape of the S/L interface at the growth front, solidification occurs in planar, cellular, or a dendritic manner [73, 76]. The various growth morphologies which depend on the thermal gradient and growth rate can be seen in Figure 2-24 [77] for some Ni-based superalloys. Figure 2-25 shows the various forms of non-planar solidification structures in a number of alloys. In dendritic growth, the growth follows specific crystal directions (i.e. the S/L front is significantly controlled by crystallographic considerations), with the growth also being opposite to the heat flow direction. The dendrites grow in an optimum alignment condition, controlled by the maximum thermal gradient and growth direction.

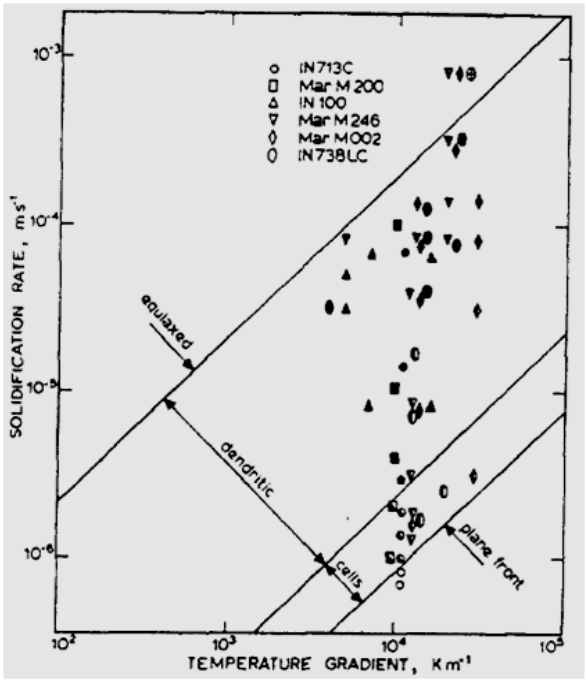

Figure 2-24: Morphologies of directionally solidified nickel based superalloys marked on log R (solidification rate) and log G (thermal Gradient) graph [77].

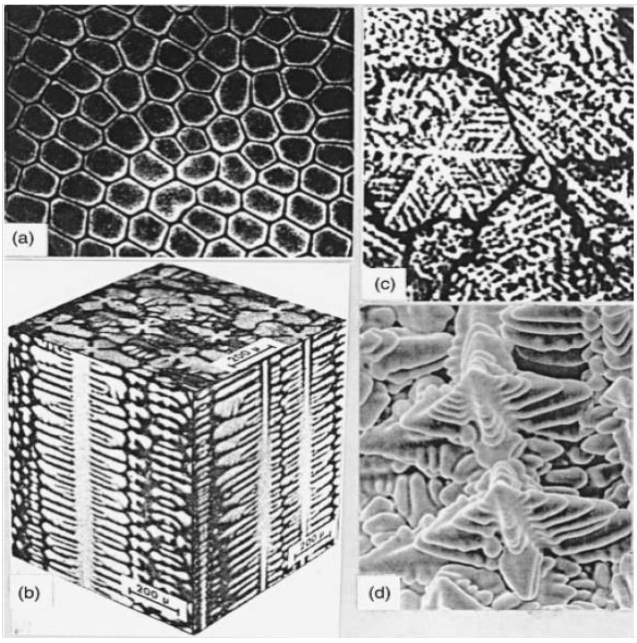

Figure 2-25: Non-planar solidification structures in alloys (a) transverse section of a cellularly solidified Pb–Sn alloy (b) columnar dendrites in a Ni alloy (c) equiaxed dendrites of a Mg–Zn alloy (d) three-dimensional view of dendrites in a Ni-base superalloy [73, 78].

2.3.2 Columnar to equiaxed transition (CET) in Ni-based superalloys

It is important to understand the factors that affect the columnar to equiaxed transition in order to predict the microstructure in the final component. From section 2.3.1 it is seen that the CET is dependent on the G and R values. For Ni-based superalloys CET occurs in the region where the solidification rate, R, is approximately 3 x 10^{-4}m/s and the temperature gradient, G, is approximately 1.5 x $l0^{2}$ C.m^{-1} [77]. In particular, for IN 718 alloy a numerical model was developed by Nastac *et al.* to obtain a solidification map showing the columnar and equiaxed zones (Figure 2-26). Also experimental work on the CET in superalloys, including IN718, indicates that in alloys with a conventional content of non-metallic inclusions such as C and N, the nucleation process which creates the equiaxed grains requires an undercooling of approximately 3.7°C at the liquidus surface [77].

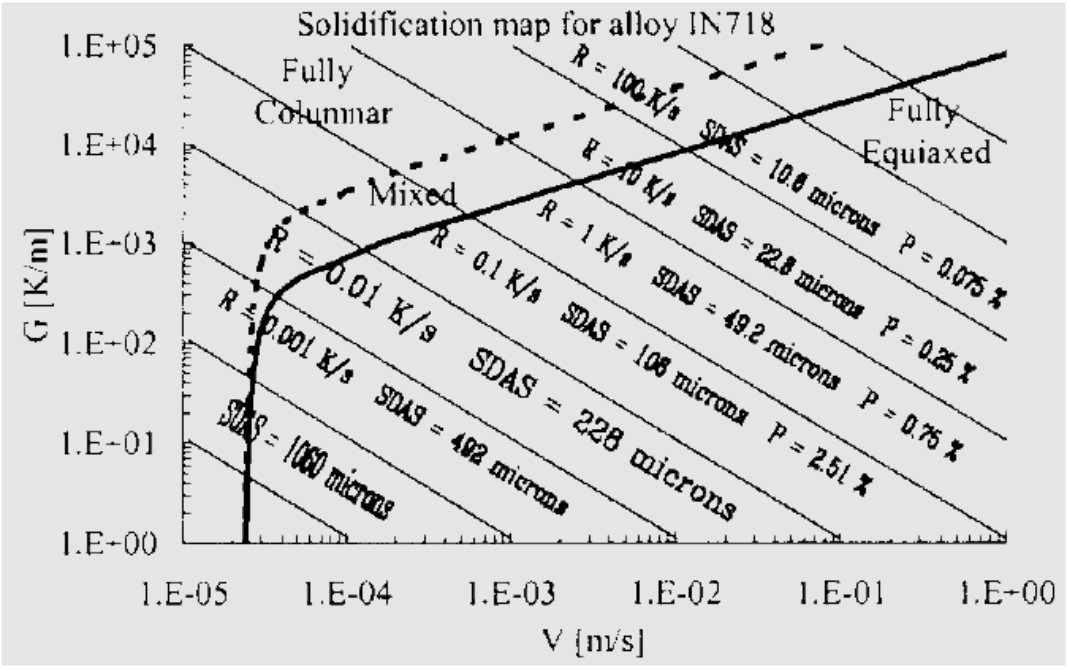

Figure 2-26: Solidification map for IN 718 alloy [79].

2.3.3 Factors controlling the melt-pool solidification behaviour

The important variables that control the size, shape and solidification behaviour of the melt-pool are the solidification rate, temperature gradient, travel speed, undercooling, and alloy

constitution. The effect of these variables on the melt pool microstructure is discussed in this section.

2.3.3.1 Solidification Rate:

The solidification rate, or growth rate (R, Units: mm/s), is the rate at which the solid/liquid interface in the melt pool advances. The growth rate of a solidification front is along the maximum thermal gradient and normal to the S/L interface [3]. R is directly related to the travel speed (υ) of the heat source [80]. In a steady state condition (e.g. welding or AM), where the heat source is moving at a constant speed (υ), solidification growth must occur in such a way that it is able to keep pace with the heat source travel speed [73], as illustrated in Figure 2-27. It is seen that for R, to keep pace with the welding speed, a condition must be met that:

$$R = \upsilon \cos\theta \qquad 2\text{-}1$$

where, θ is the angle between the surface normal and the heat source travel direction. Thus, at the top surface, assuming that the solidification front is normal to the surface, the growth rate would vary from R = 0, when θ = 90° along the fusion line to a maximum of R = υ when θ= 0° along the centreline of the melt track.

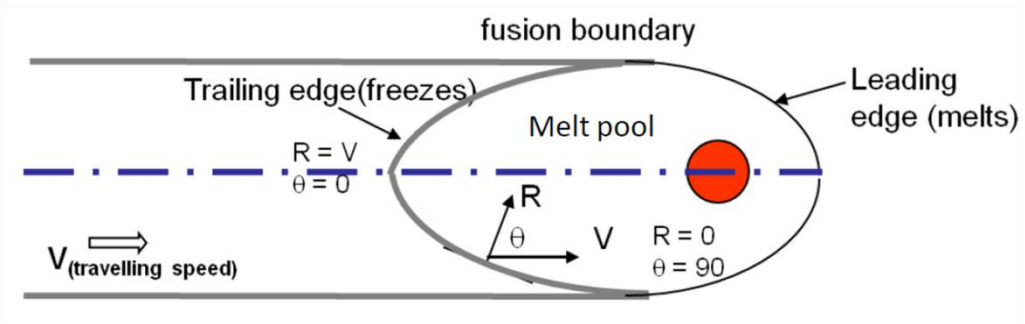

Figure 2-27: Schematic diagram showing the relationships between the heat source rate or travelling speed and the solidification front growth rate [3].

Other than the maximum thermal gradient, another important factor that influences the growth rate is the crystallographic orientation of the material. In polycrystalline, welds a wide range of growth directions is present, but a grain selection process will take place in which the grains with easy growth directions will outgrow less optimally aligned grains [73]. For example in cubic metals the ⟨100⟩ direction, which is close to the heat flow direction will outgrow the other less favourable directions [76]. So, in cubic metals directional solidification leads to a columnar microstructure with dendrites in the <100> direction.

The grain structure and crystallographic orientation in welds is determined by the grain and crystal structure of the base material, where the initial solidification starts epitaxially from the partially melted base metal grains [81-82]. Since there are preferred growth directions for the solid, a competitive growth process takes place among these grains, making them aligned with the solidification front.

2.3.3.2 Influence of travel speed

Travel speed of the heat source has a profound influence on the shape of the weld-pool and grain structure. Welds made at low to moderate weld speeds have an elliptical shape compared to high speed welds which take a tear drop shape, Figure 2-28.

In the elliptically shaped melt pool (low and moderate speed), the maximum heat input and the peak temperatures occur along the centreline. The higher temperatures in the solid immediately behind the melt pool, along the centreline, cause less rapid heat loss and result in a minimum thermal gradient along this direction, Figure 2-28.a. Meanwhile, the rate of liberation of latent heat is also a maximum at the centreline since it is directly proportional to the growth rate. Consequently, a critical growth rate exists for an elliptical melt pool beyond which the minimal thermal gradient present at the centreline cannot dissipate the generated

heat of fusion sufficiently quickly. For growth rates above this critical value, the melt pool shape changes and, becomes more elongated and tear drop shaped, Figure 2-28.b [73].

The presence of this critical growth rate and the effect of welding speed was demonstrated by Suutala [83], showing that the weld pool shape becomes more elongated and the maximum growth rate fell significantly below the weld speed, Figure 2-29.

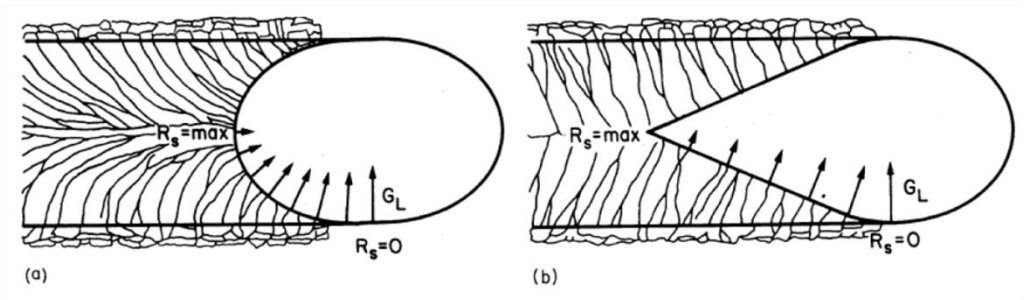

Figure 2-28: Diagram showing variation of thermal gradient G_L and growth rate R_S along solidification front for different travelling speed (a) elliptical shape (low and moderate speed) (b) tear drop shaped (high speed) [73].

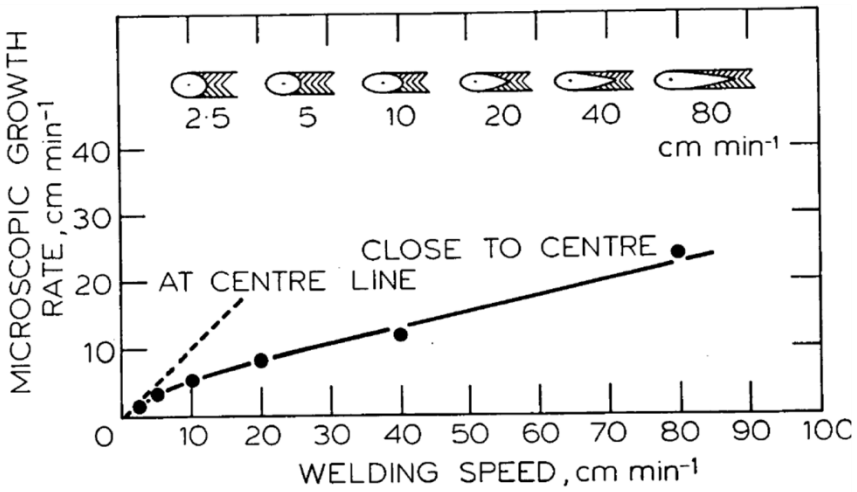

Figure 2-29: Variation of pool shape and growth rate as function of welding speed for arc welded stainless steel [73].

Also, the travel speed of the weld has an influence on the grain structure. The effect of welding speed on the grain structure can be seen in the schematic below, Figure 2-30. Very

low weld speeds would produce extremely columnar grains at the weld centre line [84]. Whereas for high welding speeds the nucleation of new grains would be sufficiently easy and equiaxed grain structure may be formed at the weld centre line[85].

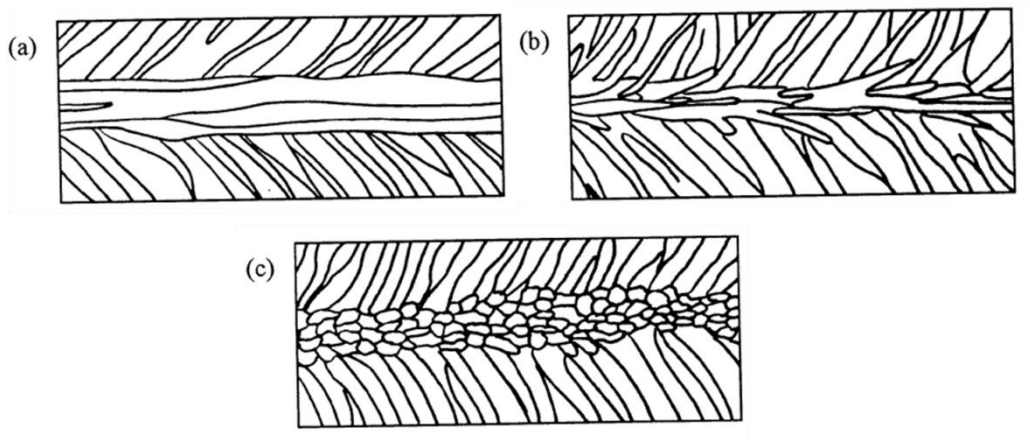

Figure 2-30: Schematic diagrams illustrating the effect of welding speed on the grain structure in welds: a) axial grains at low welding speeds b) stray grains for low to intermediate welding speeds and c) equiaxed grain structure for faster welding speeds [84].

2.3.3.3 Thermal gradient

The thermal gradients in the solid G_S and in the liquid G_L at the solid/liquid interface play a significant role in determining the solidification substructure in the melt pool. Out of these two, G_L is more critical in determining the morphology and solidification of the welds. The thermal gradient, G_L, increases as the thermal conductivity of the material decreases and also it is higher for high energy density process (e.g. electron beam welds). The thermal gradients, both G_S and G_L, decrease continuously from the fusion line to the weld centre line and the temperature gradient decreases with increase in heat input [86]. Both growth rate and thermal gradient vary considerably across the fusion zone. From fusion line to the weld centre line the growth rate increases, whereas the thermal gradient decreases the influence of such variation on the microstructure of a weld is shown in Figure 2-31.

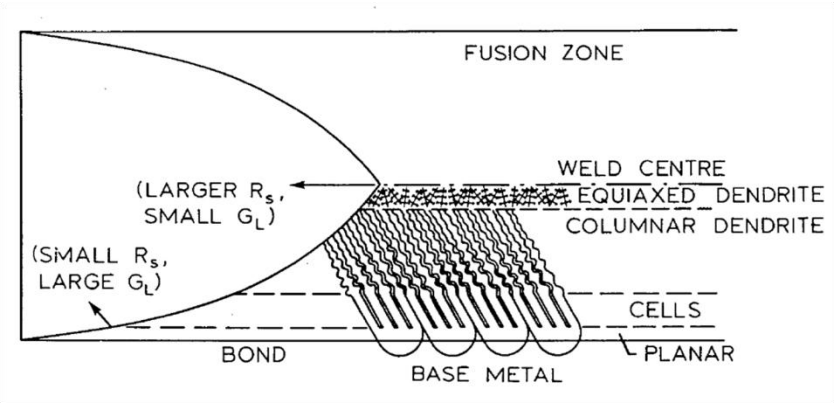

Figure 2-31: Schematic drawing of structural variation of weld microstructure across fusion zone[73].

Other important parameters that affect the melt pool microstructure is the cooling rate, $\dot{T}$, which is the product of the temperature gradient (G), and the growth rate (R), $(GR = \dot{T})$.The cooling rate mainly affects the scale of the microstructure in comparison to G/R (constitutional super cooling) which controls the morphology of the grains. Cooling rates for processes using electron beams and lasers, may vary from 10^3 to 10^6 K/s, depending on the various process parameters [73]. The details of these parameters on the grain structure in AM process in particular in Ni-based superalloys will be discussed in the microstructure of DLF section (section 2.5.3)

2.4 Residual Stresses Characterisation Techniques

Residual stresses reduce the tolerance of a component to an externally applied force. Residual stresses occur for a variety of reasons, including inelastic (plastic) deformation, temperature gradients (during thermal cycle) or structural changes (phase transformation). Heat from welding may cause localised expansion, which is taken up during welding by either the molten metal or the placement of parts being welded. When the finished weldment cools, some areas cool and contract more than others, leaving residual stresses [87].

The residual stresses can be classified into three types based on their characteristic length over which the stresses equilibrate [88] . Type I are long range stresses which equilibrate over macroscopic dimensions and are not influenced by the multiphase nature of the material. Type II residual stresses equilibrate over a number of grain dimensions and Type III stresses, exist over atomic dimensions and balance within a grain for example and are caused by dislocations and point defects [88]. For assessing the bulk residual stresses for life assessment of a component type I macro stresses play an important role, where micros stresses i.e. type II and type III are often unimportant. The different types of residual stresses that can arise are summarised in Figure 2-32. There are several measuring techniques for these stresses which will be discussed in the following sections.

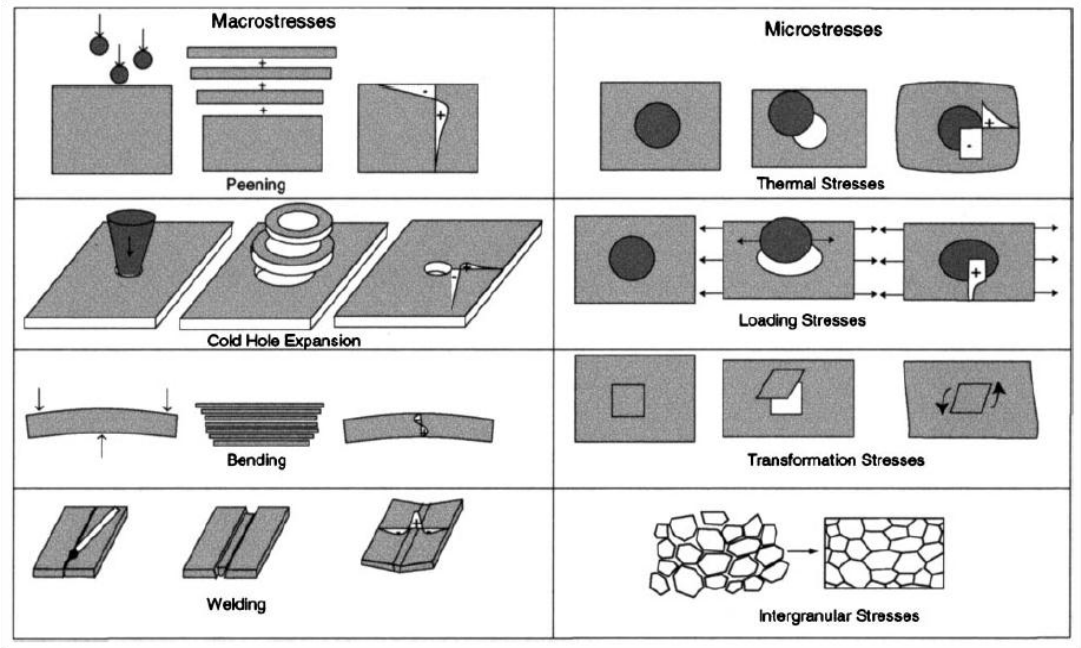

Figure 2-32: Illustration of different types of macro and micro residual stress [88].

2.4.1 Measuring Techniques

Figure 2-33 summarises the capabilities of various techniques used for residual stress characterisation, including neutron diffraction, hole drilling and contour methods which are

discussed in the following sections as they are the techniques which are most commonly used for characterising AM components.

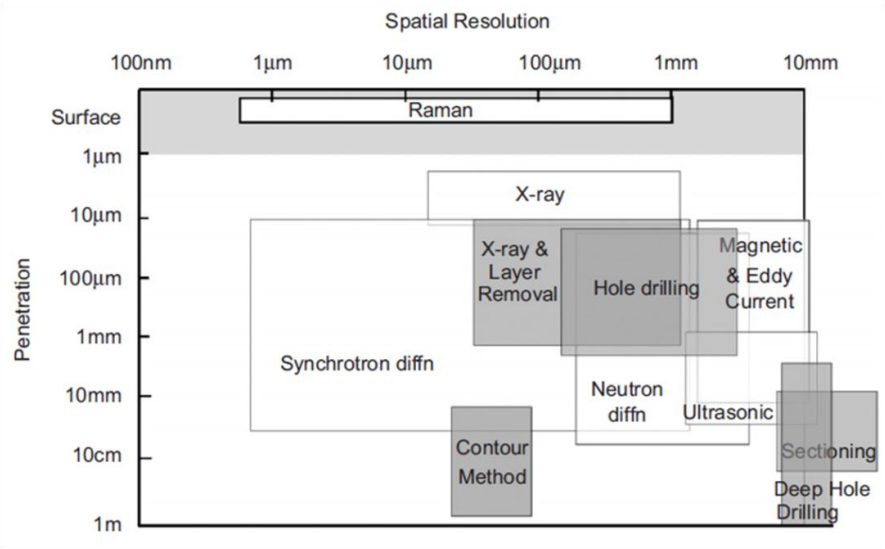

Figure 2-33: Schematic Illustration of the capabilities of the various techniques. The destructive techniques are shaded [89].

2.4.1.1 Hole Drilling Method:

It is known that the residual stresses will relax when the sample is locally machined, thereby providing data for back-calculation of the residual stresses. The same principle is used in hole-drilling whereby a hole is drilled, around which the strain is measured using a rosette of strain gauges, Figure 2-34. The residual stresses can be calculated from equation 2-2.

$$\sigma = (\sigma_{max} + \sigma_{min})\bar{A} + (\sigma_{max} - \sigma_{min})\bar{B}\cos 2\beta \qquad 2\text{-}2$$

where $\bar{A}$ and $\bar{B}$ are hole drilling constants, and β is the angle from the X-axis to the direction of maximum principal stress (σ_{max}). For the general case of a hole drilled in an infinite plate, $\bar{A}$ and $\bar{B}$ must be calculated numerically [88].

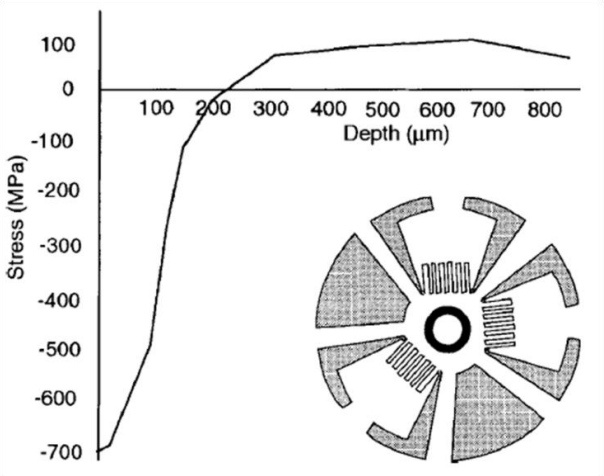

Figure 2-34: Dataset collected for stress in shot peened Ni-based alloy using hole drilling, showing a suitable arrangement of the strain gauges [90].

Although it is possible to deduce the variation in stress with depth by incrementally deepening the hole (typically called incremental hole drilling), it is difficult to obtain reliable measurements much beyond a depth equal to the diameter [91]. With a three strain gauge rosette, it is only possible to measure the two in-plane components of the stress field. Nevertheless, the method is economic, widely used and it has been applied even to polymers. If the residual stresses exceed about 50% of the yield stress, then errors can arise due to localised yielding. Additionally, it is not really practical for thin (~100 µm), or for brittle coatings [92].

2.4.1.2 Neutron Diffraction Method:

Residual stresses can be characterised using neutron diffraction, based on the principle that elastic strains are derived from the changes in the lattice spacing of the crystalline material, Figure 2-35. The stresses are calculated using the elastic properties of the material given by Hooke's law. By translating the specimen through a highly collimated neutron beam, strains within a small volume can be determined at different locations in the specimen and calculated using equation 2-3.

$$\varepsilon_{hkl} = \frac{d_{hkl} - d^0_{hkl}}{d^0_{hkl}} \qquad 2\text{-}3$$

Where, d_{hkl} is the measured d spacing for the particular hkl reflection and d^0 is the stress-free d-spacing and ε_{hkl} is the elastic strain normal to the hkl plane.

Once the strain is determined at a given location in three orthogonal directions, it is possible to calculate the corresponding stresses from equation 2-4.

$$\sigma_x = \frac{E_{hkl}((1-\upsilon_{hkl})\varepsilon_x + \upsilon_{hkl}(\varepsilon_y + \varepsilon_z))}{(1+\upsilon_{hkl})(1-2\upsilon_{hkl})} \qquad 2\text{-}4$$

Where, E_{hkl} and υ_{hkl} are the elastic constants for the direction normal to the planes for the specific hkl reflection and ε_x, ε_y and ε_z are the strains measured in the three orthogonal directions.

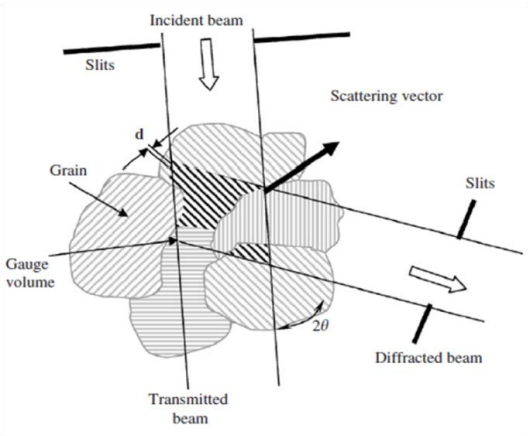

Figure 2-35: The principle of the neutron diffraction technique, for residual stress characterisation, showing the scattering vector for a Bragg reflection from the crystal planes, d [93].

One of the largest uncertainties in determining the residual stress by diffraction is the correct measurement of the strain-free lattice spacing, d_0 or alternatively the enforcement of some assumption about the state of strain or stress within the body [94]. There are various reasons

for change in the d-spacing which include compositional changes, phase transformations, change in temperatures, and integranular strains etc. So, there is a need to measure stress free d-spacing to get accurate stress measurements. Withers *et al.* [94] summarised various methods of determining stress free d_0 values and their validity, Figure 2-36, some of which will be discussed below.

Strain values from powders, filings, cubes and combs:

The d0 values can be obtained from powders or filings as they cannot sustain a long-range macrostress and so provide ideal macrostress-free reference materials. Cutting of small reference cubes, matchsticks or 'combs' a region can be freed from the constraint of the surrounding macroscopic stress field to provide a measure of d_{ref}.

Measurement in a region known to be free of macro-stress

The d values can be obtained from a point far away from the stress fields can be assumed as strain free d0 values. However this is inappropriate for welding as there is huge microstructural difference and associated compositional changes near the weld-pool.

Stress balance method

This method exploits the plane stress or plane strain conditions, where the stresses in one direction are assumed to be zero and the d0 values are back calculated. This method is particularly good for thin walled samples where the stress in the through thickness direction is almost negligible [25].

Method	Local or global	Determined or implied	Validity
Reference standard	Global	Determined	Absolute lattice spacings are not generally sufficiently well determined on strain mapping instruments
Filings/powders	Global	Determined	Often applicable for ceramics; only valid for metals if filings are representative of the alloy condition in the component
Cubes	Local	Determined	May retain intergranular stresses; vulnerable to geometrical effects if poorly positioned
Multiple measurements	Local	Determined	Absolute lattice spacings are generally well determined; measurements are relatively time-consuming
Triaxial X-ray	Local	Determined	Technically difficult to measure d^0_{hkl} absolutely; must ensure identical sample–source distance for all measurements
Extrapolation using anisotropic reflections	Local	Implied	Only effective if crystal is reasonably elastically anisotropic and two stress states can be imposed (one could be as-received); is liable to errors when plasticity can occur between the two stress states
Far field	Global	Determined	Only valid if there is no spatial variation in d^0_{hkl} and the variation for *hkl* is representative of the macrostress, and if chosen locations are actually stress-free
$\sin^2\psi$	Local	Implied	Only valid for truly plane stress (nevertheless, there are many cases when this holds, *e.g.* near surface, in thin plates/slices); sensitive to intergranular and interphase stresses which may not be zero over the sampling volume, even when macrostress is zero
Stress balance	Global	Implied	Only valid if there is no spatial variation in d^0_{hkl} and the complete area normal to the stress is mapped; variation for a_{hkl} must be representative of the macrostress; best held in reserve as a confirmation that a^0 has been correctly estimated

Figure 2-36: Table summarising the various methods for determining stress free d_0 values [94].

The other uncertainty in measuring the residual stresses is the determination of the elastic constant (poison's ratio and elastic modulus). The elastic strain recorded for a given reflection may not be representative of the bulk elastic strain [88] due to elastic stiffness mismatch between differently oriented grains and differences in the plastic yielding response of adjacent grains. The elastic constant for different planes can be determined based on the Kröner model, which is explained elsewhere [88, 95-96]. The elastic constants for different planes of IN718 were determined by Repper *et al*. [96] and are summarised in, table

Table 2-4: Young's modulus for different IN718 sample states and lattice planes determined by neutron diffraction compared with diffraction elastic constants for pure nickel calculated with a computer software based on the Kröner model [96].

Sample	Diffraction elastic constant [GPa] of lattice planes			
	{200}	{220}	{311}	{222}
Comercially available Ingot	187 ± 12	220 ± 5	197 ± 7	257 ± 9
With δ Phase	194 ± 18	203 ± 8	198 ± 6	240 ± 24
Standard industrial Heat treated	170 ± 9	208 ± 7	203 ± 14	280 ± 24
Kröner	178	232	208	258

Although, neutron diffraction is expensive compared to hole drilling, in hole drilling the residual stresses can be obtained only on the surface of the material (about 0.75 mm) whereas neutrons can penetrate much further than this and also the stresses can be measured in 3 orthogonal directions [24].

2.4.1.3 Contour Method:

Unlike neutron diffraction and hole drilling, the contour method is a destructive residual stress characterization method. In this technique, the residual stresses are characterised by carefully making a cut (generally by electric discharge wire cutting, which induces virtually no stress to the cut surface). Cutting releases the stresses from the part, which results in a slight distortion which can be measured on the deformed surface using a laser scanner. By using a finite element model, the stress contours can be calculated, Figure 2-37. The details about the cutting techniques and other measuring constraints can be found elsewhere [97].

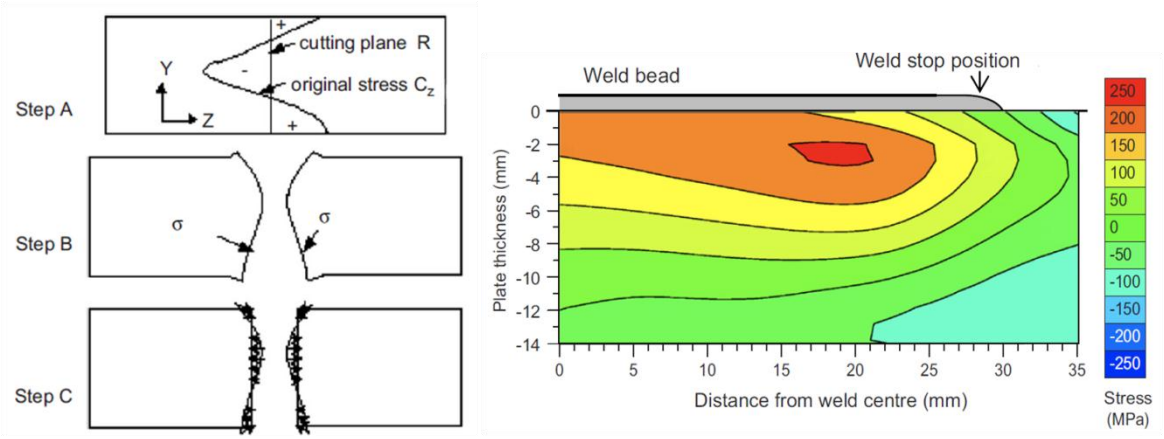

Figure 2-37: 2D schematic of the contour method showing various steps involved in residual stress measurement and residual stresses calculated around the weld bead [98].

This is a relatively new and powerful technique for residual stress characterisation which can be used for relatively thick parts where penetration of neutrons would become difficult [97]. Additionally, this method can also provide answers for component materials where the presence of multiple phases, absence of crystallinity, highly preferred orientation (e.g. single

crystals), and large grain size make the interpretation of neutron measurements difficult [99]. The method is also able to derive residual stress contours on a surface, which would take a lot of effort and beam time using neutron diffraction experiments (e.g. for shot peened specimens).

In the previous sections, 2.1 to 2.4, the literature on the types of superalloys and their strengthening mechanisms were discussed followed by a summary of the solidification theory behind the formation of different grain structures. The following section shows the Direct Laser Fabrication technique with the associated difficulties in this process i.e. build quality, microstructure, precipitation and residual stresses followed by the various modelling techniques used in predicting the residual stresses and microstructure in DLFed builds.

2.5 Direct Laser Fabrication

In this section, a brief introduction is given about DLF including the process variables and their effect on the build quality, microstructural development (including grain and precipitate morphology), texture and residual stresses development. Also, recent literature especially those of relevance to the present work are covered including the various thermal and stress models on the microstructural and textural development, emphasis is given on Ni-based superalloys literature, in particular IN718 as it is used in the present project.

2.5.1 Introduction

The basic layout of a DLF system is shown in Figure 2-38, showing the laser and its associated optical delivery systems, a powder feeding unit (consisting of powder hoppers, nozzles and carrier gas for carrying the powder), computer numerical control (CNC) unit which controls the X-Y movement of the stage and Z moment of the laser head. The deposition is typically carried out in a glove box in controlled atmosphere [100]. The process

works in a way that the desired components CAD file is sliced into layers and the layers are converted into a numerical code, which is fed to the CNC unit where the laser head as well as the stage move accordingly to produce the final part. The powder is fed though the nozzles in a controlled manner, with inert gas (usually Argon or Helium) as a carrier gas. The powder is melted and re-solidifies across the layers. The laser power, powder flow rate, layer thickness and scan speed are controlled to produce the final part.

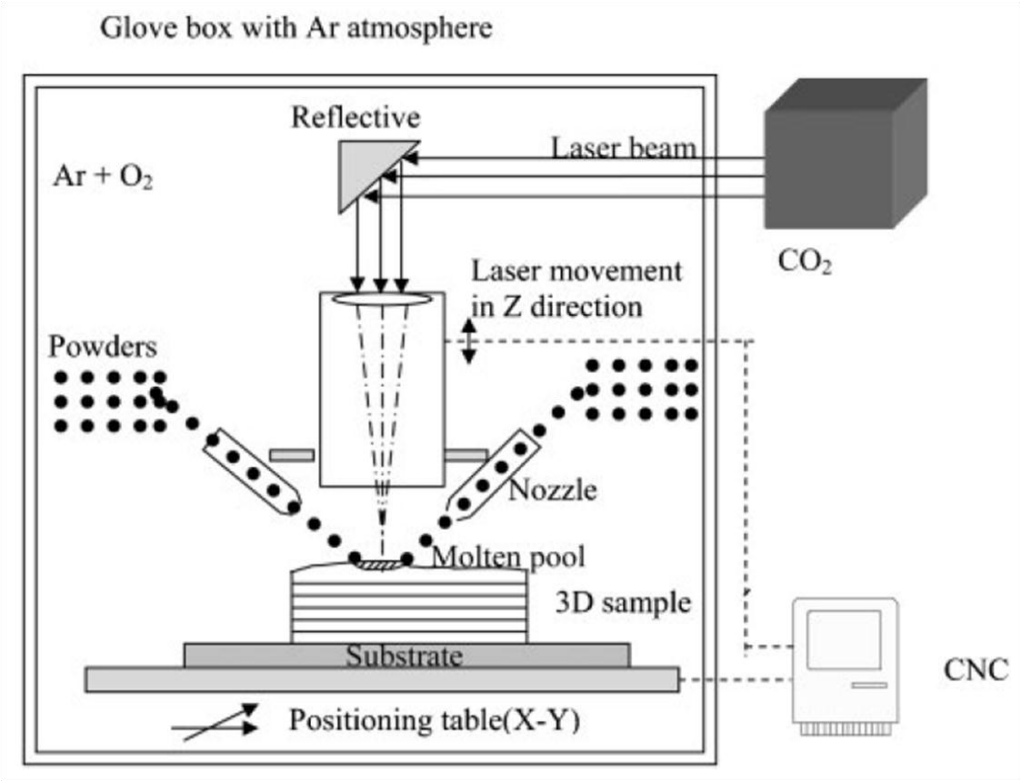

Figure 2-38: Schematic of direct laser fabrication system layout[1].

2.5.2 Build Geometry and Quality

The important factors which effect the build quality are laser power, traverse speed/ scan speed of laser beam, stand-off distance (laser focus) i.e. the distance from the laser nozzle head to the work piece when the laser beam and powder are focused on the work piece (schematic shown in Figure 2-39.a) , hatch spacing (line overlap) i.e. the distance or the % of

laser beam diameter that is overlapped by the subsequent laser pass (schematic shown in Figure 2-39.b), layer thickness, and powder flow rate. A number of studies have been performed to assess the influence of these parameters on the structural and geometrical integrity of the builds, some of which will be discussed in the following sections.

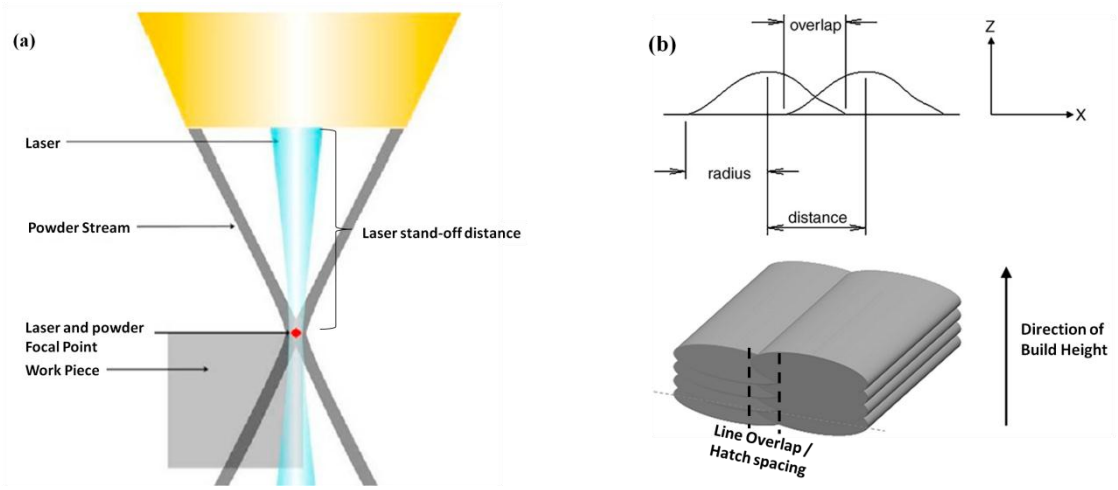

Figure 2-39: Schematic showing the a) laser stand-off distance [101] and b) line overlap / hatch spacing between layers [102] in a DLF system.

Previous work classified pore and void formation in DLF into three categories:

i) Inter-run porosity, caused by the wrong offset tracks settings of which forms near the base of deposited tracks which can be rectified by proper selection of the offset. This type of porosity can be reduced by reducing the Z-overlap distance which is shown in Figure 2-40.

ii) inter-layer lack of fusion porosity which is caused by incomplete bonding between adjacent tracks [9] which can be reduced by increasing the overlapping distance between adjacent layers.

iii) Intra-layer porosity which appear as spherical areas of porosity within a layer the cause of which is not always clear, but is thought to be related to gas dissolved or entrapped within the

melt [103]. Studies by Qi *et al.* on IN 718 builds [22] showed that selection of powder with entrapped pores would give a sound build, Figure 2-41.

Factors that can lead to porosity include inconsistent specific energy, misplaced tracks, an oxide layer preventing or hindering fusion. The process can ensure a fully dense microstructure with almost no defect at layer boundaries by carefully controlling the process parameters [1, 16, 22]. Previous work by Qi et.al, and others using DoE, and others showed that the laser power, powder flow rate and scan speed are the main controlling factors for porosity and build geometry in DLF [8-9, 104] as discussed in the following sections.

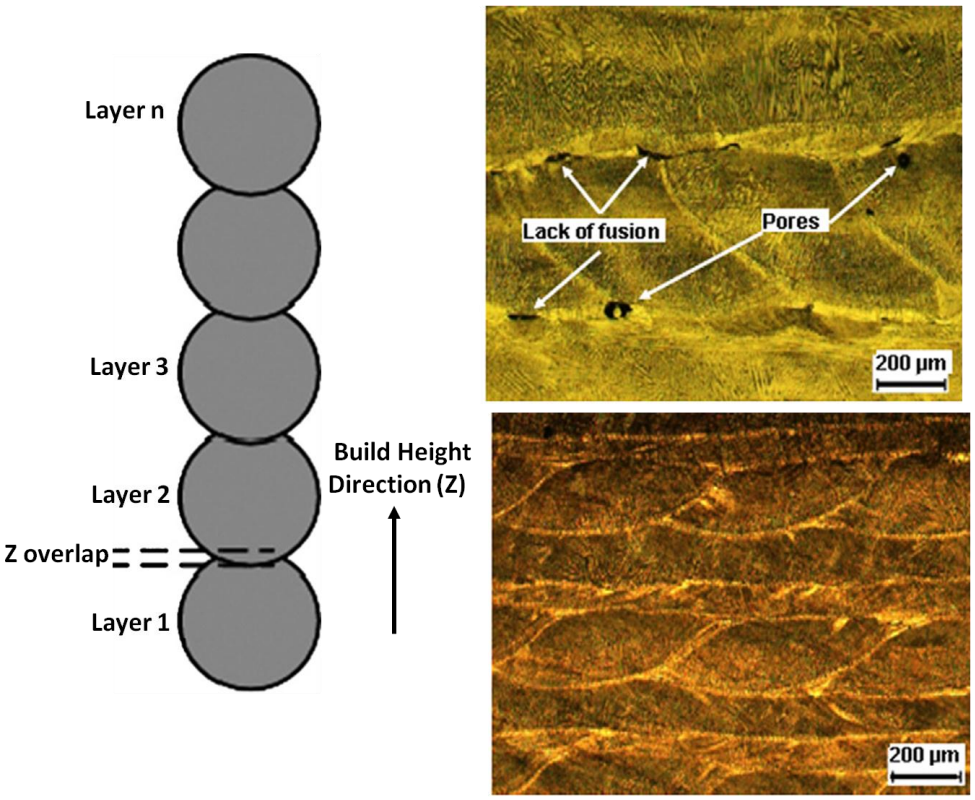

Figure 2-40: Figure showing the effect of Z-overlap on inter-run porosity in a Ni-based superalloy Nimonic 80A: a) schematic showing the Z overlap distance, b) micrograph inter-layer porosity due to large Z overlap distance, c) micrograph showing no visible inter layer porosity after reducing the Z overlap distance by 50 % [105].

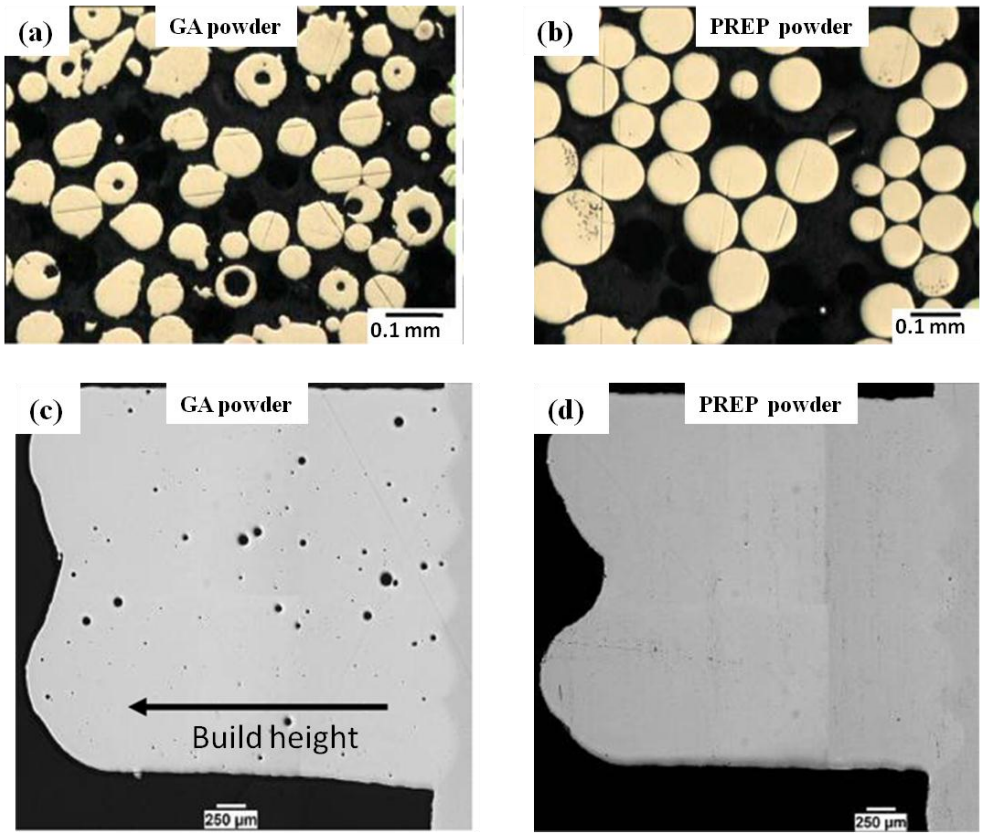

Figure 2-41: Effect of the initial porosity in the build quality in DLFed IN 718 builds: a & b) showing the cross section of gas atomised (GA) and plasma rotating electrode process (PREP) powder, c & d) showing the corresponding laser builds with different porosity levels [22].

2.5.2.1 Laser Power:

Increase in the laser power was found to result in an increase in the density and height of the build [9]. However too high laser power may cause evaporation and thus cause a change in the alloy composition [106]. Additionally, pulsed laser was found to suppress the tendency of balling, with the height of the build increasing for high duty cycles (ratio of pulse length to total cycle time) [107]. The laser defocus distance has a direct influence on the spot size, whereby larger defocus distance leads to a larger spot size and an increased bead width. Although higher laser power results in lower voids/bonding defects [108], it increases the melt pool temperature, decreasing the molten metal viscosity, which can create turbulence in

the melt pool during powder feeding, offering a mechanism for gas entrapment in the build [109].

2.5.2.2 Scan Speed:

Studies by Kobryn [9] on DLFed Ti-6Al-4V alloy showed that the build height and porosity decreases with increase in travel speed, Figure 2-42. The decrease in porosity with increasing traverse speed was not intuitively expected, but was probably a result of the decrease in the amount of powder being delivered with increasing speed [9].

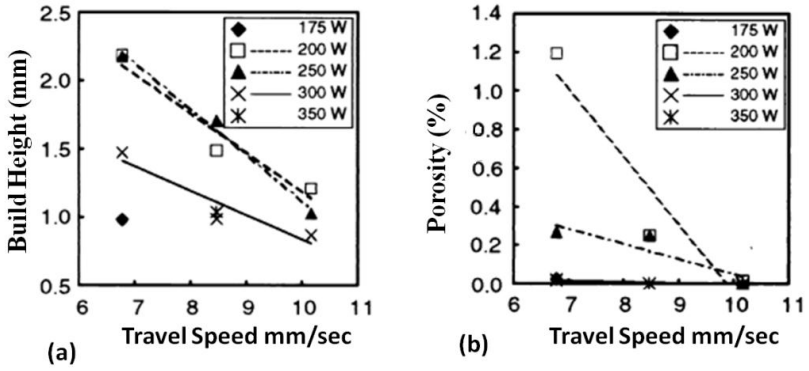

Figure 2-42: Effect of scan speed on the: a)build height and b) porosity at different laser powers in DLFed Ti-6Al-4V alloy [9].

2.5.2.3 Powder:

The powder type and quality can influence the build integrity in a number of aspects. For DLF the ideal powder size is around 50-100μm for good nozzle flow [1, 20] and surface finish of the build. The surface finish of the build can be improved by 10-30 % by reducing the powder size from 100-250 μm to 50 μm [110]. However, the use of small particle size would cause poor capture efficiency (the efficiency of powder usage/deposition) since the fine powder is dispersed by the carrier gas [1].

Increase in powder flow rate also increases the porosity due both to the increased scattering of the laser beam, by the powder as well as the increase of powder stream density into the

melt-pool, which contribute to the attenuation of laser energy coupling thereby leading to the porosity in the material [108]. This effect can be minimised with an increase in laser power where the power would be high enough for complete melting of powders even after the intervention with the high powder stream, Figure 2-43.

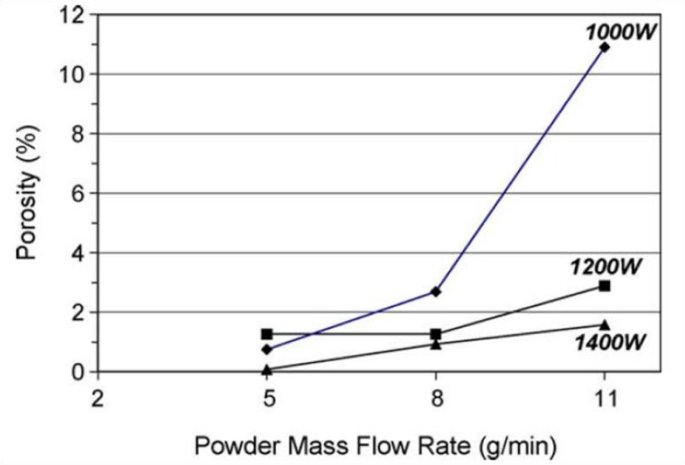

Figure 2-43: Effect of powder flow rate on the porosity of the DLFed H13 tool steel builds at different laser powers [108].

Kong *et al.* performed a study where they used experiments to optimise DLF of IN718 in order to obtain builds with minimum porosity by varying laser power, scan speed and powder flow rate.

It was observed that the porosity levels tend to increase with the increase in scan speed and powder flow rate, whereas the depth of penetration of the laser into the layers increased with decrease in scan speed and powder flow rate ,Figure 2-44, due to an effective increase in linear laser energy [101]. DLFed IN718 did not show any cracking due to the good weldability of the alloy [11, 16, 22]. However, Kong et.al have observed some cracking of this alloy at high power (1400 W) and low powder flow rate (2 g/min) and scan speeds (800mm/min) due to excessive thermal distortion at such high laser powers.

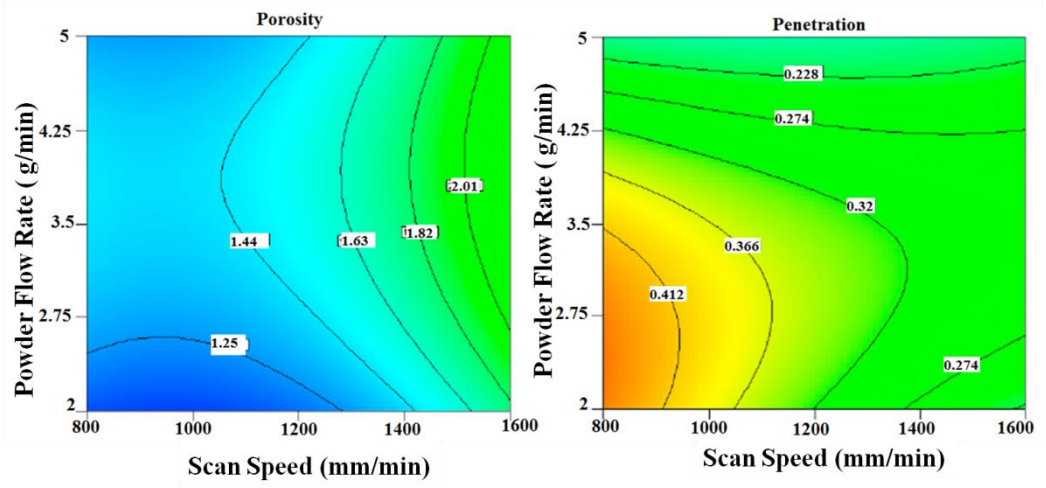

Figure 2-44: The Variation in porosity and penetration depth of laser with varying powder flow rate and scan speed at 1400W laser power and 40% overlap between layers [101].

2.5.2.4 Energy Density

Steen has shown that the laser power, scan speed and spot size are interdependent (i.e. laser power and scan speed determine the energy input per unit distance of travel), which can be given as a single unit called power density or energy density which in turn determines the melt pool size [111]. The incident energy or the energy density E(J mm^{-2}), is the most important factor which determines the build quality of the component which can be calculated by a simplified equation (equation 2-5) where P is the laser power (W), S is the scan speed (mm s^{-1}) and diameter of the spot, d [9, 112].

$$E = \frac{P}{S \times d} \qquad 2\text{-}5$$

For a given energy density, an increase in scan speed of the laser causes an effective decrease in the laser power per unit area (from equation 2-5), causing a decrease in the build height, Figure 2-42.a, while a decrease in scan speed increases the width of the heat-affected zone and lowers the viscosity of the melt pool, causing uneven build and bad surface finish due to the hydrodynamics of the molten pool, causing uneven build and bad surface finish due to the

hydrodynamics of the molten pool [113-114]. This effect is also seen in wire deposited IN 625 alloy, Figure 2-45.

Studies by Qi *et al.* on DLFed IN718 showed that the porosity of the build decreases with increase in linear energy (i.e. energy density for a given deposition length), Figure 2-46, which is due to complete melting of powders and less lack of fusion between layers at high incident linear energies [22].

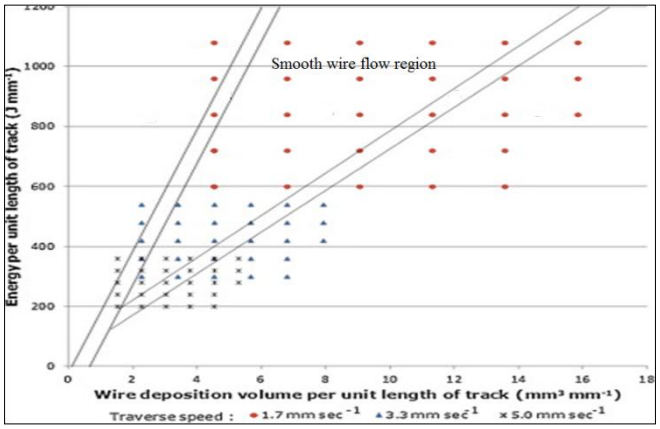

Figure 2-45: Process window showing the effect of laser power, travel speed in wire deposited IN 625 [115].

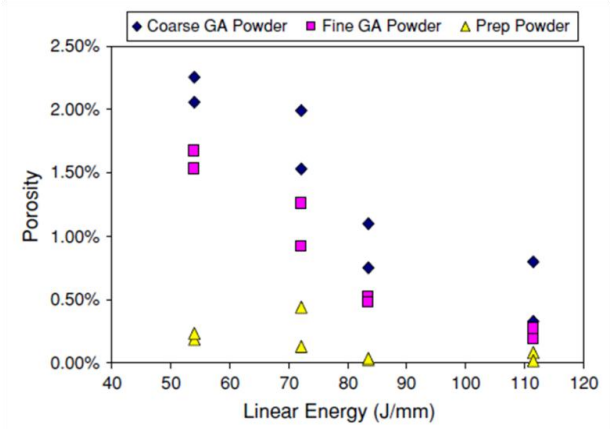

Figure 2-46: Effect of linear energy and powder type on porosity in DLFed IN718 builds [22].

2.5.2.5 Nozzle Angles:

Fearon *et al.* have proposed that the layer height can be controlled by the nozzle angles. A 45º configuration of nozzles appear to provide the optimal condition for height control of the build and the catchment efficiency [116]. The powder capture efficiency in four way nozzle is 37% relatively higher than a 3 beam nozzle (23%). Also, a 4-way nozzle gives a stable layer height to the build due to the symmetric flow of powder [8].

2.5.2.6 Scanning strategy:

The scan spacing should be sufficient to cause re-melting of the previous layer. An overlap of 30-40 % between the consecutive passes is ideal for sound builds with no lack of fusion/voids between passes [101, 117]. The thickness of the bead increases with the increase in the % overlap between the passes as shown in Figure 2-47 [118]. A orthogonally hatched build on pattern give sound quality deposits, since any major porosity/voids that arise in one layer can be easily rectified in the following layer as the bead direction is varied [119].

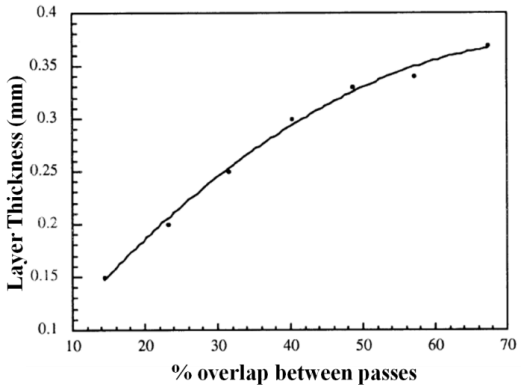

Figure 2-47: Variation of Layer thickness with % overlap between laser passes[118].

2.5.3 Microstructure

During DLF, solidification occurs rapidly in a small localised volume, and the resulting microstructures are affected by repetitive thermal cycling. In addition, solidification times are short, and steep thermal gradients may exist particularly when an intense laser source is used

[120]. The deposited material is also thermally affected by the deposition of the subsequent layers, resulting in complex thermal histories, making the prediction of the microstructures difficult [121]. DLF process variables can also influence the microstructural development including the laser power, spot size, laser traverse speed, line spacing or overlap between lines, build layer thickness, deposition pattern or path, powder shape and size distribution, powder feed rate, substrate surface finish, substrate thickness, substrate microstructure and its texture, the size and the shape of the build. Extensive research has been performed to understand the grain morphology [9, 16-17, 107, 109, 122-124], precipitation (in case of IN718 [11, 21-22, 122]) and texture [15-16, 82, 125-126] developed during DLF which is shown in the following sections.

2.5.3.1 *Dendrite Morphology of laser deposits:*

DLF builds typically show a layered microstructure with bead like morphology, Figure 2-48.a, having a fine columnar dendritic morphology, Figure 2-48.b, with very small dendrite arm spacing [17]. The interdendritic spacing was found to be 30 times smaller in DLFed CMSX-4 than a a typical as-cast microstructure [82], which could be due to the rapid cooling rate involved in DLF (~ 10^2 to 10^3 Ks^{-1}) [109].

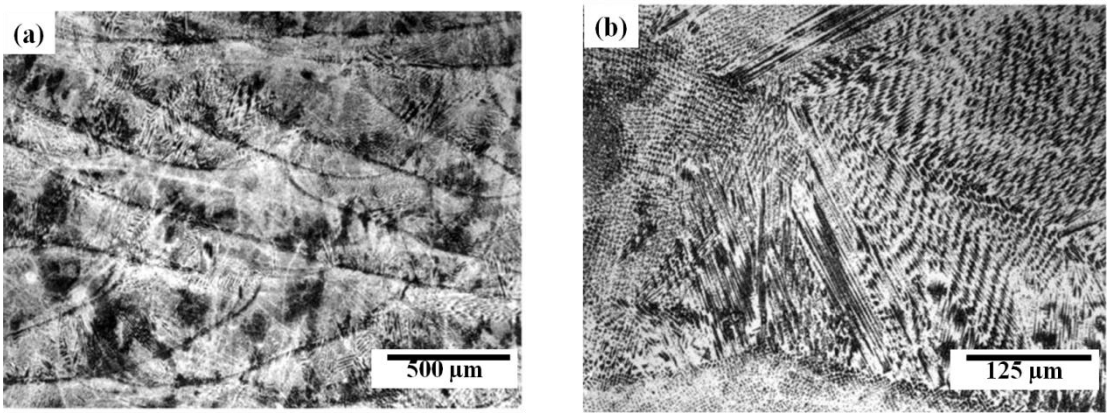

Figure 2-48: Optical micrographs of DLFed IN718 showing a) layered type morphology and b) magnified image showing fine dendrites [16].

The dendrites, in FCC crystals, tend to orient along the ⟨100⟩ crystallographic direction growing epitaxially from the substrate [12, 122], however this orientation is strongly dependent on the deposition direction used [17]. The effect of scan strategy (namely unidirectional where the scan direction is the same for each layer and bi-directional where the scan direction changes by 180º from the previous layer) on dendrite orientation was studied by Dindal *et al.* on DLFed IN 625 thin walls. Since the grains grow perpendicular to the melt pool base (along the heat flux direction), which is consistently tilted due to the scanning of laser beam from right to left and the cooling direction of the melt pool changes with the direction of laser scan a change in the direction of dendrites occurs [17], Figure 2-49.

The dendrite morphology at the interface of two layers is observed to be a fine cellular dendritic network, which is caused by dynamic heat transfer of the moving heat source and deposition mechanism in the multi-layer material [127]. During layer by layer deposition, when a new layer is deposited a limited re-melting occurs in the previous layer. Subsequently, as the molten pool solidifies, a thin nucleation zone forms at the interface [127].

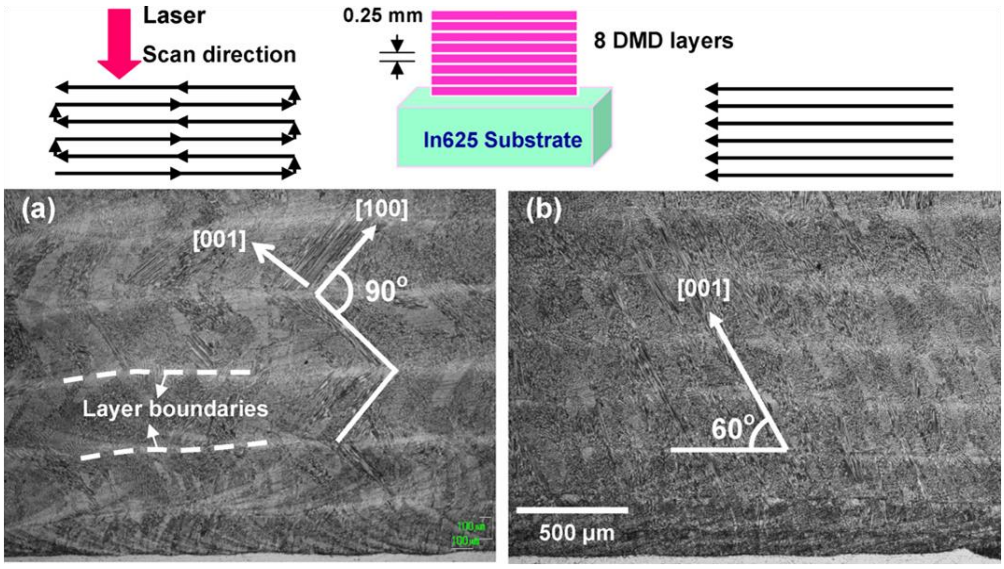

Figure 2-49: Optical micrographs of laser deposited Inconel 625 thin walls showing the effect of deposition direction on the dendrite orientation: a) bi-directional and b) uni-directional [17].

2.5.3.2 Grain morphology in laser deposits:

The incident energy, deposition path and travel speed have a strong influence on the grain morphology, size, the degree of grain coarsening and the microstructural homogeneity of DLFed builds.

The microstructures in laser deposits are very heterogeneous in appearance, with variations in grain size and grain aspect ratio occurring over relatively small distances [16, 25, 124, 126, 128]. Research published by Moat *et al.* [126] (Waspaloy), Liu *et al.* [23] and Blackwell [16] (IN718) show a banded grain structure with bi-modal grain distribution with fine grained regions lying between the large columnar regions at the edge and centre of the laser scan path respectively. These fine grain zones are the result of rapid cooling at the edge of laser scan lines (The banded microstructure is shown in Figure 2-50).

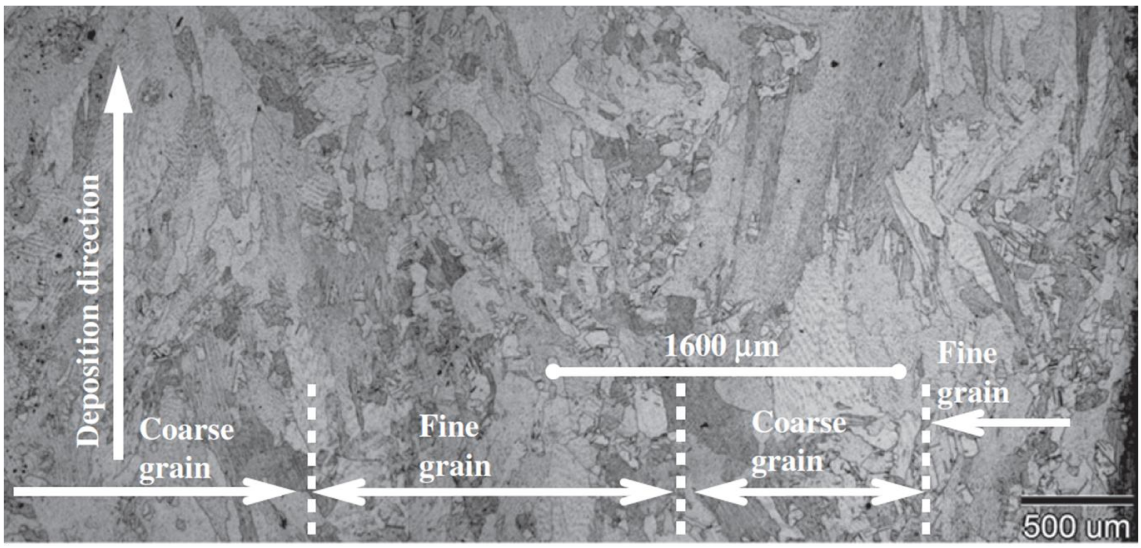

Figure 2-50: Micrograph showing banded grain structure in DLFed IN718 [23].

Work by Wu [123] and Moat *et al.* [126] showed large columnar grain structures in laser builds are detrimental for fatigue properties. However, this grain structure i.e., the grain size

and shape can be altered by choosing the right process parameters. Kobryon *et al.* showed that the grain width decreases with increasing traverse speed (Figure 2-52.a), but was largely unaffected by power level. Thus, grain width also tended to increase with incident energy (Figure 2-52.b) in Ti-6Al-4V alloy. The increase in grain width with incident energy is attributed to the cooling rate where the grain size tends to decrease with increase in cooling rate [75] that is observed in low incident energy due to a combination of low power and high speed [9].

Gaumann *et al.* developed process maps to predict the columnar-to-equiaxed transition for Ni-based superalloy CMSX-4 [129]. Figure 2-51 shows the process maps for laser deposition showing the combined effect of laser power (P) and scan speed (V) on the grain morphology for different pre-heating temperatures (T_0). It is clearly shown that increase in power increases equiaxed formation, but studies by Pinketron *et al.* on laser deposited waspaloy showed that high laser power with low powder flow rates showed columnar growth [130]. The higher laser power and lower powder flow give a larger and deeper melt pool which increases the mean value of R and if acting alone would have increased the tendency to form equiaxed grains. However, the large melt pool also promotes vigorous Marangoni flow, and there is also some evidence of more superheating in the melt-pool which could increase G [130].

It is also interesting to see that the effect of beam velocity showed a c-shaped curve i.e. scanning speeds of the order of 20 mm/s have a greater probability of forming an equiaxed morphology than scanning speeds in the range of 1 or 100 mm/s. At low velocity, an increase in V increases R without a major effect on G, leading to a decrease in the G^n/R ratio. At high velocity, the melt pool becomes smaller, leading to a higher temperature gradient. Hence, even if R is increased, the ratio G^n/R may increase. However, a treatment with high V will be

critical with respect to surface melting. With preheating the re-melting of the surface is easier and equiaxed morphology is promoted.

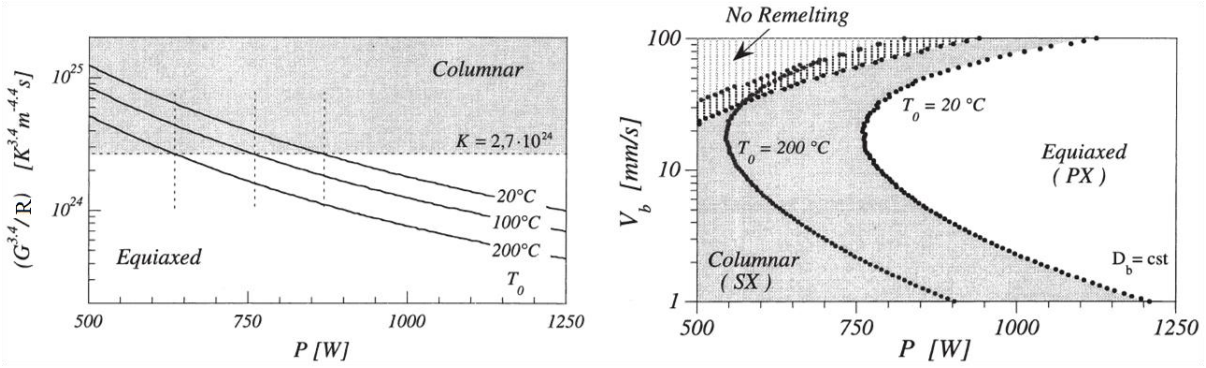

Figure 2-51: The process map showing the regions for columnar and equiaxed grain zones in laser deposited CMSX-4: (a) showing the process map for different laser power (P) and G/R ratios (b) processing map for different laser power (P) and beam scanning speed (V); at different pre-heating temperatures (T_0) [82].

Work by Moat et.al on Waspaloy suggested that use of pulsed laser with low cycle periods (fraction of time for which the beam is on) results in grain refinement. However this does not control the preferred orientation of grains [126] and also the effect of pulsed laser is not as prominent as in multi tracked thick walls as it is in thin wall deposits [25].

Also, the grain morphology is dependent on the material used for deposition where Ti alloys often feature elongated grain structure due to epitaxial growth [131], however this epitaxial growth was not observed in IN718 builds, as studied by Blackwell on IN718 [16] for similar process parameters , which was attributed to high cooling rates for IN718 compared to titanium alloys due to significant difference in thermal conductivity of these alloys.

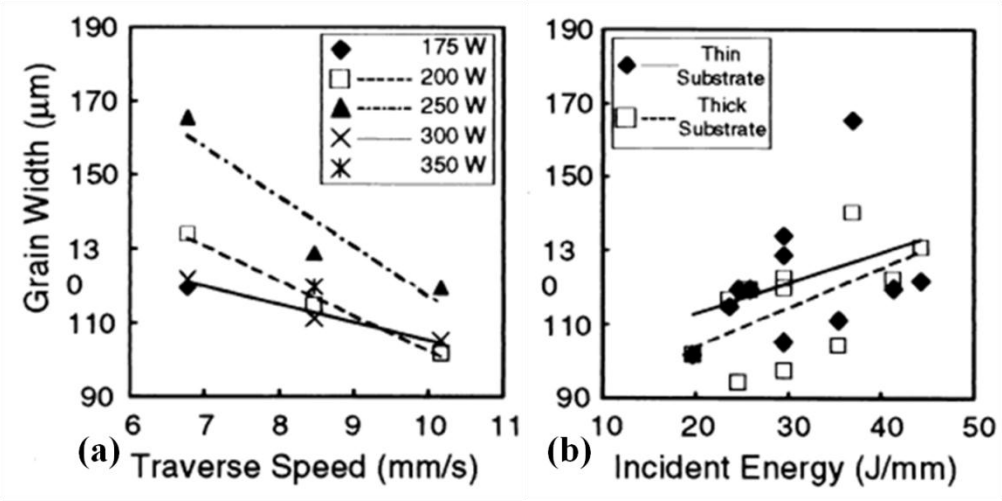

Figure 2-52: Grain width as a function of (a) scan speed/ travel speed at various laser powers and (b) incident energy for different build sizes in DLFed Ti-6Al-4V [9].

2.5.3.3 Precipitation in DLF IN718

During laser melting, the strengthening phases such as the γ" phase and the γ' phase melt in the matrix. The melt pool of the re-melted substrate alloy and the fed alloy powder form austenite in the subsequent rapid solidification stage [122]. However, unlike the simple monolayer cladding, DLF is a technology of multilayer cladding with overlapping. The accumulation of heat results in a decrease in the temperature gradient on the interface of the solid and the liquid. Besides, the direction of temperature gradient changes because of overlapping. Therefore, micro-segregation occurs in the inter-dendritic area. The high melting point elements such as Nb, Mo and Ti segregate to the columnar crystal trunk, which shows that the Nb, Mo and Ti segregated more severely than the other elements [122].

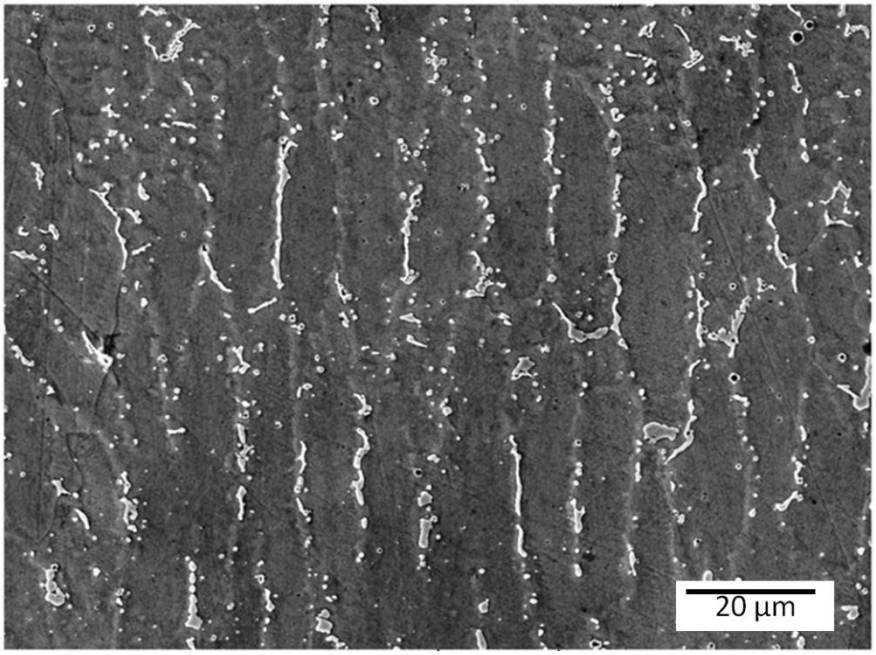

Figure 2-53: SEM micrograph showing the laves phases in DLFed IN718 [21].

All the previous microstructural studies of laser deposited IN718 samples showed Nb segregation and presence of Laves phases [11-12, 21-22, 132-133] of various shapes and sizes, Figure 2-53, depending on the processing parameters with minor amounts MC type of niobium carbides [22, 132].

The brittle irregular shaped Laves phases observed at the inter-dendritic regions deplete the γ matrix of Nb (the γ" forming element), leading to poor mechanical properties. Solution treatment (at 982 ºC for 1h) and ageing (at 718 ºC for 8 h, air cooling to 621 ºC and holding for 10h) heat treatment convert the Laves phases to δ phase, with excess Nb partially dissolving into the γ matrix, Figure 2-54.a. However, this solution treatment cannot dissolve the Laves phases completely [22]. Homogenisation heat treatment (at 1100 ºC for 1-2 h) followed by solution treatment with ageing, would completely dissolve the Laves phases into the γ matrix, Figure 2-54.b.

;

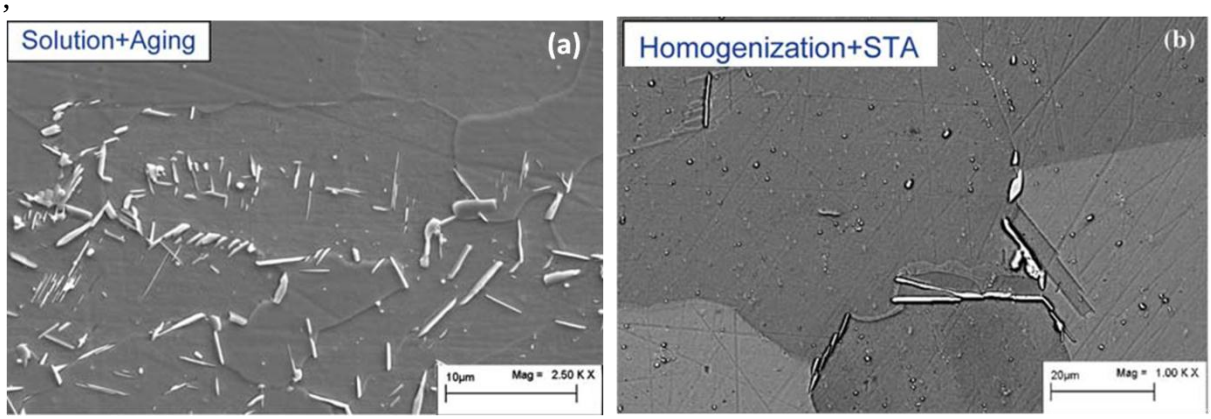

Figure 2-54: Effect of heat treatment on the precipitation in DLFed IN718: (a) Laves phase transformed to δ needles after solution + aging treatment; (b) Considerable grain growth after Homogenisation+ solution + aging treatment [22] with occasional δ phase at the grain boundaries.

2.5.3.4 Texture evolution in DLF:

The textures formed in DLF builds have not been widely studied. For FCC materials the dendrite trunks grow preferentially with the ⟨100⟩ crystal orientation closest to the heat flux, thereby selecting the orientation which is closest to the normal to the solid–liquid interface. The presence of a ⟨100⟩ fibre texture in DLF has been previously observed by Moat *et al.* [126] and Dinda *et al.* [18] in their work on laser metal deposition of Waspaloy and IN718 respectively. However, in the study by Moat *et al.* [126], the ⟨100⟩ fibre axis was found to be tilted away from growth (Nz) direction i.e. perpendicular to beam travel direction (as shown in Figure 2-55), by an amount that varied with the process conditions. This effect was attributed to the scanning pattern used, that involved a single beam path that always moved in the same direction, and the curvature of the rear of the melt pool, which changed with different beam parameters.

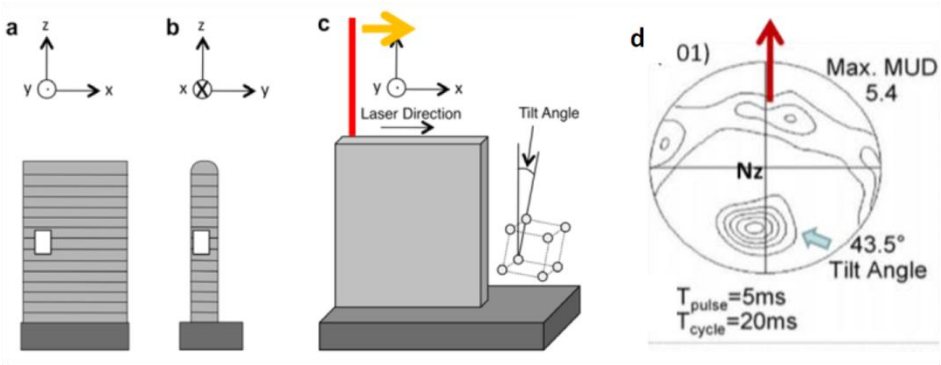

Figure 2-55: Schematic diagram of the sample cross-section geometry and texture measurement location (white rectangle box) for (a) the longitudinal direction, and (b) the transverse direction, (c) the definition of the <001> plane tilt with respect to the geometry and, d) a pole figure showing fibre texture tilted by 43.5˚ from Nz due to the unidirectional movement of the heat source along X: taken from Moat *el al*. [126] for laser deposited Waspaloy.

Studies by Dinda *et al.* [18] showed that the texture varied with the deposition path used. A fibre texture is observed in uni-directional deposition path, but if a bi-directional deposition type is used a cube texture is observed, Figure 2-56. In uni-directional deposition, the solidification is dominated by the nucleation of new grains and growth in a ⟨100⟩ direction, where only one of the ⟨100⟩ directions of columnar dendrites was oriented parallel to the heat flow direction and the two other ⟨100⟩ directions were free whereas in bi-directional pattern, pattern where each layer is 90º to the next the layer, the secondary dendrites of the previous layer can serve as a growth front for the primary dendrites of new layer which makes the dendrites grow epitaxially from the previous layer rather than nucleating new grains. Studies by Pinketrol *et al.* showed that the texture intensity diminishes with the feed rate as well as with laser power as there are more nucleation sites provided by powder feed where nucleation of new grains is preferred over epitaxial growth from previous layer [130].

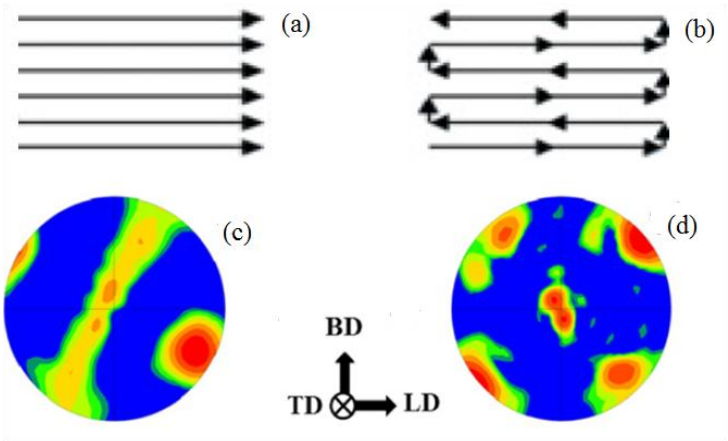

Figure 2-56: Effect of deposition direction on texture: (a) schematic of uni-directional scanning (b) Schematic of bi-directional scanning patterns; (100) pole figure of builds for c) uni-direction and d) bi-directional deposition patterns [18].

2.5.4 Post Deposition Treatment in DLF

The grain size is typically heterogeneous throughout the laser builds with bands of fine and coarse grains and non-uniform, unwanted phases (e.g Laves and δ in case of IN 718) are observed. It is important to do post deposition heat treatments to reduce the residual stresses and homogenise the precipitate segregation.

Dinda *et al.* [17] studied the thermal stability of the dendritic structure in IN625 due to post-deposition heat treatment. Figure 2-57 shows the variation in microstructure of samples annealed for 1h at different temperatures. The dendrite structure remains unchanged until 1000 ºC nucleation of the grains beginning from the layer interface and the grains are fully recrystallised with grain growth at 1200 ºC, with annealing twins which formed due to the presence of residual stresses in the as deposited builds [17]. The same effect of heat treatment on grain structure was observed by Qi *et al.* [22] for laser deposited IN718 samples, with recrystallisation occurring at 1100 ºC for 1-2h. Studies by Cao *et al.* on laser deposited IN718 samples also showed complete recrystallisation at 1100 C for 1h, with nucleation starting at the overlap area between the two successive passes, after only 15 minutes of holding time

[134]. Nucleation typically began in the overlap area where higher residual stresses exist. Refined grains expand from the overlap area to the whole area with the increase in the cycle time [134].

Heat treatment + HIPping (Hot Isostatic Pressing) above 1160 ºC on laser deposited IN718 did not show any grain growth which was attributed to the presence of fine second phase particles inhibiting grain growth, from the original powder surfaces or generated during the deposition process [16]. Although recrystallisation has occurred with equiaxed grains forming in place of columnar grains [17, 22, 134], the grain size distribution is in homogeneous, showing relatively fine grains at the edges, Figure 2-57.c as well as at the layer overlap regions [134] of the build and coarse grains at the centre. Overlap of ~50% between layers rectified this problem, resulting in a more uniform equiaxed grain structure throughout the deposit after recrystallisation [134]. However, such a high overlap rates gave very poor build quality with respect to geometrical integrity and consistency.

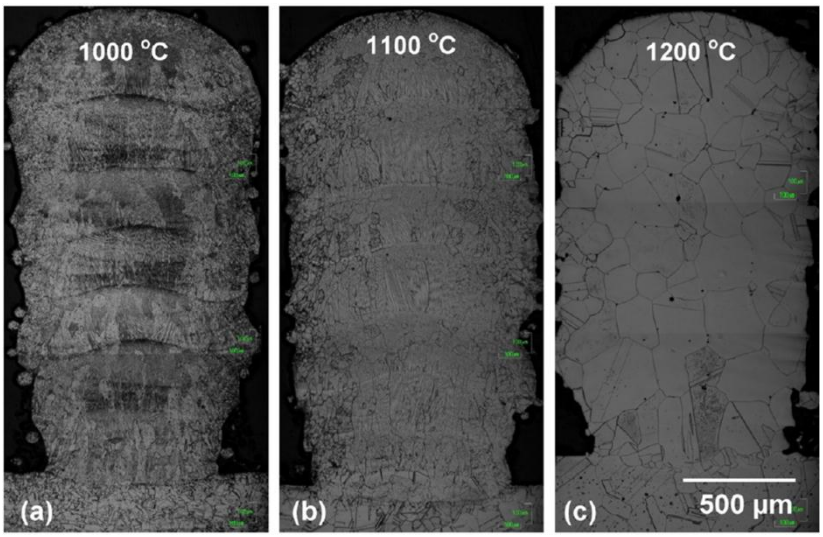

Figure 2-57: The microstructures of the laser deposited Inconel 625 sample annealed at different temperatures showing (a) No effect heat treatment on grain structure at 1000 C (b) Start of recrystallisation at the layer boundaries at 1100 C (c) Complete recrystallisation and grain growth at 1200 C[17].

2.5.5 Mechanical Properties in DLF

The mechanical properties of additive manufactured components are superior to those of cast products due to the fine dendritic structure, but are generally poor compared to wrought products. The mechanical properties obtained by various AM methods when compared with wrought and cast IN718 products are tabulated in Table 2-5.

Table 2-5: Mechanical properties of as-deposited IN718 AM parts in comparison with wrought and as-cast products.

Specimen condition (Ref)	**Tensile strength (MPa)**	**Yield Strength (MPa)**	**% Elongation**
DLF - powder [16]	1000	650	-
DLF- powder [22]	904	552	16
DLF-powder [12]	845	590	11
Wire laser fabrication [135]	828	473	28
Powder bed SLM [133]	1137–1148	889–907	19.2–25.9
Electron beam Melting [135]	910	580	22
As-cast IN718 [22]	862	758	5
Wrought IN718 (AMS) [133]	1275–1400	1030–1167	12–21

Studies by Blackwell on laser deposited IN718 builds showed that the as-deposited samples have poor tensile properties because of the un-melted/partially melted powders trapped in the deposits. However the properties can be regained by HIPping and heat treatment at 1160 ºC [16]. Qi *et al.* did not find any partially melted powders in the as deposited IN 718 samples, but the mechanical properties were still inferior to those of the wrought products [22].

2.5.5.1 Effect of Heat treatment

A series of heat treatments was performed by Qi *et al.* on as-deposited IN718 samples (direct aging, solution treatment and aging (STA), and homogenised STA treatments as shown in Table 2-3). Comparisons were made with AMS specifications for cast and wrought IN718 (Figure 2-58.a). In all cases, the heat-treated materials exhibited better tensile properties than the AMS cast properties, but only were slightly worse than the wrought properties.

With direct ageing the tensile strength increased dramatically due to the precipitation of the strengthening γ' and γ" phases in the matrix. However, the ductility was reduced due to the presence of fine Laves particles that remain at the interdendritic regions which initiate fracture during tensile testing. The traces of the Laves phases can be seen in the fractographs as white particles, Figure 2-58.b. STA treatment showed improved ductility as the Laves phases were transformed in to acicular δ phase. However, the tensile strength reduced slightly which is attributed to the increase in grain size. The homogenized STA heat treatment completely dissolved the Laves phase and enabled substantial grain growth which resulted in improved ductility but reduced the strength.

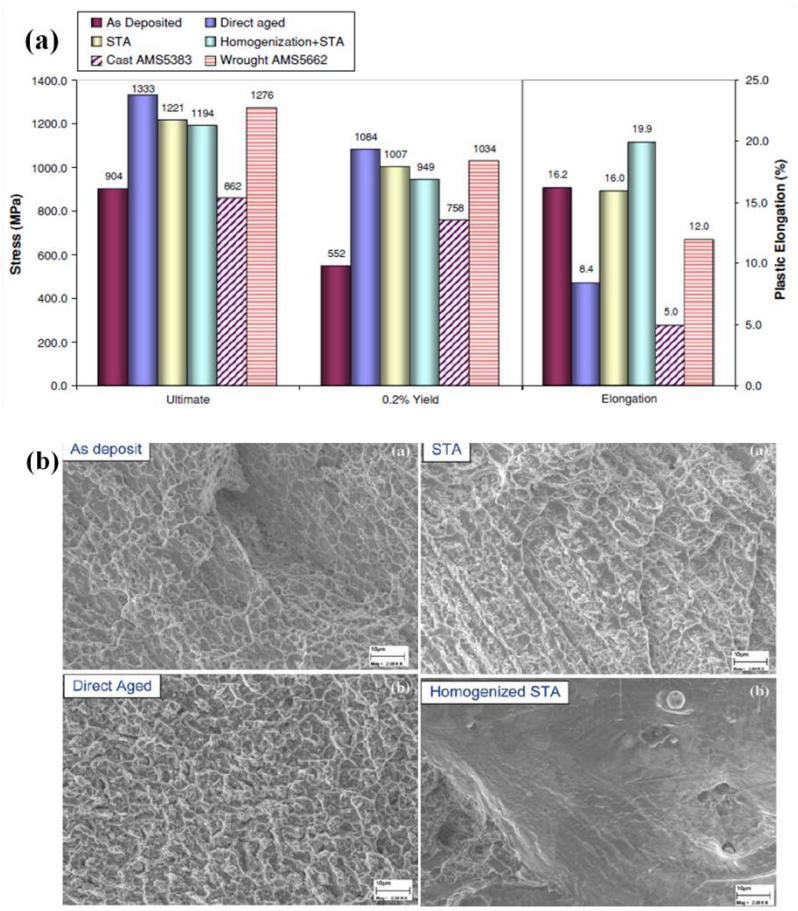

Figure 2-58: Tensile properties of DLFed IN718 samples in comparison to wrought and cast products (a) Showing the effect of heat treatment on the tensile, elongation and yield (b) fracture surfaces of the tensile samples at different heat treatments [22].

The hardness of as deposited samples of IN718 was found to be around 250 Hv which is almost half that of wrought products (440 Hv) which is due to the lack of hardening γ' and γ" phases [11, 17]. Annealing treatment at 800°C would improve the hardness to 360 Hv due to precipitation of strengthening γ′ and γ″ phases. However, heat treatment at higher temperatures would reduce the hardness due to transformation of coherent γ′ and γ″ phases to incoherent δ phase, Figure 2-59 [18].

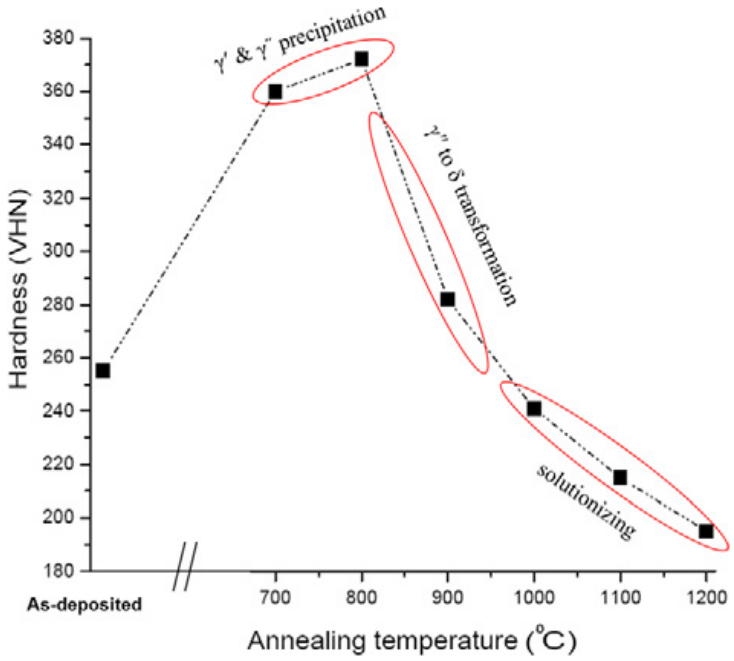

Figure 2-59: Effect of aging temperature on hardness in laser deposited IN718 [18].

2.5.5.2 Effect of Process parameters

Studies by Tabernero *et al.* [11] in DLFed IN718 showed that the mechanical properties of the deposited material is strongly influenced by the build deposition path. The ultimate tensile strength value in transverse direction to the applied load, Figure 2-60, are 55–60% lower than those obtained in longitudinal direcion showing the preence of high anisotropy due to laser tracks used.

The mechanical properties are also affected by the type of powder used. As deposited samples using GA powders showed inferior mechanical properties compared to PREP powder deposits due to pores present in GA powders [12]. The stress rupture life (186 h) of heat treated PREP powder deposited IN718 samples was higher than that of cast samples (23 h) by a factor of approximately 8.0. However the ductility of the stress rupture samples were still lower than those of cast samples due to the presence of continuous thin film of Nb-rich MC type carbides along the grain boundaries [12].

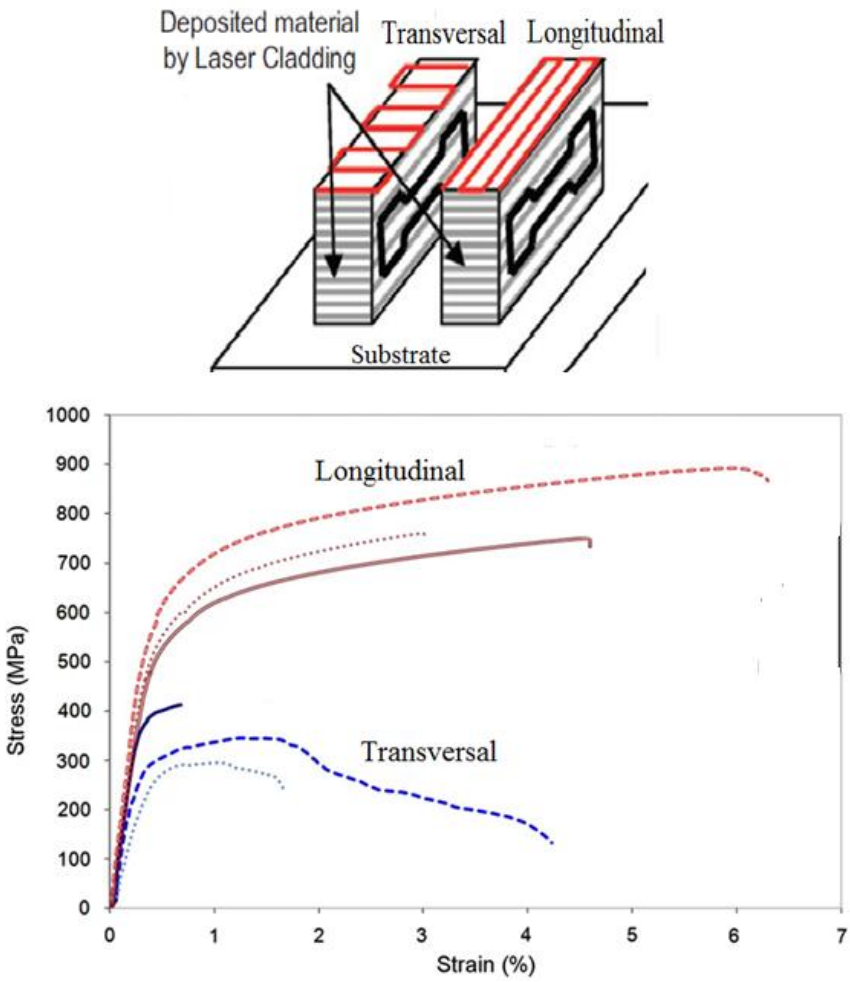

Figure 2-60: Stress strain curves at different locations on a IN718 deposits in longitudinal and transverse deposition directions [11].

2.5.6 Distortion and Residual Stresses in DLF

One of the most critical issues that limit the quality of the parts produced by DLF is the presence of thermal induced residual stresses. These stresses result from the transient thermal cycling and the associated expansion and contraction of materials [136]. They can cause warping, delamination or cracking, and poor surface finish defects in the final part. When material is deposited on a substrate by high energy laser beam, it causes distortion due to these residual stresses, in the substrate. For repairing or depositing features on an existing component, it is unacceptable to have large deformations in the final parts. The residual stresses (especially the tensile) negatively affect the structural integrity of the build.

In the AM process the residual stresses and distortions are similar to the multi-pass welding process where a localised rapid heating and cooling cycle occurs. A large area of compressive stresses is generated ahead of the melt-pool with tensile stresses at the end of the melt-pool as illustrated in Figure 2-61. When a bead is deposited, as the sum of stresses in any directions is zero, the tensile stresses in the build are compensated by compressive stresses in the substrate of the adjacent deposited layer.

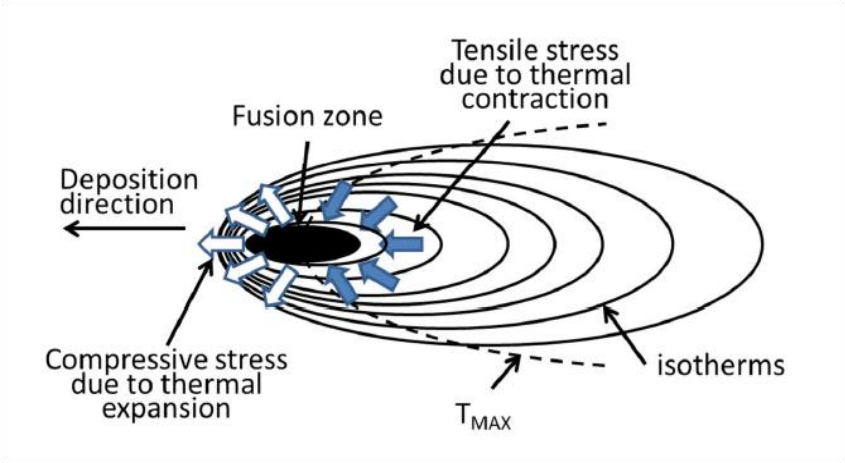

Figure 2-61: Temperature and stress field around a welding heat source [137].

As we have repeated weld beads in AM, complex tensile and compressive stress fields are observed which are often undesirable [25, 87]. However, to date the measurement of these residual stresses has received relatively little attention [24-25, 138-141]. Very limited work is available in the literature to determine the effect of process parameters on residual stresses developed during laser deposition either through experimental [24-25, 138, 141] or modelling routes (which is discussed in detail in section 2.5.7). The other important problem due to residual stresses is the distortion of the component. The stresses and the resulting distortion are dependent on the process parameters especially the deposition path, power density applied during deposition which will be discussed in the following sections.

2.5.6.1 Effect of Process parameters on Distortion and Residual stresses:

Previous studies showed that deposition path and pre-heating of the substrate has a significant effect on the residual stresses and distortion in DLF. Studies by Klingbeil *et al.* on MIG welded square blocks [136] and Nickel *et al.* on DLFed rectangular annealed 1117 steel blocks [142] showed that a spiral deposition path showed more average warping than a normal bi-directional deposition path. Studies by Fessler *et al.* on DLFed INVAR and 316 Steel showed that a deposition strategy that allows much of the deformation produced during cooling to occur before the deposit is fully constrained will reduce the warping. In this approach, the surface area of the deposit is significantly increased by depositing a series of small patches, which are later joined together to form large patches of material. However, good bonding of the deposited layer cannot be achieved by this approach due to insufficient re-melting between layers [143].

A combination of substrate preheating (to reduce initial thermal mismatches) and substrate insulation (to exploit preheating by the process itself) could give substantial payoffs in limiting the residual stress-induced warping [136]. Also, initial layers of laser deposition

make a significant contribution to the deformation in the substrate rather than the later stage of deposition.

Rangaswamy *et al.* [24] characterised the residual stress development, using neutron diffraction and contour methods, in IN718 laser deposited multi-track thick rectangular walls (25 mm× 5 mm × 100 mm) and square pillars (13.5 mm × 13.5 mm × 45 mm). It was found that there were negligible stresses parallel to the motion of the melt-pool, but significant stresses along the growth direction (i.e. perpendicular to the substrate), Figure 2-62. However, Studies by Moat *et al.* [25] on DLFed Waspaloy walls by neutron diffraction and contour methods observed that the magnitude of the longitudinal and transverse stresses depend on the location of the build, where near the tops of the deposited walls, the longitudinal stresses are tensile towards the mid-length of the wall, while the stresses perpendicular to the substrate are negligible. By contrast near the base of the walls, the stresses along the direction of the deposit are small, while the stresses perpendicular to the substrate are compressive at the centre and tensile towards the ends, Figure 2-63. FEM work by several researchers also predicts tensile stresses near the surface and compressive stresses perpendicular to the substrate [139, 141, 144]. Wang *et al.* [139] predicted compressive vertical stresses within the mid region of the structures and tensile stresses towards the edges. This is in good agreement with the work of Rangaswamy *et al.*[24], although the accompanying experiments by Wang [139] were not presented to conclusively verify the models. Small depositions on a relatively large substrate show a different type of stress distribution. FEM as well as Neutron diffraction studies by Ding [137] in long rectangular Ti4Al4V build plates using wire arc deposition showed that the maximum stresses were present along the deposition direction, Figure 2-64.

A limited influence for track raster pattern was found on the residual stresses in the build for thick walls, Figure 2-62.a-c [24, 139, 144]. However, FEM by Ehsan *et al.* on single layer

deposits, showed that the deposition strategy has a significant effect on the final residual stress of a single layer laser deposited rectangular part [145] where a bi-directional deposition pattern has lower stresses than when using a spiral deposition path. Work by Huihui *et al.* also showed that deposition direction has a significant influence on the residual stress and equivalent plastic strain distributions, whereby the deposition in the reverse direction for alternate layers gives better results [141]. Further, it was found that the deposition of the last layer dominated the residual stress of the whole component due to the stress-release effect of the final layers on the earlier layers.

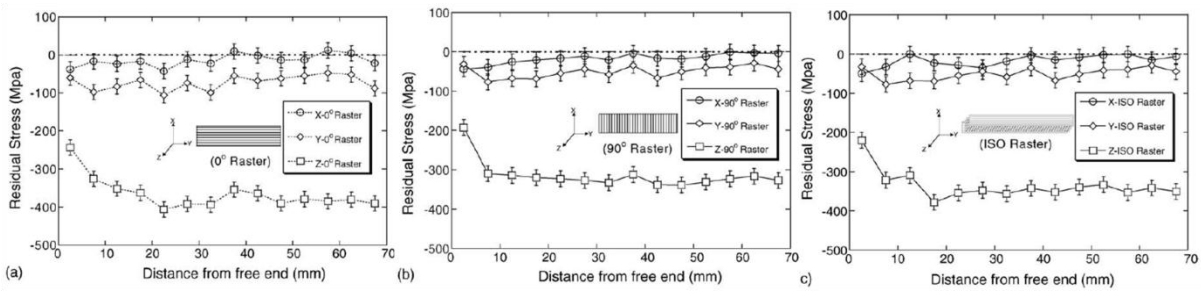

Figure 2-62: The three components (X,Y parallel to the motion of melt-pool and Z- along the growth direction) of stress in rectangular samples as function of position along the growth direction for different rastering/deposition directions showing negligible stresses in X and Y directions and compressive stresses along growth direction [24].

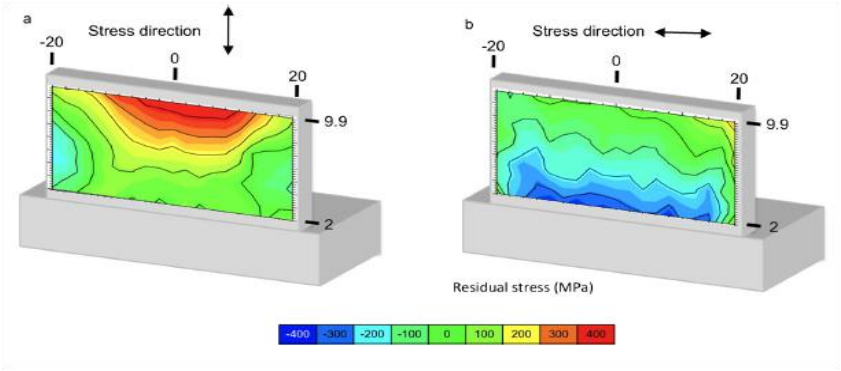

Figure 2-63: Residual stress contours in 5 mm thick Waspaloy deposits characterised by contour method a) longitudinal i.e. along the melt-pool moving direction and b) along build growth i.e. perpendicular to the substrate [25].

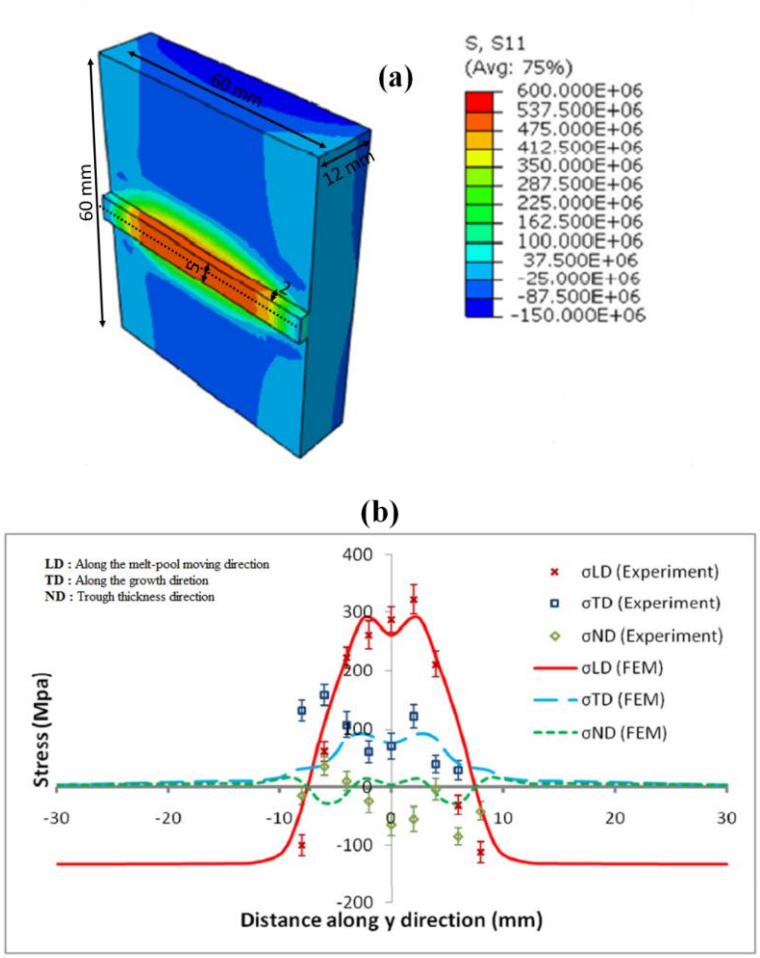

Figure 2-64: Principal stress distribution along the length of thin stainless steel base plate of 60 mm long and 12 mm thick due to 3 layer wire arc deposition of size 5 mm wide and 2mm thick: (a) Stress in longitudinal direction (along 60 mm) distribution in the plate (b) Stresses in the three directions in the base plate along the length (along dotted lines in figure a) [137].

2.5.6.2 Control of residual stresses and distortions

There are many techniques that have been developed for minimising the effects of residual stresses and distortions in DLF.

Studies have been made where novel methods were used as a tool for residual stress control (e.g. using the pulse parameters of a diode laser deposition system) [25, 138, 146]. The residual stress profiles are weakly dependent on the pulse parameters, most notably an increase in tensile stress gradient with increasing duty cycle, but the maximum residual

stresses are largely unaffected [25, 146]. The laser speed has little effect on the residual stresses, when the laser power was adjusted to maintain the same heat input [139, 144].

The temperature distributions in DLF of ~ 10 mm thin plate samples during the depositing process showed that edges of any geometry are much hotter during the initial solidification and cooling cycle than the interior section [109, 147]. Based on this, Vasinonta *et al.* proposed that adjusting the process variables to maintain the same molten pool temperature at the centre and edge of the part and reducing the dwell time of the laser at the end points of the raster should lead to reductions in the residual stresses [147]. Further reductions in the final stress state may be possible through auxiliary heating to control the bulk cooling gradients and final cooling cycle of the component [147], although no experimental evidence was presented. The use of substrate preheating in Ni-based superalloys would generally not be desirable due to the age hardening behaviour of these alloys.

2.5.7 Thermo-Mechanical Modelling of DLF

Many researchers have employed modelling to predict the temperature profile [148-153], distortion [142, 151, 153] and resulting thermal stresses [1, 136, 141-142, 145, 154-155] in DLF components due to the limitations of experimental stress measurement during laser processing. This section discusses the relevant laser heating principles, followed by a literature on the analytical and finite element thermal and thermo mechanical models of DLF.

Laser Heating Principles:

CO_2 and Nd: YAG lasers are the two most popular industrial lasers used in DLF operation. A CO_2 laser consists of a glass tube which is filled a gas mixture of approximately 80% He + 15% N_2 + 5% CO_2. The CO_2 laser provides continuous power at a wavelength of 10.6 µm. Nd:YAG laser is a solid state laser, which emits a beam of wavelength of 1.06 µm [111].

It is important to understand the interaction of laser with the material since the laser is used as heat source in DLF. When the laser hits the substrate, the beam will be partially reflected, partially transmitted and partially absorbed, which can be represented as below:

$$R+A+\tau=1 \qquad 2\text{-}6$$

where, R is the reflectivity, A is the absorption, and τ is the transmission.

The values of R of various materials are shown in Figure 2-65. Table 2-6 shows the absorption coefficients of different materials and various wavelengths. These parameters are dependent on the characteristics of laser and the material used. Generally speaking, the absorption of a material is increased with wavelength [111], and reflectivity varies with the surface roughness of the material. If the roughness of the surface is less than the beam wavelength, the radiation will be received as if it was a flat surface [111].

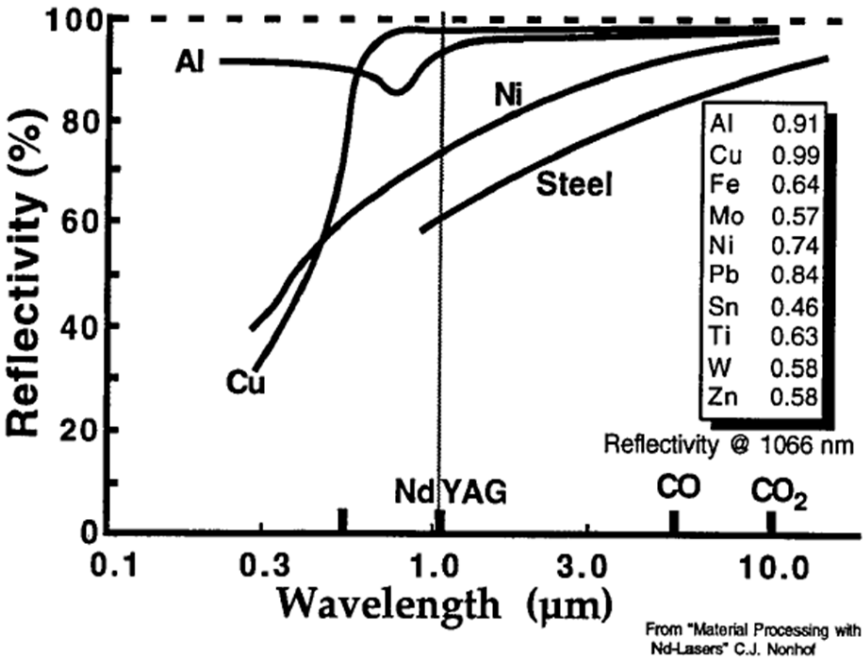

Figure 2-65: Reflectivity of some materials as a function of wavelength (inner table showing the reflectivity values for 1.06µm radiation) [156].

Table 2-6: Normal, spectral absorption of materials at important laser wavelengths [157]

Material	300–600 nm	1.06 μm	10.6 μm
Aluminum, smooth		0.06 – 0.2	0.03 – 0.06
rough		0.2 – 0.4	0.1 – 0.4
Beryllium	0.8	0.5 – 0.8	0 – 0.08
Chromium	0.35 – 0.40	0.3 – 0.4	0.06 – 0.10
Copper, polished	0.05	0.04	0.01 – 0.03
rough	0.05	0.1 – 0.3	0.0[illegible] – 0.10
oxidized	0.85	0.5	
Germanium	0.05 – 0.3	0.05 – 0.65	0.6 – 0.7
Gold	0.7 – 0.1[a]	0.02 – 0.04	0.01 – 0.02
rough			< 0.12
Iron, polished	0.37 – 0.40	0.25 – 0.32	0.12
Molybdenum, polished	0.4 – 0.5	0.25 – 0.35	0.05 – 0.15
Nickel	0.5	0.15 – 0.35	0.05 – 0.15
Platinum	0.5 – 0.3[a]	0.25 – 0.30	0.03 – 0.08
Rhodium	0.2 – 0.5	0.15 – 0.25	0.05
Silicon, undoped	0.35 – 0.55[a]	0.7	0.25 – 0.38
doped			< 0.75
Silver	0.95 – 0.03[a]	0.03	0.02 – 0.10
Tungsten	0.5	0.35	0.03 – 0.3
Carbon (graphite)	0.75	0.8 – 0.9	0.7 – 0.9
Alumina (Al_2O_3)		0.05 – 0.1	0.90 – 0.99
Magnesium oxide (MgO)		0.2	0.93 – 0.98
Silica (SiO_2)	transp.	transp.	0.9
Zirconia (ZrO_2)		0.1 – 0.2	0.85 – 0.98
Silicon Carbide (SiC)	0.8 – 0.9	0.85 – 0.95	0.8 – 0.9
Silicon nitride (Si_3N_4)	0.6 – 0.7	0.6 – 0.8	0.9

Many analytical and numerical laser deposition models have been developed to understand the laser-powder interactions to predict the temperature attained by the powder, the interaction between the laser induced melt-pool and the powder stream in order to predict the geometry of the layers, and finally thermal, metallurgical and mechanical property evolution due to laser deposition, considering the influence of the process parameters.

2.5.7.1 Analytical Models:

The heating/cooling during laser processing employ classic heat transfer theory [111]. The analytical models based on these theories are highly simplified due to limited calculating ability. They have limitations due to the variety of assumptions made concerning the spatial and temporal dependence of the laser heat source and geometry of the sample that is being irradiated. However, these models are good for predicting the process conditions suitable for deposition such as how much laser power is required to melt the powder, and for how long the power must be applied.

The initial thermal models used Rosenthal's solution for the moving line source for simulating single pass welding to predict the required powers and speeds for laser welding[111]. The Rosenthal models integrated the temperature solution of the line source over time and motion by making $X=X_0+\upsilon t$, where X is the travel distance of the laser beam, υ is the scan speed and t is the time. As long as the thermal diffusion coefficient, thermal conductivity k and absorption rate are known, the required power can be predicted for a given depth of penetration and alternatively the penetration depth can be measured when the input power is known [111]. The drawback with the models is that the laser is treated as a line source instead of a more realistic Gaussian beam source. Moreover conductivity is the only heat transfer effect considered and the material properties are assumed to be temperature-independent. DLF is a much more complicated process than laser welding which involves several other parameters; however this is a quick and reasonable way to predict the approximate laser power required for initial deposition trials.

Later, Pavelic *et al.* suggested that the heat source should be distributed and developed a Gaussian distribution of flux deposited on the surface of the workpiece [158] which achieved significantly better thermal predictions.

Keeping laser deposition in mind, a more accurate heat model was proposed by Labudovic *et al.* [159] by using Green's function (equation 2-8). Unlike Rosenthal model, they have taken convection and radiation into account and considered mean thermal flux density within the area of the laser beam scanning rather than a simple line source.

$$T(x,y,z,) = T_0 + \int_0^t \int_{-\infty}^{\infty} \int_{-\infty}^{\infty} G(x,y,z,t,x',0,z,t',\upsilon) \times AI(x',y',t')dx'\,dy'\,dt' \qquad 2\text{-}7$$

Where, Green's function G (x, y, z, t, x′, y′, z′, t′, υ, K, k) represent the temperature at (x, y, z) at time t due to a point source of unit strength generated at (x′, y′, z′) at time t′, which is moving with velocity υ where K is the thermal conductivity of the material and k is the

Boltzmann's constant (1.38066×10^{-23} Ws/K). By integrating the product of the Green's function G with the actual absorbed mean power density, I, over the dimensions of the laser spot and time, the temperature T (x, y, z, t), induced by the laser beam moving over the surface (y′=0), is obtained.

Picasso [160] also proposed a simple 3D analytical model which is used to calculate the temperature distribution of the substrate as well as the melt-pool shape during laser deposition, while considering one very important factor i.e., attenuation of laser power due to powder. It is found that the final laser power is 20% less than the power supplied. Fu et.al [161] developed a theoretical model for laser and powder particle interaction during laser cladding, which considered the powder delivery angle and suggested that the laser power attenuation increases with the angle of powder delivery.

Peyre *et al.* [150] proposed a 2 dimensional analytical solution to calculate the temperature attained by the powder before deposition based on analytical model developed by Qi *et al.* [162]. The laser power absorbed by the powder particles and the temperature attained by them before reaching the substrate was calculated based on this model. The calculated temperature of the powder varied with powder jet radius and powder particle diameter (Figure 2-66). This analytical model to calculate the initial temperature of powder was coupled with a numerical model to further calculate the melt pool shape and other thermal profiles.

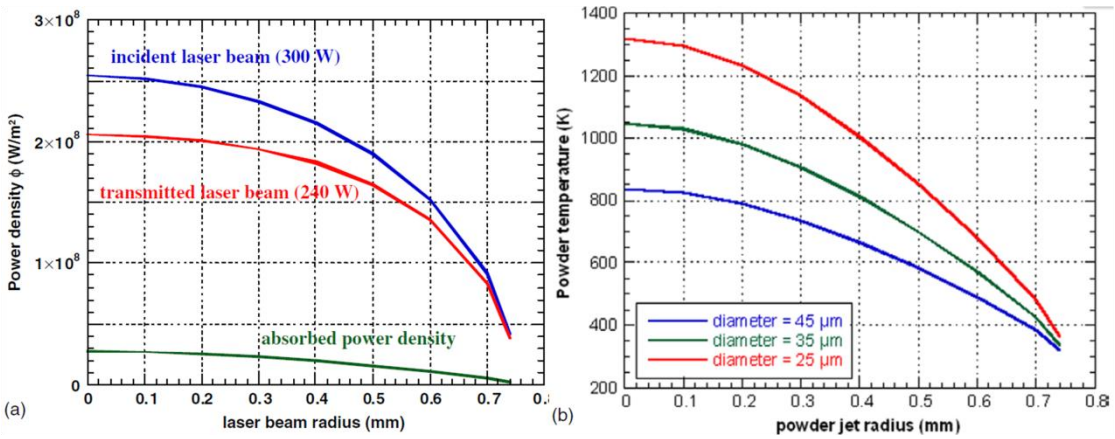

Figure 2-66: Temperature at the surface of the substrate laser powder : (a) laser beam attenuation by a $1ms^{-1}$ Ti6Al4V powder flow at 2 g min−1 and (b) temperature distribution of the powder stream just before dissolving in the melt pool [150, 162].

In spite of the relative simplicity, these analytical models are useful to improve the understanding of the process and to select the appropriate parameters and establish a process map. However, when considering complex substrate geometries and nonlinear material properties these analytical solutions can no longer be obtained. Therefore, a numerical method is necessary although it needs large computational times.

2.5.7.2 Numerical Models:

Finite element method (FEM) is one of the most popular numerical methods to solve differential equations. Efforts have been made by many researchers to make use of this method to solve thermal and thermo-mechanical problems. Three dimensional transient thermo-mechanical models are widely used in welding and related AM studies. However due to the large computational times involved in these processes there are several obstacles to its use in simulating complex geometries with millions of melt-pools in AM.

Based on the complexity of the models, FEM models can be divided as basic models which consider simple heat flux on top of the melt pool, standard models which use temperature-dependent material models, accurate models which define the shape of the melt-pool and

finally very accurate models which have very fine meshes and small time steps for higher accuracy [163]. The basic and standard models are good for predicting the residual stresses accurately which reduces computational time whereas the accurate and very accurate models are time consuming but good for microstructural studies [163]. For residual stress measurements, which is the main study of this project, correct heat input could be considered rather than detailed melt-pool shape to reduce the computational time involved with accurate and very accurate models.

Transient thermo-mechanical models:

The transient thermo-mechanical models utilise time increment scheme to model the moving melt-pool to simulate AM process. To reduce the computational time thermo-mechanical models are usually carried out in two stages, in the first stage the thermal model is performed to calculate the nodal temperatures and after the exact nodal temperatures are achieved these temperatures are transferred to mechanical models and this is called weakly coupled problem [164].

For transient FE models the following aspects are to be considered:

- FE Mesh and element selection
- Heat Source (see analytical models section above)
- Material Model and elements activation

FE Mesh element selection:

Meshing is important to have accurate results and reduced computational time. The straightforward way of reducing the computational time is to use 1D or 2D models. However, studies showed that these models could not provide accurate distortion values although a huge reduction in computational time is achieved [165-166]. Use of a graded mesh with fine

meshing near the melt-pool and coarse mesh at a point away from the melt-pool would reduce the computational time [167]. However, a graded mesh is useful for welding whereas in AM with millions of melt-pools in entire parts a graded mesh is of little use. To eliminate this problem an adaptive mesh was developed where dense element mesh is developed following the moving heat source [168-169]. Although, the automatic meshing technique is helpful in reducing the computational time, a separate code has to be written for implementing this method as no commercial software is available to use this technique.

Material Model and element activation:

Most FEM studies use temperature dependent thermal properties for analysis. Lindgren (2001b) has summarised various material models in his review paper. The phase transformations can be ignored except for the latent heat in the thermal models. It is difficult to obtain all the temperature dependent materials data for thermo-mechanical modelling. In order to simplify this, Zhu *et al.* [170] investigated the effect of material properties on the results and found that thermal conductivity has the most significant effect on the temperature distribution in thermal models whereas in mechanical modals temperature dependent yield stress plays an important role in distortion and residual stress. So, these two temperature-properties are sufficient for relatively accurate results with other properties being those at room temperature.

To simulate laser deposition with reduced computational time "element birth technique" is developed [166] where, all the element in the deposition are de-activated and are activated as the deposition progress. A subroutine is required for this approach to activate the elements on-by-one and it significantly reduces the computational time. The other technique is " quiet element approach", where all the elements are present during the model but the element which are away from the melt-pool are made passive by setting the material properties, with

very low thermal conductivity and stiffness, which does not affect the rest of the model. Although this model is computationally efficient, Chiumenti *et al.* [151] suggested that fictitious temperature gradients and strains can be accumulated in this approach due to improper material data used.

Other computationally efficient models:

All the above routes would reduce the computational accuracy but this reduction may not be sufficient when dealing with millions of melt-pools. There are several other statistical and transient computational methods, which can reduce the complexity of the models. There is the local-global method where a small scale local 3D transient model was built to calculate these plastic strains which were introduced as the initial strains in a global elastic shell model in order to get the global distortions of the whole part [171]. The other method is sub-structuring where a complicated non-linear model is used at the heat influence region, while a linear model is used in the rest of the region [172]. Although, both these methods are efficient they require complex coding and there is no commercial tool present to implement these. There are several statistical methods to reduce the computational time, which is out of scope for this thesis and the details of these methods can be found elsewhere [137, 164, 172].

2.5.7.3 Thermo-Mechanical Modelling of AM

FE modelling of metallic AM is quite limited when compared to welding processes. Most of the AM models used Transient thermo-mechanical models. The thermal behaviour during DLF of thin stainless steel wall was modelled successfully by Hofmeiser *et al.* [109]. During the model the temperature of the nodes were set at the melting temperature and the elements were set at that temperature for a time period equivalent to the laser dwell time. The model computed the final temperature of the substrate as well as the elements and stored the data. For subsequent elements, this previous stored data was used as the initial condition. This

process was repeated for all events until the geometry was complete [109]. This model is very simple and does not use any DLF process parameters like laser power and cooling effects due to convection and radiation and does not calculate the geometry of the build or the resulting thermal stresses.

Later work by Labudovic *et al*. used similar principle of "element birth method" and modelled melt-pool dimensions, temperature and stress distribution in one bead width thin wall laser deposits. The moving laser beam is simulated using the ANSYS Parametric Design Language (APDL) to provide the heat boundary conditions at different positions at different times. This model combined with an analytical model was able to successfully predict the melt-pool depth as well as the temperature and stress profiles for different laser powers and scan speeds. Work by Wu *et al.* also predicted the temperature profile and residual stresses in single bead walled Ti6Al4V deposits at different locations using "element birth method" of the build and also resulting microstructures at different locations of the build [1, 121]. Chin *et al.* presented a thermo-mechanical model, which is an improvement to Hofmeiser's model, for predicting temperature and thermal-stresses in laser deposited droplet columns [173]. Convection and radiation conditions were imposed on the top surface and constant temperature on the sides. Latent heat released during solidification was also considered in the model. The model suggested that pre-heating of the substrate and choosing optimal deposition path would reduce the residual stresses.

None of the laser cladding models took into account the effects of power attenuation due to the powder particles, during the process. Later several authors considered the effects of shadowing of the particle cloud, heat absorption of particles, and overlapping of traces on the heat flux [150, 154, 174-175] but did not consider the effect of phase transformations i.e., melting and solidification and also the heat transfer, fluid motion inside the melt pool. Many researchers later considered the hydrodynamics of the liquid metal [152-153, 162, 176] where

temperature and fluid velocity inside the melt-pool were computed and measured which successfully predicted the final melt-pool shape and resulting deposit height.

The effect of deposition path on residual stress development was modelled by several authors and it was shown that deposition path plays an important role in residual stress development [145, 149]. Zhao *et al.* [141] developed a finite element model for thermal stress evolution, and the residual stress distribution in a single-pass multi-layer weld-based rapid prototyping. In this study they modelled the residual stresses developed after each deposited layer and also studied the residual stresses in the substrate. All these models developed so far were based on single pass laser clad (which were either single bead models or thin walls with few layers high). In 2010, Chiumenti et.al [151] characterised the material behaviour by a thermo-elasto-viscoplastic constitutive model coupled with a metallurgical model. He modelled the residual stress formation and predicted the areas prone to crack formation on wire-based laser deposits. He predicted that the interface between the deposit and the substrate is more prone to cracking.

All the studies discussed so far were made on single bead thick wall samples which are not used in practical AM applications where multi-layer thick walls are deposited. Not much work has been done on multi-layers walls due to the complexity of the process as well as huge computational time involved. Recent work by Ding [137] on Wire Arc Additive Manufacturing (WAAM) addresses this issue where large AM parts were modelled for distortion and residual stresses. The model uses a steady-state thermal model, which provide fast predictions of temperature distribution for the long WAAM deposited walls and saves 99% computational time compared to a conventional transient model. The nodal transient temperature histories from the thermal results are used as the thermal load in the 3D mechanical model. The model results match accurately with the experimental results from neutron diffraction.

Research gaps in Modelling:

Limited work is available in the literature for thermo-mechanical modelling of AM parts of which very few models in DLF in particular. Most of these models developed are to a small scale and hardly can be used for practical applications. Also not much effort has been made in validating these models with experimental results. The optimisation of build parameters need to be investigated for minimum residual stresses in practical applications. Ding has successfully modelled large WAAM parts for practical applications however the validation is made on the small parts. Also the effect of post deposition heating and delay between layers which has an effect of residual stresses is not considered.

2.6 Summary of literature: Key findings and areas on investigation

A detailed literature review of the microstructural and residual stress development due to DLF of IN718 has been performed, including thermal-stress modelling of the processes. The following points summarises the current state of knowledge

Geometrical accuracy and build integrity:

- From the literature, it is found that the build quality and microstructure of DLF samples are strongly dependent on the process parameters and the key process parameters are identified to be laser power, scan speed, powder flow rate and deposition path.
- Several process windows were developed for builds that give minimum defects, and a successful scale up of the builds was also shown. However, the defect distribution in the build with various process parameters is not addressed.
- As DLFed parts experience different thermal histories at different locations of the build, the same process parameters may not be suitable for building the entire parts.

So, investigations have to be made towards selecting different process parameters at different locations of the build.

Microstructure and Texture:

- AMed deposits have a very heterogeneous appearance, with variations in grain size and grain aspect ratio occurring over relatively small distances due to the fast and repeated thermal cycles associated with the process. The microstructure of DLF builds of IN718 show a banded grain structure of columnar and equiaxed zones. However, a detailed investigation on the melt-pool size and grain distribution was not performed as well as the reason for the fine grain zones was not clearly understood.
- The orientation of the grains in the build is strongly dependent on the direction of the moving heat source. The literature review on the DLF technique shows that the dendrites tend to orient along the ⟨100⟩ crystallographic orientation growing epitaxially from the substrate. Studies by a few authors showed the presence of a ⟨100⟩ fibre texture in DLF samples is due to the alignment of grains towards the moving heat source. However, the texture of the individual layers as well the effect of laser power and the conditions which promotes the texture in the build has not been studied in detail.
- The effects of substrate orientation as well as the effect of process parameters on the texture need to be studied if DLF is considered for repair applications.
- Microstructural studies of laser deposited IN718 samples showed large Nb segregation at the inter-dendritic regions and presence of Laves phase instead of strengthening γ' and γ'' phases due to the cooling rates associated in the process. A solution + ageing treatment is proposed to dissolve the Laves phases and to precipitate the strengthening. However, the precipitate morphology needs to be studied after heat

treatment to see the effect of precipitate morphology with a standard heat treatment used for cast products.

- The effect of process parameters on the precipitation has not been studied in detail, which is required for designing the post DLF heat treatments.

Residual Stresses:

- The Parts produced through DLF are often known to have undesirable complex residual stress fields due to very high localised heating and cooling rates. However, to date the measurement of these residual stresses has received relatively little attention.
- The literature is focused on residual stress characterisation of thin walls or blocks, however the effect of geometrical scale-up on residual stress is yet to be understood
- The effect of process variables on the residual stresses have been studied by several authors with validation by experimentation, however the effect of post annealing scans or delay between layers, which would give significant variations in heating and cooling cycles, on the residual stresses is not studied.
- Most of the studied concentrated on the stresses developed in the build and substrate. However, it is also interesting to know how the residual stresses and distortions vary with the size of the build w.r.t substrate.

Thermo-mechanical modelling:

- There are large numbers of analytical and numerical models which have been developed to assess the residual stresses developed in DLF of the deposits but limited effort has been made to validate these results experimentally.
- The models developed are mostly for small builds or single bead thick walls. Very limited modelling effort has been made on DLF of real time applications or to validate the results experimentally.

- Also, limited research has been done aimed at reducing these residual stresses and at the same time see the effect of these process conditions on the microstructure of the build.

2.6.1 Potential for further study

Overall limited amount of data has been published on microstructure evolution, texture and residual stresses development during DLF. So far individual research programmes have concentrated on only one of the many process variables in DLF i.e. geometrical accuracy, microstructure, residual stress, modelling to predict and optimise the stresses and microstructure. DLF is highly sensitive to process parameters and the parameters which suit best for geometrical accuracy may not be appropriate to optimise microstructure and/or residual stresses. There is therefore the need to understand the build process so that conditions can be identified that minimise stresses whilst also optimising the microstructure

Despite the rapid rise in publications, the following areas have not been adequately addressed in the literature:

- Influence of the geometric design freedom of DLF, and its effect on the microstructural and texture components of IN718
- The evolution of texture and grain selection during DLF of IN718.
- Control of the microstructure, and in particular how to obtain a uniform grain structure in DLF builds, through process parameter optimisation
- The relationship between the microstructure, texture and key deposit parameters.
- The development of residual stresses in the build as well as the substrate and its optimisation though process parameters, via both modelling and experimentation.
- The development of residual stress models and their validation though experimental routes.

Therefore, in the current study, the aim of the project considers the most important key aspects of these questions as mentioned in the introduction chapter in section 1.4

Chapter Three

3 Materials and Experimental Methods

3.1 Introduction

This chapter describes the experimental procedures used to produce DLFed IN718 samples in this project as well as the characterisation techniques used to assess their structural integrity and microstructural development. A description of the DLF (laser blown powder system) setup located at the University of Birmingham (UoB) is presented, alongside the process parameters utilised in building the samples. The chapter also includes a description of the microscopic techniques that were used to characterise the samples, as well as the neutron diffraction method that was used to characterise the residual stress development.

3.2 Materials

Gas atomised IN718 powder (supplied by Sandvik Osprey, UK) with a size range of 45-106 µm, was used for all the work in the project. The chemical composition of the powder is shown in Table 3-1

Table 3-1: Chemical composition of the IN718 powder batch (provided by the supplier) showing the weight % of the alloying elements.

Elements	**Ni**	**Cr**	**Fe**	**Nb**	**Mo**	**Ti**	**Al**	**C**	**B**	**O**	**Si**
Wt %	53.34	18.2	18.9	5.1	3.1	0.9	0.29	0.025	≤0.005	≤0.004	0.14

3.3 Direct Laser Fabrication (DLF) Experimental setup

DLF IN718 samples were produced using the Quantum laser deposition system at UoB, Figure 3-1. The system is fitted with a Wegmann-Baasel CO_2 laser (maximum power of 1750W), Figure 3-1.a. The powder is fed in a controlled manner using a Sulzer Metco 10-C model powder feeder, Figure 3-1.b. The working space of the system in (X, Y, Z) co-ordinates is 300 mm × 300 mm × 350 mm (Figure 3-1.c). The powder hopper is motor-driven and the powder is fed into the melt-pool though a 4-nozzle assembly built in-house (Figure 3-1.d). The samples were deposited in a controlled Argon atmosphere, with oxygen level being kept below 50 ppm, and monitored using a silicon crystal sensor. Argon is used as carrier gas for powder (at a flow rate of 5.5 l/min), as well as being a shielding gas to protect the lens from the particles that rebound from the deposit. The increment in the Z-axis (i.e., the spacing between the consecutive layers of deposit) was typically maintained at 0.3 mm for all the builds unless otherwise stated. The process of deposition is explained in section 2.5.1.The experimental parameters used to manufacture thin walls, thick walls, and solid blocks are defined in the following sections.

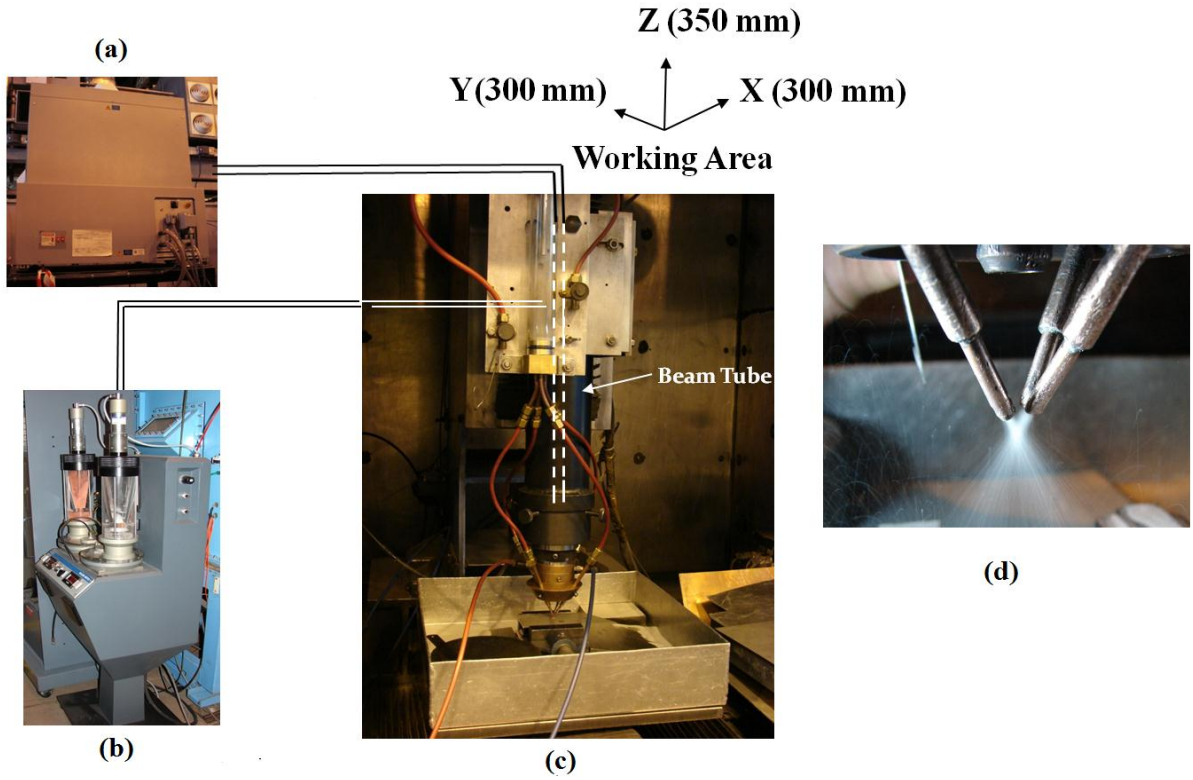

Figure 3-1 : a) DLF system at UoB showing: a) The CO_2 laser, b) powder feeder, c) glove box with a 3-axis head, and d) a four nozzle assembly showing the powder focus.

3.4 IN718 Builds

The DLFed IN718 investigations were performed in several stages, which can be summarised in three stages: thin walls, thick walls and solid blocks.

3.4.1 Stage I: Thin Wall samples

A study was performed to identify a process window that can produce IN718 builds of sound build quality for thin walled builds (20 mm wide (X) × 10 mm high (Z) × 0.7 mm thick(Y)). This stage included three separate, yet related, studies. The first study is focused on the influence of the process parameters (deposition direction, scan speed and powder flow rate) on the process feasibility study and microstructural development. The second study used DoE to assess the impact of the process variables on the build geometry. Finally, a third study was

performed to assess the influence of laser power, one of the most significant parameters identified in the second study, on the grain size and precipitate morphologies.

Firstly, samples of single bead thickness (~ 1 mm) were deposited when varying the scan speed, powder flow rate, and deposition path keeping laser power constant at 390 W. Table 3-2 shows the series of samples deposited for the preliminary study. These deposits were made in both unidirectional and bidirectional deposition paths (as shown in Figure 3-2).

Table 3-2 : Various deposit parameters with constant power of 390 W.

Power (W)	**Scan Speed (mm/min)**	**Powder Flow Rate (g/min)**
390	200	18 (samples B1 and B2)
		33
		55
	300	18
		33
		55
	400	18
		33
		55
	500	18
		33
		55

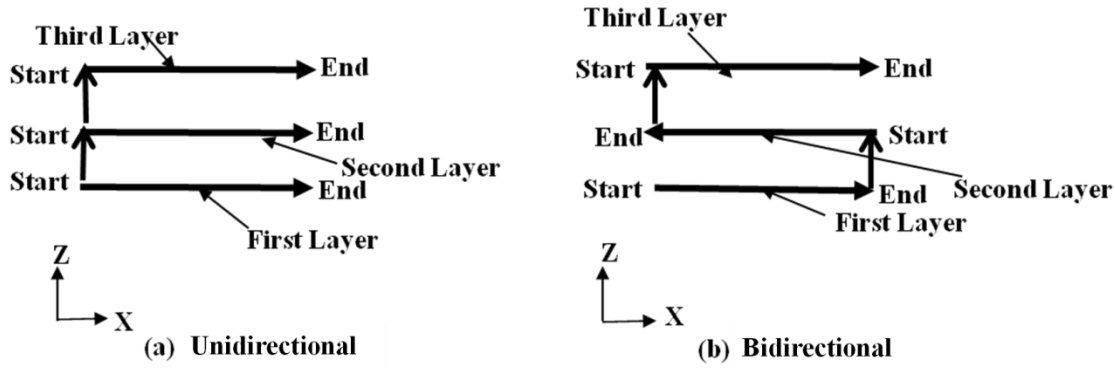

Figure 3-2: Deposition modes (movement of the head) in a) Unidirectional (as in B1) and b) Bidirectional (as in B2) paths.

Once the preliminary process parameters were identified then the three process parameters were varied to obtain a focused process window. However, as varying all the three process parameters at the same time requires a large number of experimental trials, in the second study a statistical approach was implemented using Design of Experiments (DoE), where few deposits were made that can represent the entire set by varying the laser power, scan speed, and powder flow rate. A set of experiments was designed by DoE approach, which was implemented through DESIGN EXPERT V.7. Three factors and three level (factors and levels shown in Table 3-3) full-factorial CCD design matrix was developed.

Table 3-3: Process factors and corresponding levels in the DoE study

Level / Factor	Low	Intermediate	High
Laser Power (Watts)	300	375	450
Scan Speed (mm/min)	300	400	500
Powder flow rate(g/min)	18	36.5	55

It is important to assess the most significant process parameter in the process, and also to develop a model which can assess the build geometry (build height and thickness, which is most important during repair), when the input process parameters are given. A Quadratic equation for deposition height and width was developed in this stage correlating the dominant deposition parameters. A two-way analysis of variance (ANOVA) is used for this assessment.

By studying the microstructure of the above samples, it was found that laser power has a strong influence on the grain and dendrite morphology. To further assess the effect of laser power, in the final study, thin walls were deposited by increasing the laser power while keeping the other process parameters constant (scan speed at 200 mm/min, powder flow rate of 18 g/min and bidirectional deposition path). At a very high laser power (910 W), the powder flow rate was varied to increase the overall power density further, since further increase in the laser power would damage the lens and also the build would contact the nozzle making the deposition difficult. Table 3-4 shows the process conditions used, where all the deposits were made with a bidirectional deposition path.

Table 3-4: Parameters with varying laser power and powder flow rate.

Power (W)	**Scan Speed (mm/min)**	**Powder Flow Rate (g/min)**
390	200	18
474	200	18
580	200	18
693	200	18
910	200	12
910	200	8
910	200	5 (sample B3)

3.4.2 Stage II: Thick Wall Samples

For any practical repair applications, generally multiple wall thickness builds are used. So, in this stage (a scale up of thin walls) thick wall samples (35 mm wide (X) × 10.5 mm high (Z) × 2.1 mm thick (Y)) were built on a thick walled forged IN718 substrate (38 mm wide (X) × 2.1 mm thick (Y) × 34 mm tall (Z)) for demonstrating repair applications (as shown in Figure 3-3.a). The engineering drawing showing the from view, top view and side view of the same is shown in Appendix A-I. The deposition was made with the best process parameters chosen from the thin wall study with no bonding defects or excessive/low deposition rates (A laser power of 390W, scan speed of 300 mm/min and powder flow rate of 18.3 g/min).

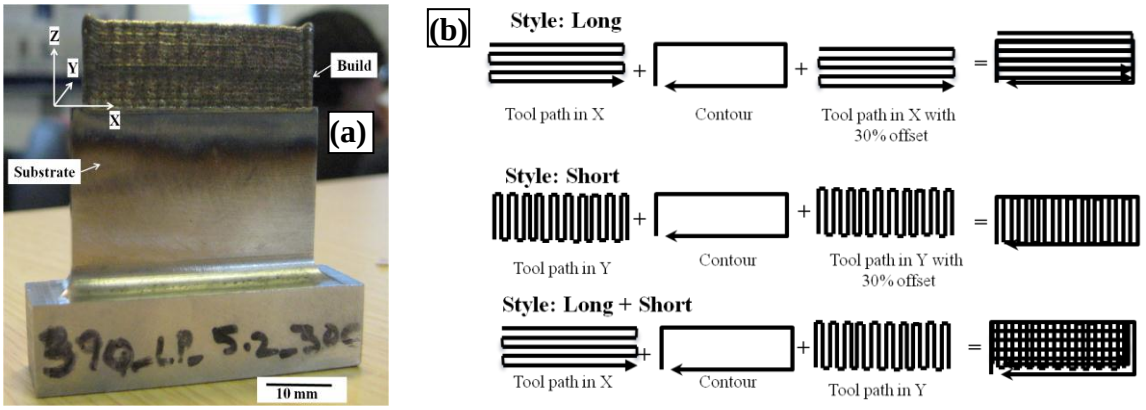

Figure 3-3: a) Thick wall build sample and b) different deposition paths used in stage II.

During DLF repair, the main concerns are the development of residual stresses in the build, as well as in the substrate. Residual stress characterisation was performed on these builds, and as will be discussed a variation in deposition path and scan strategy was employed to assess the influence of the deposition path on the residual stress development.

This study is divided into two parts: First, the influence of deposition path on residual stresses developed in the build and substrate was investigated. Several builds, with varying deposition paths, were deposited while keeping the other parameters constant. Long, short and mixed

(hatched) deposition paths were used as shown in Figure 3-3.b. In an attempt to reduce the porosity in long and short deposition paths, an offset of 0.5 mm was maintained between the layers i.e., if layer 1 start at X=0 co-ordinate, then layer 2 would start at X=0.5 mm and layer 3 would again start at X=0. Similarly an off-set is maintained in the Y direction for long deposition path.

In the second part, the influence of the scan strategy on the residual stresses and microstructure was studied. Two deposition strategies were employed, where deposition was made with a post laser scan (with a defocused laser beam after each layer of deposition) and alternately employing a delay between the layers (where the deposition is delayed by one layer deposition time). Three samples were built for each processing condition, which were used in residual stress characterisation and microstructural analysis. The detailed list of parameters with different deposition paths and scan strategies are given in Table 3-5.

Table 3-5: Various deposition paths and strategies employed for thick wall samples

SNo.	Deposition path	Offset of layer	Scan Strategy
1	Long(L)	Yes	No delay
			Delay of ~50 s (1 layer)
			Post laser scan
2	Short(S)	Yes	No delay
			Delay of ~50 s (1 layer)
3	Long + Short (M)	No	No delay

To avoid characterising the residual stresses in the entire build for each process parameter using any experimental characterisation, a finite element model was developed to predict the temperature and residual stress distribution generated during DLF. In order to calibrate the thermal model, thermocouple measurements were made on the substrate during deposition. In

this case, thick walls of size 30 mm wide (X) × 3 mm high (Z) × 4mm thick (Y) were deposited on a thick walled substrate of size 32 mm wide (X) × 4 mm high (Z) × 50 mm thick (Y), representing the repair process in the actual parts. The size of the substrate is slightly thicker than the actual part (Figure 3-3), to accommodate the thermocouples easily. The temperature measurement locations and other details are discussed in section 3.5.

3.4.3 Stage III: Solid Blocks

For hybrid manufacturing applications, where large builds are deposited on existing structures, this stage addresses this via a further scale-up in the build size.

Cuboidal blocks 15 mm thick (X) × 15 mm wide (Y) × 10 mm high (Z) were deposited on a 2mm thick IN718 substrate (machined from a cast IN718 block). The process parameters obtained from thin and thick walls did not produce geometrically sound builds for solid blocks. Therefore optimisation studies were performed again (using DoE) to obtain builds with minimum defects. A full-factorial CCD design was used, as in thin walls, where experiments were developed for three process factors (laser power, scan speed, and powder flow rate). Each factor is varied over three levels: high, intermediate and low, with low being the process parameter in stage I for thin walls. The process factors and corresponding levels are shown in Table 3-6.

Table 3-6: Process factors and corresponding levels

Level / **Factor**	**Low**	**Intermediate**	**High**
Laser Power (Watts)	390	474	558
Scan Speed (mm/min)	200	300	400
Powder flow rate(g/min)	18	25.5	33

The porosity was measured using quantitative image analysis and was used as a response variable to generate a quadratic function, identifying the significant parameters that affect the porosity. A square-hatched deposition path was used (as shown in Figure 3-4), with a hatch spacing of 0.5 mm and a Z increment of 0.3 mm for all the deposits.

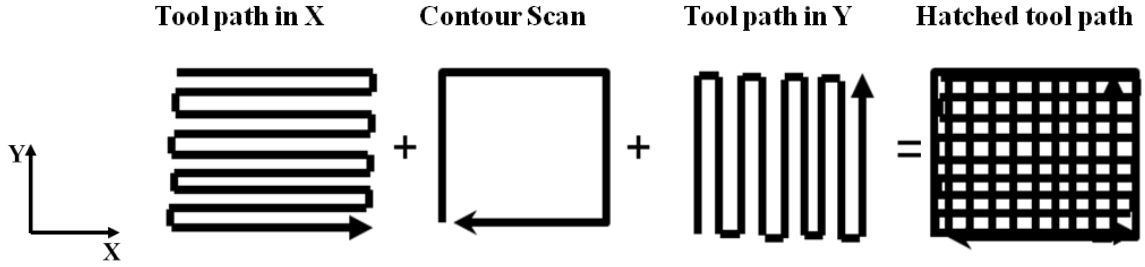

Figure 3-4: The hatched type laser deposition path employed for solid blocks, showing the infill deposition path in X and Y directions, with a contour scan after each layer.

After obtaining the optimum parameter for deposition from the DoE, the depositions were made on a curved substrate (to simulate hybrid manufacturing of a specific component of interest) to study the residual stress development as a result of laser deposition. Rectangular solid blocks 30 mm wide (X) × 10 mm thick (Y) × 10 mm high (Z) were deposited on a curved IN718 substrates 120 mm long (X) × 60 mm wide (Y) × 2.5 mm thick (Z), cut from a large IN718 ~ 1m diameter hollow cylinder (Figure 3-5). The engineering drawing showing the from view, top view and side view of the same is shown in Appendix A.

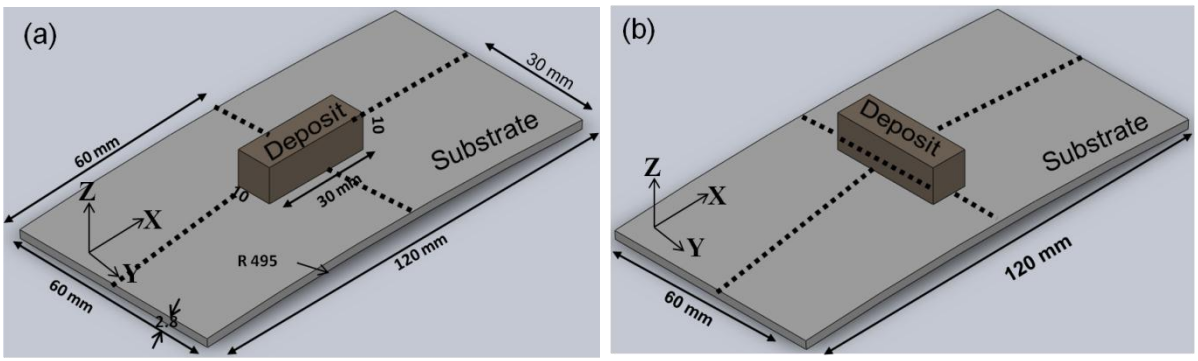

Figure 3-5: schematic illustration of solid blocks deposited on the curved substrates (with a radius of curvature of ~ 495 mm) showing deposits: a) parallel to X-direction, and b) perpendicular to X direction.

In order to assess the influence of DLF parameters on the distortion and residual stress development, as well as obtain the identify the optimum deposition condition with minimum distortion and stresses, various depositions were performed varying the deposition paths (Figure 3-6), laser power, and build direction with respect to the substrate (parallel to the X-axis in Figure 3-5.a and perpendicular to X axis in Figure 3-5.b). The distortion and residual stresses were characterised across the dotted lines in the substrate, shown in the Figure 3-5. Table 3-7 shows the list of process parameters that were studied in this stage.

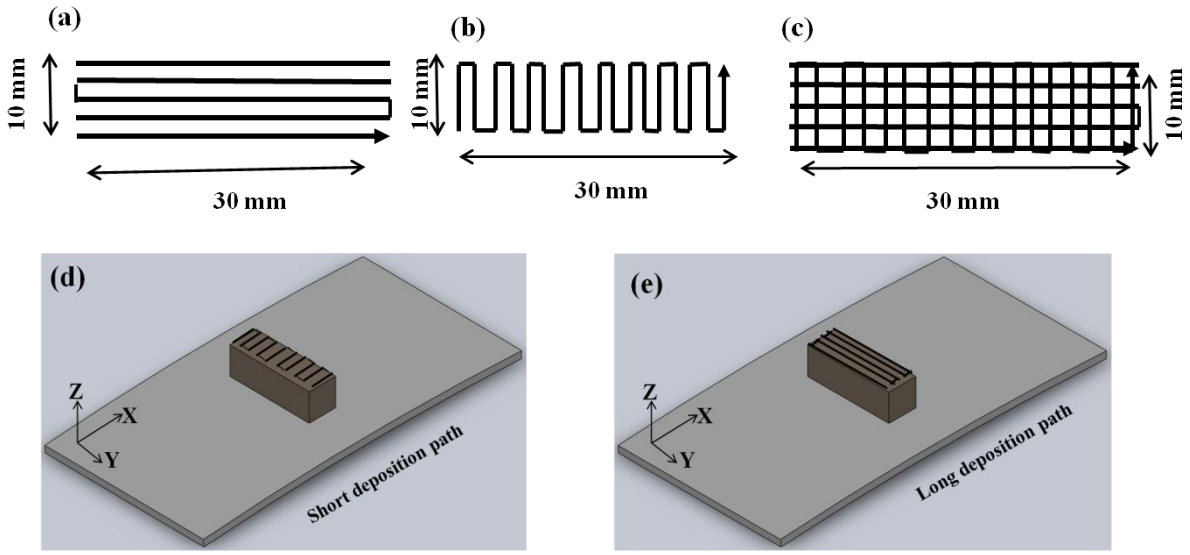

Figure 3-6: The various deposition paths that were used in depositing rectangular blocks on the curved substrates : a) long, b) short, and c) hatched; d) and e) show how a deposition path is laid for short and long deposition paths.

Table 3-7: Process parameters for the deposits on the curved substrates, with a scan speed of 500 mm/min at the first few layers and 400 mm/min in the rest of the build. Powder flow rate was kept at 25.5 g/min.

S.No	Dimensions (X × Y × Z)mm	Deposition path	Offset	Laser power
1	10 × 30 × 10	Long	Yes	474
2	10 × 30 × 10	Short	Yes	474
3	10 × 30 × 10	Hatched	No	474
4	10 × 30 × 10	Hatched	No	600
5	30 × 10 × 10	Hatched	No	474

A further study was performed where the build almost covered the entire substrate. In this study, to exaggerate the effect of deposition path, an 80 mm (X) × 20 (Y) mm deposit was made covering a large portion of the plate of size 100 mm (X) × 32 mm (Y) × 4 mm (Z). The

deposition was made with a scan spacing of 0.7 mm, with no overlap between successive passes. Three different deposition paths: long, short, and mixed (combination of long and short) as shown in Figure 3-7, were used in this study. From the previous studies, it was understood that the effect of deposition on the substrate will be only for a few layers, since, as the deposition progresses, the fluctuation in the temperatures experienced by the substrate becomes limited. So, a total of 10 layers of 0.3 mm thick were deposited for this study. To correlate the distortion due to deposition with the cooling rates associated with various deposition paths, temperature measurements were taken at different locations in the substrates. The details of which are given in section 3.5.2

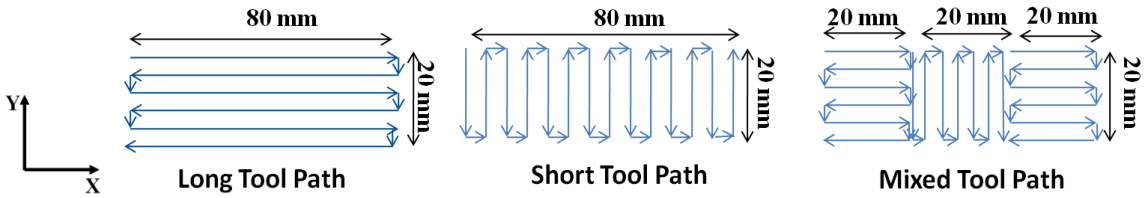

Figure 3-7: The different deposition paths employed for stage III distortion studies.

Finally a further scale up was performed to assess the residual stress distribution in the substrate due to scaling-up, to a square block 30 mm wide (X) × 30 mm thick (Y) ×10 mm high (Z) was deposited on a curved substrate (Figure 3-8). The engineering drawing showing the from view, top view and side view with the exact dimensions is shown in Appendix A.

The process parameters of 474W laser power, 25.5 g/min powder flow rate, and scan speed of 500 mm/min in the first 5 layers and 400 mm/min for the rest of the build with a hatched type of deposition path were employed, which was the optimum condition that would give maximum structural integrity, minimum stress and distortion.

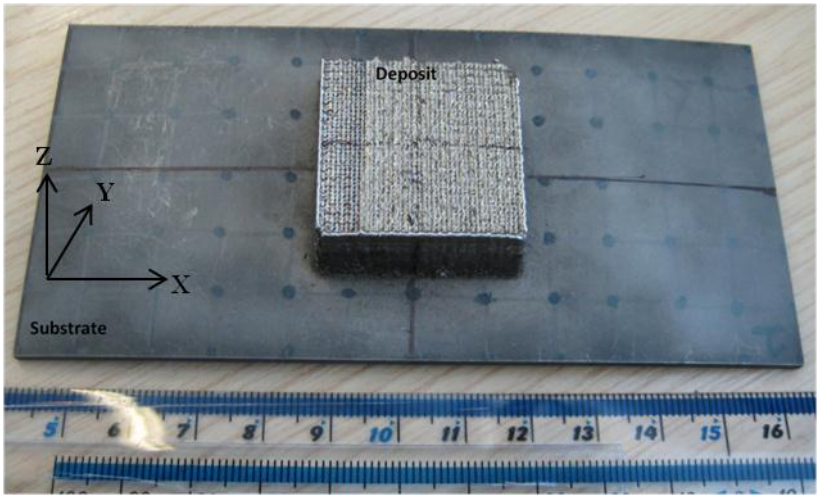

Figure 3-8: Solid block of size 30 mm×30 mm×10 mm on a curved IN718substrate.

3.5 Thermocouple measurements

3.5.1 Thermocouple measurements for FE model Validation

In stage II temperature measurements were recorded on the substrate to validate and fit the thermal model. A mixed type (long +short) deposition path was used with the same process parameters as used in the stage II deposition.1 mm deep holes at 5 different locations (as shown in Figure 3-9) were drilled in the substrate where the thermocouples were inserted. The thermocouples were coded as TC1, TC2, TC3, TC4 and TC5 respectively for the locations 1 to 5. K-type Chromel / Alumel thermocouples were used with maximum operating temperature of 1350 ºC. Temperature changes in the substrate during deposition and cooling were monitored. A data logging system (Pico Log) was used to collect the information at a frequency of 10 Hz.

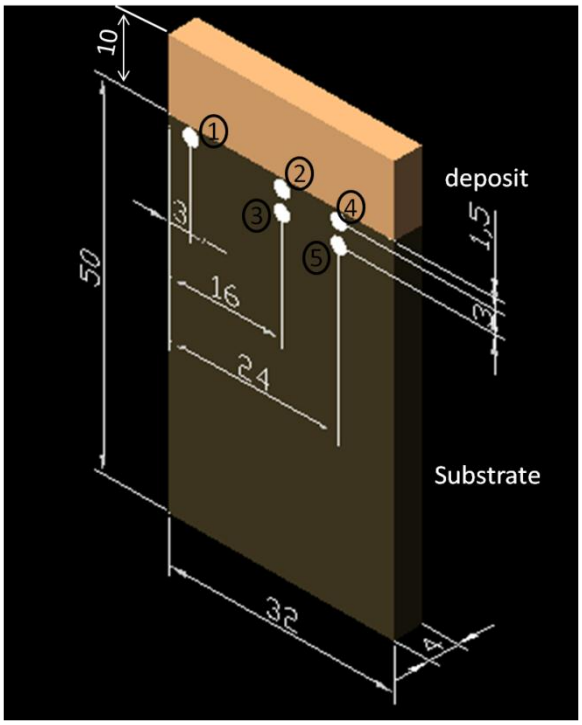

Figure 3-9: Schematic showing thermocouple locations for thick walls (the white dots representing the thermocouple location).

3.5.2 Correlation of distortion with corresponding cooling rates

To assess the influence of cooling rates on the distortion and the residual stresses in stage III builds, thermal cycles were recorded in the substrates with different deposition paths. 8 holes (1 mm deep) were drilled on the back of the substrate (Figure 3-10.a) at locations 5, 20, 30, 40, 60, 70, 80, and 95 mm from the edge of the substrate at the mid width of the substrate. K-type thermocouples were inserted in the holes for measurements. To remove any residual stresses due to hole drilling, a stress relief heat treatment was performed at 955°C for 1 h, with ramp up and ramp down rates of 3°C/min. The back of the substrate was scanned before and after deposition using a Co-ordinate Measuring Machine (CMM) laser scanner as described in section 3.7. The cooling rates were calculated based on the thermal measurements at each thermocouple location, as the ratio of difference in the peak and trough

temperatures of a temperature peak (ΔT) to the time taken (t) for this change in temperature when a laser beam passes the thermocouple location.

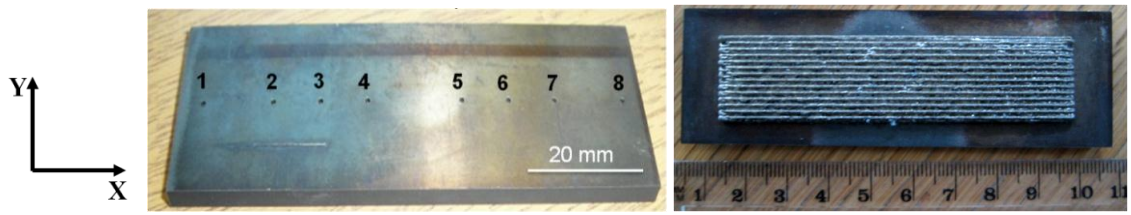

Figure 3-10: a) Back side of the substrate showing the location of thermocouples and b) Long type of deposition path on the substrate.

3.6 Microstructural Characterisation

3.6.1 Sample preparation

Metallurgical samples were sectioned using either a precision cutter fitted with a SiC cutting wheel or by wire Electric Discharge Machining (EDM). Depending on the investigation being carried out, samples were either sectioned vertically along the build direction (Z), to view the X-Z plane, or transversely to the build direction to view the top view (X-Y plane), Figure 3-11. Samples were hot mounted in conductive bakelite. For samples in Stages I, II (thin and thick walls) the X-Z plane was investigated whereas for solid blocks (stage III) all the planes were investigated.

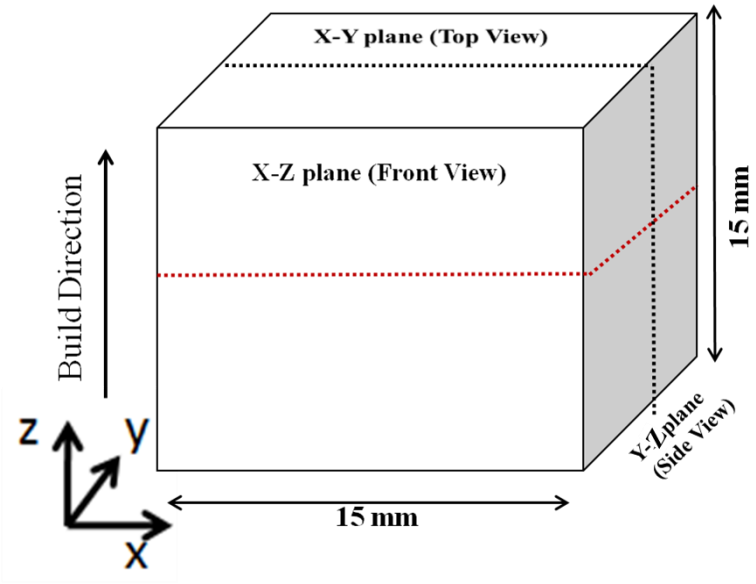

Figure 3-11: Diagram (not to scale) illustrating the investigated planes in the builds (red: X-Y (top) plane, black: X-Z (side) plane).

All mounted specimens were ground using a coarse grit paper (p240) to produce a flat surface and to remove any contamination from the cutting process. Further grinding was carried out in steps down to a p2500 finish, followed by polishing with diamond suspensions with a particle size of 9 μm followed by 6 μm, to a final polishing using a 0.05 μm colloidal alumina suspension.

Two different etchants were used depending on the features of interest: To reveal the solidification microstructure (dendrites and intermetallic phase etc), samples were etched by submersion for 5-10 in waterless Kalling's reagent (5 g $CuCl_2$ + 100 ml HCl + 100 ml ethanol [177]), then rinsed with ethanol and dried. To reveal the precipitates and grain boundaries, samples were electrolytically etched in a 10% phosphoric acid (H_3PO_4) solution in H_2O (by volume).

3.6.2 Image analysis

Image analysis was performed using ImageJ (R) software to quantify the porosity and to measure the grain size.

This procedure was followed to quantify porosity and grain size using ImageJ:

For porosity measurements, the image was thresholded to produce a binary image isolating the relevant features. For grain size measurement, the outline of the grain was highlighted by paint and then a threshold of this outline would pick the grains as particles. 'Particle Measurement' feature in ImageJ was used to take the various measurements from the particles to calculate the particle area fraction and particle/grain sizes. For grain size measurement, an equivalent ellipse is fitted to the grains and the feret maximum is considered as the grain size. The ratio of feret maximum to feret minimum is taken as the aspect ratio of the grains.

3.6.3 Optical Microscopy

Both etched and un-etched specimens were examined under the Leica^{TM} microscope.

The following investigations were performed using Optical microscopy:

Porosity: Porosity in the deposits was quantified using a set of images taken in the sectioned planes of an un-etched sample, covering the entire build. For thin and thick walled builds porosity measurements were taken in the X-Z plane (front view), whereas for solid blocks, in stage III, the measurements for all the three X-Y, Y-Z ad X-Z planes was taken as the overall porosity. The minimum resolvable pore was around 0.5 µm.

Solidification microstructure: For thin walls, the dendritic morphology, orientation and other precipitate features were investigated by taking a series of images on the etched, deposits covering the entire build. For solid blocks, macro-images were taken in a large 5 mm × 5mm

area, using a Keyence™ microscope, to observe the overall bead morphology. Also, images were taken on the single beads to observe the dendrite orientation within the bead.

3.6.4 Scanning Electron Microscopy (SEM)

The metallographic samples were further examined using SEM to study the microstructural development in the grains and to study the secondary phase. Secondary electrons (SE) and back-scattered electrons (BSE) imaging modes were used to generate topographic and compositional information about the specimen respectively; SEM was used for the following investigations:

i) Powder characterisation: this was performed to assess the powder size distribution, morphology and microstructure. A JEOL 6060 microscope (operated at 20 kV) was used for this study. Powder particles were mounted on a conductive tape, and imaged to observe their external morphology. 10 images were captured at 100× magnification, allowing for several hundred particles to be analysed for particle size distribution using image analysis. Bakelite mount and ground powder particles were imaged to observe the grain structure using BSE imaging, and the presence of internal pores using SE.

ii) Grain Size: The grain size of the samples in stage I was measured by capturing and stitching several images at 200 × magnifications to obtain a 2 mm × 2 mm area. The images were captured using a FEI Sirion FEG-SEM in the BSE mode, operated at 10kV. Around 300 grains were quantified to analyse the grain size distribution in each sample.

iii) Secondary phases: A JEOL 7000 SEM, equipped with Oxford Instruments Energy Dispersive X-ray spectroscopy (EDX) detector, was used to investigate the chemical composition and microstructure of the intermetallic phases for various samples in thin walls, thick walls, and solid blocks. The SEM was operated at 10kV for imaging and 20kV for EDX analysis.

3.6.5 Electron Backscattered Diffraction (EBSD)

EBSD was carried out on the samples in the three stages to investigate the macro and micro-texture development. Grain size distribution was also quantified in the builds by using channel 5 software. A FEI Sirion SEM was used to generate EBSD maps, showing the crystallographic orientation of the individual grains. A large area was mapped by taking several EBSD maps, each at 200× magnification, and stitching them together to form an overall map of approximately 2 mm × 10 mm in size. For these large area maps, to obtain macro-texture, a 5 µm step size was used. Further mapping was performed, to obtain micro-texture, over small areas of dimensions 200 µm × 200 µm with a step size of 2 µm, especially at layer interfaces where the fine grain zones were present. The data was analysed using HKL Channel 5 Mambo to construct the pole figures. {100} γ pole figures were constructed with the growth direction in the centre (parallel to vertical Z direction) to understand the orientation of the grains and texture. The pole figures were plotted for individual layers, as well as for the entire build.

3.7 Distortion Measurements

Measurement by 3D Micro-Coordinate Measurement Technique:

To measure the degree of deformation during DLF in the curved substrates (in stage III), Infinite Focus Real3D, an optical 3D micro coordinate measurement system from Alicona^{TM}, was used to measure the off-plane distortion. Series of images were captured along the dotted lines in Figure 3-5 (along X axis and Y axis). The X, Y, and Z co-ordinates along these lines were obtained by processing the series of images by Mex 3D^{TM} software, which gives the co-ordinate points in an excel file.

Measurement by CMM:

To measure the distortion in stage III (rectangular plates and solid blocks on curved substrates) the substrates were scanned before and after deposition using an Impact 1000 CMM fitted with Kreon laser scanner (**Error! Reference source not found.**). The CMM is quipped with virtual DMIS software. The system has a resolution of 9 µm. The 3D data points collected using the scanner were cleaned to reduce the noise in the points, and converted to CAD models using Geomagic studio 8 software. These models, before and after deposition, were compared to assess the degree of distortion using Geomagic Qualify 8 software.

3.8 Residual Stress Characterisation using Neutron Diffraction

Neutron diffraction experiments were performed to characterise the residual stress development in the DLF builds. Measurements were performed using SALSA (the strain scanning beam line at the Institut Laue-Langevin, ILL), Grenoble, France [178] for thick walls (in stage II) and STRESS-SPEC, the residual stress and texture diffractometer (FRM II) Garching, Germany [179] for the curved substrates in stage III. The experimental setup at SALSA, is shown in Figure 3-12. A monochromatic beam of neutrons having a wavelength of 1.64 ˚A was used to measure the γ {311} Bragg reflection giving a nickel peak at ~98°, resulting in a near-cubic diffracting gauge volume. An effective diffracting gauge volume of 0.5 mm ×0.5 mm ×0.6 mm was used for thick walls (in Table 3-5), whereas 2 mm ×2mm ×1.8 mm gauge volume was used for solid blocks on curved substrates (in Table 3-7). Lattice spacing measurements were made in the three orthogonal directions at various locations of the build and the substrate to assess the localised residual stress variation across and along the deposits. Elastic strains were calculated using:

$$\varepsilon_{hkl} = \frac{d_{hkl} - d^0_{hkl}}{d^0_{hkl}} \qquad 3\text{-}1$$

where d_{hkl} is the measured d spacing for the particular hkl reflection and d^0 is the stress-free d-spacing and ε_{hkl} is the elastic strain normal to the hkl plane.

$$\sigma_x = \frac{E_{hkl}((1-\upsilon_{hkl})\varepsilon_x + \upsilon_{hkl}(\varepsilon_y + \varepsilon_z))}{(1+\upsilon_{hkl})(1-2\upsilon_{hkl})} \qquad 3\text{-}2$$

where E_{hkl} and υ_{hkl} are the elastic modulus if 205 MPa and poisons ratio of 0.284 for IN718 based on the Kroner model and other literature [24, 95-96] Young's modulus of 205 GPa and Poisson's ratio of 0.284 were used, for the direction normal to the planes for the specific the {311} reflection and ε_x, ε_y and ε_z are the strains measured in the three orthogonal directions.

3.8.1.1 Measurement of d^0:

One of the crucial uncertainties in calculating the residual stresses comes in the determination of the lattice spacing for stress-free samples (d^0) [88]. The value of d^0 can change due to local changes in composition and microstructure as is inevitable in complex alloys. As the microstructure of the build and substrate are significantly different, location-specific stress-free lattice spacing were determined. For d^0 measurements in thick walled samples or in the curved substrates a stress balance method is employed where the stresses in the through thickness direction is assumed to be zero and the stress free d^0 is back calculated. However, for residual stress analysis in the solid block (in stage III), 2 mm thick and 10 mm diameter discs were sectioned by EDM from the middle of the substrate and these were used as the strain free d^0 coupon.

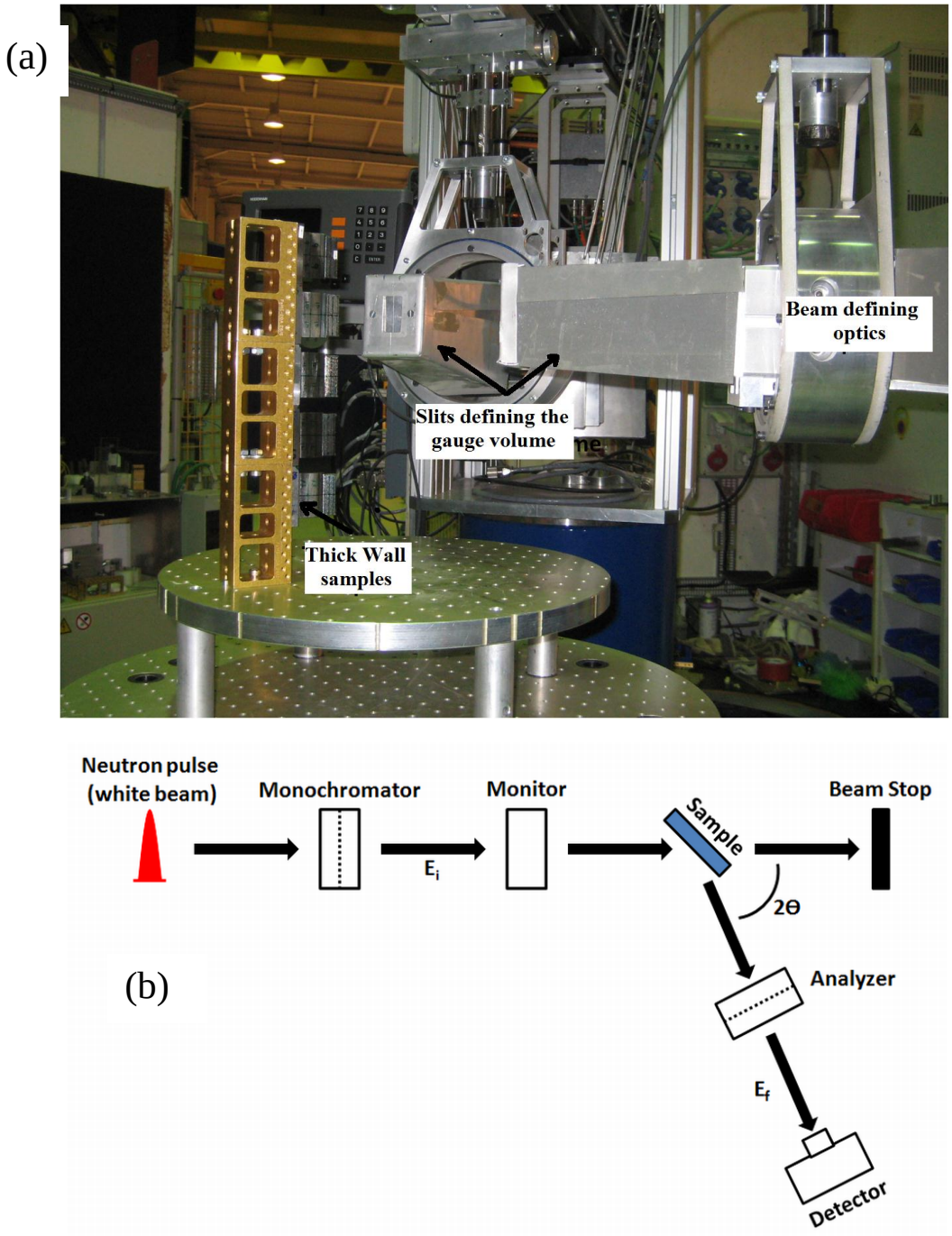

Figure 3-12: (a) Neutron diffraction setup at SALSA, ILL Grenoble for measuring the stresses in thick walls (b) schematic of neutron diffraction.

3.9 Hardness

Hardness measurements were performed using a Struers^{TM} Vickers hardness testing machine, equipped with Ecos work flow software. A hardness contour map was generated for the thin walled samples (stage I) where hardness measurements were taken at intervals of 1 mm for

the entire build. For thick wall samples (in stage II), hardness measurements were taken across the build substrate interface (5 mm on each side) at a distance of 300 µm between successive indentations. All the measurements were performed using a load of 200 g applied for 5 s.

3.10 Heat Treatment

To study the impact of post-DLF thermal treatment on the microstructural inhomogeneities in the builds, a standard homogenisation treatment followed by solution treatment and ageing was performed on the thick wall deposits (stage II) according to the industrial standard AMS-5383D heat treatment method used for cast IN718 [22]. Microstructural and hardness measurements were also performed on these samples to compare with the un-heat treated samples. The heat treatment was carried out in a vacuum furnace according to the temperature-time plot as shown in Figure 3-13.

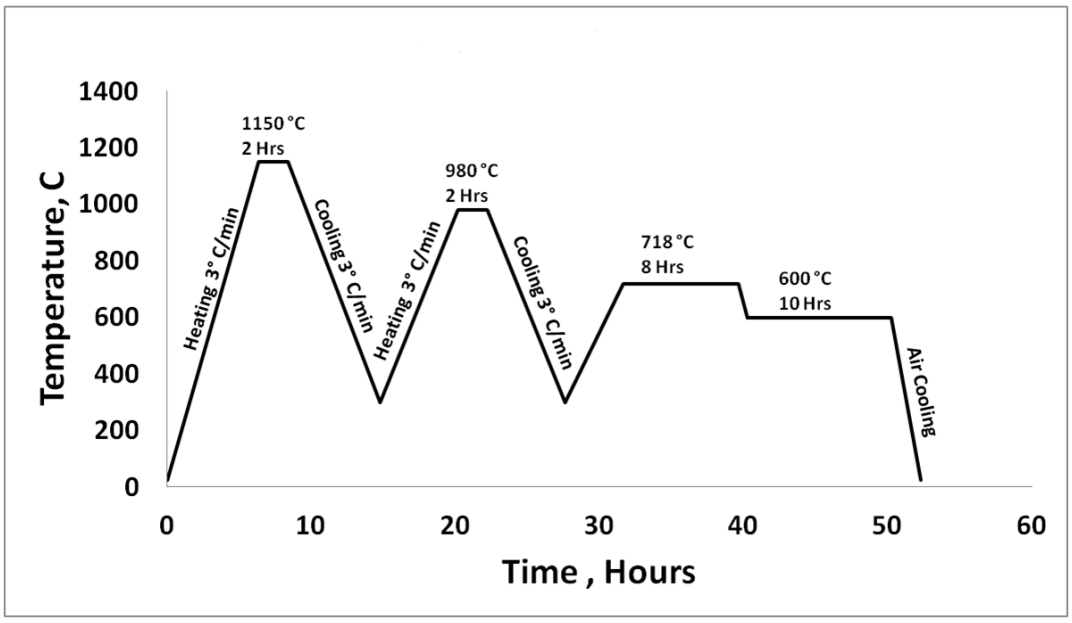

Figure 3-13: Post DLF heat treatment cycle for IN718 routine used in the current investigation based on [22].

Chapter Four

4 Process Window Development for DLF of IN718

This chapter is concerned with the DLF process optimisation of IN718 thin walled builds (stage I), thick walled builds (stage II), and solid blocks (stage III). Additionally, microstructure and size distribution of the as-received powder is presented.

4.1 Introduction

Before characterising the samples for the microstructural in-homogeneities, it is important to produce geometrically sound builds. Especially during repair, the height and thickness of the builds should have the target dimensions, with minimum porosity in the build.

Based on the literature survey, it was evident that there are several process parameters that would affect the deposition geometry and porosity (is section 2.5.2). In this chapter, studies were undertaken to identify the process parameters which have a strong influence on the deposition geometry. A statistical model was developed to predict the build geometry (i.e. height and thickness of the final build for a given set of process parameters). Also, this chapter aims at understanding the pore distribution in the build, and aims at reducing the porosity of the build to minimum. Prior to DLF processing, an examination was carried out on the as-received powder to confirm its size distribution, morphology and chemical composition.

4.2 Powder Characterisation

The as-received powder was examined to assess the morphology and size distribution of the particles using SEM.

4.2.1 Morphology and Size Distribution of Powders

The gas atomised particles of the IN718 powder (supplied by SANDVIK OSPREY) were <106 μm, Measurement by image analysis, illustrated in Figure 4-1, showed that the size varies between ~2 to ~120 μm with 90% of powders between 40 and 100 μm.

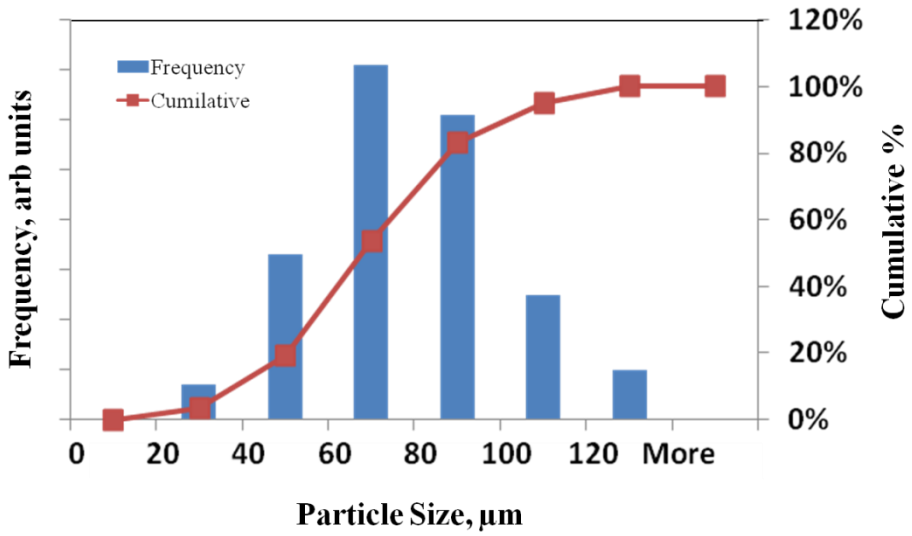

Figure 4-1: Powder size distribution of gas atomised IN718powders.

Figure 4-2 shows the gas-atomised IN718 powder particles, typical of those that were used in the present study. The powder particles are not geometrically uniform (i.e round), having a rough surface finish. It is also observed that very fine satellite powder particles (~< 5 μm) were attached to the large powder particles, which would prevent them from being dispersed by the argon flow from the nozzles. Further examination of the cross-section of powders showed that the as-received powders were not all fully dense. Hollow particles were frequently observed, as shown in Figure 4-3.a. The pores in these hollow particles are present as a result of entrapped argon or due to shrinkage during atomisation [180]. Thus, the entrapped argon could be present in finished DLF structures. The back scattered image of the

polished powders showed a dendritic microstructure inside the powder particles (Figure 4-3.b).

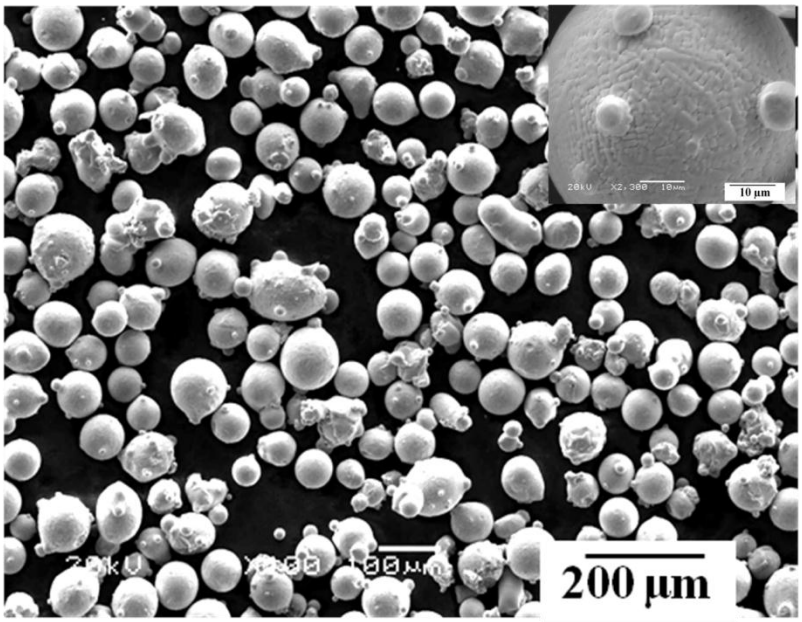

Figure 4-2: SEM micrograph of gas atomised IN718 powder particles, with an insert micrograph showing the surface of a large particle.

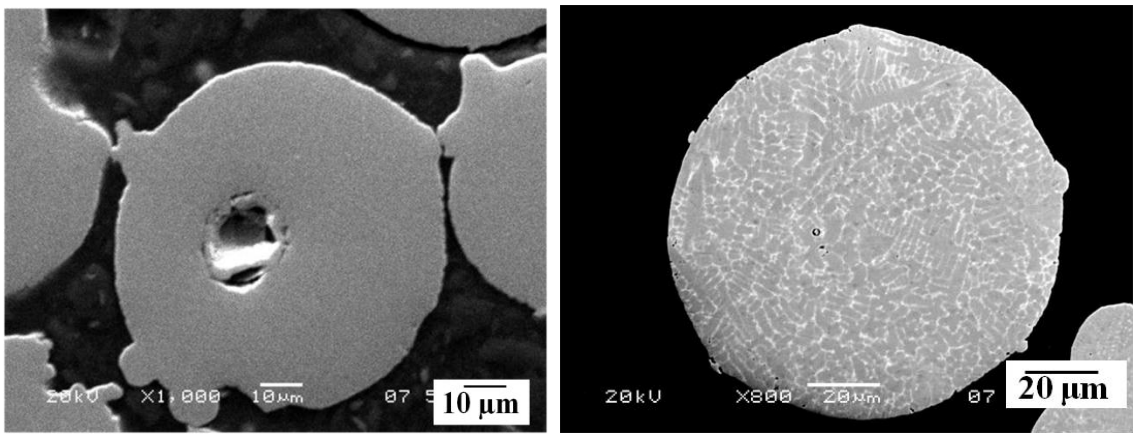

Figure 4-3: BSe micrographs for the cross section of the powder showing a) inherent porosity, b) dendrite morphology inside powder particle.

The powder should be ideally spherical in shape, with the powder size > 50 µm because the argon carrier gas, which is used to carry the powder to the laser focal point, could blow the powder away if the powder is finer than 50 µm [1]. Also studies by Qi *et al*. showed that

powders in the size range of 40-75µm resulted in less porosity in the build than the coarser powder, as the chances of gas entrapment is higher in coarser powders than in fine powders [22].

4.3 Parametric Study for Thin Walled builds (stage I)

A preliminary study was performed on thin walled builds, by varying the scan speed and powder flow rate at a constant laser power to understanding the influence of these parameters on the build quality, and also to identify the range of parameters in which a structurally sound build is feasible. Later, statistical model was developed which can predict the thickness and the height of the deposit using Design of Experiments (DoE) approach. The initial parameters of this approach were chosen based on the preliminary study.

Figure 4-4 shows the thin walls built with various process parameters, at a constant laser power of 390 W. From the figure, it is obvious that there are various problems encountered during the build. At high scan speed and low powder flow rates, the deposit has a wavy structure (Figure 4-4.a). With a further increase in scan speed, the deposit starts to fail (Figure 4-4.b) which is due to reduced capture efficiency of the powder. At high powder flow rates, lumps were observed in the first few layers of the deposit. Most of the energy supplied by the laser is used in heating the cold substrate, and the remaining energy is in-sufficient to melt the larger amounts of powders, forming these lumps in the first few layers (Figure 4-4.c). It was also found out that unidirectional laser builds are thinner and smaller than the bidirectional deposited sample (Figure 4-5). In bidirectional builds, the laser power is continuous and the amount of heat accumulated is more than in unidirectional deposited samples, where the laser is switched-off between the layers, causing more powder to melt and thus giving more build height and thickness (Figure 4-4.d-e and Figure 4-5). The other important observation was the discolouration of the sample surface, which is readily seen on

the surface of the build (Figure 4-4.f). The polished samples were analysed for oxygen pick-up by inert gas fusion method [181]. Table 4-1 shows the amount of oxygen picked up during laser deposition at different laser powers both in air and in controlled Ar atmosphere (50 ppm in the chamber). It can be seen that with the increase in power, the oxygen pick-up increases. However, the amount of oxygen picked-up in this process is in permissible levels.

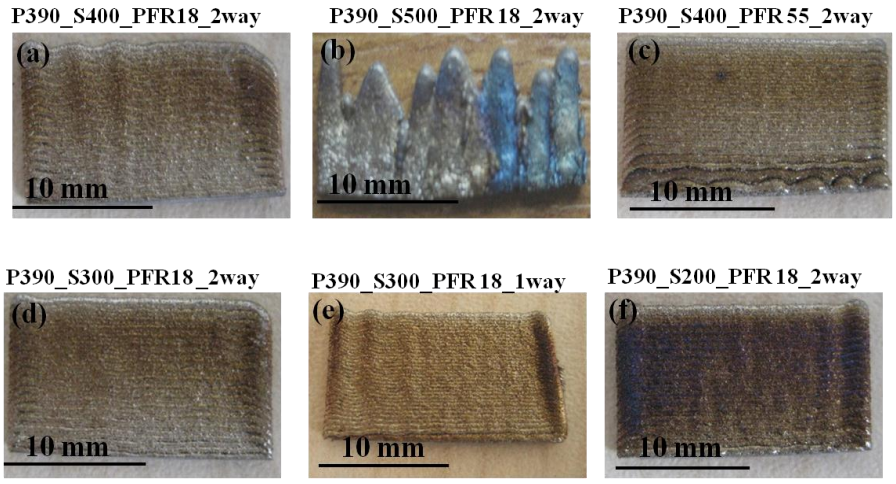

Figure 4-4: Various problem encountered in the builds: (a) to (f) show thin wall builds with different process conditions as shown in the figure where P stands for laser power in watts, S is the scan speed in mm/min and PFR is the powder flow rate in g/min.

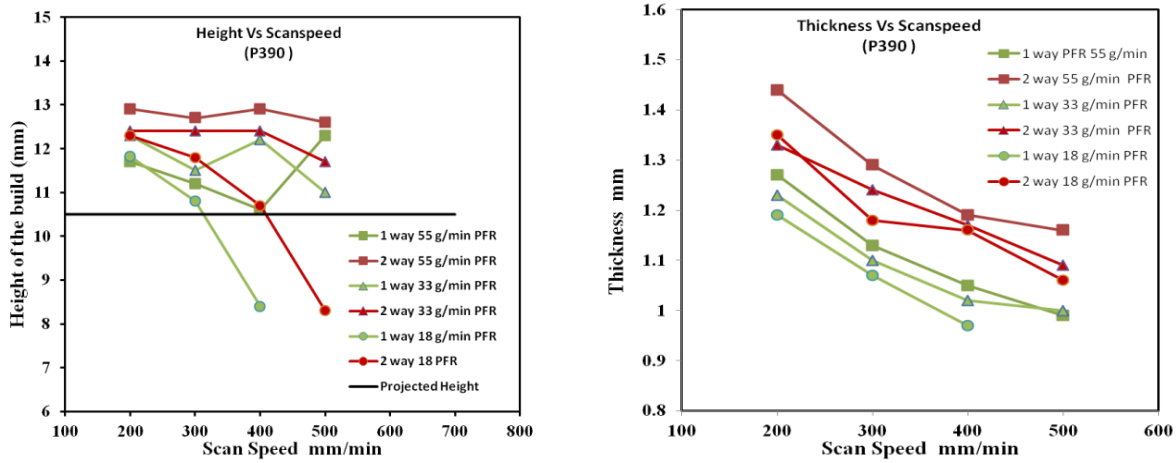

Figure 4-5: Variation of height and thickness of the samples at different scan speeds and powder flow rates for Unidirectional and bidirectional builds.

Table 4-1: Oxygen pick-up in the build during laser deposition in controlled Ar atmosphere and air at two laser powers keeping scan speed at 200 mm/min and powder flow rate at 18.6 grams/min.

Power (W)	Oxygen level in the glove box (ppm)	Oxygen content in the build (ppm)	Oxygen content in the powder (ppm)	Oxygen pickup (ppm)
390	30	80	40	40
390	built in air	160	40	120
474	30	110	40	70
474	built in air	200	40	160

4.3.1 Effect of build parameters on thickness and height

From the preliminary studies, it becomes obvious that the thickness and height of the build substantially varies with process parameters. During laser deposition, the build height and thickness should be controlled in order achieve the desired height, and thus avoid contacting the nozzles during deposition, and also should not have thicker/thinner bead size which would create a problem during overlap between layers while depositing solid blocks. From the literature, it is known that the factors which influence the deposition dimensions of DLF deposits are laser power , scan speed and powder flow rate[8, 108]. In the present study DoE was performed to show the effect of these factors i.e., laser power scan speed and powder flow rate on the average thickness and height of the build. Additionally, to obtain an empirical model that can predict these responses for any combination of the working parameters, analysis of variance (ANOVA) approach has been used [182]. A full-factorial central composite design (CCD) experiment was conducted with these dominating factors. The details of the central composite design methodology can be found in Montgomery's Design and Analysis of Experiments [183-184]. Table 4-2 lists the three factors and three levels full-factorial CCD design matrix containing 22 running conditions (each factor is repeated twice to increase the accuracy of the model). Thin walled builds (20 mm in length and 10.5 mm in height) were deposited with each of the conditions in Table 4-2. The build height and thickness were measured and listed correspondingly. A quadratic transfer function

correlating the dominating factors and the build width and height, was developed as a result of the CCD experiments.

Table 4-2: Central composite DoE running conditions and the corresponding bead width and height measured using a screw gauge (±0.05 mm).

		Factor 1	**Factor 2**	**Factor 3**	**Response 1**	**Response 2**
S.No	**Run**	**A:Scan Speed**	**B:Powder Flow Rate**	**C:Laser Power**	**Thickness**	**Height**
		mm/min	**gm/min**	**Watts**	**mm**	**mm**
1	1	300	36.5	300	0.7	11.58
2	11	500	18	300	0.62	7.2
3	12	300	55	300	0.85	12.62
4	8	500	55	300	0.81	12
5	22	300	18	450	1.6	11.7
6	5	500	18	450	1.1	10.47
7	14	300	55	450	2.11	12.8
8	2	500	36.5	450	1.61	10.87
9	20	300	36.5	375	1.09	12.54
10	15	300	36.5	375	1.16	12.58
11	10	500	36.5	375	0.95	11.33
12	18	500	36.5	375	0.97	11.84
13	13	400	18	375	1	10.54
14	6	400	18	375	0.96	10.84
15	7	400	55	375	1.07	12.96
16	17	400	55	375	1.03	12.8
17	4	400	36.5	300	0.65	10.64
18	19	400	36.5	300	0.62	11.6
19	3	400	36.5	450	1.9	11.4
20	21	400	36.5	450	1.86	11.3
21	9	400	36.5	375	1.07	12.54
22	16	400	36.5	375	1.09	12.52

4.3.1.1 Thickness

Figure 4-6.a shows the model fit for the thickness of the sample at different process parameters. Values of the R-square and adjusted R-Square, a measure of model fit, showed that each of the models described fit reasonably well and these were 96% and 93% respectively. In statistical hypothesis testing, the P-value is the probability of obtaining a result at least as extreme as the one that was actually observed [185]. The smaller the P-value (significant if less than 0.05), the more important is the factor. Table 4-3 shows the P values for each process parameter and the interactions. From these values, it can be seen that all the three process parameters are significant for the thickness of the build, out of which laser power is the most significant factor. However, the interaction between the process parameters is not very significant. From Figure 4-7, it can be seen that the effect of laser power on the thickness of the build is more than the scan speed and powder flow rate. It is seen that the thickness of the build decreases with scan speed and increases with laser power and to a lesser extent with the powder flow rate, which is in good agreement with the literature [9, 101]. Using a general second order polynomial equation, an empirical model was constructed based on the critical parameters, (i.e. laser power, and scan speed, and powder flow rate and their interactions). Using 4-1, it is possible to predict the equivalent thickness of the build at any value of each process parameter even if it was not one of the pre-selected levels. The value of each coefficient under each quality characteristic is displayed in Table 4-4.

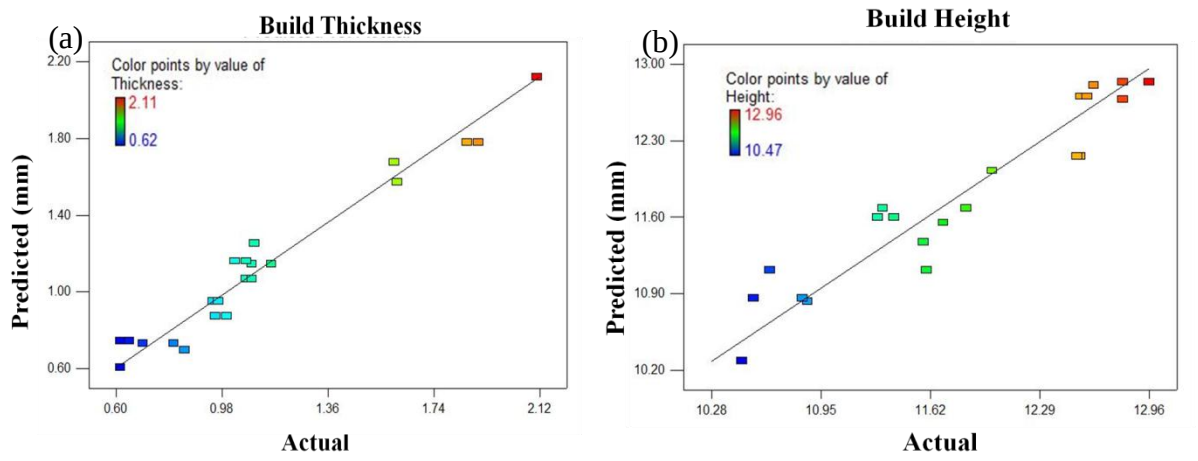

Figure 4-6: The model fit showing the predicted and actual values for: a) build thickness and b) build height.

Table 4-3: Process parameters and corresponding P-value with significant factors highlighted.

	Thickness	Height
Scan speed (A)	0.0141	0.0046
Powder flow rate (B)	0.0025	< 0.0001
Laser power (C)	*< 0.0001*	0.0003
Interaction AB	0.7710	0.8882
Interaction AC	0.1742	*0.7159*
Interaction BC	0.2060	0.0102

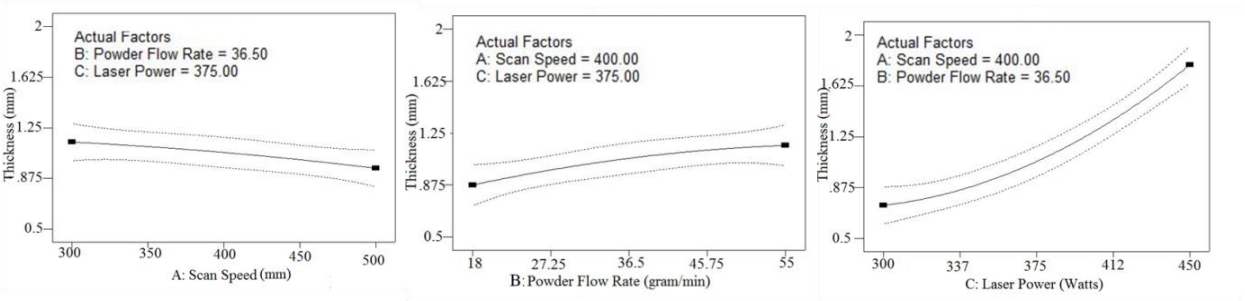

Figure 4-7: Effect of individual process parameters on the thickness of the build.

$$Build\ Thickness\ or\ Height\ = X + x_1 * A + x_2 * B + x_3 * C + x_4 * A * B + x_5 * A * C + x_6 * B * C + x_7 * A^2 + x_8 * B^2 + x_9 * C^2 \quad (4\text{-}1)$$

Where, A is the scan speed, B is the powder flow rate and C is the laser power and x_1 to x_9 are the model coefficients indicated in Table 4-4.

Table 4-4: Coefficient values corresponding to process parameter.

	Thickness (mm)	**Height (mm)**
Constant (X)	2.312419841	-26.63682272
x_1	0.004741551	0.005196321
x_2	-0.014399788	0.386972956
x_3	-0.016924659	0.158875094
x_4	1.23874E-05	2.25225E-05
x_5	-1.21333E-05	-1.18E-05
x_6	7.41742E-05	-0.000636637
x_7	-2.01667E-06	-1.00167E-05
x_8	-0.000145605	-0.001263209
x_9	3.4637E-05	-0.000166696

4.3.1.2 Height:

Values of the R-square and adjusted R-Square, for build height are 93% and 88%, respectively. The model was fitted reasonably well (Figure 4-6.b). From the P values, it is seen that the three process parameters and the interaction between laser power and scan speed are significant in the model with powder flow rate and scan speed being the most prominent factors. The height of the build increases almost linearly with powder flow rate and decreases with scan speed (Figure 4-8). The reason for the decrease in build height with the increase in the scan speed can be attributed to the poor powder capture efficiency at high scan speeds. The deposition height increases with laser power until a certain laser power and later there is a decrease in the build height (Figure 4-8.c). Generally, with the increase in laser power, the bead height would increase and as the build progresses, the bead height in each layer increases and the overall build would grow higher than the desired height. This causes the build to slightly move further to the focal point of laser causing an under-deposit. The other significant factor in the model is the interaction between laser power and powder flow rate. The deposition height tends to increase linearly with powder flow rate at low laser powers

however with an increase in laser power the deposition height tend to be almost constant or show a slight decrease (Figure 4-9). With the increase in the laser power, the melt-pool size would increase, which causes an increase in capture efficiency of the build. When the powder flow rate is increased at this stage it causes an increase in the build height and as discussed previously the extra increase in build height causes the build to move away from the laser focus. Finally the equivalent height of the build can be measured for any given parameters by Equation4-1 and Table 4-4.

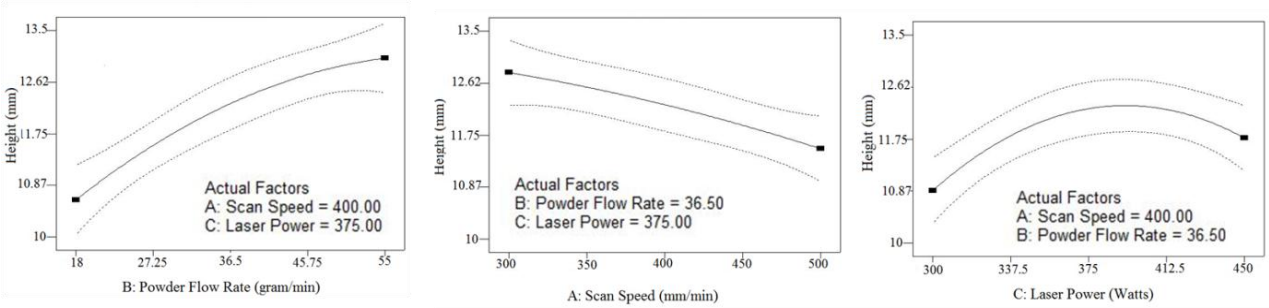

Figure 4-8: Effect of individual process parameters on the height of the build.

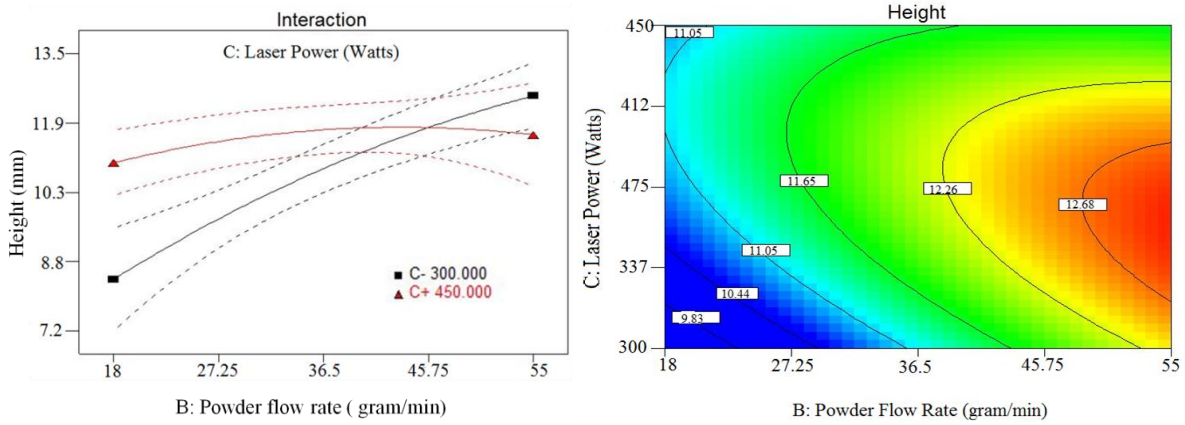

Figure 4-9: Graph showing the interaction between laser power and powder flow rate at a scan speed of 400 mm/min.

4.3.2 Validation of Statistical Model on Thick Walled builds (Stage II)

One of the best build parameters from these experiments which showed a good build quality (P 390_SS 300_PFR18) was chosen to build 2.4 mm thick walls (0.4 mm for surface finish operation) on a 2 mm thick substrate to simulate repair of components (builds shown in

Figure 3-3). The height and thickness of the build for long (L), long + short (L+S) and long + post-scan (L+P) deposition paths were measured and the average value of three samples was plotted against the model as shown in Figure 4-10. The graph shows that the height and thickness measured is within 5% of the model prediction (calculated from equation 1-1) showing a confidence level of 95% for the models.

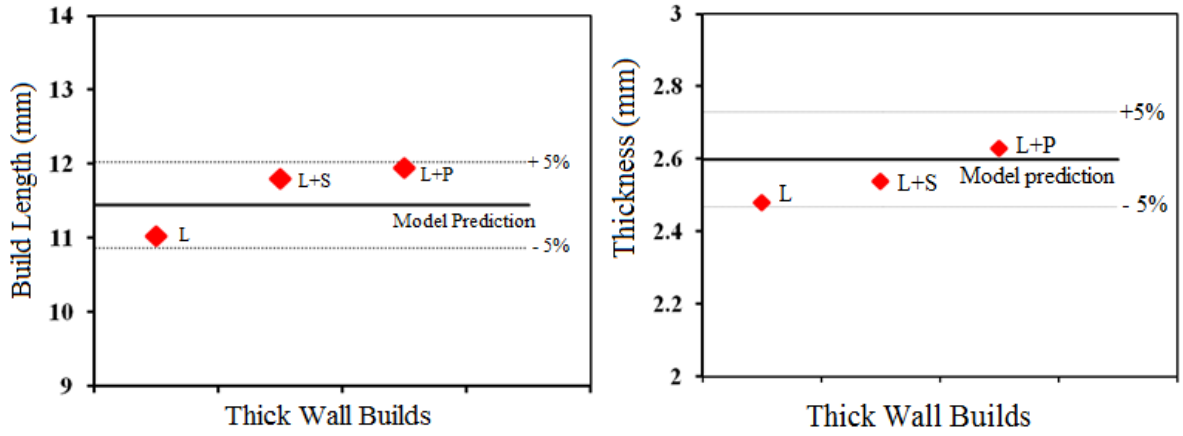

Figure 4-10: Comparison of height and thickness of one bead for the thick wall builds with the model derived from DoE.

4.3.3 Porosity

4.3.3.1 Thin walls (stage I)

The Porosity was measured by taking series of images across the build in a 5 mm × 5mm area. Figure 4-11.a and b show the pores present in thin walls, for unidirectional and bidirectional deposited samples at a power of 390W. Spherical pores were observed in the build that were spread throughout the sample. Both unidirectional and bidirectional deposits displayed a pore density of 0.2 ± 0.1 %. This shows that at a given laser power, 390W in this case, the deposition path does not have a strong influence on porosity. It is known that the pores in DLF deposits can be attributed either to the porosity originally present in GA powder[22], or created during the process within the melt pool as a result of molten metal fluidity or turbulence (due to excessive superheat[22]). The pore size varied from 40–100 µm, which is bigger than the porosity observed in the powder. Since the pores were spherical

(Figure 4-11.c), it can be inferred that the porosity is due to gas entrapment from the process as well as from the GA powder [22]. Figure 4-12 shows the variation of porosity with laser power. With the increase in laser power the porosity increases. The use of high laser power would increase the melt pool temperature, decrease the molten metal viscosity, and increase turbulence in the melt pool and thus increase the extent of gas-entrapment in the build [109]. The fluidity would also relate to the inter-pass temperature and time for heat dissipation between passes.

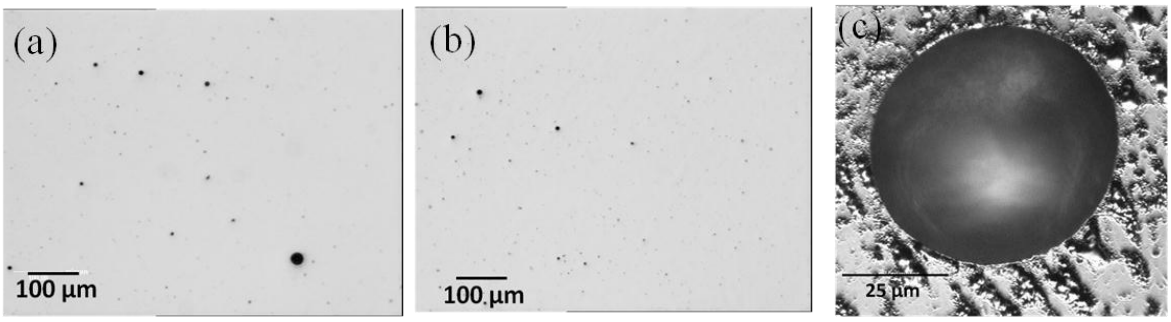

Figure 4-11: Porosity in the thin wall samples: a) Unidirectional build, b) bidirectional deposited with 390W laser power, 200 mm/min scan speed and, 18 g/min powder flow rate, and c) enlarged image of a pore.

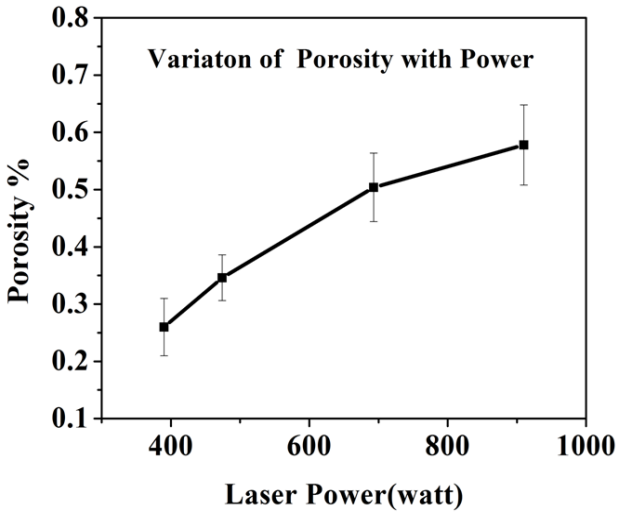

Figure 4-12: Variation in porosity with laser power at a scan speed of 200 mm/min and a powder flow rate of 18 g/min.

4.3.3.2 Thick Walls(stage II)

All the thick wall builds (described in experimental section 1.3.2) did not show any bonding defects. Figure 4-13 shows an optical micrograph of the build in a large 15 × 10 mm area (obtained by stitching series of 100 × magnification optical micrographs). The optical micrographs did not show any bonding defects except some gas porosity distributed sporadically in the build. The porosity was similar to the gas porosity that was observed in thin wall deposits and it is around $0.2 \pm 0.03\%$.

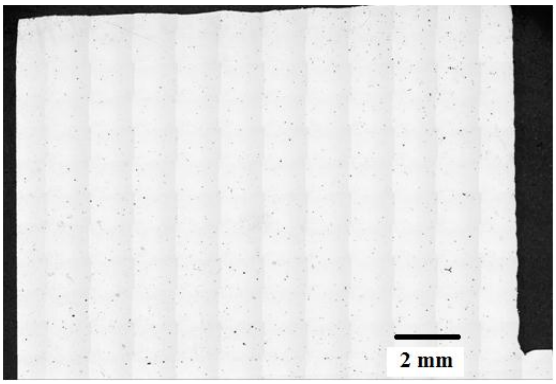

Figure 4-13: Optical micrograph of polished thick walled build (P390_SS300_PFR18_L).

4.4 Solid Blocks (stage III)

Although the best process parameters that were obtained from thin wall builds could produce good thick wall builds, these parameters were not able to produce sound solid blocks. In solid blocks, the time taken to deposit 1 layer is much more than the thick walls and the layers would cool down before the next layer is deposited, unlike in thick walls where the bottom layer is still hot and easy to re-melt. Also, as seen in thin wall, lumps were formed at the bottom most layers, as the major part of laser power is used up in heating the substrate rather than melting the powder. Optimisation studies were performed to investigate the influence of the laser power, scan speed, powder flow rate keeping the hatch spacing to 0.5 mm in order to obtain sound builds. Table 4-5 shows the lists of three factors and three levels full-factorial CCD design matrix containing 16 running conditions. Solid blocks (15 mm thick × 15mm

wide × 10 mm high) were deposited with each of these conditions. Series of images were taken covering the entire build in all the three sides of the build (front view, top view and side view) and porosity values were obtained by imageJ. An average value of porosity, of all the three sides of the build, is tabulated in Table 4-5. A quadratic transfer function correlates the dominating factors and the porosity was developed as a result of the CCD experiments (Equation 4-2). However, the porosity varied drastically within the build, so a qualitative measurement of the build showing the variation of porosity across and along the build would be of more interest than the quantitative measurements.

Table 4-5: Central composite DoE running conditions and the corresponding porosity.

S.No	**Run**	**Scan speed (A) (mm/min)**	**Powder flow rate (B) (gram/min)**	**Laser power (C) (Watt)**	**Porosity (%)**
1	12	200	18	390	2
2	5	200	18	558	1.5
3	14	400	18	390	2.1
4	11	400	18	558	1.27
5	16	200	33	390	5
6	13	200	33	558	10
7	10	400	33	390	2.3
8	15	400	33	558	2
9	4	300	25.5	390	2.5
10	7	300	25.5	558	1.7
11	9	200	25.5	474	3.5
12	8	400	25.5	474	1
13	6	300	18	474	2
14	2	300	33	474	7
15	3	300	25.5	474	1.75
16	1	300	25.5	474	3

$$Porosity = -14.98951 + 0.099380 * A - 1.42195 * B + 0.080706 * C - 1.76167E - 003 * A * B - 8.37798E - 005 * A * C - 1.76167E - 003 * B * C - 4.67931E - 005 * A^2 + 0.031681 * B^2 - 8.75753E - 005 * C^2$$

4-2

Where A is the scan speed, B is the powder flow rate and C is the laser power.

The optimisation study from the DoE showed that the set of process parameters which gives minimum porosity (<0.1%) was P558_SS400_PFR25.5. In order to understand the variation of porosity along and across the build images were taken (2 mm strips) from bottom to top and side to side of the front view of the build, along the dotted lines, Figure 4-14. ImageJ was used to threshold the pores and defects, and the variation of porosity is plotted.

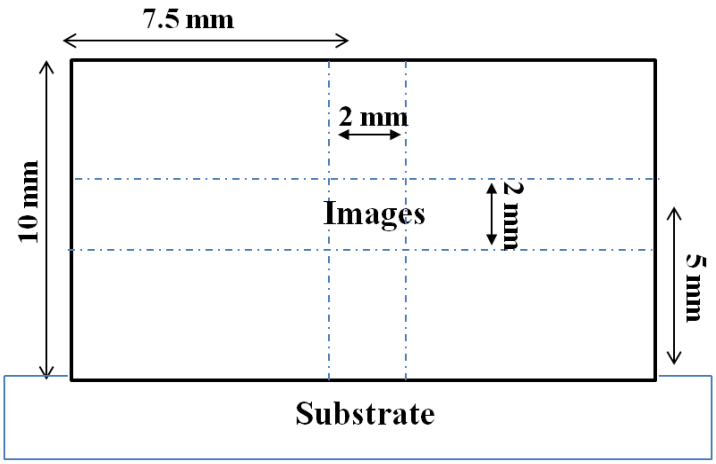

Figure 4-14: Locations in the solid blocks where the images were captured for porosity measurements.

The porosity level in the build with the best process parameters from the model was 0.74%, which is much higher than the predicted value. Figure 4-15.a & b show the variation of porosity across and along the build. The largest pore size in the bottom layers (i.e., near the substrate) was around 500 μm, which is like a cavity or void whereas the maximum pore size

is around 100 μm in the rest of the build, which is similar to the gas porosity seen in thin walls. Although there was a considerable scatter in the porosity, it was clear that the porosity fraction close to the substrate was the lowest (0.003), which suggests that there is good bonding between the substrate and the build. The reason for this is attributed to the preparatory laser scan without powder. After the first layer, the porosity increased in the consecutive layers, possibly due to the large thermal gradient between the cold substrate, which acts as a heat sink absorbing the heat from the melt pool. The cold substrate causes rapid or premature freezing of the melt pool giving rise to some un-melted particles and poor bonding between layers. This problem could be alleviated by decreasing in the powder flow rate in the initial layers (Process condition of P558_SS400_PFR18). However, with such low powder flow rates, the build fails to reach the projected height leading to failure (Figure 4-15.a). After a few layers of deposition when the build is away from the cold substrate the porosity, due to un-melted particles caused by rapid freezing of the melt pool, decreases. So, a combination of process parameters is recommended for a sound overall build with low powder flow rates in the first few layers of the build and later an increase in the powder flow rate. Figure 4-15.b shows the variation of porosity across the build. Across the build (from edge to edge), the porosity was higher at mid-height and width locations compared to the edge of the build. Due to the hatched deposition path, the edges of the build usually stay hotter than the centre, which promotes bonding at the edges.

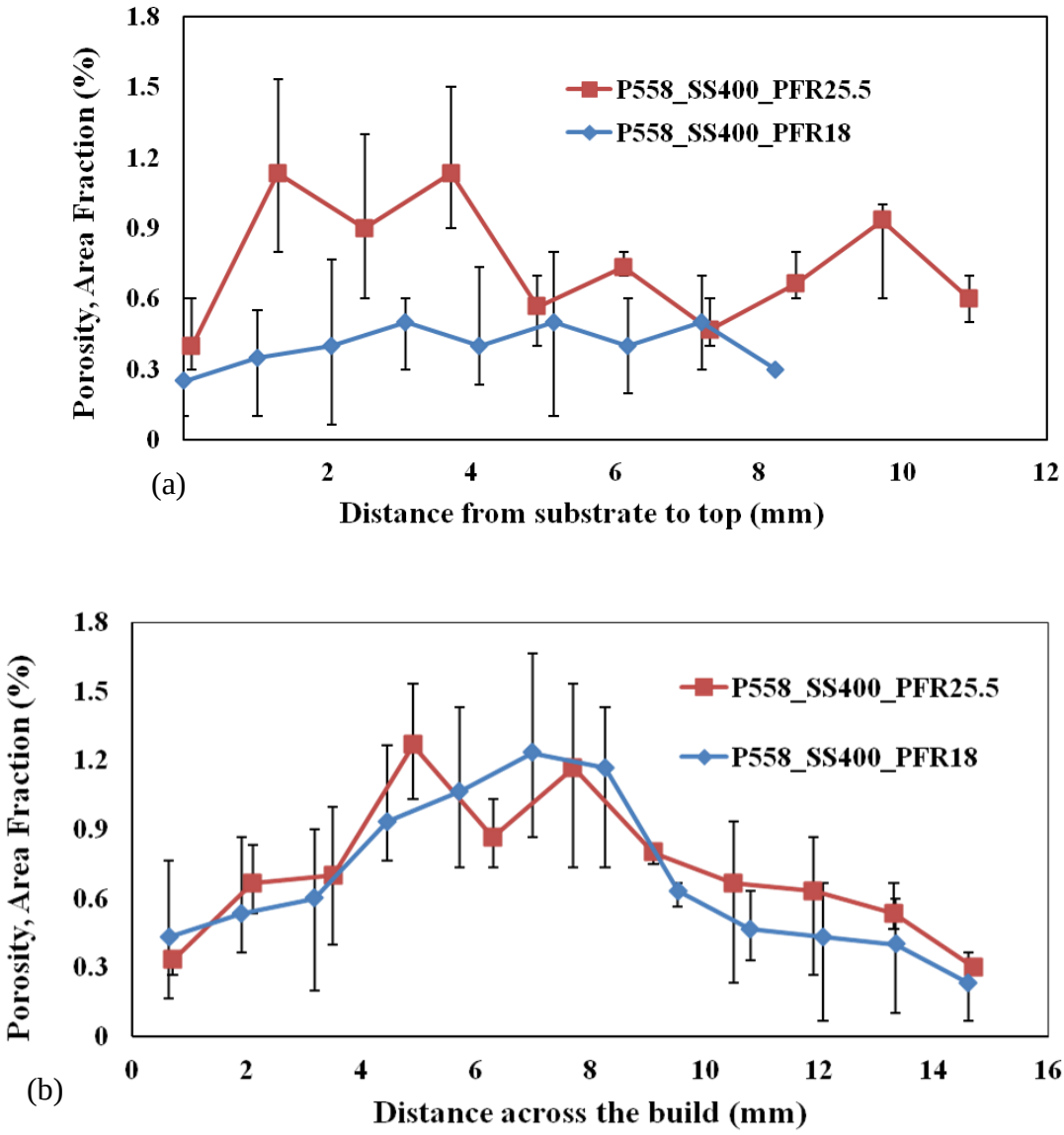

Figure 4-15: Spatial variation in porosity (a) along the height of the build (b) across the length/width of the build.

4.5 Summary

IN718 has shown excellent processability and does not display any crack susceptibility that is observed in other Ni-based superalloys. The study is focused on developing a process window for IN718 to obtain builds with minimum porosity and high geometrical accuracy. An empirical model was successfully developed based on the key process parameters (laser

power, scan speed and powder flow rate) to find the build geometry for a given set of process parameters, which was valid on thick wall samples (about 5 layers thick) as well. Although the same amount of energy density is supplied, the process conditions with could produce a fully consolidated thin walls and thick walls are not valid for solid blocks. This shows that for a given material the build integrity is highly dependent on the build geometry which in-turn determines the time allowed for the previous layer to cool down before the next layer is deposited. The statistical method employed for thin wall builds is no longer valid for thin wall builds as the porosity varies at different locations of the build for a given set of process parameters. So, a combination of process parameters with high laser power and low powder flow rates at the locations where there is larger heat suction (near the substrate) and with faster scan speeds and high powder flow rates at locations where a heat built-up is present would produce an overall sound build with less deposition time. The current study should be taken only as a guide line to choose the initial process conditions and in real life components with varying dimensions the process has to be tailored according to the thicknesses at various sections of the component and ideally an all-encompassing model should be developed to dynamically vary the processing parameters to best suit each slice of the deposit.

Chapter Five

5 Thermal and Thermo-Mechanical Modelling of DLF: Model and Validation

5.1 Introduction

It is important to know if there are any residual stresses present in the parts, especially when the parts are used in load bearing applications, to avoid premature failure in service. DLF components are prone to have residual stresses due to non uniform cooling rates associated in the process. As it is difficult to characterise the residual stresses in the part experimentally it is useful to predict the stresses via modelling. In the present chapter, three dimensional transient thermal and thermo-mechanical finite element models (FEM) of DLF are presented, to predict the thermal fields and residual stress development in the build, as well as in the substrate of thick-walled samples, as seen in stage II, simulating laser repair. Firstly, the thermal model was developed and validated with thermocouple measurements performed in the substrate. Later the thermo-mechanical model was developed based on the input parameters from the thermal model. After the stress distribution was achieved, various simulations were run, varying the deposition path and scan strategy in order to obtain the optimum scan strategy and deposition path that gives minimum residual stresses. The predicted residual stresses were validated using neutron diffraction results (residual stress characterisation). Although the model was primarily developed to understand the residual stress development in the build, the temperature distribution obtained from the model was useful in understanding the grain structure development that was observed experimentally in the builds (chapter 6). All the modelling work in the thesis was performed using a

commercial finite element code, ABAQUS 6.11 at PRISM^2 group cluster, at the University of Birmingham.

5.2 Modelling Strategy

Based on the literature survey (section 2.5.6), DLF builds are prone to residual stress formation due to the high temperatures up to melting and above, and the high cooling rates involved in the process. It is quite tedious and expensive to run several experimental trials for various process conditions and experimentally characterise the residual stresses. As such, a thermo-mechanical model would help in understanding the residual stress development in the build layer-by-layer, which is difficult to measure though an experimental route. The deposition process was modelled using "element birth technique" [166], where all the elements constituting the deposition are activated step-by-step (as explained in the literature review chapter). The process occurs in several steps; in the first step all the elements, which constitute the deposit, are deactivated to be activated in later stage of the analysis. As the analysis goes on, the deposition elements will be activated one by one, based on the deposition path employed. A heat flux is applied on the top of the element simulating the laser deposition process. Once the heat flux is applied for a certain amount of time, the heat flux is moved on to the next activated element.

The process of activating the elements one by one is a tedious process in ABAQUS as a step needs to be created during each element activation, and there are around 3500 elements for depositing a complete thick wall (Figure 3-3), which requires 3500 steps to be created. In order to avoid this, a user subroutine was implemented, where the input file for ABAQUS was generated through C++ programming. With this subroutine, the elements will be activated one by one automatically according to the chosen/prescribed deposition path chosen. This numerical technique increases the complexity of the model. However, there will

be no wastage of additional computational time for the elements that are not active during deposition.

Once the element is activated, the heat flux is applied on top of the element. Although the energy distribution in a cross section of the laser beam may differ, in practice two types of approximation are popular. The first is to assume that the laser beam profile is a uniform circular spot of radius R_s [149], the other more popular approximation is to use a Gaussian distribution of the intensity within the spot [150, 154, 160]. However, to simplify the model and to reduce the calculation time, the heat flux was applied uniformly on the top surface of each element in the present model. An accurate temperature profile of a laser beam is not considered here as the model is primarily developed to understand the residual stresses developed (macro-scale), rather than the microstructural developments, which is not in the scope of this study. Lindgren reported that the overall distortion and residual stress are sensitive to the total heat input, but are not very sensitive to the shape of the heat source [163].

5.3 Thermal and Thermo-Mechanical Model Set-up

5.3.1 Governing Equations

5.3.1.1 Thermal model equations:

Although there are large numbers of variables involved in DLF, heat transfer occurs by three main mechanisms; conduction, convection and radiation. In DLF, the sample absorbs energy from the laser source, and the energy is lost through melting the material, through conduction, convection and radiation. There will also be a heat gain through latent heat during solidification of the alloy, Figure 5-1. The simplest form of this can be given in the equation below[186]:

$$Q_{stored} = Q_{supplied} - Q_{conduction} - Q_{convection} - Q_{radiation} \pm Q_{Latent} \quad 5\text{-}1$$

where Q_{stored} is the stored energy in the material which can be written as

$$Q_{stored} = \rho C_p \upsilon_s \left(\frac{\partial T}{\partial t}\right) \quad 5\text{-}2$$

Where ρ is the density of the material (Kg/m^3), C_p is the specific heat of the material (J/kg. K), υ_s is the volume of the deposit sample (m^3), T is the temperature (K) and t is the time (s).

$Q_{supplied}$ is the laser power used as an input on the surface of the deposit, which is the laser power (P) multiplied by the efficiency (e) of the laser, and the absorption rate (γ), and attenuation of the laser by powder flow rate (β). The actual energy that goes into the melt-pool is considered as the efficiency of the laser process (η) in the thesis, which will be only a fraction of incident energy after all the losses.

$$Q_{supplied} = \eta . P, \text{ where} \qquad \eta = e.\gamma.\beta \quad 5\text{-}3$$

$Q_{conduction}$ is the energy lost via conduction, which can be written as

$$Q_{conduction} = \lambda \upsilon_s \nabla^2 T, \qquad \frac{\partial^2}{\partial x^2} + \frac{\partial^2}{\partial y^2} + \frac{\partial^2}{\partial z^2} = \nabla^2 \quad 5\text{-}4$$

where λ (W/m.K) is the thermal conductivity of the material. The convection and radiation can be written as

$$Q_{convection} = hA_0(T - T_\infty) \quad 5\text{-}5$$

and

$$Q_{radiation} = \varepsilon \sigma A_0 (T^4 - T_\infty^4) \quad 5\text{-}6$$

where h is the convection coefficient, A is the heat transfer surface area, T_∞ is the ambient temperature, ε is the emissivity of the material and σ is the Stefan-Boltzmann constant (5.67 × 10^{-8} $W/m^2.K^4$) and Q_{latent} is the latent heat of solidification.

From the above equations, Equation 5-1 can be written as

$$\rho c v_s \left(\frac{\partial T}{\partial t}\right) = \eta.\gamma.P - \lambda v_s \nabla^2 - hA_0(T - T_\infty) - \varepsilon\sigma A_0(T^4 - T_\infty^4) \pm Q_{latent} \qquad 5\text{-}7$$

The laser energy supplied is the heat flux on a certain surface area of the material, which is equivalent to the spot size (Γ). The supplied energy per element can therefore be written as $\frac{Q_{supplied}}{spot\ size}$ which is

$$Q_{flux} = {}^{\eta \times P}/_{\Gamma} \qquad 5\text{-}8$$

As the laser is applied only on the top surface of each element, the boundary condition for the top surface can be given as:

$$Q_{flux} = \lambda v_s \nabla^2 T + hA_0(T - T_\infty) + \varepsilon\sigma A_0(T^4 - T_\infty^4) \pm Q_{latent} \qquad 5\text{-}9$$

For all the other surfaces of the element, there will be only heat loss via conduction, convection and radiation which can be given as:

$$\lambda v_s \nabla^2 T + hA_0(T - T_\infty) + \varepsilon\sigma A_0(T^4 - T_\infty^4) = 0 \qquad 5\text{-}10$$

As the initial condition, the temperature is made equivalent to ambient temperature T_0 i.e.

$$T(x, y, z, 0) = T_0 \qquad 5\text{-}11$$

Equation 5-7 can be solved by using the above boundary conditions (Equation 5-9 to 5-11) to predict the temperature profile.

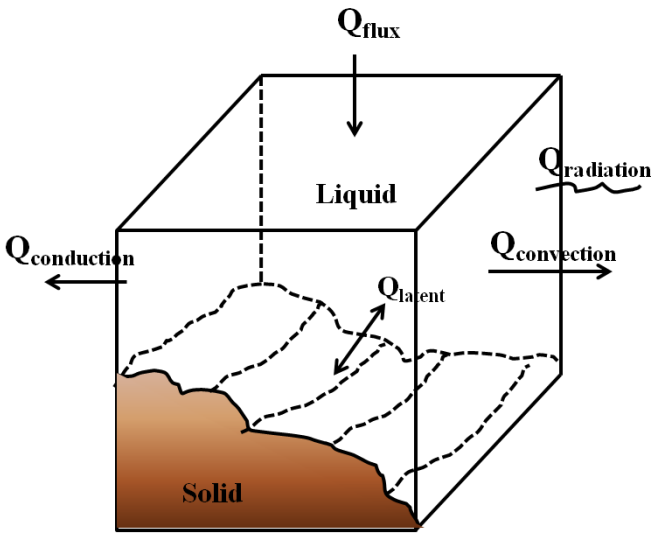

Figure 5-1: Schematic illustration of a melt-pool showing the heat input and losses.

5.3.1.2 Thermo-mechanical model equations

Materials expand or contract with temperature changes; therefore thermal strain depends on the present temperature and the initial temperature, which is independent of stress. The total strain ε_{total} in a body can be represented as:

$$\varepsilon_{total} = \varepsilon_e + \varepsilon_P + \varepsilon_T \qquad 5\text{-}12$$

where $\varepsilon_e,\ \varepsilon_P\ and\ \varepsilon_T$ are elastic, plastic and thermal strain respectively [187-188]. The elastic response by linear elasticity relationship can be given as

$$\{\sigma\} = D_e\{\varepsilon_e\} \qquad 5\text{-}13$$

where σ is the total stress tensor, ε_e is the elastic strain tensor and D_e is the elasticity tensor matrix, which is temperature-dependent. Isotropic yielding occurs when the stress increases to beyond the yield stress in all directions as plastic straining occurs. The yielding function can be written as

$$f(\sigma) = \sigma_0(\varepsilon_P, T) \qquad 5\text{-}14$$

Where $\sigma_0\ is$ the equivalent stress is ε_P is the plastic strain and T is the temperature. The thermal strain can be described as

$$\varepsilon_T = \alpha\ (T - T_0) \qquad 5\text{-}15$$

where α is the thermal expansion coefficient of the material.

The modelling work in this thesis is performed by ABAQUS using a coupled temperature-displacement method [187]. For the analysis of stresses in ABAQUS, a J_2-theory of plasticity is used with the specification of equivalent strain increments being determined by tabulated flow stress data (listed in Appendix B). The formulation and implementation of the plasticity models is out of the scope of this thesis and the theory behind the model can be found in the ABAQUS user manual (ABAQUS 6.11 theory manual section 4.3.1) as well as from [189-190]

5.3.2 Geometry, mesh, boundary conditions and simplifying assumptions

5.3.2.1 Thermal model:

The thermal model was developed and validated using the experimental thermal measurements on a thick walled substrate, shown in Figure 3-9. The thick walls of length 30mm (in X direction), width of 3.8 mm (in Y direction), and a total of 10 layers of size 0.3mm each were deposited on a substrate of size $32^X \times 4^Y \times 50^Z$ mm. The problem was treated as transient 3D model, and elements of type DC3D8 were used.

The sizes of the FEM meshes significantly influence the accuracy of the model, as well as the computational time; fine mesh would give accurate results, but would take a longer time for calculation. A balanced mesh was used in the current model, with finer mesh sizes near the build and coarse mesh away from the build. Figure 5-2 shows the mesh for the thick wall. The elements in the substrate were made coarse in the Z-direction (1 mm) to reduce the

computational time. However, the first 3 rows i.e., 1 mm of the substrate below the deposit were made finer (0.125, 0.375 and 0.5 mm) as the change in temperature is large in this region.

During the experimental deposition, there was an overlap of 30% between the adjacent passes, but to simplify the model this overlap was not considered. The width and height of each element in the build was determined by dividing the actual width and height of the build by the number of passes used in laser deposition, whereas the length of the element can be determined by measuring the cross section of the bead by optical microscopy. The average bead length was around 0.35 mm, which was used as the element length. The deposition was divided into 85 elements in the X-direction, 10 elements in the Y-direction and 10 elements in the Z-direction. A total of 8500 elements were used for the deposition. The substrate is held in position by a clamp (steel clamp of size 10 mm on each side), which was also included in the model and a thermal boundary condition is applied on the outermost face of the clamp, which was set to ambient temperature of 25°C.

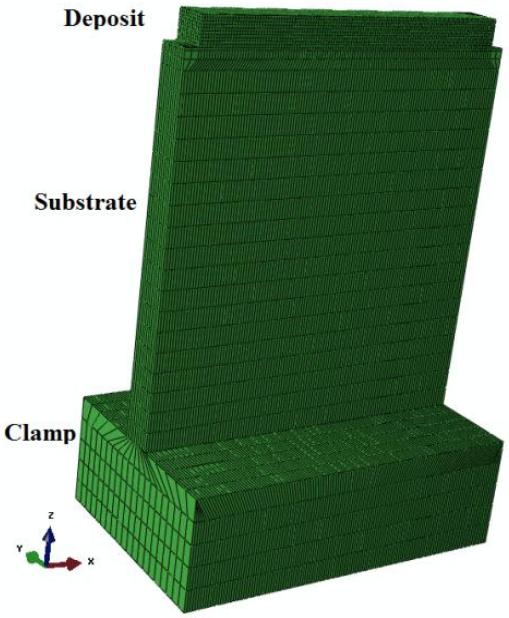

Figure 5-2: Meshing of the thermal model for a thick walled sample (stage II) showing the build, substrate and clamping.

For the model a long + short deposition path was employed as seen in Figure 3-3.b. Once an element was activated, a heat flux was applied on the top surface of the element for a time, dt. The time step (dt) was determined by the scan speed (400 mm/min) as shown below.

$$dt = \frac{element\ size\ in\ X\ direction}{scan\ speed} \quad 5\text{-}16$$

The heat flux is calculated as below as:

$$Q_{flux} = \frac{\eta \times P}{A} \quad 5\text{-}17$$

where, Q_{flux} is the heat flux and A is the top surface area of the element. A is obtained by multiplying the element size in X and Y directions. P is the laser power used in the deposition (390 Watts) and η is the efficiency of the laser process.

The total modelling process can be divided into the following steps:

Step 1: The temperature of all the elements in the substrate and deposit is taken as 25°C and all the elements in the deposit are deactivated.

Step 2: A pre-scan was employed, where a heat flux is applied in element-by-element on the top surface of the substrate. The heat flux was applied, based on the deposition path employed and the time step was calculated based on Equation 5-17. The heat losses would be through conduction for all the elements, the convection and radiation losses are from the outermost elements of the substrate. After the pre-scan, the substrate was made to cool down for 5s, the waiting time for the powder to run through the nozzles for deposition.

Step 3: The deposition starts in this step where each element was activated one by one based on the deposition path as in step 2. A Heat flux was induced on the top surface of the activated element for a time, dt, based on the scan speed. All the elements were activated till the deposition is complete.

Step 4: The part was allowed to cool down by conduction, convection and radiation to room temperature.

As all this process is made inside a glove box in Argon atmosphere, also with argon as a carrier gas (at the rate of 5.5l/min), it is difficult to model the convection losses associated with the process. The convection coefficients were previously determined by L.Qian [186] for the current system at UoB, while depositing Ti6Al4V walls. The values were determined to be ~25 W/m^2 K during deposition and ~5 W/m^2K during cooling. The convection coefficient values are higher during heating because of the forced convection by the Ar gas blown into the melt pool while carrying the powder as well as the Ar gas used in protecting the lens from powder spillage. For radiation losses, the emissivity of IN718 was taken from the literature as 0.4 [191].

The other factor, which is quite difficult to measure, is the efficiency of the laser itself. The fraction of the laser power supplied gets attenuated due to reflection (both by powder and substrate) and also by heating of the excess powder, which was not used in the actual deposit (only about 6% of the powder that is blown is used in the actual deposit due to the four nozzle assembly used in the present system, the value is higher for improved nozzle systems). Also, another factor that contributes to the reduction in the efficiency of the process is the absorptivity of the material (i.e., only a fraction of incident energy would absorbed by the material). From the experimental observation, it showed that the laser beam itself is 100 % efficient. The other two factors which cause the energy loss (power attenuation by powder and absorbtivity) are very difficult to measure or calibrate individually. Thus in this thesis, both these values are calibrated together and termed as the efficiency of the process (η).

The net heat input needs to be defined accurately as it has a significant influence on the temperature distribution. In order to determine the final heat flux after all the above losses, a

trial and error method was employed where the efficiency of the process was kept initially at 0.35, based on the average efficiency of the laser process found in the literature [111, 120-121, 150, 192], to calculate the temperature histories. This data was compared with the measured thermocouple data. The efficiency was adjusted until the temperature measurements match the predictions as closely as possible.

5.3.2.2 Thermo-Mechanical Model:

The stress model was developed on the thick walled samples of geometry given in Figure 5-3.a, which is slightly different from the temperature model. The thermo-mechanical model also uses 3D elements of type C3D8T and the modelling strategy and assumptions are the same as in the thermal model. Figure 5-3.b shows the mesh generated for the model, with the red dots showing the thermal boundary condition on the clamp (temperature of 25°C is applied at the end of the clamp). The mesh was made finer in the first 1 mm of the substrate to increase the accuracy of the results. Various simulations were run by varying the deposition path and scan strategy to understand their effect on residual stresses that are developed (Table 5-1). The efficiency of the laser obtained from the thermal model was used here, and the resulting residual stresses obtained by varying the deposition path and scan strategy were validated by neutron diffraction residual stress measurements.

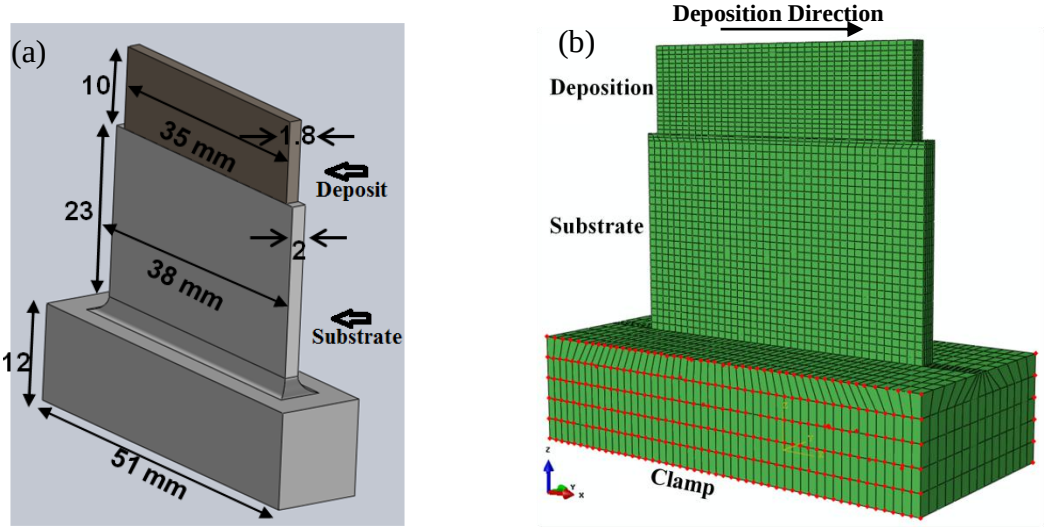

Figure 5-3: (a) Geometry of the thick walled deposits used for thermo-mechanical modelling, and (b) mesh of thick walled section, showing the clamped surface at the base (dotted in red).

Table 5-1: Deposition paths and scan strategies used in the simulations (laser power: 390W, scan speed 300 mm/min and powder flow rate of 18.46 g/min).

SNo.	Deposition path	Scan Strategy	Job_ID
1	Long	No delay	Test_L
2	Short	No delay	Test_S
3	Long+short	No delay	Test_M
4	Short	Delay of 50s	Test_SD
5	Short	Post scan after deposition	Test_SP

5.3.3 Model calibration for η and efforts for reduction in computational time

5.3.3.1 Temperature measurements

Temperature measurements were taken in the substrate at 5 different locations (Figure 3-9.a) using K-type thermocouples. Figure 5-4 shows the measured temperature profile of the substrate at 5 different locations during DLF. The temperature profile was taken on a mixed type of deposition path, where the deposition was made with altering layers of short and long

deposition path. The temperature reached during pre-scan was lower than that during the actual deposition, because the substrate is initially cold. However, when the first build layer was deposited, the heat input resulted in an increase in temperature. As the deposit progressed, the laser moved away from the substrate and from the thermocouple locations. Thus, a drop in the temperature was observed after the first layer of deposition. The maximum temperature, 1.5 mm below the deposit, is around 600°C. This peak temperature was obtained when the laser head was exactly above the thermocouple.

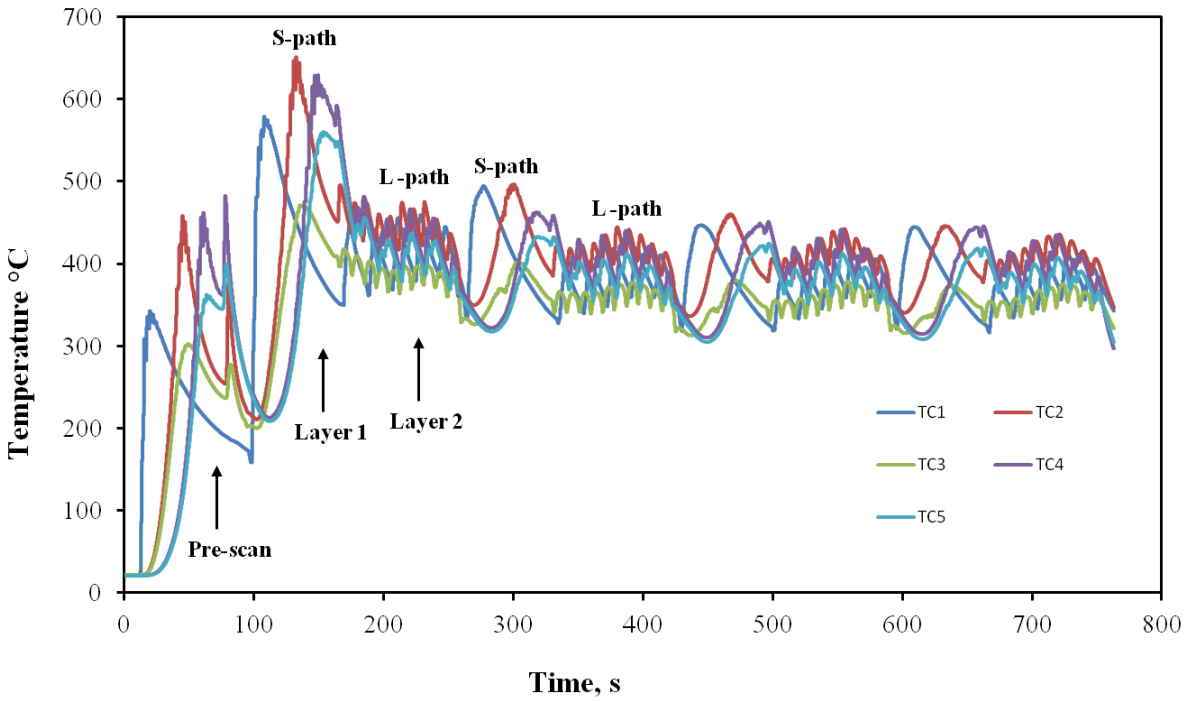

Figure 5-4: Temperature on the substrate at five different locations during DLF for deposition with a pre-scan and 8 layers (Laser power: 390W, scan speed: 400 mm/min, deposition path: short+ long).

5.3.3.2 Model Calibration

As noted above the efficiency of the laser is an unknown parameter. The simulation was run with initial efficiency of 0.35, based on the average efficiency of the laser deposition process, and then altered till the calculated values matched the experiential temperature readings.

Figure 5-5 shows the model temperature reading for the pre-scan with various efficiency values (short path). The thermocouple data matched well with the model data for an efficiency of 13%. The reasons for the very low value in the efficiency are the reflectivity issues in CO_2 laser and the large attenuation of laser power by the powder stream. Studies by Pyere *et al.* observed a value of 0.35 at various scan speeds, powder flow rates and laser powers for Nd: YAG deposited Ti–6Al–4V alloy whereas with a CO_2 laser the value was taken as 0.18 [186]. Studies by Liu *et al.* showed that the absorption decreased with the laser defocus reacting as low as 0.21 for a defocused CO_2 laser during DLF of IN718 [192]. The other important factor, which affects the efficiency of the laser, is the attenuation due to powder flow rate. In the current deposition, only 6 % of the powder that is blown in to the system went to the actual build. Work by Qi *et al.* suggested that by increasing the powder flow rate or the laser powder interaction distance (i.e., nozzle standoff distance), the attenuation of laser power increases [162]. The total attenuated laser powers were in the range of 7%–21% of the original laser power with a 6–12 g/min powder flow rate and a 7–10mm interaction distance. In summary there is a large power loss during laser material processing due to reflection and laser attenuation due to powder. Most of the DLF experiments suggest that the fraction of energy utilised, for any material, is only 10-20% of the energy supplied [186]. The efficiency of the process is found to be only 20-35% [10, 120, 145, 193] of that obtained when using a laser as a heat source for different materials and processing conditions. Higher efficiency factors of 60% [3, 194], and 80% [78, 151] were observed for the electron beam and electric arc beam heat sources, typically with a circular Gaussian heat distribution function.

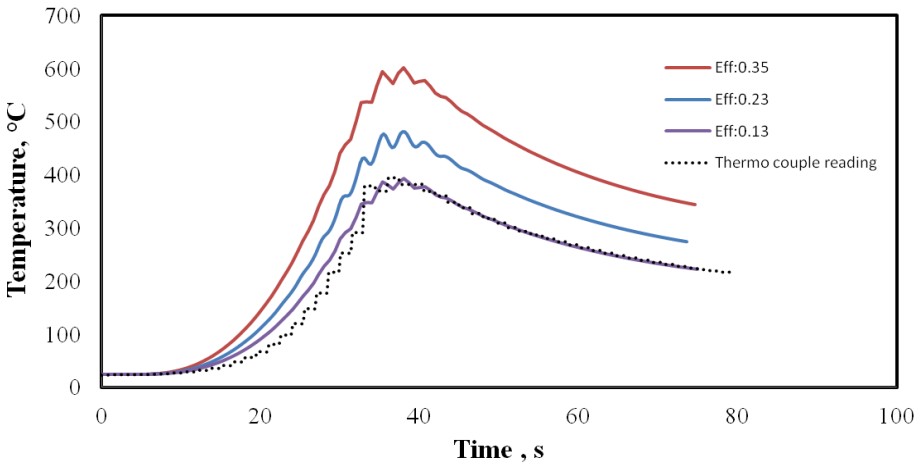

Figure 5-5: Thermal reading on location TC1 for simulation run with different efficiencies (dotted line showing the actual thermocouple data for pre-scan).

There are various input parameters and several assumptions in the model. Table shows the parameters that are inputted to the model

Table 5-2: Various input parameters used in the model

S.No	Parameter	Assumption/Literature/calibrated	Value
1	Thermal Conductivity (λ:W m^{-1} K^{-1})	Temperature dependent data taken from literature [195]	In Table 5-3
2	Specific heat capacity (C_p: $JK^{-1}Kg^{-1}$)	Temperature dependent data taken from literature [195]	In Table 5-3
3	Density (ρ :Kg/m^3)	Temperature dependent data taken from literature [195]	In Table 5-3
4	Latent heat during solidification (Q_{latent} : J/Kg)	From literature [195]	210 KJ/Kg
5	Stefan-Boltzmann constant	constant	5.67×10^{-8} $W/m^2.K^4$
6	Emissivity (ε)	Taken as constant from literature [191].	0.4
7	Convection coefficient (h: W/m^2)	Previously determined by L.Qian [186] for the current	during deposition: $25W/m^2$ K

		system at UoB, while depositing Ti6Al4V walls.	during laser switch off : $5W/m^2K$.
8	Ambient temperature (T_0)	Experimentally determined	25°C
9	Spot Size / heat transfer surface area (Γ: m^2).	Experimentally determined	35×10^{-5} m (in Y) × 60×10^{-5} m (in X i.e. along laser beam moving direction)
10	Layer height	Experimentally determined	30×10^{-5} m
11	Volume of the deposit (υ_s : m^3)	Experimentally determined by measuring the build volume	Spot Size × layer height
12	Stress, strain data at different strain rates and temperatures	Taken from Literature [196]	Graphs plotted in Appendix B
13	Laser power (P: $kg \cdot m^2/s^3$)	Experimentally determined	390W
14	Scan speed (S: m/min)	Experimentally determined	0.3 m/min
15	Time step (dt: s)	Determined by dividing the element size in the deposition direction with scan speed	variable
16	Efficiency of laser process (η)	Initially taken as 0.35 and calibrated with thermal measurements	0.13

5.3.3.3 Reduction in computational time

A simple thermal model as above needs 8500 elements to be activated (i.e., 8500 steps to complete a 10 layer deposit). By activating one element at a time, the models will take a vast amount of computational + CPU time. For example, a simple thermal model would take 32h (the time for coupled temperature-displacement was around 6 days for a layer) on a 4-processor system to do one layer of deposition. In order to reduce the computational time, the mesh was coarsened. Figure 5-6.a shows that, if the mesh size of the substrate was doubled, the temperature prediction drops by 100°C at 1 mm below the deposit, without a significant decrease in computational time (the computational time is reduced to 20h instead of 32h). Another approach is to activate multiple elements at a time, which showed a little effect on

the temperatures predicted (Figure 5-6.b). The computational time was reduced by 4 folds with activation of 4 elements at a time, instead of 1 element (i.e., the CPU time was 8h for depositing one layer compared to 32h while activating one element at a time), showing that multiple element activation is a good approach to reduce the computational time of the model.

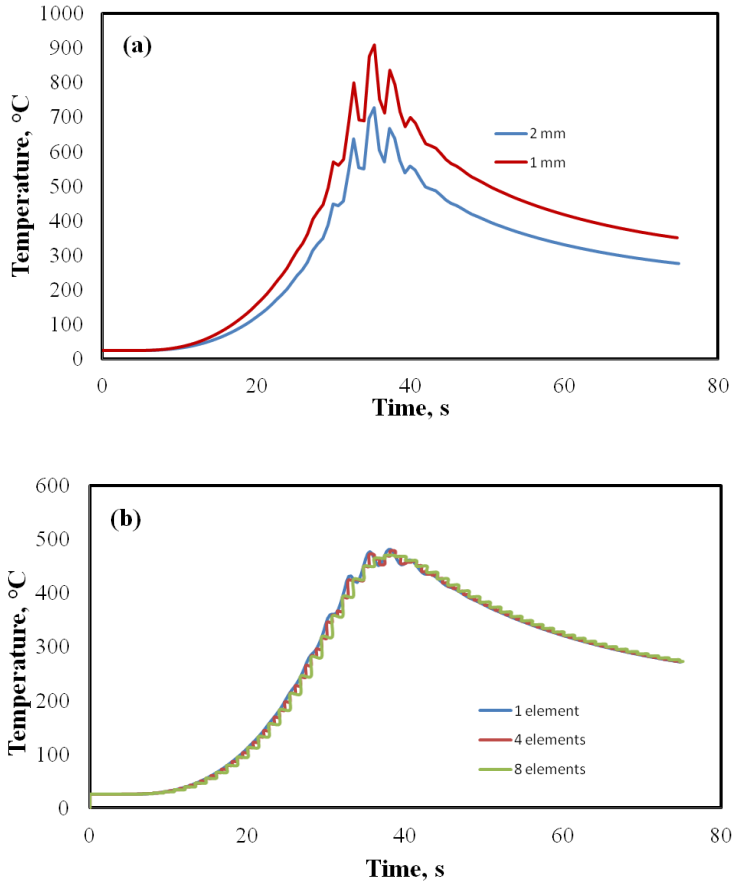

Figure 5-6: Element and mesh optimisation, showing (a) the variation in temperature with mesh size (temperature taken at 1 mm below the deposit) and the (b) variation in temperature with multiple element activation (temperature taken at 3 mm below deposit).

5.3.4 Material Properties

The temperature-dependent thermal and mechanical properties of IN718 were used in this model. The thermo-physical properties were taken from the literature [195] and are tabulated in Table 5-3. The latent heat of fusion was taken as 210 KJ/Kg [195].

Table 5-3: Temperature dependent density, heat capacity an thermal conductivity of IN718 (* melting range) [195].

Temperature (°C)	Density (kgm^{-3})	Heat Capacity (C_p: $JK^{-1}Kg^{-1}$)	Thermal Conductivity (λ: $W\,m^{-1}\,K^{-1}$)
25	8190	435	8.9
100	8160	455	10.8
200	8118	479	12.9
300	8079	497	15.2
400	8040	515	17.4
500	8001	527	18.7
600	7962	558	20.8
700	7925	568	21.9
800	7884	680	26.9
900	7845	640	25.8
1000	7806	620	26.7
1100	7767	640	28.3
1170*	7727	650	29.3
1336*	7400	720	29.6
1400	7340	720	29.6
1500	7250	720	29.6
1600	7160	0.72	29.6

Temperature-dependent mechanical properties were also required to analyse the stresses during deposition and this data was also taken from literature [196]. The yield stress is the key mechanical property in DLF, as it has a significant effect on the residual stresses and distortions [137]. Thus, accurate temperature-dependent yield stress data must be used for the model. The thermal expansion coefficient of the material with temperature and the stress-stain curves at different strain rates and temperatures were taken from the experimental and modelling results from the work by Grant [196]. The plots of these values are shown in Appendix B.

5.4 Thermal and Thermo-Mechanical Analysis and Validation

5.4.1 Thermal Predictions

The thermal data for the model matched well with the experimental values at all the thermocouple locations for multiple element activation, even though the efficiency was calibrated at one thermocouple location, using singe element activation model. Figure 5-7.a shows the fitted and measured temperatures at different thermocouple location on the substrate (Figure 3-9.a) during pre-scan. Figure 5-7.b shows the temperature reading for thermocouple No.5, during pre-scan +6 layers of deposition, which fitted well with the experimental data.

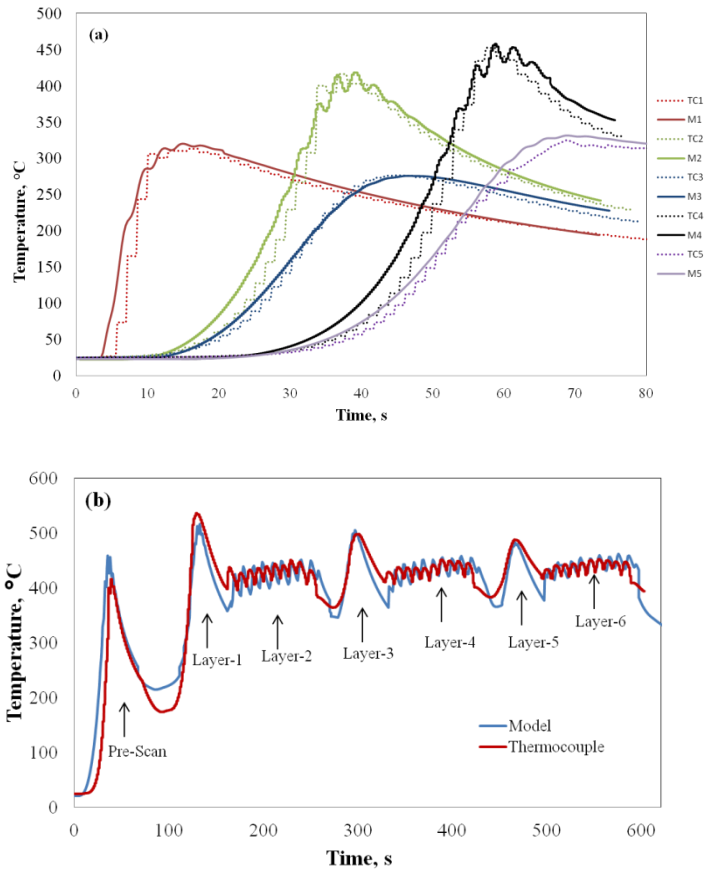

Figure 5-7: Comparison of thermocouple and predicted data. (a) At all the 5 thermocouple locations (TC) for pre-scan and (b) at location TC5 showing pre-scan+6 layers.

5.4.2 Thermo-Mechanical Model

The elasto-plastic model was developed to understand the residual stress development in the deposit as well as in the substrate during DLF, which will be useful for repair applications. Several models were run, varying the deposition path and strategy to understand their effects on the residual stress development, as well as to obtain a parameter that gives minimum residual stresses. Finally, the models were validated with experimental residual stress measurements using neutron diffraction.

5.4.3 Results and Validation

Figure 5-8 shows the Von Mises residual stress distribution in the build and the substrate after deposition and cooling down to room temperature. From the figure, it is evident that the maximum stress is concentrated at the bottom of the substrate (bold arrows pointing towards bottom edges). The reason for this high stress concentration is due to sharp change in the geometry at the corner, where fine mesh size is required to predict the correct stresses. However, refining the mesh size at that location was a bit difficult for the method employed in generating the mesh in this thesis (C++ program to generate the mesh). However, the high amount of stress in this location may be ignored as the residual stresses measured experimentally showed that the effect of deposit would be there at the vicinity of 10 mm from the deposit. However, in the future a better method may be employed for generating the mesh and refining the places where a steep change in cross sections are present.

Other than this, the residual stresses were mainly concentrated at the build-substrate interface region (area shown in dotted arrows), where the stress was more concentrated at the corners of the interface. The predicted stress at the deposit substrate region was around 260 MPa, with a maximum at the corners of ~310 MPa. The stress is also concentrated on top of the build region, ~ 1 mm below the free end of the deposit at around 200 MPa.

DLF is similar to multi-pass welding, where each layer gets re-heated by the previous layer and the resultant stresses are mainly due to the high cooling rates associated with the weld bead and due to the repeated heating cycles (heating, cooling and reheating). These variations in cooling and heating cycles, at different locations of the build, cause unequal balance of elastic and plastic flow in the material which results in residual stresses[137].

Figure 5-9 shows the temperature distribution at various layers of deposition, with the top portion of Figure 5-9 showing an enlarged view of the melt-pool. During pre-scan, the maximum temperature reached by the substrate was around 1300°C, just about the melting point of the alloy. The low temperature in this region was due to the initial cold substrate which acts as a heat sink. As the deposition progresses, the maximum temperature reached by the build increases. The maximum temperature reached by the deposit was ~ 1808, 1929 and 2000°C for 1^{st}, 4^{th} and 14^{th} layers, respectively. As the deposition progresses, and moves away from the cold substrate, heat build-up or accumulation of temperature was observed. After a few more layers, the heat accumulation in the build saturates and the melt-pool temperature almost remains constant at 2000°C (seen in 14^{th} and 19^{th} layers of the deposit).

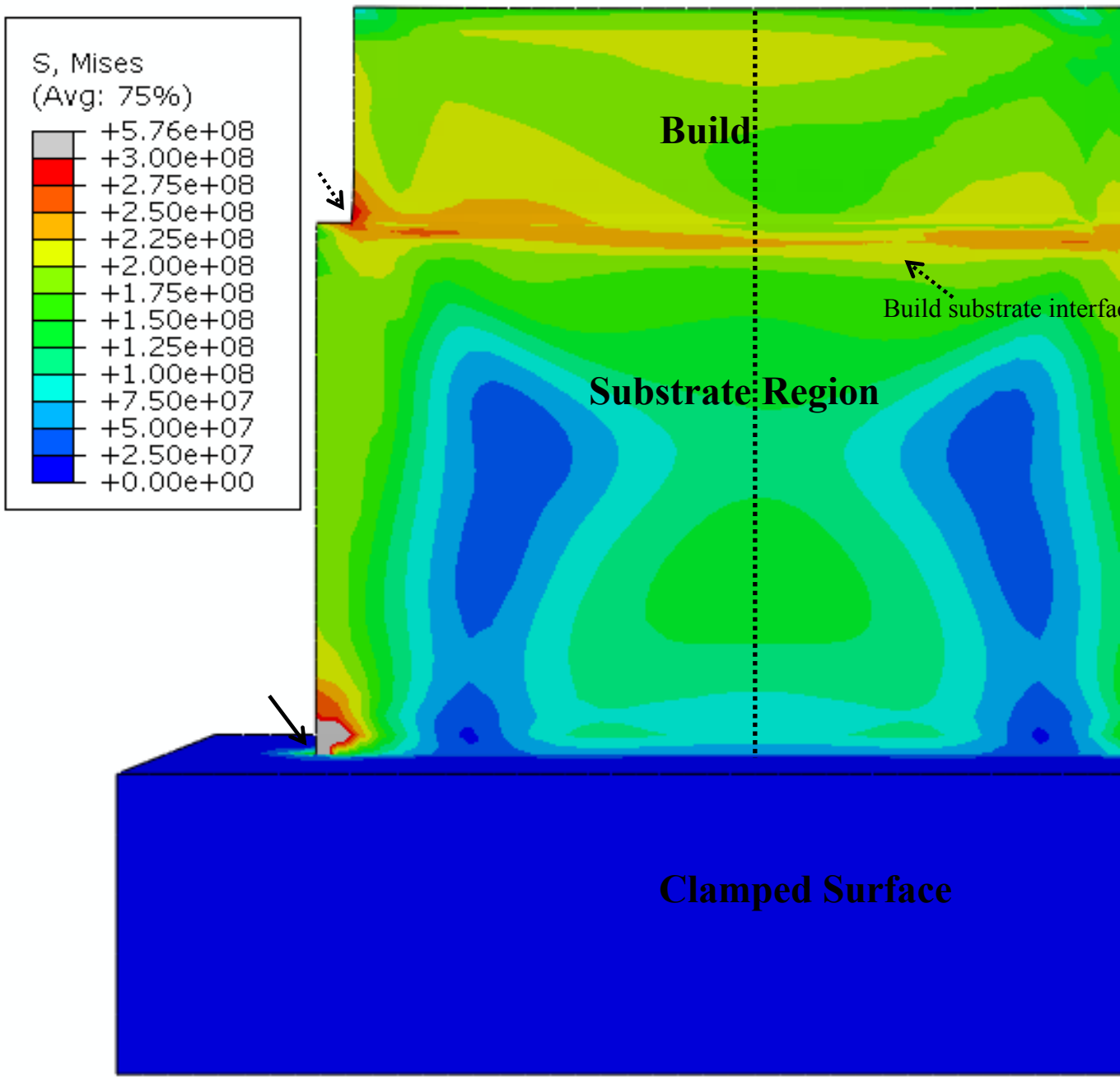

Figure 5-8: FEA model showing the Von Mises stress distribution in the build due to DLF in the short deposition direction with process parameters of laser power: 390W, scan speed 300 mm/min and powder flow rate of 18.46 g/min.

During the deposition of the first layer of the build, the temperature reached by the layer below was less than the melting point of the alloy, showing that during deposition of the first layer, there is no complete re-melting of the previous layer (substrate in this case). As the deposit progresses, in the 4th layer, the layer below i.e., the 3rd layer is partially melted where

the top portion of this layer reaches the melting point of the alloy. In the 14th and 19th layers complete melting of the previous layer was observed. From the figures, it is also seen that the edges of the deposit reached a higher temperature than the centre of the deposit, as the edges of the build, where the laser head turns results in higher temperatures because of the increased dwell-time.

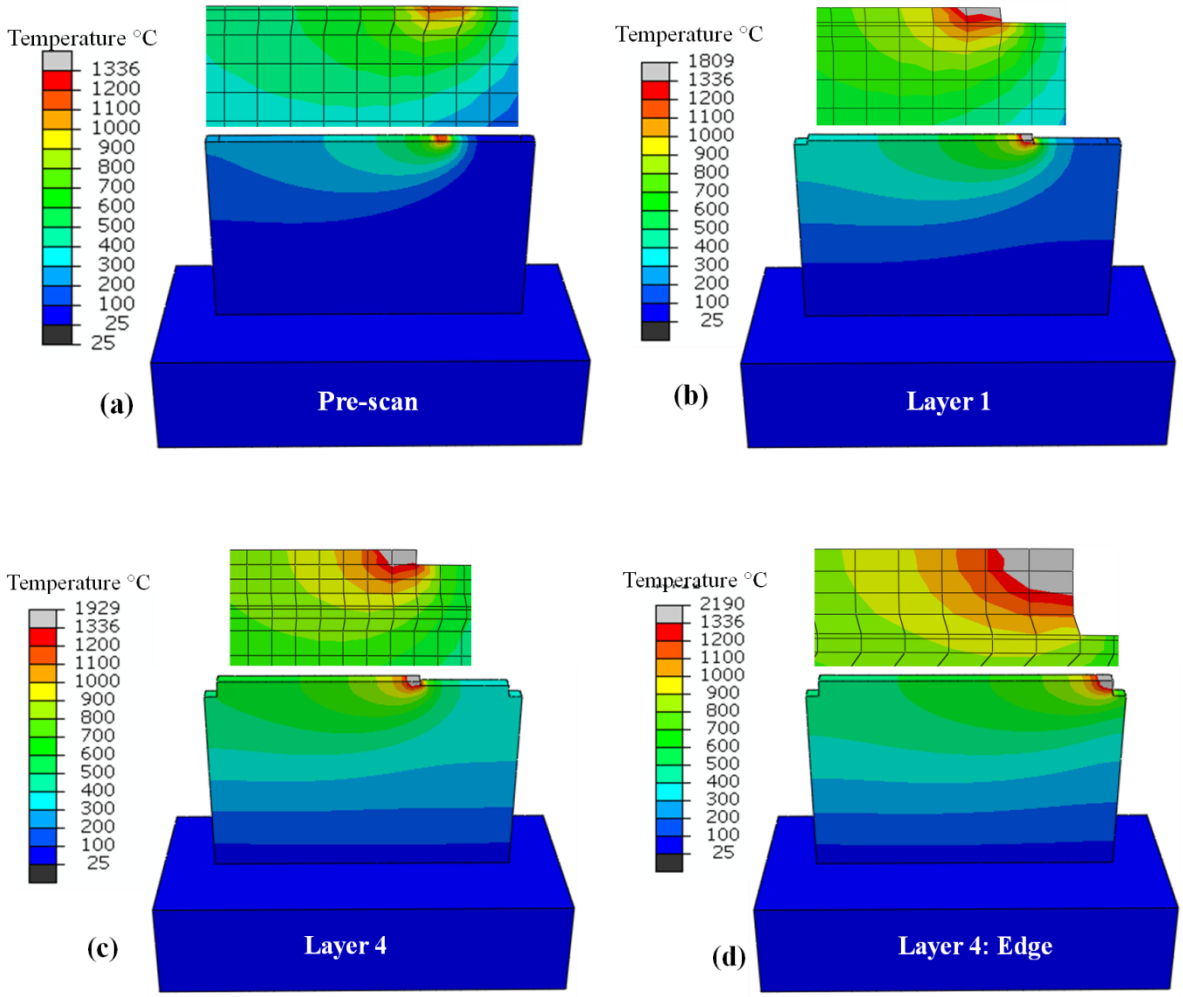

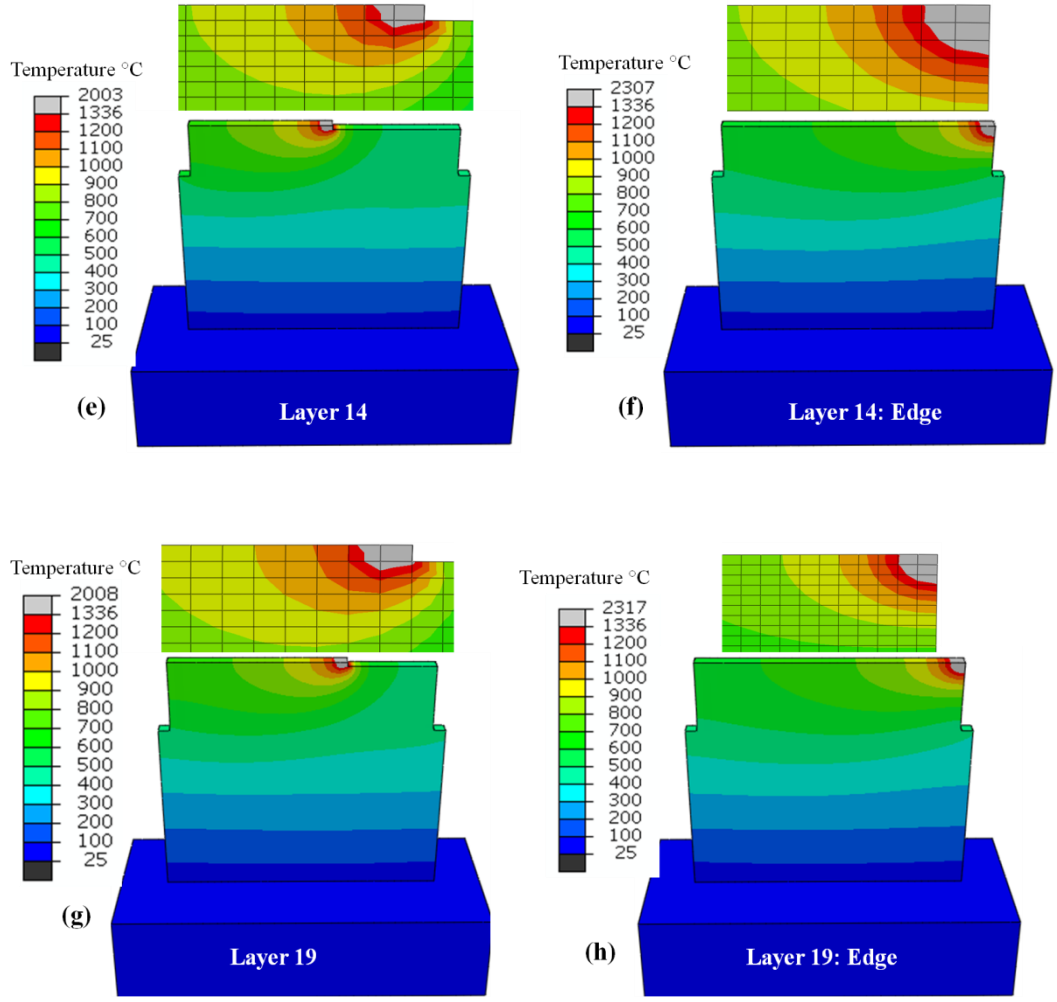

Figure 5-9: Model results showing the temperature distribution at various layers of deposition during DLF with process parameters of laser power: 390W, scan speed 300 mm/min, powder flow rate of 18.46 g/min, and short deposition path (a) during pre-scan (b) 1st layer (c-d) 4th layer with beam in the middle and edge (e-f) 14th layer when the beam is in the middle and edge (g-h) 19th layer when the beam is in the middle and edge (The upper figures show the enlarged view of the bead, grey area showing the temperature which is above the melting point of IN718 of 1336°C).

Due to the moving heat source, the temperature gradient has two components; one is along the deposition/melt-pool moving direction, and the other is along the build direction i.e., the direction normal to the melt-pool/parallel to the deposit growth direction. In order to understand the residual stress due to these two thermal gradient components the stresses are plotted in three components representing the three directions in Figure 5-10. The three components are:

S11: Stresses in the longitudinal direction/direction of the moving melt pool (X-direction, σ_x).

S22: Stress in normal direction/through thickness direction (Y-direction, σ_y).

S33: Stress in the transverse direction/ direction along the deposit growth (Z-direction, σ_z).

The above representation was used in all the models and the direction of these stresses is marked in arrows as shown in Figure 5-10. From the figure, it is evident that the σ_x is the dominant stress of the three stress components, which is due the high cooling rates in the direction of movement of the melt-pool. The variation in the cooling rates at different directions of the melt-pool leads to anisotropic shrinkage, as well as less restraint to shrinkage in the S33 direction, compared to S11 direction leads to higher σ_x when compared to S33. The stresses in the Y-direction are minimum or negligible (around 20-30 MPa) due to the limited material restrain in the through-thickness direction.

Figure 5-10.a shows the stress distribution in the build in the S11 direction. The FE model shows that the top portion of the build has a concentration of tensile residual stresses (~200 MPa), just below the free surface. The tensile stresses show an approximate parabolic profile, and the stresses on the upper most portion of the deposit are very low due to the stress balance effect on a free surface[24]. For any component, if there is a concentration of tensile residual stresses in the part, there will be a compressive stress somewhere in the part to compensate these tensile stresses. In this case, the compressive stress (~-180 MPa) is concentrated in the substrate just below the deposit-substrate interface.

Figure 5-10.c show the stress distribution in the deposit direction (Z-direction). In this direction, the stresses are compressive at the middle with compensating tensile stresses at the edges. In the build, the compressive stresses are concentrated near the build-substrate interface (~-80 MPa) and the stress on the top of the deposit is zero. In the substrate

compressive stress is observed at the centre (~-140 MPa), with compensating tensile stresses at the edges (~ 200 MPa). The clamps in the bottom of the substrate act as a dominant heat sink in the Z-direction. Conduction is the dominant factor in cooling, resulting in shrinkage of the material, compared to convection and radiation. After the deposition is complete, and the laser beam is switched off, the material starts to cool down, causing large shrinkage in the free edges of the deposit, which has less surrounding material than the centre of the deposit. The shrinkage is larger in the centre than at the edges, generating tensile stresses in the edge and compression in the centre.

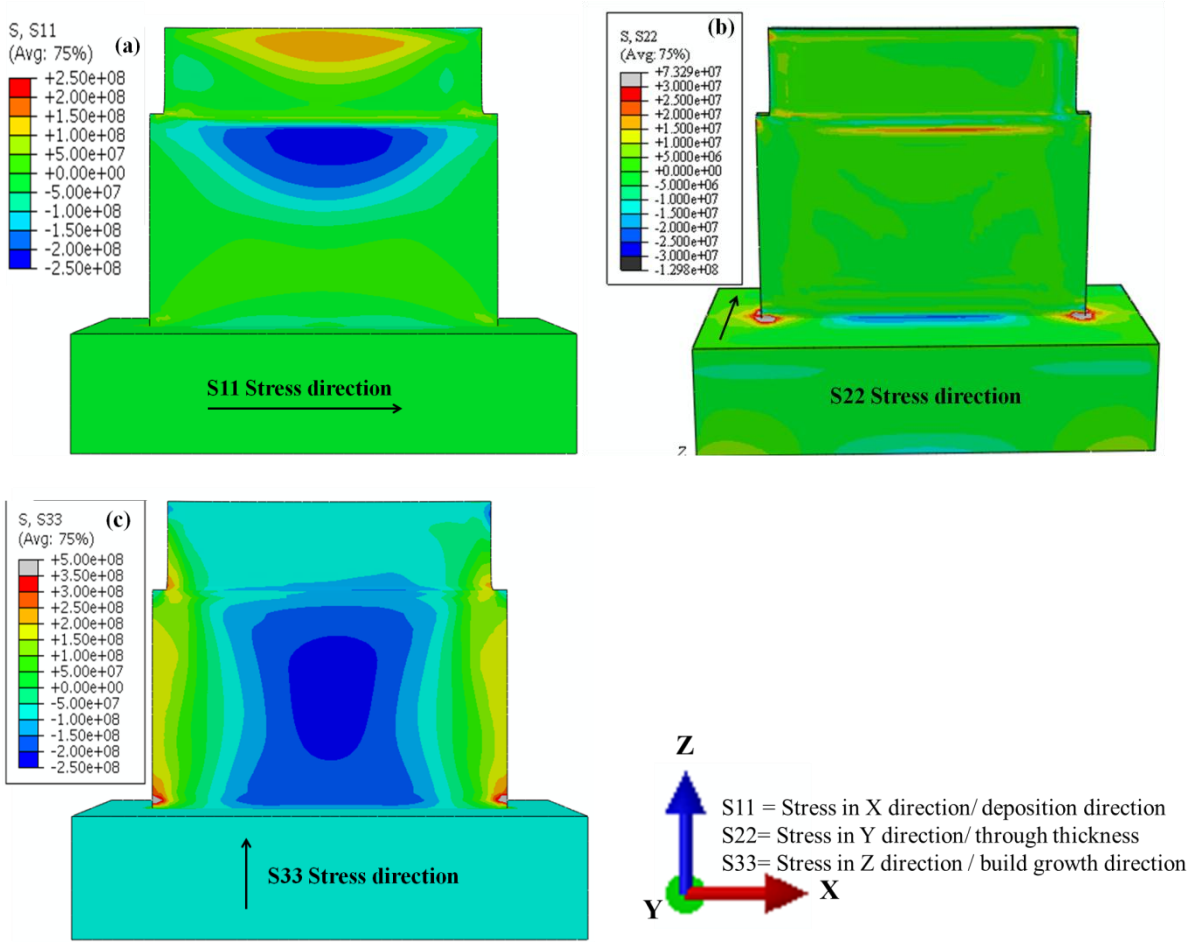

Figure 5-10: FEA model results, showing the residual stresses in the three different directions of the deposit. (a) S11 (b) S22 (c) S33 (The process parameters are: laser power of 390W, scan speed 300 mm/min, powder flow rate of 18.46 g/min and short deposition path).

5.4.3.1 Validation:

Although the model is calibrated and validated by thermal results, to test the capability of the model the predicted residual stresses are also validated. In order to validate the residual stresses in the model, the stresses were compared with neutron diffraction experiments. Residual stresses were characterised at various locations of the deposit along the length (dotted line Figure 5-8). An effective diffracting gauge volume of $0.5mm^X \times 0.5mm^Y \times 0.6mm^Z$ was used for the measurement, using a monochromatic beam of wavelength 1.64 A° using the γ{311} Bragg reflection. The γ-Nickel peak at ~98° was measured in the three principal directions. To calculate the residual stresses from the lattice strains, a Young's modulus of 205 GPa and a Poisson's ratio of 0.284 were used [24]. The strain free d-spacing is an important factor in characterising the residual stresses in the material. However, it will be inaccurate to use a d^0 value taken from one particular strain-free location in the substrate or the deposit, as they have different microstructures due to different cooling rates in the manufacturing routes employed. As we have seen from the model that the stress in the through thickness direction is almost negligible (~ 20 MPa max and zero in almost all the locations), a stress balance method was employed in characterising the residual stresses where the stresses in the through thickness direction is assumed to be zero and the d^0 values are back calculated. That resultant d^0 values were used to calculate the stresses in the X and Z-directions. This method was successfully employed previously in characterising the residual stresses in laser fabricated waspaloy by Moat *et al.* [25].

Figure 5-11 shows the FE predictions which show a similar trend to the experimental results in both the X and Z directions in the build region. However, the experimentally measured compressive stress at the interface in the deposit side were slightly higher (~ 50 MPa), than the model's prediction and are lower in the substrate side (~50 MPa). This variation could be because of two factors. As neutron diffraction uses a gauge volume of $0.5 \times 0.5 \times 0.6\ mm^3$,

the stresses get averaged out across this region, giving a lower value than the actual. The second reason for this difference is the use of the stress balance method where the stress in the Y direction is assumed to be zero. However, there is a tri-axial state of stress in this region and the stress in the Z direction in the model shows around 30 MPa, rather than zero as assumed.

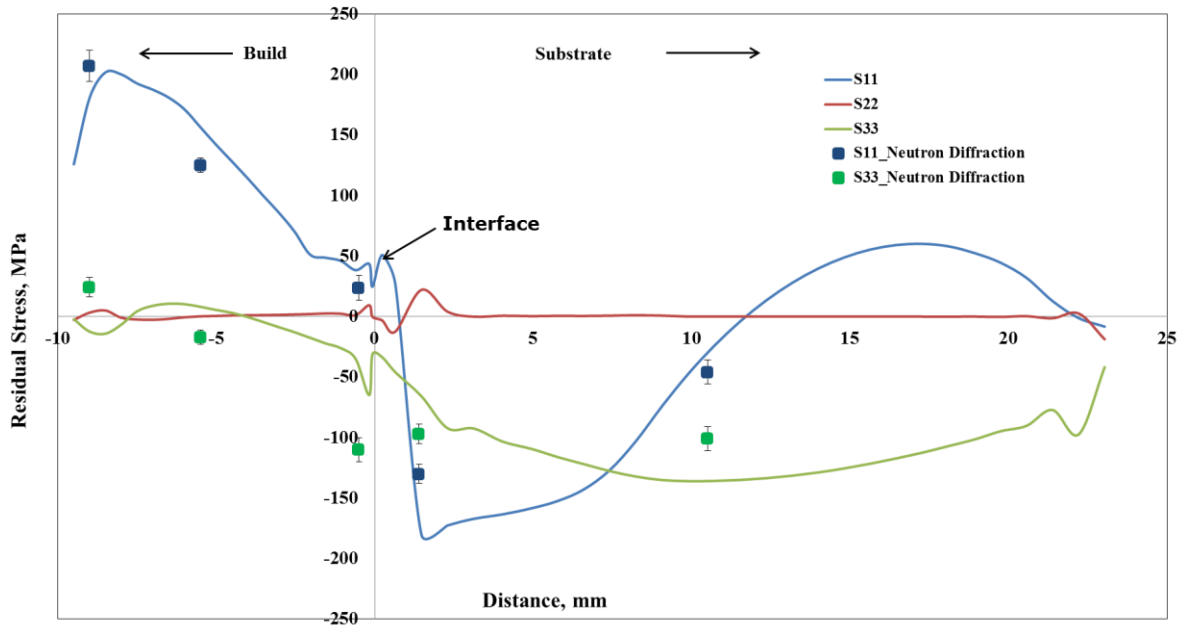

Figure 5-11: Residual stresses in all the three directions plotted across the deposit (along the dotted lines in Figure 5-8). The points represent the stresses characterised by neutron diffraction experiments.

5.4.4 Discussion

From Figure 5-11, it is evident that the maximum stress is in the X direction (S11) with tensile stresses in the deposit and compressive stresses in the substrate. The tensile stress in the deposit is a maximum at the top of the deposit (200 MPa) and gradually decreases towards the bottom of the deposit, to almost zero (20 MPa). In the substrate region the S11 stresses are slightly tensile (50 MPa) at the deposit substrate interface region with the stresses dropping steeply to compressive (-180 MPa) within 1.5 mm of the substrate.

When a laser beam hits the substrate, it would cause a melt pool and the material would start to expand locally due to the heat input. Due to this thermal expansion, the cold material ahead and below the laser beam experiences a compressive force resulting in compressive stresses ahead and below the laser beam position. This is represented schematically in Figure 5-12 based on the explanation given by Eshelby [197].

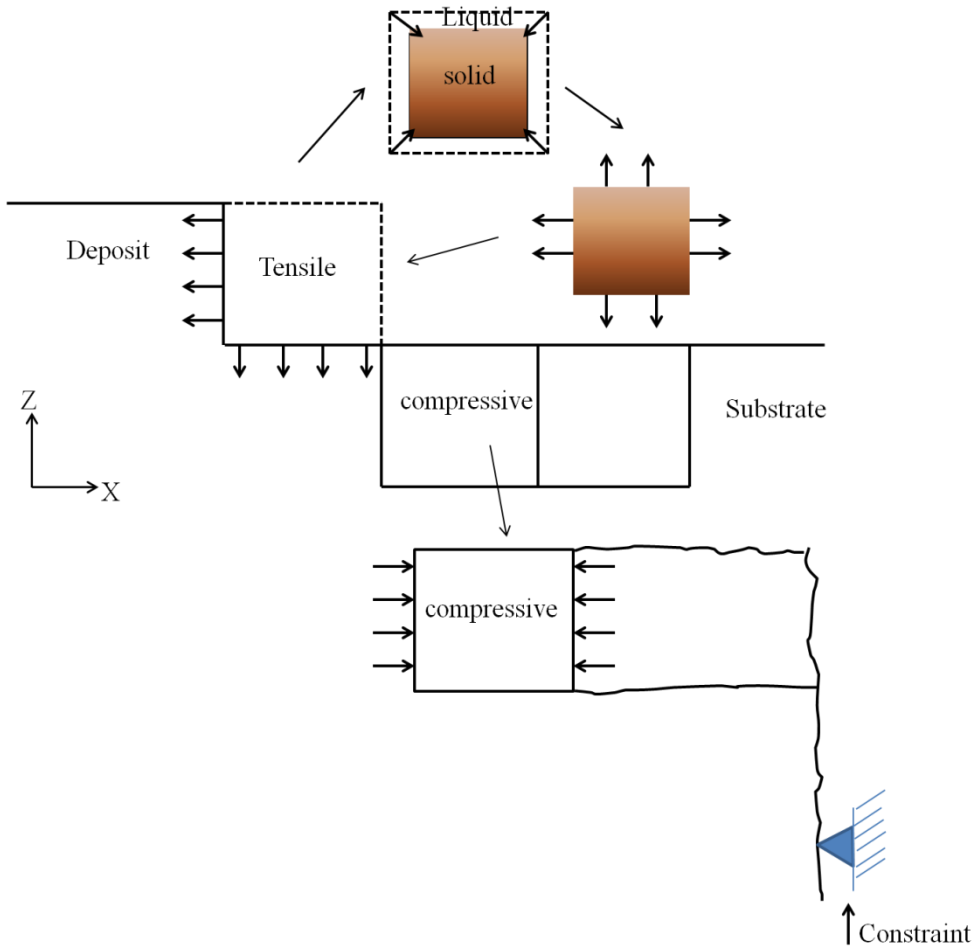

Figure 5-12: Schematic diagram showing the tensile and compressive stresses generated near a melt-pool.

In order to understand the residual stress development during deposition, the predicted stress distribution was shown at different stages of the deposit in Figure 5-13. From Figure 5-13.a, it is evident that within the fusion zone no stresses are generated. This is because at such high temperature near the melting point of the material, it will show little or no resistance to

deformation. When the laser heat source moves away from that position the material cools down and contracts, which will be restrained by the surrounding material, putting the material in tension.

Figure 5-13.b shows the stress distribution after 1 layer of deposition. We can see that the build region has a tensile stress due to rapid cooling. The stresses are mainly concentrated in the centre of the build, rather than in the edges as the free edges can expand without any constraint. To balance these stresses, compressive stresses are formed on the substrate with a similar shape distribution. When the next layer is laid on top of the first layer, the stresses would relax due to the heating cycle, but due to the cooling cycle after deposition the stresses would re-appear. As the deposition progresses, the region which is under the tensile stress moves away from the substrate (Figure 5-13.b - e). Figure 5-14 shows the variation of stresses as the deposition progresses. During the pre-scan, the top portion of the substrate has a high tensile stress of 471 MPa and the compensating compressive stress of -190 MPa at 3.25 mm below. In the first layer the tensile stress value is around 480 MPa and the compressive stress -230 MPa. As the deposition progresses it is observed that the maximum tensile stress value is still at the top of the deposit however the value of this stress is reduced to 450, 400, 360, and 330 MPa for the 2^{nd}, 3^{rd}, 5^{th} and 9^{th} layers respectively. The corresponding compressive stresses are -242, -257, -283 and -314 MPa. After the 5^{th} layer of deposition, not much change is observed in the maximum stress value.

The stress distribution can be explained with the temperature distribution in Figure 5-9, where during the deposition of the first layer, the substrate is at room temperature so the melt pool would cool very quickly and this quick shrinkage restrained by the solid material at the bottom giving rise to high stress state. As the deposition progresses the layers below the deposit are also hot and would allow expansion of the deposit and after 5 layers of deposition

the effect of the cold substrate diminishes and the deposit temperature reaches a steady state and variation in the maximum tensile stress is not seen after 5 layers of deposition.

After deposition the stresses relax where the maximum tensile stress of the deposit gets reduced from 295 MPa to 175 MPa, as the material cools down to room temperature. For any material the stress consists of two components; the elastic part and plastic part. When the laser beam is switched off, the material cools down. The elastic portion of the stress disappears in the regions which are able to expand freely.

The tensile stresses are parabolic in shape in the top of the build. This is because the material is allowed to expand freely in the edges due to the limited constraint and thus have low residual stress values and as we move inside the deposit the surrounding material constraints make it difficult for the material to contract freely and an increase in stress is observed in these regions showing a parabolic stress distribution. A similar kind of stress distribution has been previously observed by Moat *et al.* in DLFed 5 mm thick Waspaloy builds using a pulsed diode laser with an input energy density of 10.5 J/mm^2 and a travel speed of 10.5 mm/s, where the stresses were characterised using the Contour Method [25].

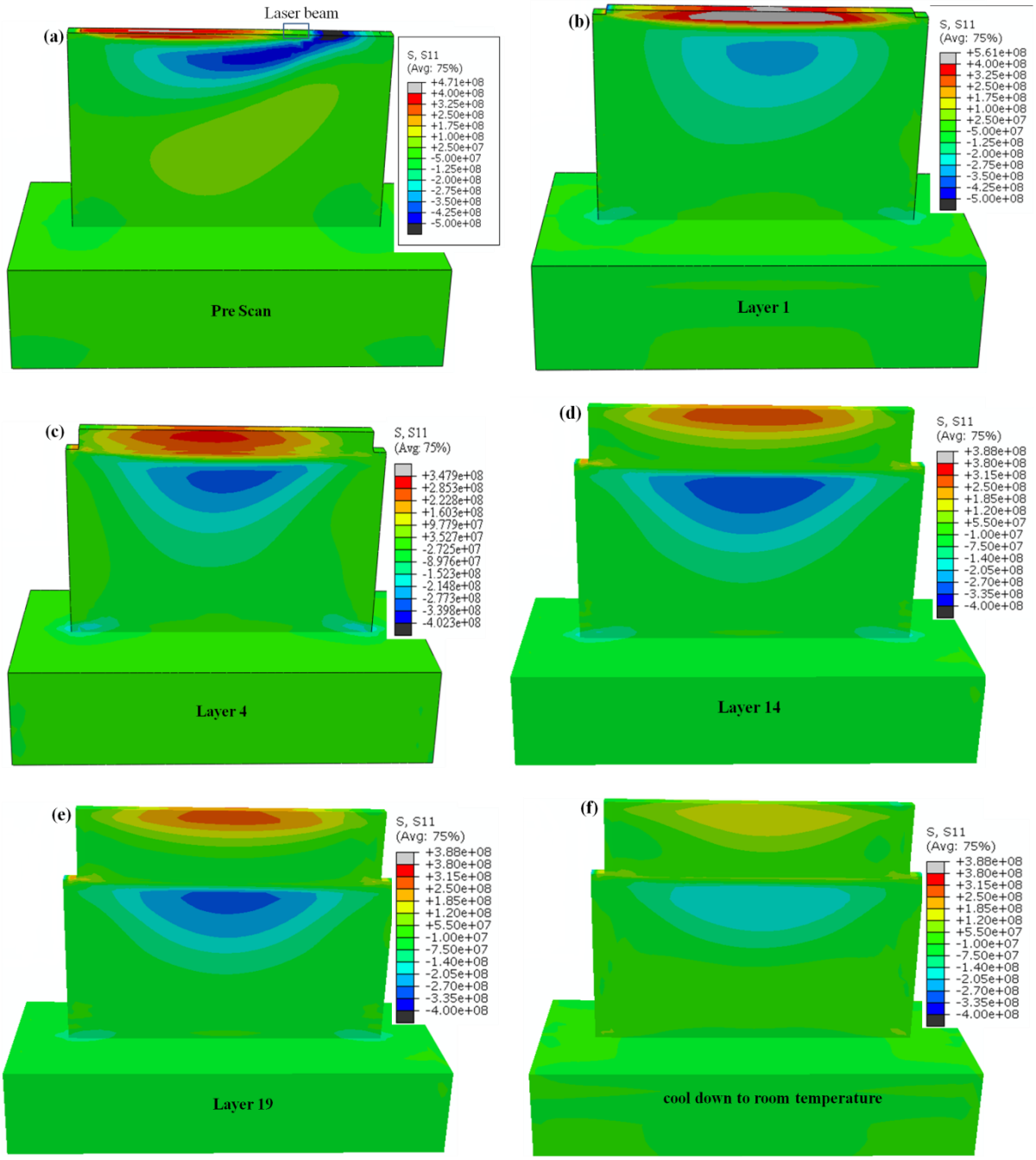

Figure 5-13: Stress in S11 direction during deposition of (a)pre-scan (b)1st layer (c)4th layer (d)14th layer (e)19th layer (f) after cooling down to room temperature.(The process parameters are: laser power of 390W, scan speed 300mm/min, powder flow rate of 18.46 g/min and short deposition path).

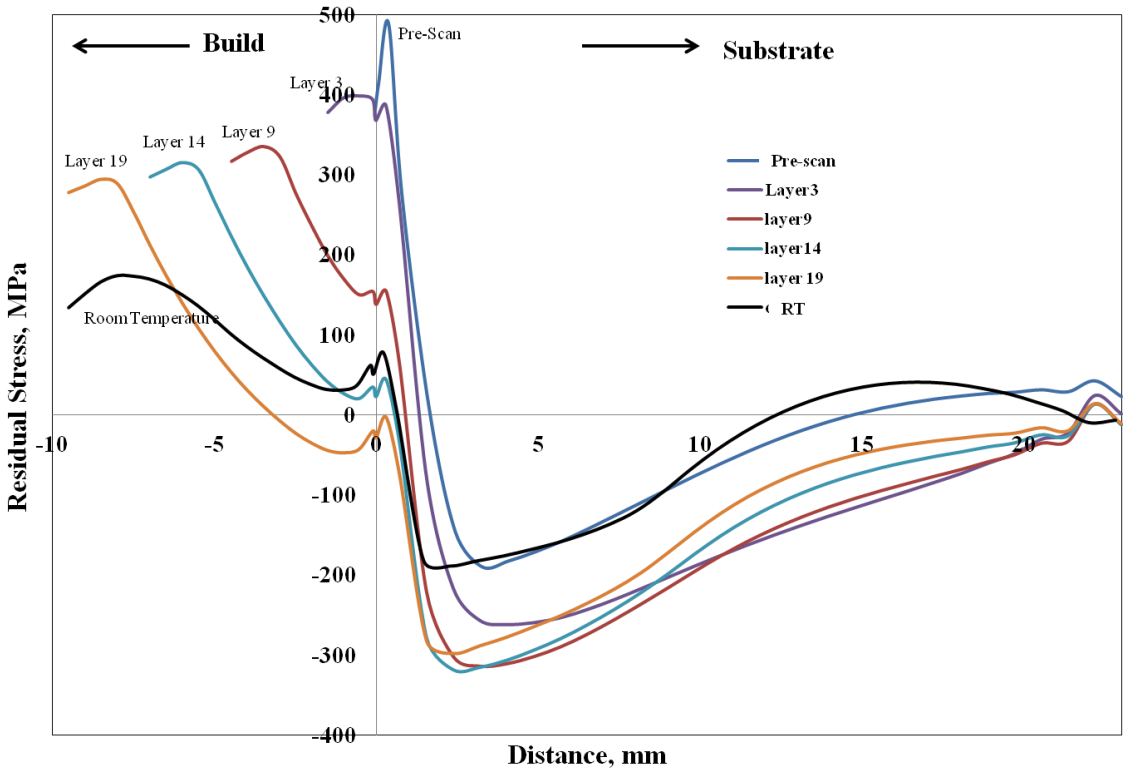

Figure 5-14: Residual stresses in the S11 (σ_x) directions plotted across the build (along the dotted lines in Figure 5-8) at different layers of the build.

5.4.4.1 Variation in Deposition-Path

From the previous section, it was shown that the residual stresses were the result of unequal balance of elastic and plastic flow, which is caused by the variation in heating and cooling cycles experienced by the deposit. Thus, the process parameters that affect these cooling rates would have an influence on the residual stresses developed. In this section, the effect of the deposition path, an important process parameter which has an effect on the temperature history of the deposit, has been studied. For this study, three types of deposition paths were studied which are short (S), long (L) and mixed type deposition path (M) (i.e., alternate layers of long and short deposition paths), in order to find an optimum deposition path condition with minimum residual stresses. The laser head movement for these deposition paths are shown in Figure 3-3.b.

Figure 5-15 shows the Von Mises stress distribution for all the three deposition paths. From the figures, it is evident that the residual stress distribution is similar in all three cases with high stress concentration at the top of the deposit and at the interface. However, the short deposition path has slightly higher stresses at the deposit-substrate interface. Figure 5-16 shows the variation of σ_x and σ_z in the substrate, and in the deposit along the centreline. The stress distribution in all three deposition paths is similar; however the long deposition path has slightly higher residual stresses (by ~50 MPa) than the short and mixed deposition paths.

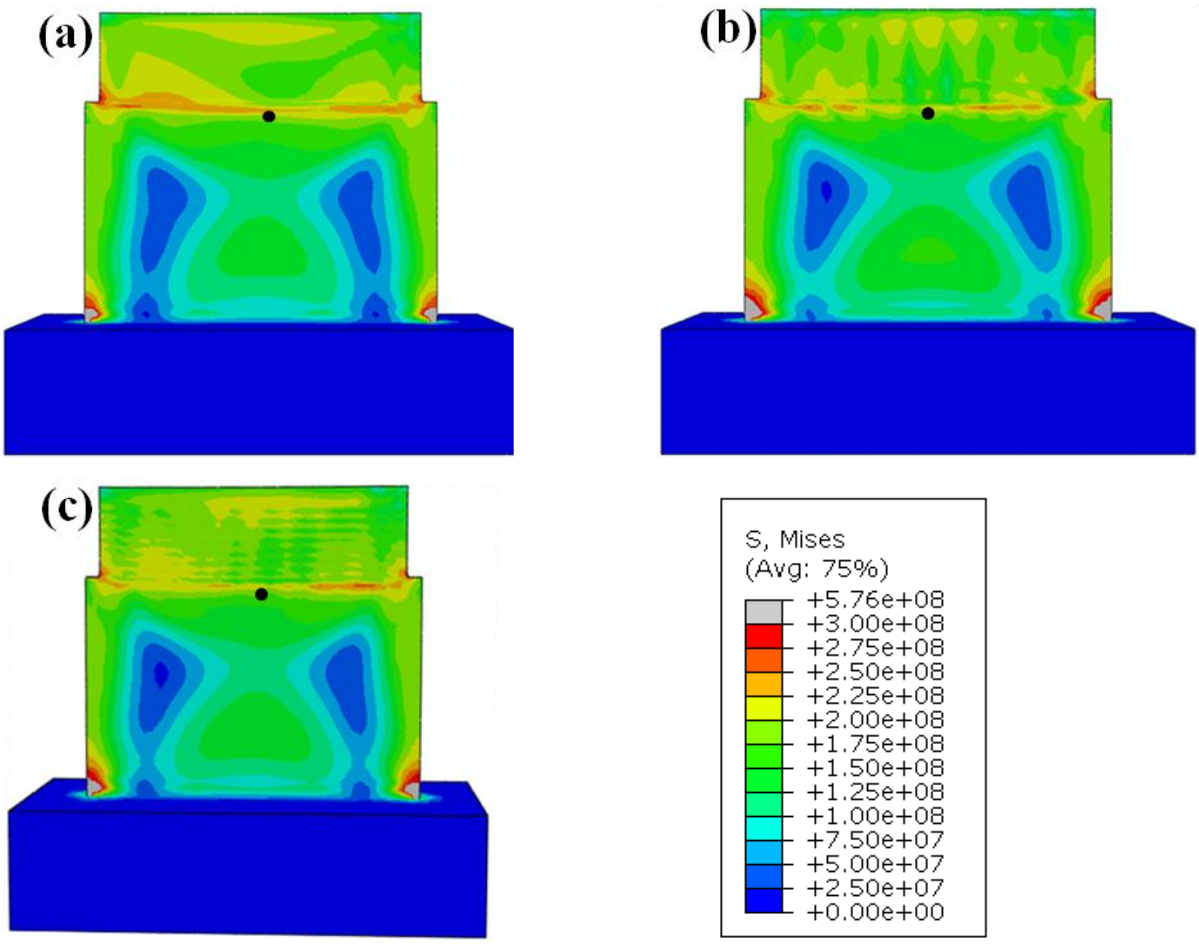

Figure 5-15: Von-mises stresses distribution with various deposition paths (a) Short (S) (b) Long (L) and (c) Mixed (M). (The process parameters are: laser power of 390W, scan speed 300 mm/min, powder flow rate of 18.46 g/min).

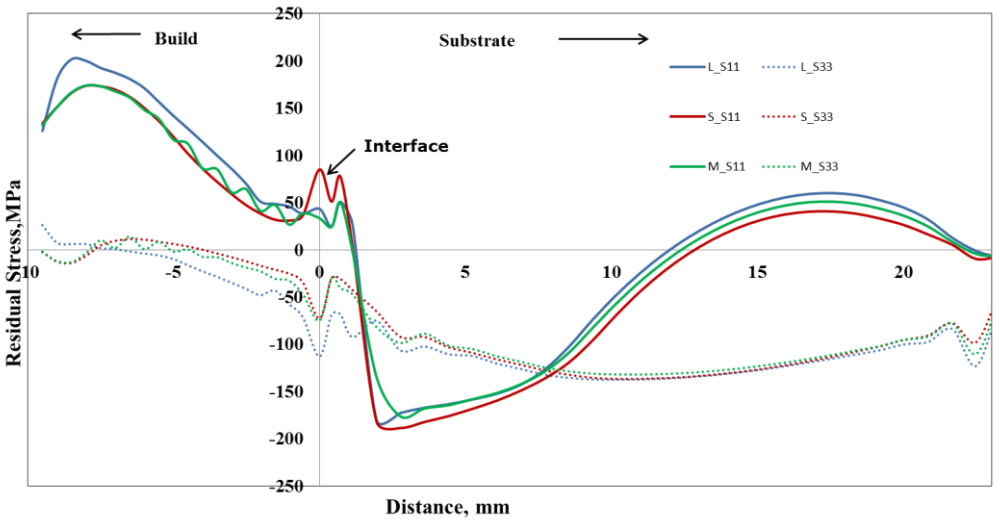

Figure 5-16: Stress distribution in S11 (σ_x) and S33 (σ_z) direction for long, short and mixed deposition paths at the mid-section of the deposit (dotted region in Figure 5-8).

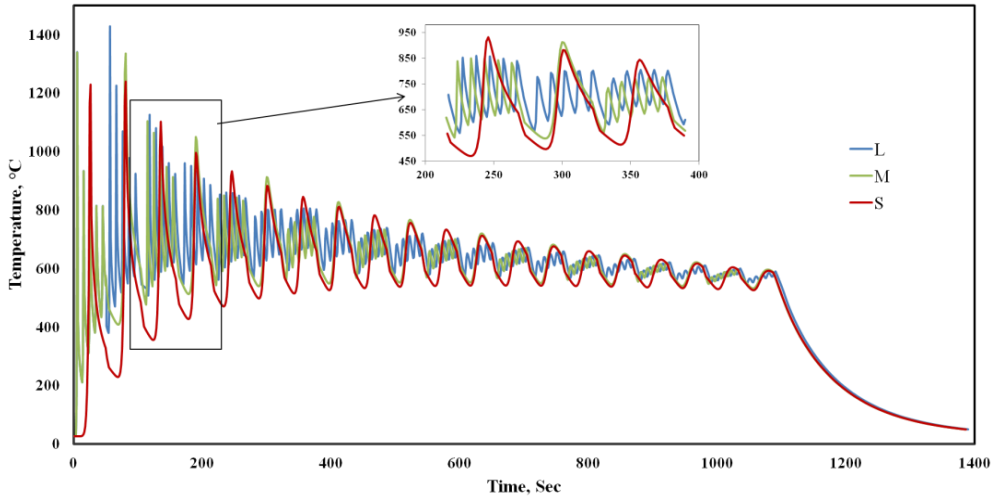

Figure 5-17: Temperature histories experienced by the substrate during various deposition paths (model results).

Figure 5-17 shows the thermal histories experienced by the top of substrate at middle, as marked in the black dot in Figure 5-15, for different deposition paths. At a given point in the substrate, for a short deposition path, the temperature gradually increases to the peak temperature, (i.e. from 27°C to 1230°C) in 12.4s giving a heating rate of 97°C/s. Whereas for a long deposition path, the heating and cooling takes place more quickly (i.e. from 27°C to

1338°C) it would take only 2.13s giving a heating rate of 615°C/s. For a given layer of deposition, although the maximum and minimum temperatures attained are not as steep as that using the short deposition path, the long deposition path experiences 5 heating and cooling cycles. This would cause an increase in residual stresses in long deposition path.

The stress at the interface in S11 direction is higher for the short deposition path by ~50 MPa and similar variation in stress is observed in long deposition path in the S33 direction. This is because of the direction of the laser beam in the short deposition path and long deposition paths are perpendicular to each other and so the residual stresses will be higher in the corresponding perpendicular directions.

5.4.4.2 Variation is scan strategy

From previous studies, it is evident that when a new layer of material is added the residual stresses in the previous layer are reduced due to the annealing effect. However, these stresses are generated again during the cooling cycle. In order to understand this effect better, a post scan and delay between layer strategies has been employed in this study. For the delay, the deposit was allowed to cool down for 50s (the time taken to deposit a layer), so that the material is allowed to cool down and the deposit expand before the next layer gets deposited. For post-scan strategy, the layer was scanned with a de-focused beam (diameter of 1.5 mm) after deposition in order to have a stress relieving effect on the layer.

To simulate the delay strategy the model is left to cool via conduction, convection and radiation for the time taken to deposit one layer after each layer of deposition. In order to simulate the post-scan strategy a heat flux with lower laser power is applied on the top of the layer following the deposition with a similar deposition path as the layer itself. The power of a defocused beam is calculated as below:

The laser beam intensity profile, I (W/m^2), of a circular Gaussian beam can be given as:

$$I = \frac{2P}{\pi r_1^2} \exp[\frac{-2r_0^2}{r_1^2}] \quad 5\text{-}18$$

Where P is the average laser power, r_1 is the laser beam radius and r_0 is the distance from the centre of the laser beam. In the present section if a point source is considered the term r_0 would become zero. So equation 5-18 can be written as

$$I_0 = \frac{2P}{\pi r_1^2} \quad 5\text{-}19$$

If the laser beam is defocused the maximum intensity of the laser beam would be reduced but the total area under the Gaussian curve of the focused and defocused beam would be the same. So,

$$\int_{-\infty}^{\infty} \frac{2P_1}{\pi r_1^2} = \int_{-\infty}^{\infty} \frac{2P_2}{\pi r_2^2} \quad 5\text{-}20$$

By equating the integral of equation 5-19 with the values of initial beam radius r_1 , Laser power P_1 (390 W) and final beam radius r_2, the approximate laser power for the defocused beam P_2 was around 182 W.

The attenuation of laser power due to powder flow would not be present here as there is no powder involved in the post-scan process the efficiency of laser was taken as 30% (based on the literature [111, 120-121, 150, 192]), instead of 13% as measured with powder in section 5.3.3.2, during post scan.

Thermal Profile for various scan strategies:

Figure 5-18 shows the temperature profile in various layers, resulting from a short deposition path with a delay between layers. All layers reach the same maximum temperature of 1800°C, unlike in the short deposition path direction where heat accumulation is observed as the deposition progresses (Figure 5-9). A delay between layers dose not lead to heat accumulation in this case and each layer attains a uniform heat distribution. Figure 5-19

shows the temperatures reached by the top portion of the substrate during deposition of the three scan strategies. From the figure it is seen that during the short deposition path the layer would cool down substantially before the next layer is laid. For post-scan strategy, although the maximum and minimum temperatures experienced by the deposit are the same compared to short deposition path, the post scan strategy deposit stays at a higher temperature for twice the time as in the short deposition path.

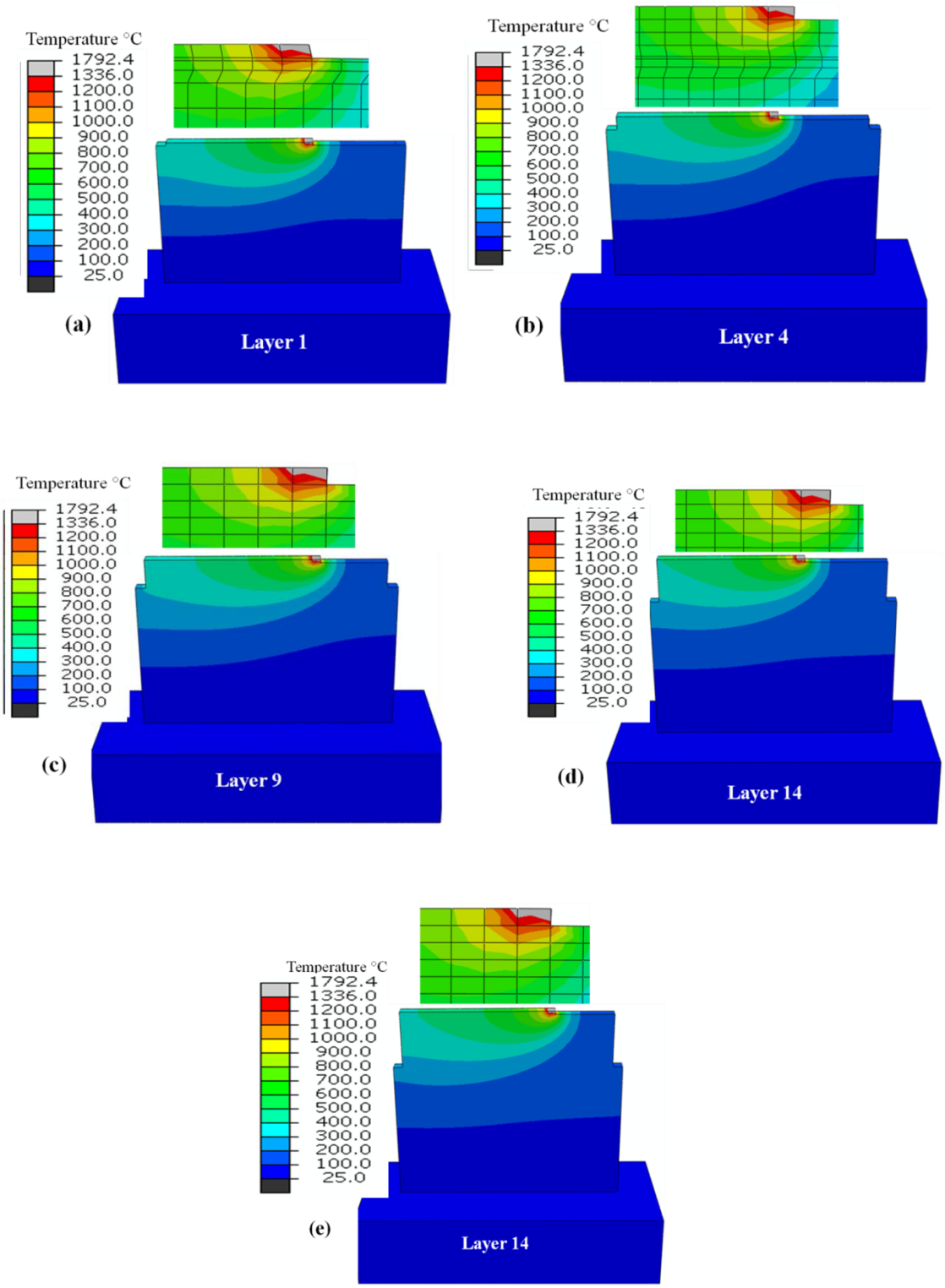

Figure 5-18: Model results showing the temperature distribution at various layers of deposition during DLF with process parameters of laser power: 390W, scan speed 300 mm/min, powder flow rate of 18.46 g/min and short with delay deposition path (a) 1st layer (b) 4th layer (c)9th layer d) 14th layer and e)19th layer (The upper figures show the enlarged view of the bead, grey area showing the temperature which is above the melting point of IN718 of 1336°C).

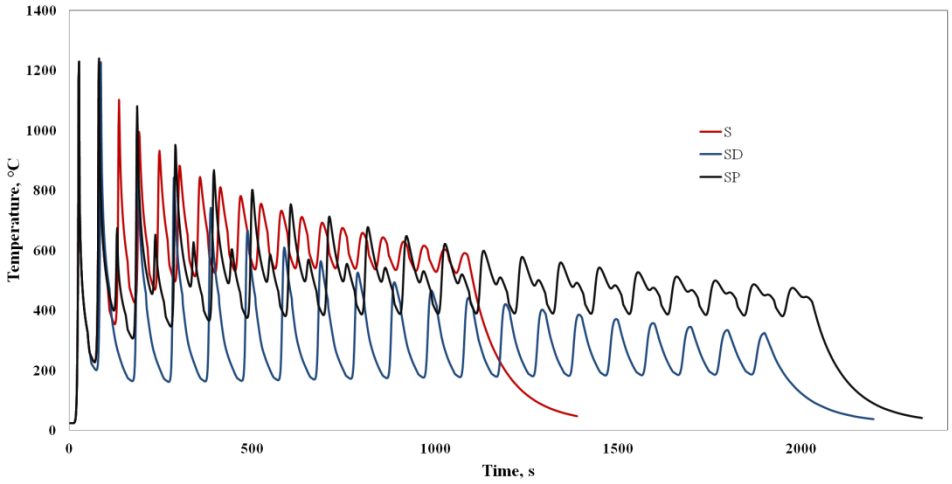

Figure 5-19: Temperature histories experienced by the substrate during various scan strategies.

Stress Distribution:

Figure 5-20 shows the Von Mises stress distribution for these strategies. From the figure it is evident that the stresses in the top portion of the deposit are clearly higher in delay strategy however the stress concentration in the deposit-substrate interface is less than in a deposition without a delay.

To understand the stress distribution better the stresses in S11 and S33 directions were plotted along the centre line for all the three strategies in Figure 5-21.a & b. A variation in stresses is observed along the centre line for both S11 and S33 directions and the variation of the stress level is less in S33 compared to S11 direction. The stresses are higher in delay when compared to actual deposition or with post scan. For post-scan strategy the stresses are almost zero in the deposit-substrate interface however the residual stresses are slightly higher than the short deposition path but lower than short + delay path.

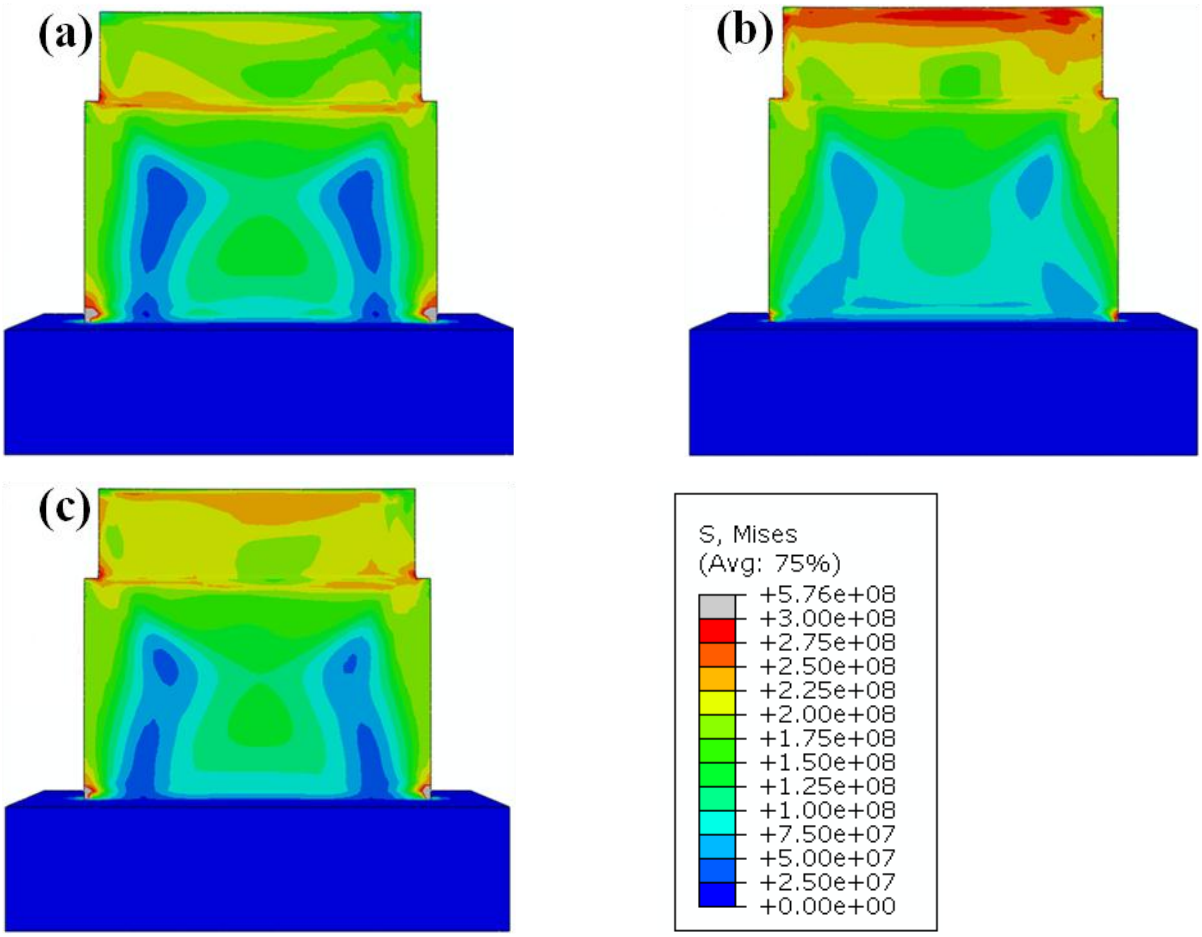

Figure 5-20: Von-Mises stresses distribution with various deposition strategies: a) Short (S), b) short + delay (SD) and c) short + post scan (SP). (The process parameters are: laser power of 390W, scan speed 300 mm/min, powder flow rate of 18.46 g/min).

From the Figure 5-19 it is evident that in the SD deposition path the temperature decreased substantially before the next layer is deposited due to the cooling cycle employed. The temperature of the layers decreases to around 163°C before the next layer is deposited for SD deposition path which is lower than the other two deposition strategies. The cold material would therefore have higher residual stresses in SD than the other two deposition strategies. For post-scan strategy the residual stresses are expected to reduce due to the annealing effect of the post laser scan however such reduction is not observed as the layer would eventually cool down for a certain time before the post-scan. Alternatively, In the future a low power laser beam may be used following the melt-pool to avoid rapid cooling as observed here.

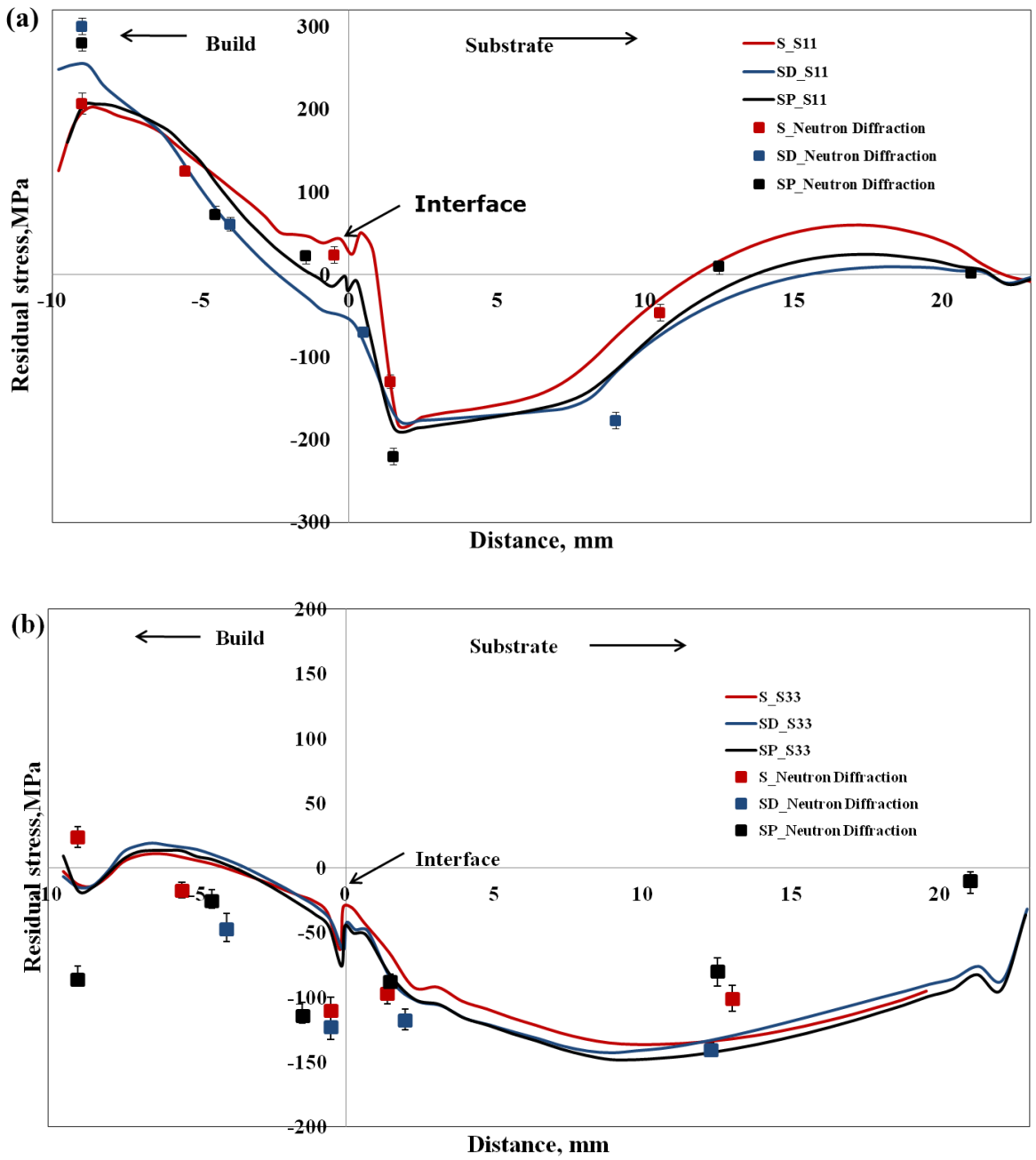

Figure 5-21: Stress distribution for short, short+deay and short+post scan strategies at the mid-section of the deposit (dotted region in Figure 5-8) in: a) S11 (σ_x) and b) S33 (σ_x) directions.

5.5 Summary

The thermal and thermo-physical models were successfully developed to understand the residual stress distribution during DLF for repair applications. The efficiency of the DLF process is very low (13%) due to the power attenuation by the excess powder flow and low absorption of CO_2 lasers. The maximum stress experienced by the deposit is ~0.3 times the tensile yield strength of IN718 (~1100 MPa [24]) which is lower than that required for crack formation, but still would require a stress relieving heat treatment after repair. The stresses are higher in the X direction than in the other two directions, as the maximum cooling rate is present in the direction of laser beam movement. The stresses are mainly concentrated at the deposit substrate interface and at the top portion of the deposit where high cooling rates occur. The deposition path has low variation in residual stresses in thin walled deposits where as the scan strategy have an influence on residual stresses in the deposit. A short deposition path show lowest residual stresses when compared to a delay or post deposit scan strategies, but the reduction is not enough to avoid the necessity of post deposition heat treatments.

Chapter Six

6 Microstructure and texture evolution in DLF

6.1 Introduction

This chapter addresses the assessment of the microstructural inhomogeneities in DLFed IN718. The microstructural inhomogeneities can affect the mechanical properties in IN718; including the inhomogeneities in grain size, chemistry, precipitate type (e.g carbides, Laves, γ', γ'', etc) size and their morphology, and texture. Large columnar grains result in poor fatigue properties, but demonstrate good creep properties. During DLF, the repeated thermal cycling and the variation in cooling rates, which are controlled by the process parameters, could affect the grain size development and the scale and nature of precipitates. Thus, it is important to understand the effect of these factors and also to identify the process parameters that would result in the desired microstructure.

The microstructural study has been done initially on thin-walled samples of single bead thickness to study the dendrite morphology, grain structure and texture development, identifying the effect of the key process parameters (e.g deposition direction, laser power, etc). In the second step, the builds were scaled-up to thick wall samples, where the microstructure of builds with multiple overlaps was studied; focusing on the microstructure in the overlap region between passes (around 2mm thick with 5 overlaps). Later, a complex deposition strategy was employed, whereby a delay between the successive layers was employed combining with post scanning of the previous layers in an attempt to limit the residual stresses and to influence the grain morphology. Additionally, a standard heat treatment was performed on these samples to dissolve the Laves phase and to precipitate the

strengthening phases. Finally, microstructural studies were performed to quantify the inhomogeneities in grain morphology and in precipitates with the change in the build thickness. In this study, the 3-dimensional bead morphology was studied in addition to the effect of the substrate texture on the build texture development. The microstructural study in this chapter aims to give an overall understanding of the microstructural evolution during DLF, and the effect of the key process parameters on the microstructure and texture.

6.2 Effect of Process Parameters on the Grain Structure and Texture: Thin-walled builds (stage I)

6.2.1 Effect of Deposition Path

To understand the effect of the deposition path on the grain structure and texture, thin-walled builds of unidirectional (B1) and bidirectional deposition (B2) paths were studied, while keeping the other process parameters constant (laser power 390W, scan speed 200 mm/min and powder flow rate of 18 grams/min). Figure 6-1 show optical micrographs for B1 and B2 builds (X-Z plane as per the notation in Figure 3-2).

The microstructure of the as-deposited samples showed a layered structure, with a thin demarcation of small dendrites at the interface between the layers, as highlighted with arrows, Figure 6-1 (taken at the bottom portion of the build 2 layers above the substrate). The size of the layers (i.e. the mean track height) was ~500μm for B1 compared to 350μm in B2. Each layer contained aligned inclined dendrites, which were contained within the layers and which did not grow across the layers for both builds. The layers were separated by a thin layer of fine dendrites (5-10μm in dia.) in both builds, with B1 showing a larger interlayer zone than in B2. The dendrite arm spacing (DAS) [198] was relatively fine (~5μm) for both the deposits, compared to the typical DAS in cast microstructures (10μm -40μm), which can

be attributed to the rapid cooling rate during DLF (10^2-10^3 $K.s^{-1}$) [109]. This was also previously observed in DLFed IN718 [12, 22].

Comparing both builds, significant microstructural differences were observed, especially with respect to the dendrite growth morphology. In B1, the dendrites were uni-directionally oriented at an angle of ~50-60˚ to the substrate in all the layers (Figure 6-1.a), with the inclination tracking the rear of the melt pool, whereas the dendrites were oriented in a zigzag fashion in B1, and intersecting at the interface between the layers at an angle of ~90-100˚ (Figure 6-1.b). In both cases, the dendrites were oriented along the moving heat source. This microstructural inhomogeneity was previously reported in the literature [199-200], and was related to the influence of the vertical flux (q_x) and horizontal heat flux (q_z), as well as the dendrite orientation of the previously deposited layers (Figure 6-1.c).

If q_x is due to the moving heat source, and q_z due to the heat sink effect by the substrate, then q_r is the resultant heat flux, which is along the dendrite growth direction. In B1, the laser is switched off for 6s between the layers, while the laser head moves back to the starting point. Also, the carrier gas was not interrupted, thus causing the build to cool down substantially before the next layer is deposited. In B2, the laser beam continuously moved back and forth for deposition. This would allow only half the time for cooling, with no forced cooling between the layers. Thus, in B1, the layers would be at a lower temperature than B2 before the next layer is deposited. From the validated finite element model developed for thick-walled multi-pass laser deposition in chapter 5, it was predicted that a delay of 50s between the layers would reduce the layer temperature by ~ 400°C before the next layer is deposited. Due to this larger heat accumulation in B2 than in B1, the dendrites are expected to grow more vertically in B2. Moreover, the change in the dendrite orientation across the layers would depend on the dendrite orientation in the previous layer. As the dendrites tend to grow

perpendicular to the previous layer's dendrites, this makes them oriented more towards the q_r direction [199].

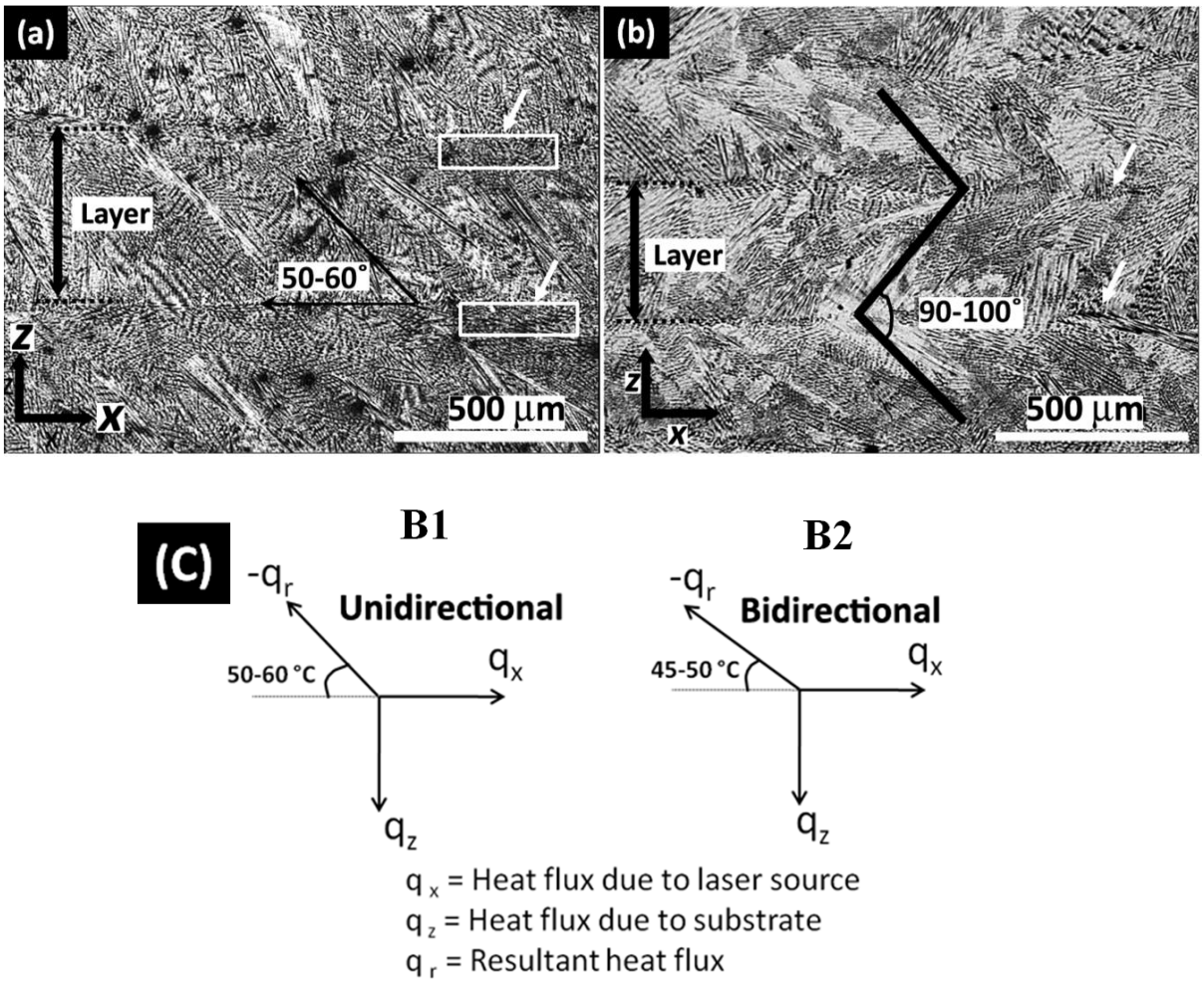

Figure 6-1: Optical micrographs showing the dendrites orientation and layer demarcation in (a) B1, (b) B2 and (c) schematic illustrations of the heat flux directions (not to scale).

Further examination of the microstructural inhomogeneity in the grain structures was performed using SEM with BSE imaging and EBSD. Figure 6-2.a & b show the SEM micrographs of B1 and B2 in the X-Z plane. To combine the grain structure with the orientation development, EBSD maps were created, covering 2 layers of the build. Figure 6-2.c & d are the Inverse pole figure (IPF) coloured EBSD maps plotted on the build for B1 and B2.

Both builds revealed a banded grain structure, with very fine grains, more prominent in B1, at the layer interface. Also, in B1 the grains in the uppermost part of the layer are inclined almost parallel to the laser beam direction.

In welding, the grains start to nucleate from the fusion line to the weld centre line i.e. from the tail of the melt-pool and grow to the centre due to the maximum thermal gradient in this direction. At the centre of the weld -pool the grain size depends on the weld-pool speed, where for welds with low to medium weld speeds, more columnar or stray grains are observed than in high weld speeds where equiaxed zones are observed. At low welding speeds, the epitaxially grown dendrites curve towards the heat source, so that the maximum thermal gradients present at the solid–liquid interface, are maintained as growth proceeds. Also, at low speeds the central region of the weld becomes wider and stray grains are observed [73] (shown in Figure 2-30). This phenomenon of inclined grains was previously observed by Normal *et al.* in Al alloy welds at a speed of 7 mms^{-1}[84], similar to the laser scan speed used in this current study. However, neither this type of grain growth, nor the fine grain zone is observed in B2 (can be seen clearly in Figure 6-2.c&d). The reason could be that in B2, due to the heat accumulation, the fine grain/ stray grain zone would be completely re-melted when the next layer is deposited. This can be seen from the layer size where the size of each layer is around 500µm for B1 compared to 350µm for B2.

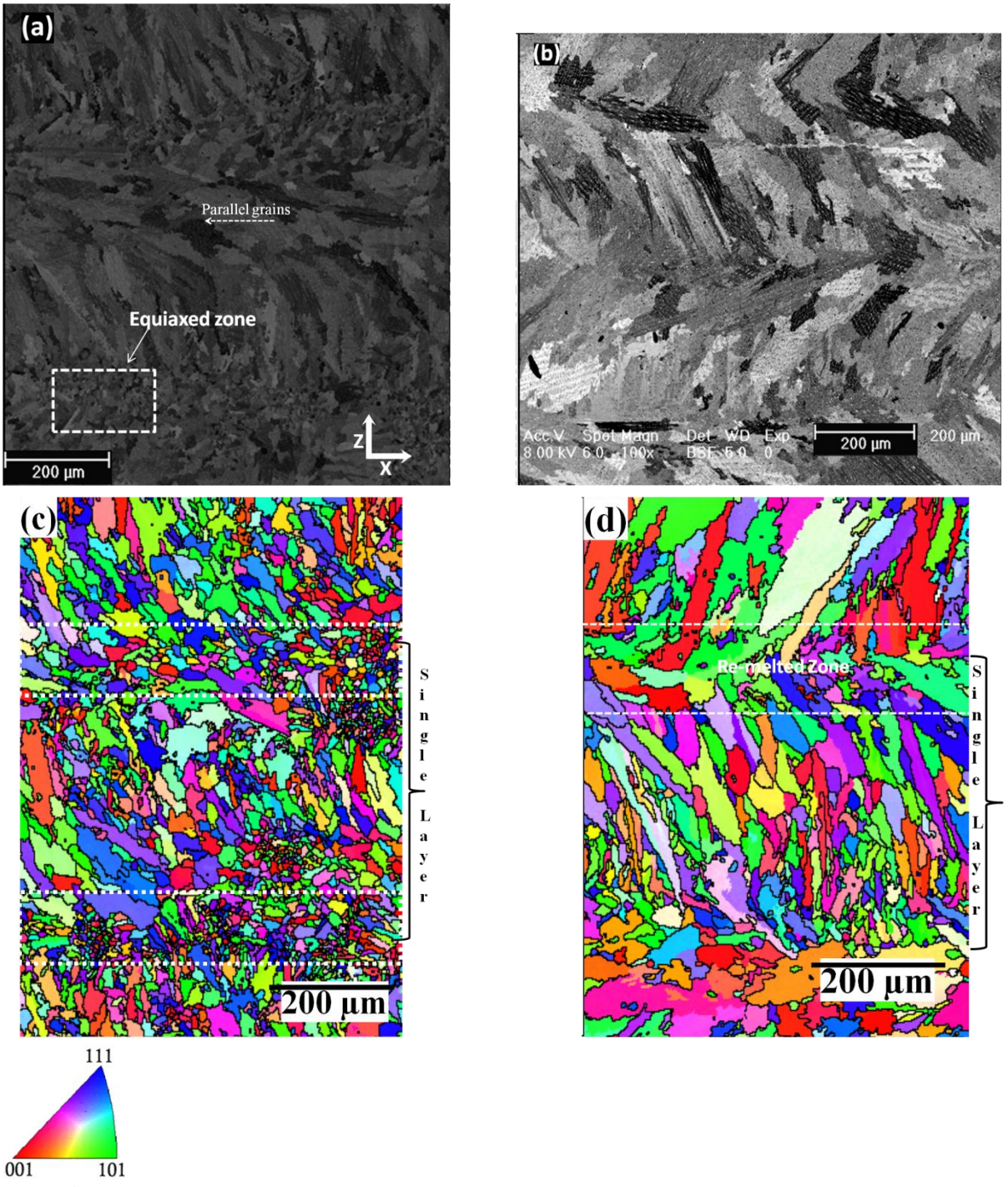

Figure 6-2: The grain structure development due to DLF, showing the grain structure in (a) B1 with the equiaxed grain region between the layers and (b) in B2 showing the absence of a similar region. EBSD-IPF map of (c) B1 and (d) B2, also showing the same features.

6.2.1.1 Grain size

To quantify the microstructural inhomogeneity in terms of the grain size, the grain size distribution was measured over an area of 1 mm ×1 mm for both the builds in the X-Z plane, Figure 6-3. Columnar grain of different sizes and aspect ratios were observed in both the builds. In B1, the columnar grains appeared slightly smaller than in B2. In B1, the fine grain band was observed (Figure 6-2.a) to have an average grain size of ~40µm. Figure 6-3 shows the grain size distribution in B1 and B2. From the histograms it is evident that the average grain size in B1 is lower than in B2. Also, the grain aspect ratio in B1 is higher than in B2 (i.e. the grains in B1 are more elongated, Figure 6-3.c &d). Figure 6-3.e & f show the grain size distribution in the fine grain zone in B1. The grain size in this region is around 10µm, with most of the grains having an aspect ratio < 2.

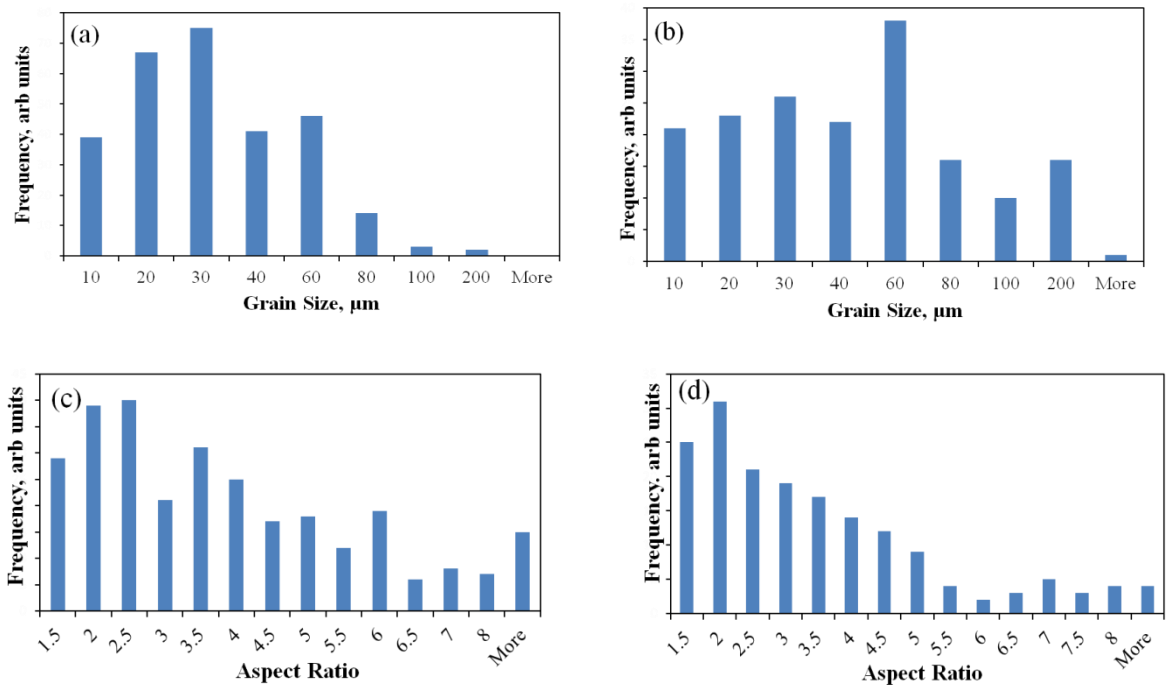

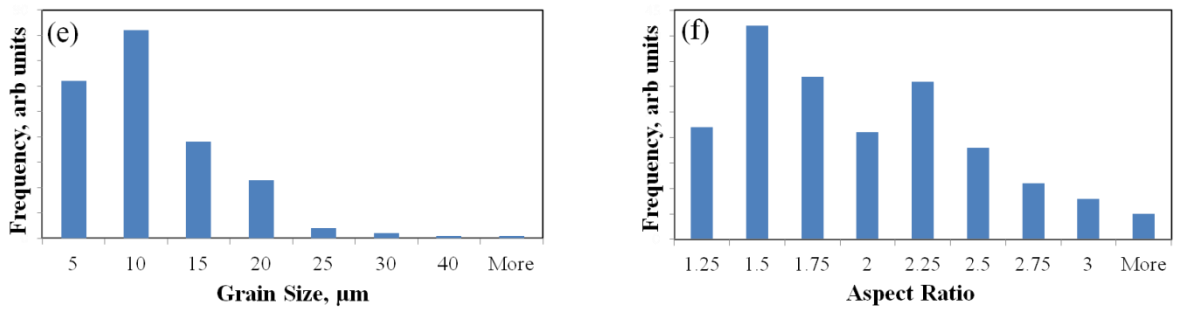

Figure 6-3: Grain Size distribution in B1 and B2 (a and b); Aspect ratio of B1 and B2 (c and d); Grain size and aspect ratio of fine grain zone between layers in B1 (e and f).

The higher frequency of larger grains in B2 could be due to the higher heat accumulation as a result of the continuous laser heat input. In B1, the laser beam is switched off between layers leading to faster cooling rates and fine columnar grain structures.

6.2.1.2 Texture

Figure 6-4 shows a schematic representation for dendrite orientation in the B1 and B2 based on observation of the grain orientation and dendrite morphology, using EBSD maps and BSE imaging of a large area of 1 mm × 5 mm from the bottom to the top for both the builds (Figure 6-5). The banded (fine and coarse grains) structure is obvious throughout the build. This banded structure was previously observed by Blackwell in DLFed IN718 [201], where it was attributed to the high thermal conductivity of Ni-superalloys that leads to rapid cooling during DLF, suppressing epitaxial growth.

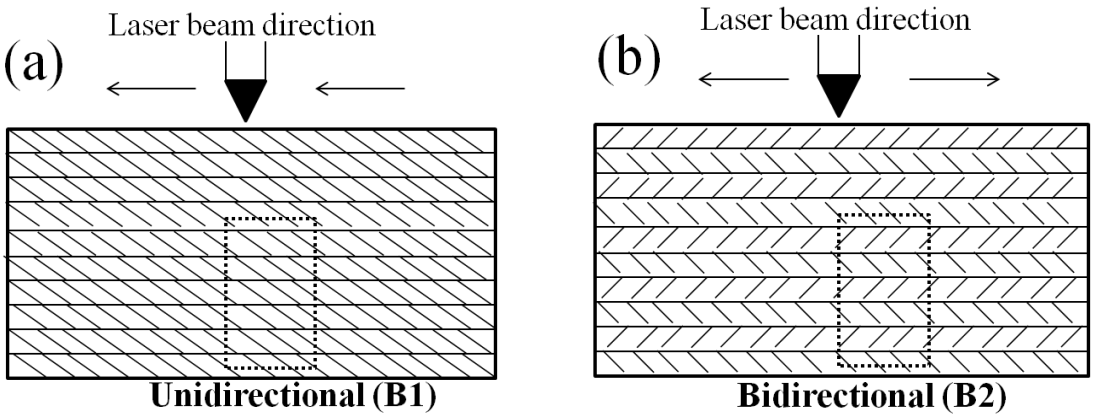

Figure 6-4: A Schematic illustration showing the dendrite orientations in B1 and B2 based on the microstructural observation of entire builds (not to scale). The dotted box represents the areas from which large EBSD maps were plotted (Figure 6-5).

In B1, the fine grain zone between the layers was very obvious in the first few layers (Figure 6-5.a), but it then becomes less obvious as the deposition progresses. The fine grain zone thickness was around 150-200μm at the base of the build decreasing to 20μm at the top (5mm from base). In B2, the fine grain zone is not as obvious as in B1. In powder DLF, the amount of powder that is captured in the actual melt-pool is ~ 10-30 % of the actual powder sprayed in to the melt pool [20]. This excess powder would drop on to the deposit and stick in a semi solid state. At the lower section of the build (near to the substrate) the build cools down substantially due to the heat sink effect of the substrate. When the next layer is deposited, the laser energy supplied is used up in heating the cold layer and completely melting these semi solid particles which are stuck to the end of the melt-pool. This can be explained by the thermal model in chapter 5, where the temperature attained by the substrate during pre-heating is around 1336 °C which is raised to 1808 °C during the first layer of deposition. As the deposition progresses, a heat build-up is observed where the build reaches a temperature of 2003°C at the 14th layer of deposition (The temperature distribution and the melting of the layers in clearly shown in Figure 5-9). So, this heat build-up is spread across 2 layers as we

go up the build, which would help in re-melting and consolidation of previous layers, thus melting the excess powders sprayed during the deposition.

Figure 6-6 show the {100} pole figures generated from the EBSD maps for both builds, with build direction along the growth direction (Z). The {100} cubic texture appears to have an approximate tilt of 30° to the Z-direction. B2 shows a slightly stronger cubic orientation (4.5× random) than B1 (3.3× random). During solidification for FCC metals, <100> direction is the favourable growth direction along the heat flux [73] as is observed here. The tilt in the orientation of the grains is due to the moving heat source, where the grains would tilt towards the heat flux direction. Figure 6-6.c & d show the pole figures for the entire (1 mm × 5 mm) maps, which show a more random texture. From this, it can be inferred that the builds have a random macro texture, with the individual layers showing a weak cubic (micro) texture.

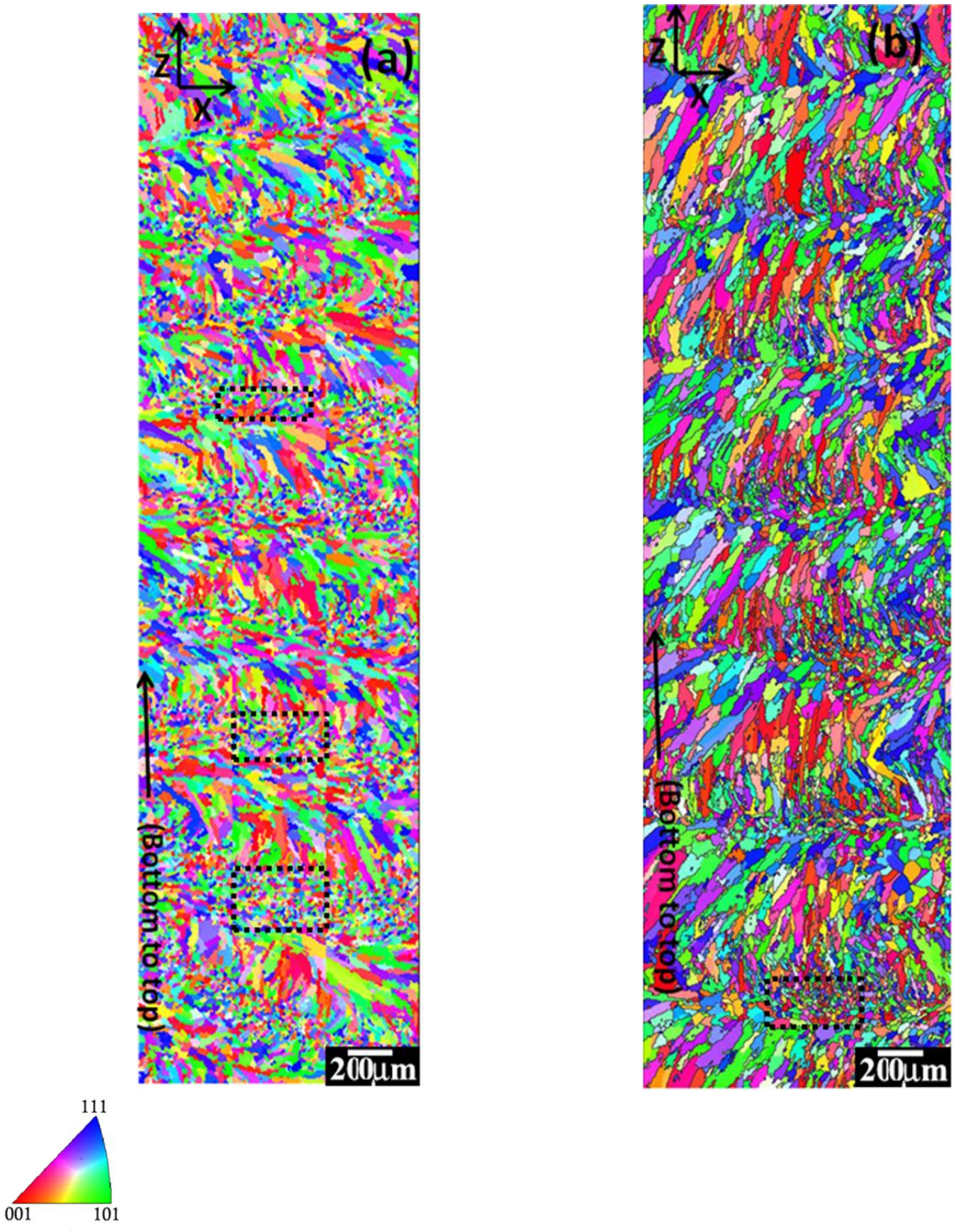

Figure 6-5: EBSD maps for Unidirectional (a), bidirectional deposits (b). The dotted boxes show the equiaxed grain regions.

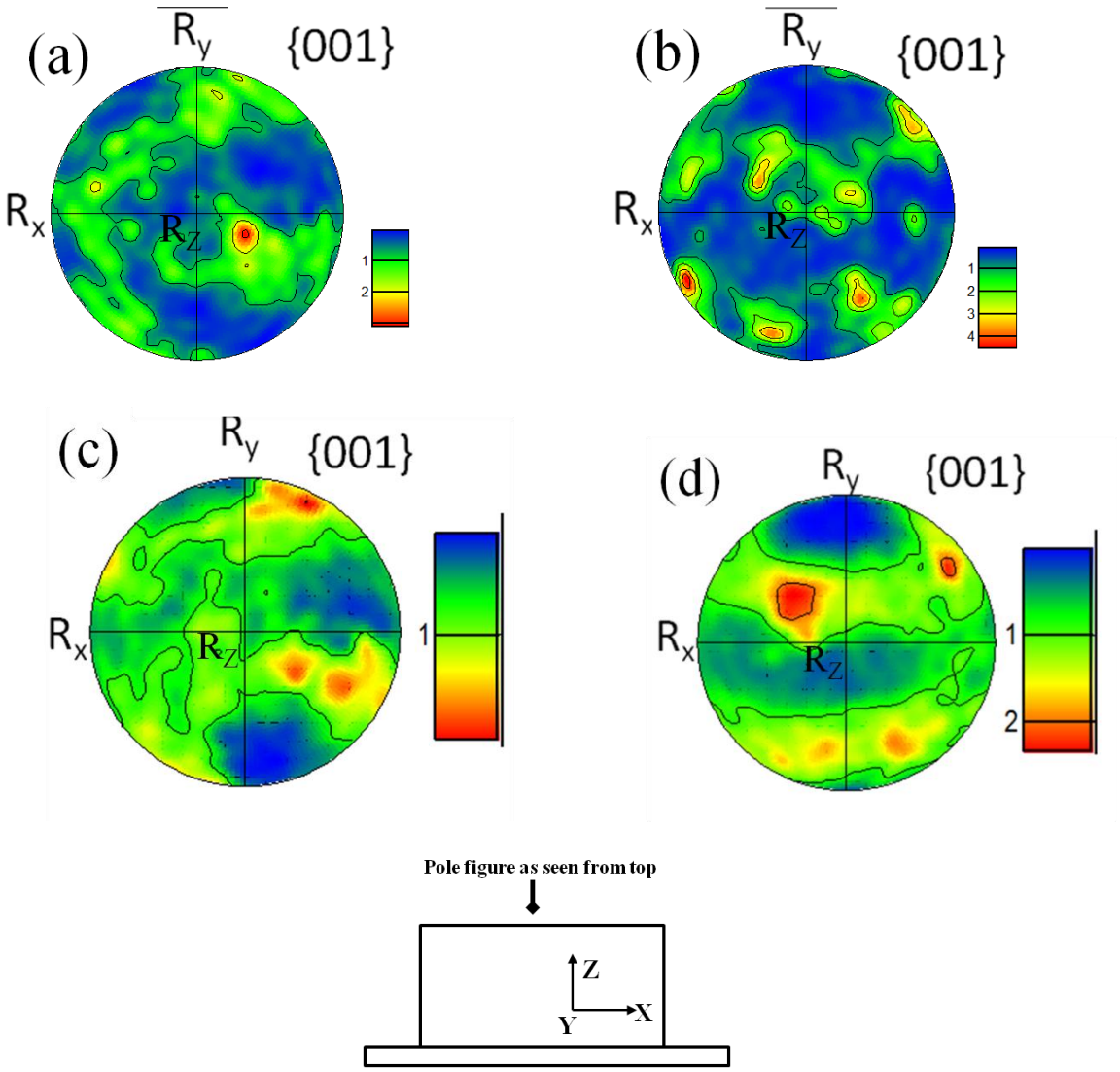

Figure 6-6: {100} pole figures plotted parallel to the Z direction, on one layer of a) B1 and b) B2 depositions, and of the entire map for c) B1 and d) B2 (bottom picture shows the schematic of the build with directions).

6.2.2 Effect of Laser Power

To study the effect of laser power on the microstructure, builds were made with higher laser powers than used for B1 and B2 of 474, 580, 693 and 910W, while keeping the other process parameters of scan speed (200 mm/min) powder flow rate (18g/min) and bi-directional deposition path constant. At 910W, laser power as the build approaches the nozzle, the powder flow rate was reduced to 5g/min (builds B3) to avoid contact.

Figure 6-7.a shows the dendrite orientations with increase in laser power to 910W in B3, where the dendrites are aligned at an angle of ~80˚ to the substrate, suggesting that the resultant heat flux is almost vertical. Furthermore, the demarcation between the layers seen in the case of low power deposition was not observed, (Figure 6-1.a & b). It is clear that the heat input was high enough in B3 for the dendrites to grow epitaxially, rather than by re-nucleating across the layers. After the losses due to power attenuation and radiation, it is known that only a limited fraction of the laser energy (as low as 4%) is consumed in melting the powder, whereas ~90% of the laser energy is absorbed by the substrate or the prior layers [18]. It is believed that the continuous high power heating increased the melt pool temperature as well as completely re-melting the previous layer so that the dendrites grew from the previous layers, and hence no demarcation was observed between the layers.

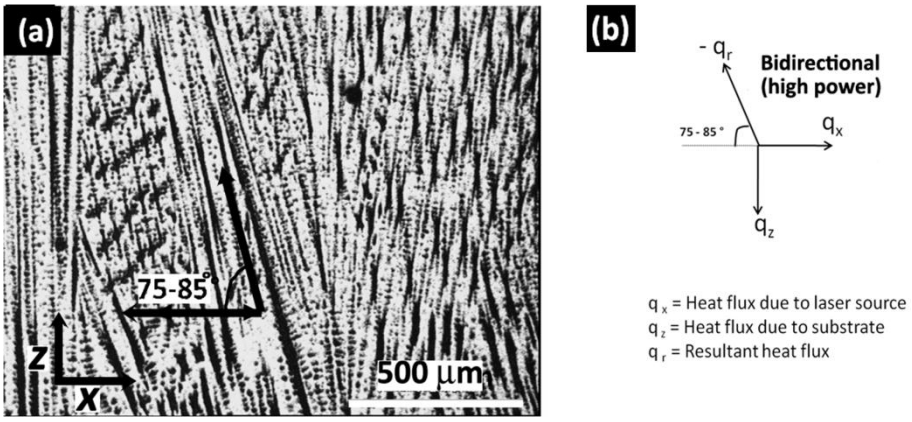

Figure 6-7: a) Optical micrograph showing the dendrite orientations in B3 and (b) a schematic illustration of the heat flux directions (not to scale).

6.2.2.1 Grain Size

To investigate the variation in grain morphology and grain size with laser power, SEM micrographs were taken for the various laser powers, covering a large area of 2 mm × 2 mm. From Figure 6-8, it is evident that with increase in laser power the grains get more columnar, with the demarcation between the layers diminishing. At 390W, most of the grains are 60-80µm in length with an aspect ratio of around 2-3. With increase in laser power to 580W the

grains grew longer and more columnar with most of the grains with their feret max (F_{max}) in the range of 100-200 µm with an aspect ratio of 3-5. At a power of 910W and powder flow rate of 12g/min the grains grew more columnar with large areas of the micrograph having the F_{max} of the grains in the range of 200-400µm and an aspect ratio of 5-10 (Figure 6-9). Decrease in the powder flow rate to 5g/min (B3) resulted in the creation of long columnar grains (2-3 mm long, with an aspect ratio of ~30) in the plane of sectioning (Figure 6-8.f). These columnar grains contain elongated regions which are bright and therefore of higher atomic mass suggesting that the powder is completely melted and cooled slowly causing segregation in the high atomic mass elements. These large columnar grains were seen previously by Moat *et al.* [10], when using an energy density of 11.75J/mm^2 in Waspaloy™ for a pulsed ND:YAG laser. It is clear that the different deposition strategies and the high laser power resulted in considerable microstructural changes in the grain size and morphology. It is likely that this would also result in differences in the texture.

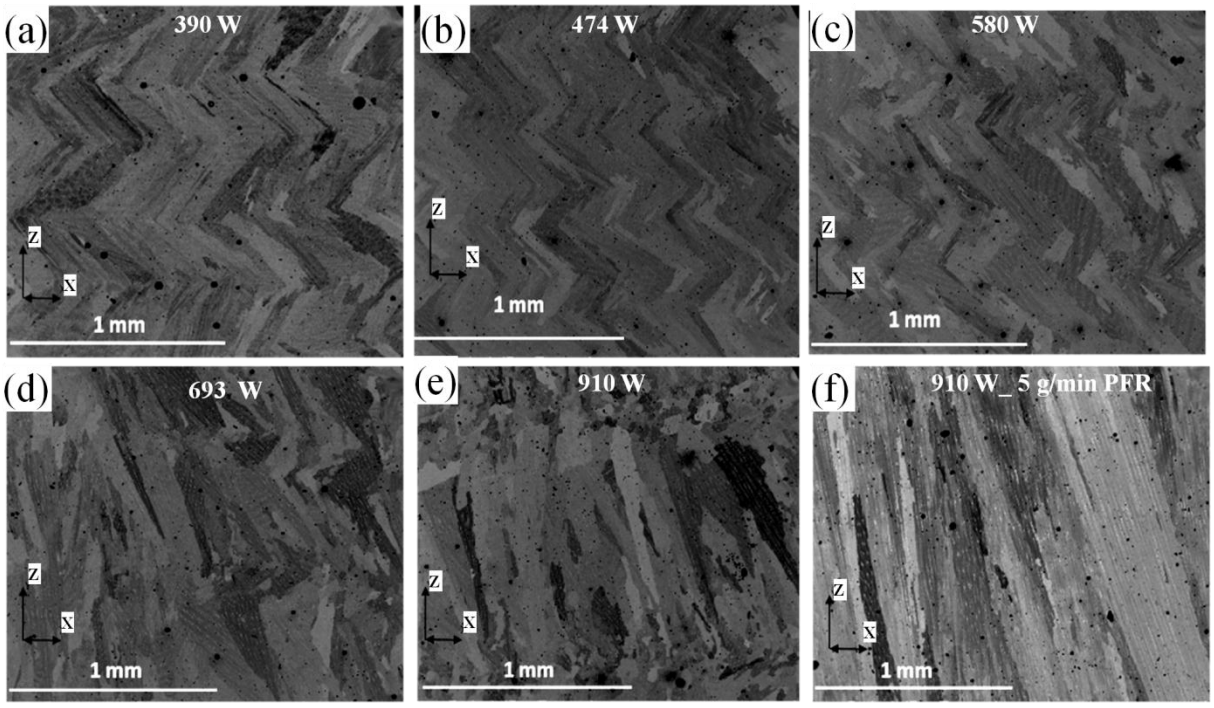

Figure 6-8: BSE micrographs showing the influence of laser power on the grain morphology and size at a constant scan speed of 200 mm/min in bi-directional laser deposits: a) 390W, b) 474W, c) 580W, d) 693W (all at a powder flow rate of 18 g/min), e) 910W at 12 g/min, and f) 910W at 5 g/min (B3).

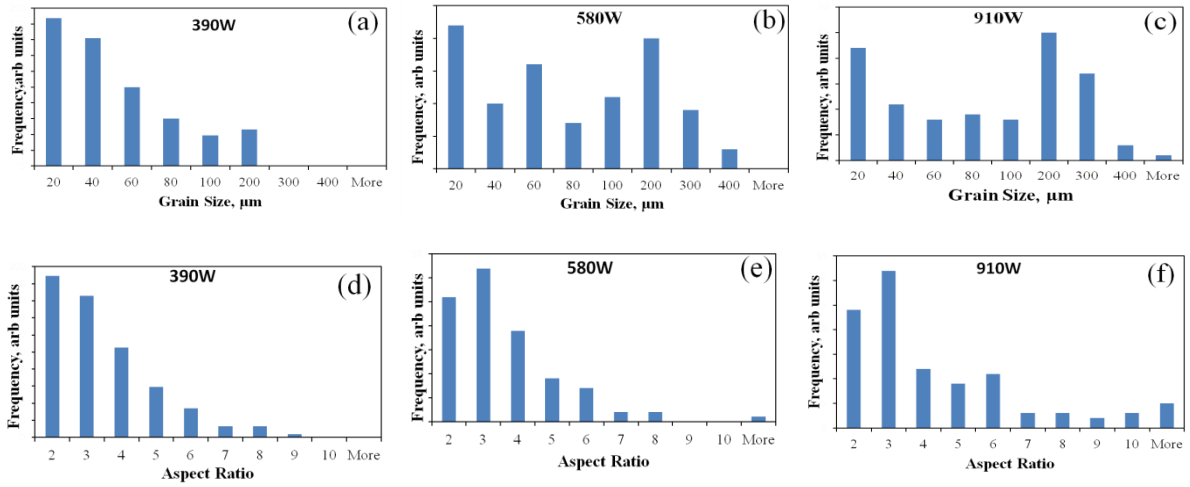

Figure 6-9:(a-c) Variation in grain size with laser power at 390, 580, and 910 W (12 g/min) and the aspect ratio for the corresponding grain sizes (d-f).

6.2.2.2 Texture:

To compare the texture and grain orientation in high power builds, an EBSD map was created from bottom to top of B3 covering a large area of 2 mm × 8 mm for the build in Figure 6-9.f. The build initially started with small columnar grains, progressing to very large columnar grains. It is important to note that the substrate was a rolled IN718 sheet, with a uniform fine grain rolled structure. Following the initial pre-scan, the first grain layers (at the build-substrate interface) form by nucleation from the existing grains. As reported by Hofmeister *et al.* [109], high laser powers are associated with lower cooling rates. The melt pool temperature gradually rises with the increase in the build height due to the reduction of the heat sink effect of the substrate. As a result, the grain structure gets coarser with increase in the build height. Furthermore, it would be expected that the high melt pool temperature and the continuous heat flux during the bi-directional high power deposition would lead to complete re-melting of the previous layers, leading to epitaxial growth of the grains. Eventually, while depositing the final layer in the build the heat input is discontinued, leading to rapid cooling. Due to this a demarcation is observed in the final layer with small columnar grains.

It is known that solidification under varying conditions leads to three different grain morphologies, 1) fully columnar, 2) columnar plus equiaxed, and 3) fully equiaxed. Different morphologies can be obtained by controlling the thermal gradient (G) and the solidification rate (R) from the bottom to the top of the melt pool. There are various process parameters (e.g. laser power, travel speed, substrate temperature and beam diameter) that affect the G and R-values, which in turn influence the grain morphology of the sample. Process maps were developed by Gaumann *et al.* to predict the transition from equiaxed to columnar microstructure, based on Hunt's model for columnar and equiaxed growth of dendrites [129], where a lower G/R ratio would provide columnar growth. Studies by Gauman showed that an

increase in laser power would lead to higher G/R value, promoting equiaxed growth. However, the nucleation sites (N_0), also play an important role for columnar to equiaxed transition temperature (CET) where more nucleation sites promote equiaxed grains. With an increase in powder flow rate, the number of nucleation sites would increase, thus promoting equiaxed grains at lower powers. At lower laser powers, columnar growth would start at the bottom of the melt-pool, however due to high powder flow rate, the number of sites increases. The higher laser powers give a larger and deeper melt pool, which increases the mean value of R. If acting alone, this would have increased the tendency to form equiaxed grains. However, the large melt pool also promoted vigorous Marangoni flow. There is also evidence of more superheating in the melt-pool which could increase G [130].

In the current study, at lower laser powers, re-melting of the previous layer is limited by the cold substrate, leading to equiaxed partially melted powder particles at the layer interfaces. Although a columnar grain structure is observed within the layers at lower laser powers as suggested by Gaumann *et al.*, the grains are not completely columnar throughout the build. Also, the fine grain zone between layers disappears as the build progresses, due to heat accumulation and sufficient energy to partially or fully re-melt the previous layers. This heat accumulation in the build was previously measured by Pinketron *et al.* in thin walled waspaloy [130]) although single crystals or large directionally solidified columnar grain structures are not achieved. For the condition with low powder flow rate and high laser power (as in Figure 6-9.f), the laser power is increased as the powder flow rate is decreased which gives fewer nucleation sites (N_0), hence encouraging more columnar growth. Also, at such high laser powers, complete re-melting of the previous layer would occur and the dendrites would grow from the previous layers, rather than nucleating independently.

The columnar grains in the build tend to tilt towards the resultant heat flux direction, which is from the side to the centre of the build, as the sides are cooler than the centre due to

convection losses (schematic shown in Figure 6-10.b). Preferential grain growth was observed, where the grains, which were not growing along the heat flux direction, are suppressed to give way for the grains that have the favourable orientation. This behaviour is generally seen during directional solidification [44].

The other interesting feature that was observed in the builds was that the edge of the build had columnar grains that were more vertical than those in the centre, as shown in Figure 6-10.b. At the edge of the build, where the laser beam path is reversed, the laser would stay for a longer time than in the remaining part of the build. This leads to a higher temperature in this (edge) location. From the temperature predictions in the thermal model in chapter 5 for thick walled builds, Figure 5-9, the edge of the build is predicted to reach a maximum temperature of 2309°C compared to other locations of the build at (~ 2003°C). Also, at the edges of the build, re-melting is predicted to be present for 2 subsequent layers, whereas in the centre re-melting observed only for half of the previous layer. This higher heat accumulation and complete re-melting of the previous layers would have caused the grains to nucleate from the previous layer rather than independently nucleating, thus giving rise to vertical grains at this particular location of the build.

B3 also showed a strong texture (21× random), where the microstructure resembles a directionally-solidified structure, with a preferred orientation, whereby the grains grew epitaxially parallel to the {001} planes, as this is the crystallographically favoured orientation for FCC alloys [45]. A fibre texture was observed instead of the cubic texture. This can be attributed to the moving heat source where back and forth movement of the heat source would constantly rotate the grains as well in this heat flux direction giving an overall fibre texture. This fibre texture was previously observed in DLF Ni-superalloys by Pinketron and Moat *et al.*, even when a pulsed laser was used [15, 107].

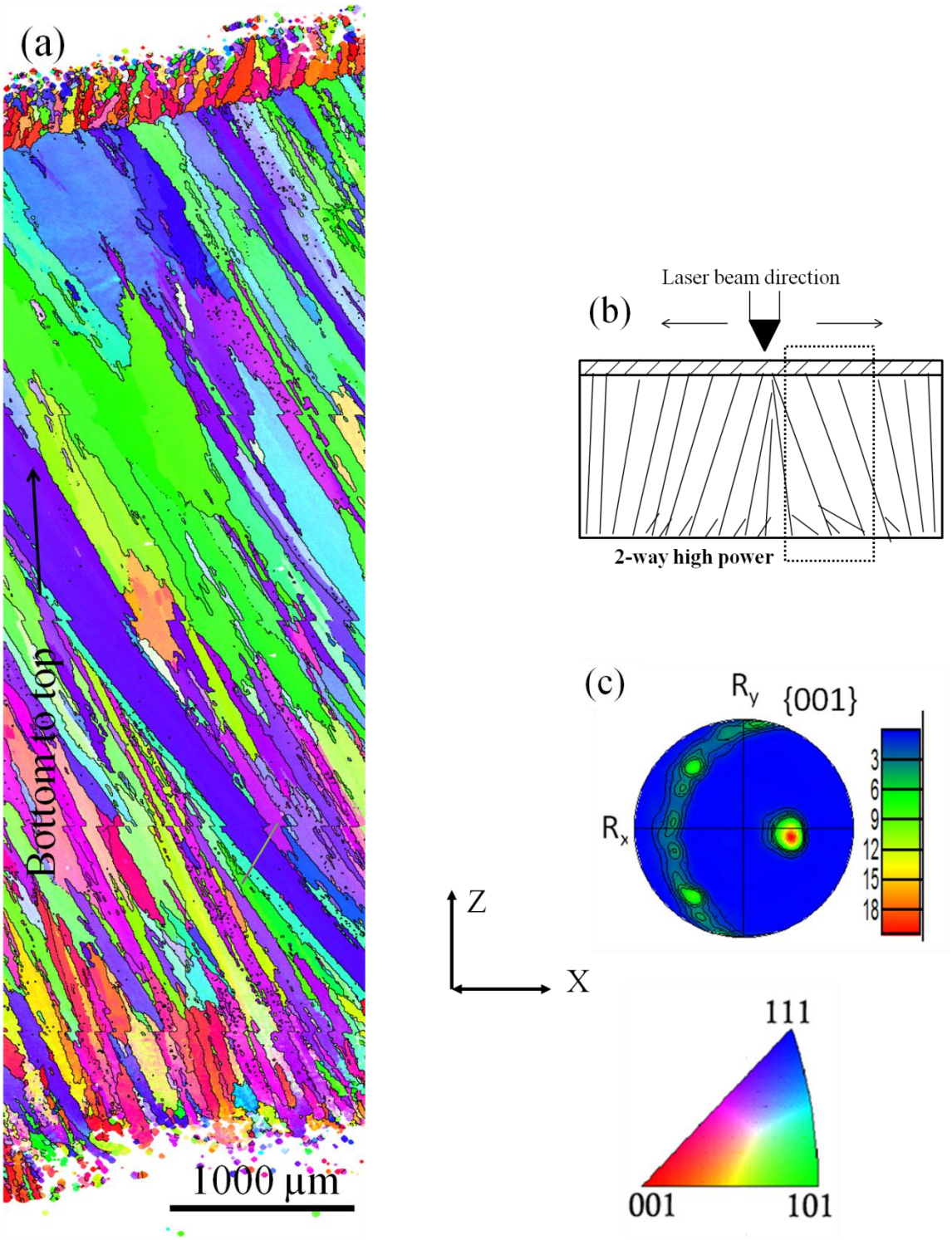

Figure 6-10:a) IPF coloured EBSD map showing large columnar grains in B1 b) A schematic diagram of the grain/ dendrite orientation of the entire build (not to scale) with the dotted box showing the region mapped by EBSD, and c) {100} pole figure plotted parallel to Z (growth direction).

6.2.3 Summary

The process parameters have a significant influence on the microstructure. The grains orient along the moving heat flux direction, giving banded grain morphology for low laser power. With increase in laser power, the grains tend to grow completely as columnar grains as in directional solidification; a potential approach to improve the creep properties. Semi-solid powder particles were observed at the lower layer of the build, which could potentially cause mechanical failure in the build. These un-melted particles could be reduced by using a lower powder flow rate during the deposition of the initial layer near the substrate, or by employing a deposition path which involves less cooling between layers (bidirectional deposition path in this case), or to use higher laser powers in the first few layers. The deposition has an overall random texture at low laser powers where deposition path has a very little influence on the texture, whereas an increase in laser power led to significant microstructural changes from random oriented into strong texture, showing that the development of texture is dependent on the laser power.

6.3 Effect of Scan Strategy on Grain Structure: Thick Walled build (Stage II)

To mitigate the grain size and texture inhomogeneities, a scan strategy was employed by pre-heating each layer of a build, as well as giving a delay between the layers of deposition. Figure 6-11 shows the effect of scan strategy on the microstructure of the build. From Figure 6-11.a, a normal deposition (without any scan strategy), it can seen that the grains are contained within each layer, with smaller grains at the bottom of the build, which increase in size as the build progress. Also, the demarcation between the layers slowly starts to disappear. The grain size was around 70µm, with a maximum grain size of 200µm and the

average grain size has increased to 120µm with some grains as big as 800µm. This can be seen in the top portion of the EBSD map, where the grains were larger and growing from the grains in the previous layers, rather than independently nucleating at each layer. This can be explained by the thermal model, Figure 5-9, where at the bottom portion of the build (until 4 layers of the build), the previous layers would only re-melt at the top portion and as the build progress, the previous layers are completely re-melted (due to heat accumulation) and the grains would grow epitaxially from the previous grains rather than nucleating independently.

Figure 6-11.b shows the EBSD map for a deposition path with a delay. The grain size distribution was found to be more uniform throughout the build, when compared to a normal deposition with a demarcation at each layer interface. The average grain size of the build is around 75µm for all the layers with a maximum grain size of around 300µm at the middle of the build. This can be explained by the temperature profile obtained from the thermal modal (the delay strategy, Figure 5-18). The temperature reached by the layer is around 1804°C which remains the same throughout the build. The layer cools down during the delay with no heat accumulation in the build. This caused the melt pool to heat only a small top portion of the previous layer, which may not provide sufficient energy to re-melt the previous layers, making it difficult for the grains to grow epitaxially from previous layers. Rather, the grains would nucleate independently at each layer giving a uniform and fine microstructure throughout the build.

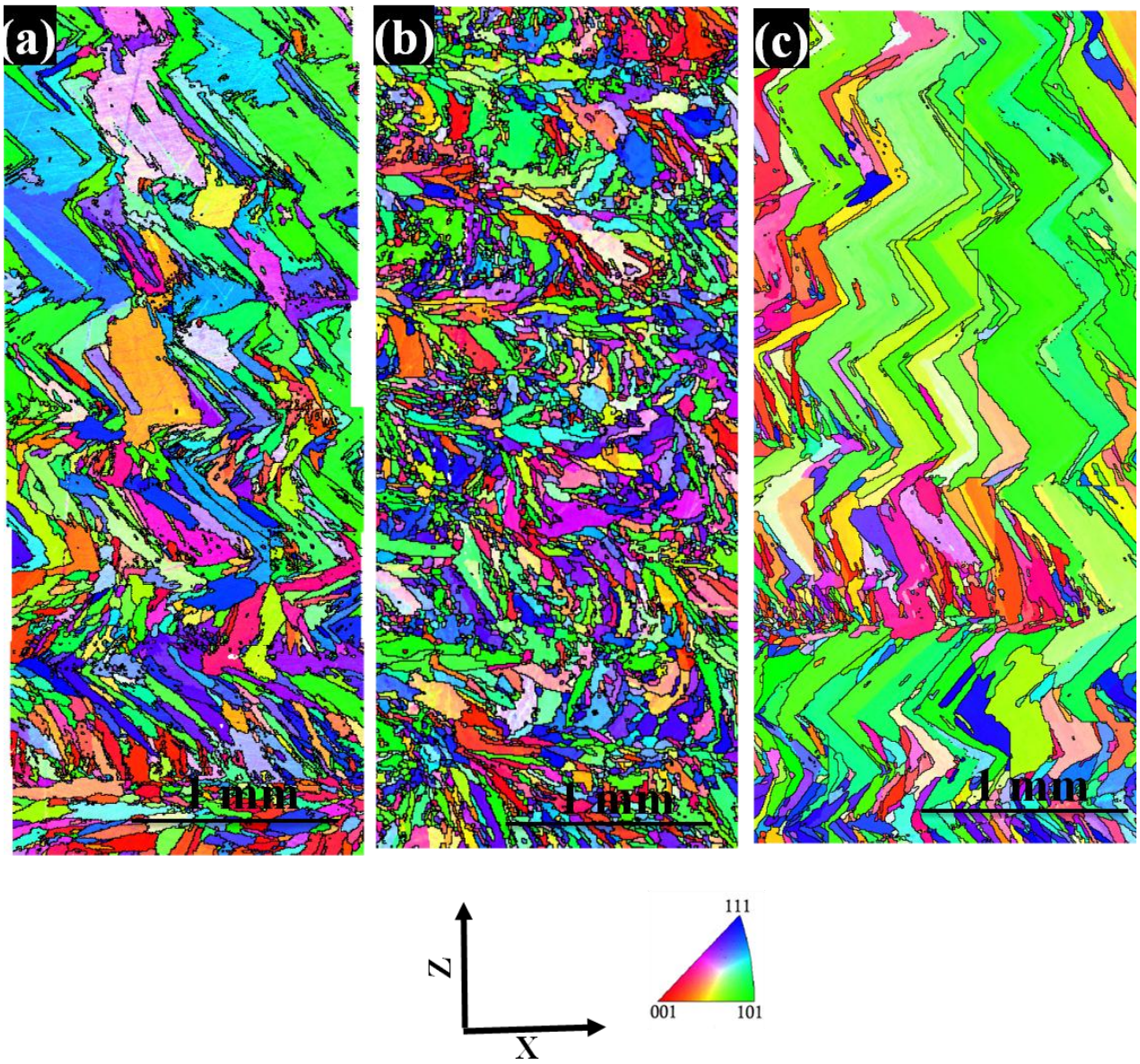

Figure 6-11: EBSD maps (2 mm × 5 mm area from bottom to top) in the XZ plane of the thick walled samples, showing the grain distribution in different scan strategies a) long b) long+ delay c) long+ post scan (with other process parameters constant).

Figure 6-11.c shows the EBSD map for a deposition path with a post scan strategy, where it can be seen that there is significant grain growth in the build after 4-5 layers of the build. The average grain size of the deposit is around 150µm for the bottom layers, with F_{max} of 500µm for the bottom five layers. As the build progress, the F_{max} was observed to be around 1400µm. The large grain size could be due to the large amount of heat accumulation during

post scanning, where the layer would be heated by a laser beam nearly to its meting temperature without any powder that could initiate the grains to grow from the previous layers.

Figure 6-12 shows the pole figures for all the scan strategies. It becomes evident that long and long + delay deposition paths have a very weak cube to fibre texture (2.7 × random for long and 1.5 × random for long + delay strategy), similar to that observed in the thin walled samples. Conversely, the post-scan strategy showed a strong cube texture (10.5 × random) with a slight tilt from the centre. The very strong texture in this specimen is due to the epitaxial growth of the grains from the previous layer of the same orientation.

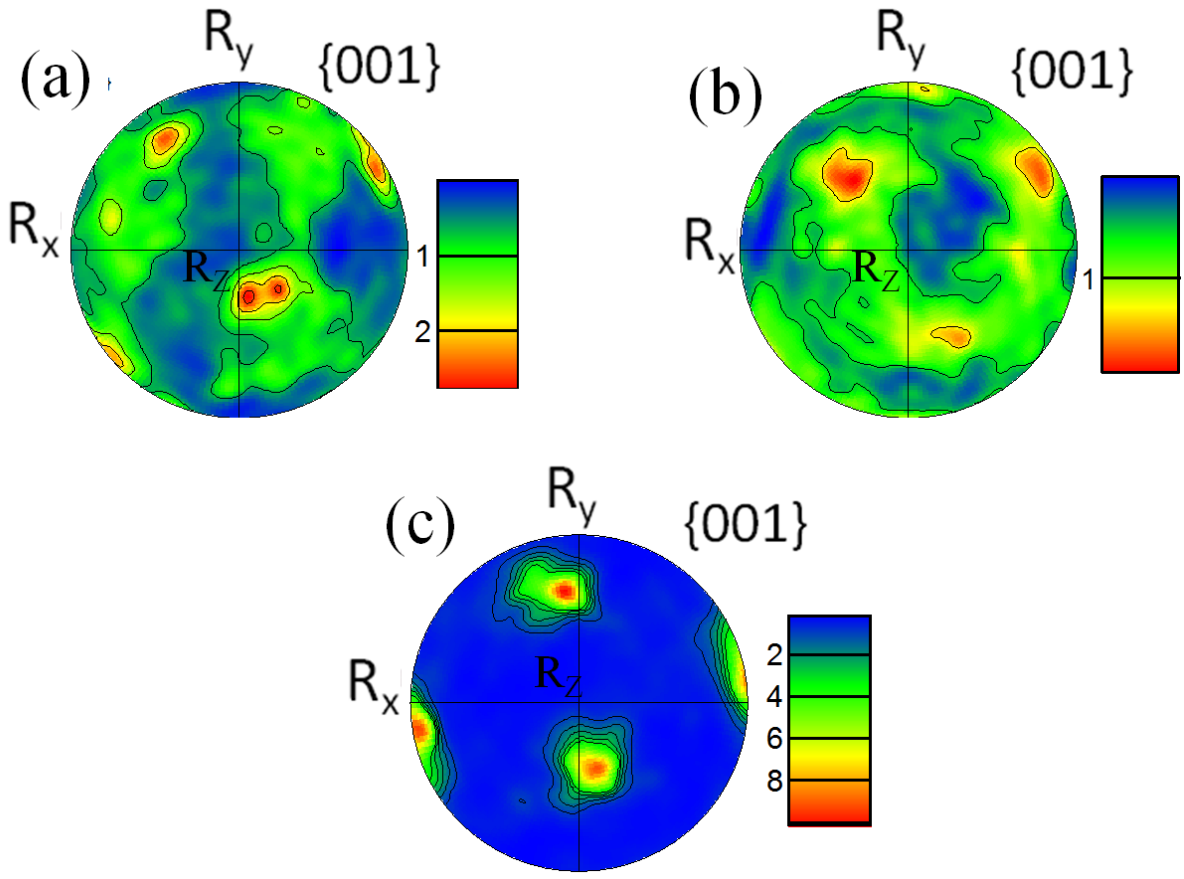

Figure 6-12: {100} nickel pole figures plotted as seen from the top of the build for a) long b) long+ delay c) long+ post scan strategy for the maps in Figure 6-11.

6.4 Microstructural Development in DLFed Solid Blocks (Stage III)

The grain morphology and texture in the XZ plane (i.e., the plane parallel to the growth direction) was studied for thin and thick walls, which reflect the conditions used in repair applications. It is also important to study the bead morphology in a three-dimensional build profile, to understand the microstructure of the build due to scaling-up to solid blocks, which is generally used in actual near net-shape parts or hybrid manufacturing. The grain morphology and distribution in all the three planes of the build was investigated. Then, a three dimensional view of a melt pool was constructed schematically based on the EBSD maps of the three planes of a single bead.

Figure 6-13 shows the bead morphology of the build in the XZ plane. The bead morphology resembles those commonly observed in multi-pass welds. Figure 6-13.a shows the layered structure where the alternate layers show the front view and side view of the bead (as marked as FV and SV in Figure 6-13.a). It was observed that the bead size is slightly larger and non-uniform at the bottom (close to the substrate), and becoming more uniform at the top layers; the differences can be attributed to the rapid cooling rates in the first layers close to the substrate. Figure 6-13.b shows the top view of the build with the hatched type morphology, which is similar to the used deposition path (Figure 3-4).

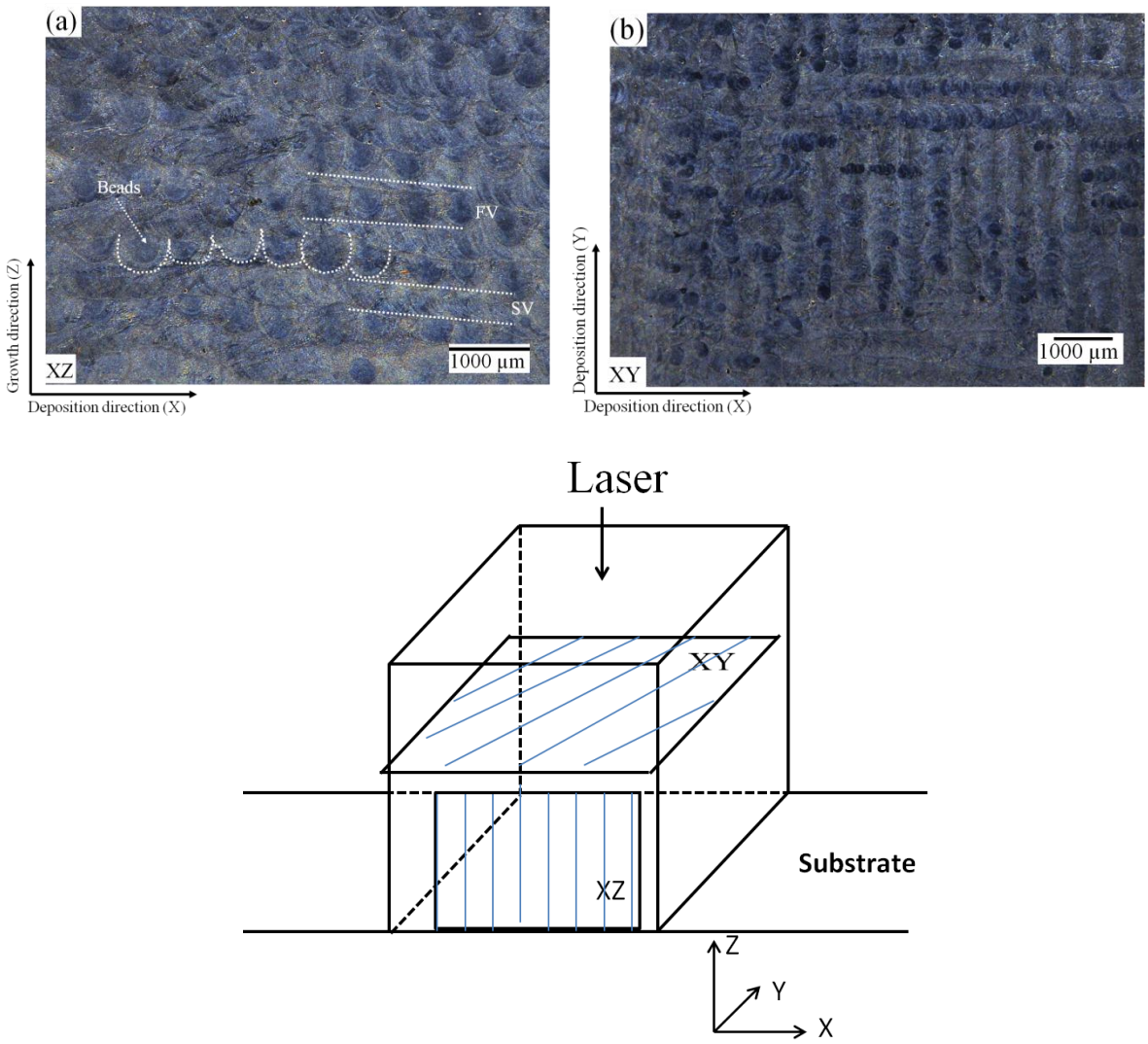

Figure 6-13: Optical micrographs for the solid block structure showing (a) the XZ plane (showing beads from bottom to 5 mm) and (b) the XY plane (taken at a plane 5 mm from the substrate) ; schematic showing the locations from which the micrographs were taken.

6.4.1 Bead Morphology:

Figure 6-14.a shows the microstructure of a single bead taken from the top layers of the build. The bead looks more elliptical than the bottom layers, which are more circular. The variation in bead shapes can be observed by comparing Figure 6-14.a, to the SEM micrograph and EBSD map taken from the bottom layers of the build (Figure 6-14.c). It was observed that the dendrites grew from the bead boundary to the centre, and were mostly contained within the single bead boundary (i.e. within the laser pass), unlike in previous studies where the dendrites were found to traverse to the next layer [12, 23]. The reason for this contradiction

could be the fact that the laser power (the heat input) is lower in this study, than in previous work [126]. The dendrite transfer can also be seen in thin walled builds with increase in laser power (in section 6.2.2). The dendrites were generally fine, with 5µm arm spacing due to the high cooling rates associated with DLF, which is also seen in thin and thick walled samples.

An EBSD map was constructed on the bead that was taken from the lower layers to understand the grain size distribution. It was found that there is a bimodal grain size population across the bead which was previously reported by Liu *et al*. [23]. Generally, a single bead can be divided into three regions (Figure 6-14.c):

Region A: Containing very fine equiaxed grain region in the bead boundary, with a mean grain size of ~ 5µm (equivalent diameter, DEq). This region was thicker at the bottom layer, than in the top layers.

Region B: Exhibiting a columnar zone from the boundary to the centre with a mean size of ~50-100µm and an aspect ratio of 2-5.

Region C: Coarse equiaxed to elongated grains at the centre, with a mean size of ~10-20µm and an aspect ratio of 1-2.

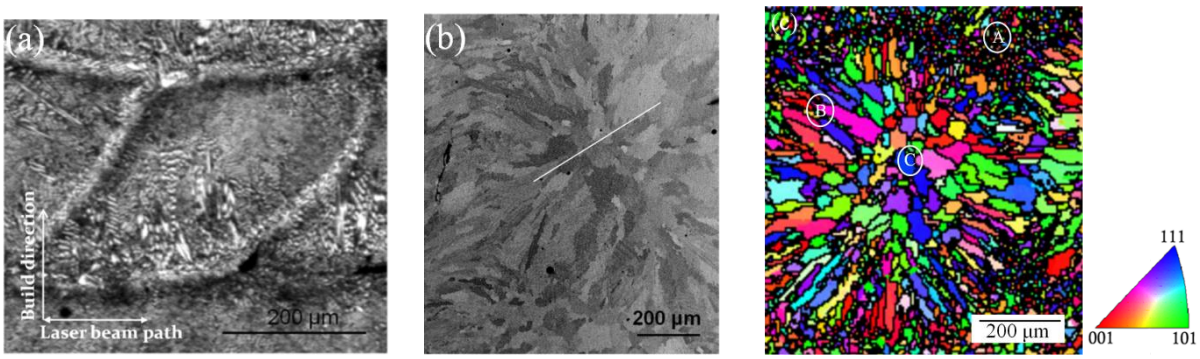

Figure 6-14: Microstructure of DLF IN718 solid block in the XZ plane, showing (a) an optical micrograph for the bead morphology showing the dendrites (white bands) protruding from the bead boundary to the centre, (b) BSE SEM micrograph of a bead showing columnar grains from the bead boundary to centre, and (c) IPF, map of the bead showing the grain morphology with different regions marked as A, B and C.

The very fine grain zone (Region: A) is similar to the one observed in the bottom layers of thin-walled samples, which contain un-melted powder particles. As a Gaussian distribution is assumed for the laser beam power in laser deposition, the maximum temperature would be expected to be at the centre of the beam, resulting in the maximum thermal gradient being in the direction from the edge to the centre of the bead. As a result, the first grains to nucleate are the ones along the maximum thermal gradient, growing epitaxially from the bead boundary to the centre (Region B). The third region at the centre (Region C) appears to be an equiaxed zone which was previously observed at the centre of the weld bead in aluminium alloy welds[85]. It is expected that as the dendrites grow from the bead boundary to the centre, solutes will be rejected (as in casting), resulting in increased nucleation, and hence forming the equiaxed grains zone at the centre [73]. At the front view of the bead, these grains could also be a cross section of columnar grains at the centre. In order to confirm this and also to simulate the bead morphology, EBSD maps were constructed on the three planes of the build.

Figure 6-15.a shows the EBSD micrographs of the different planes of the build. From the YZ view, it can be seen that the deposition has a layered structure with columnar grains growing from the substrate, then an equiaxed grain band, followed by a columnar band again. It is known that the consecutive layers are perpendicular to each other. Thus, the grains in the second layer could be still columnar, but look equiaxed as this layer is seen in a plane perpendicular to the laser beam. Based on the EBSD data, a 3D bead-shape model can be generated to visualise the grain morphology in the deposited layers, Figure 6-15.b. It can be suggested that the bead possibly has an ellipsoidal shape, based on the microstructural observations (Figure 6-14 and Figure 6-15.a), which resembles the model suggested by Suutala [15] for the beads formed in stainless steel fusion welds produced using similar speeds (300 mm/min). However, the top view (i.e. plane XY) of the build suggests that the

grains are not completely equiaxed, but have a combination of these and elongated columnar structures.

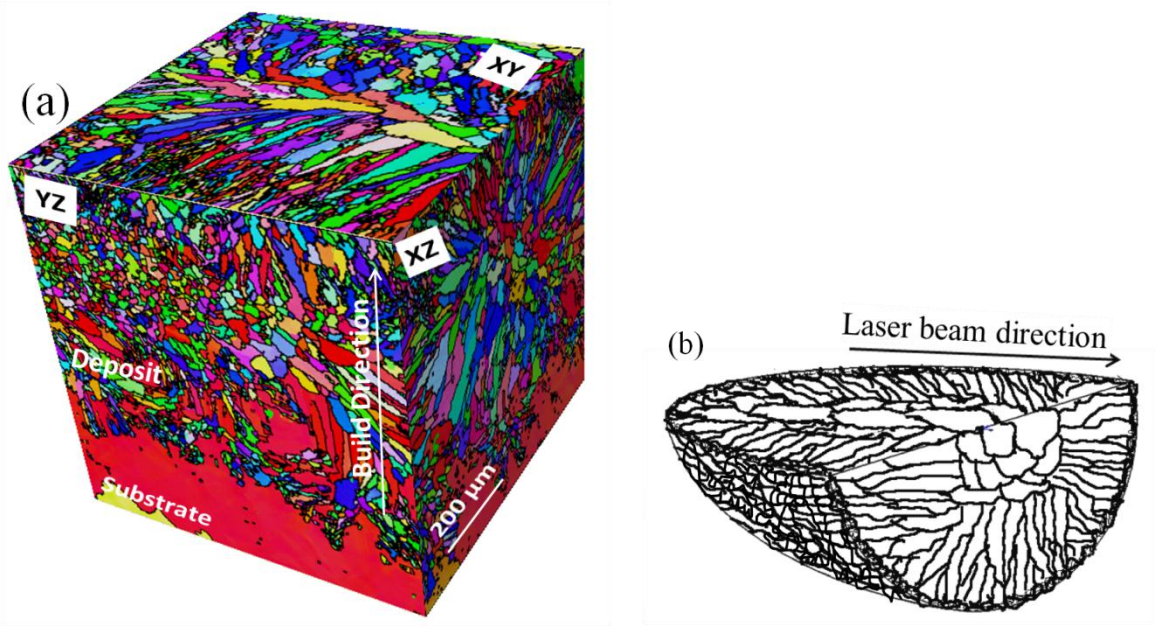

Figure 6-15: (a) Inverse pole figure (IPF) map showing the XY, XZ and YZ planes of the build, (b) Schematic showing 3D bead morphology.

Figure 6-16 show the EBSD mapping of the top plane, mapped at mid-height of the build, and showing two deposition passes. The grain structure, due to the alternate deposition passes, resembles a weld microstructure [202] , displaying a generally random texture with very weak {100} cube texture for the two layers. The columnar grains tend to be oriented along the maximum thermal gradient, which is along the centreline of the moving heat source. The deposition path follows a zigzag pattern, where the two passes are in opposite directions. Each pass is ~500µm wide, with an overlap of 300µm. This overlap was maintained in order to obtain a porosity free build. It is believed that when the second pass intersects the first pass, the columnar grains would melt and form a re-melted zone, which has equiaxed grains.

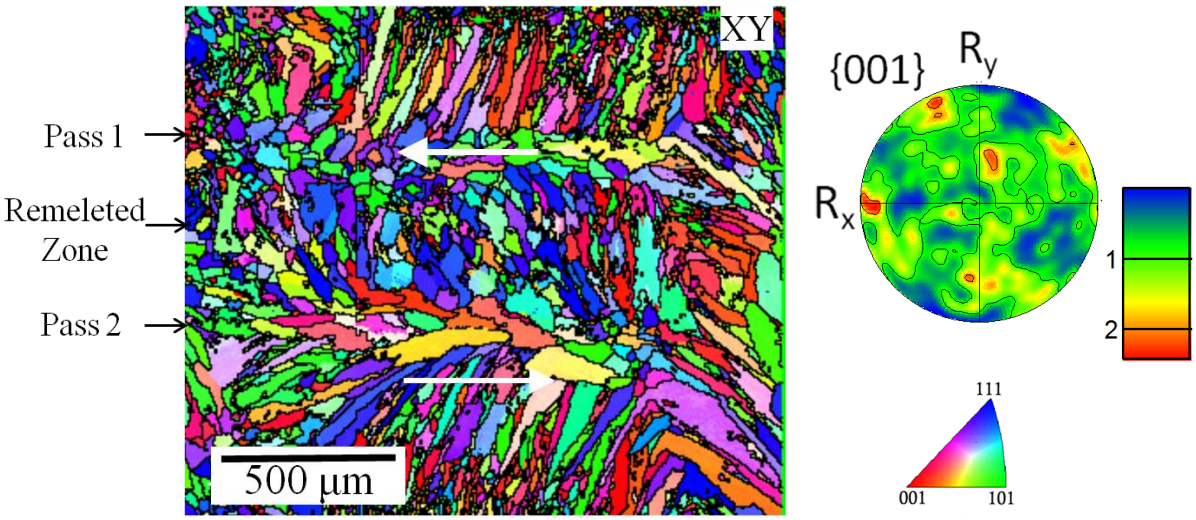

Figure 6-16: IPF map of the XY plane (top view) of the build showing the overlap of two passes, and the corresponding pole figure for the two layers.

6.4.2 Grain Size

Figure 6-17.a shows the grain size distribution of the solid block in a 1 mm × 1 mm (measured in the area shown in Figure 6-16). The grain structure shows a bi-modal distribution, with 65% of the examined area covered by columnar grains of size of 50-100µm, and 15% with grains in the size range of 10-20µm with very few grains at the centre of the build having grain size above 100µm. Figure 6-17.b shows the maximum and average grain size measured in an area of 1 mm × 1 mm area from the top to the bottom of the build. The average grain size tends to increase from the bottom to the top of the build. For the top layers of the build, the heat sink is the previously deposited hot layer, unlike the bottom layers where the heat sink is the cold substrate. As the heat does not get dissipated much in the top layers, the grains tend to grow slightly larger than the layers below. There is an exception in the first layer, due to the pre-scan employed before deposition (to improve the build-substrate bonding) which makes the substrate hot for that moment. In the final layer, there is no heat from the laser and the layer cools down very quickly. This is the reason for the decrease in the maximum grain size at the uppermost layer. The reason for the very low mean grain size (20-30µm) is the very fine grains present at the bead boundary. The mean

grain size increases slightly as the build progresses from the bottom to the top. These fine grains could be un-melted semi-solid particles as seen in thin and thick-walled builds in the previous sections. These fine grains were previously observed by Blackwell [2] on the fracture surface of a laser build. Although the build produced a fine grain structure, the grain size distribution suggests that the build has non-uniform grain size distribution throughout the build due to difference in the cooling rates present at different locations of the build. Due to this the grain growth may not be uniform during post deposition heat treatments.

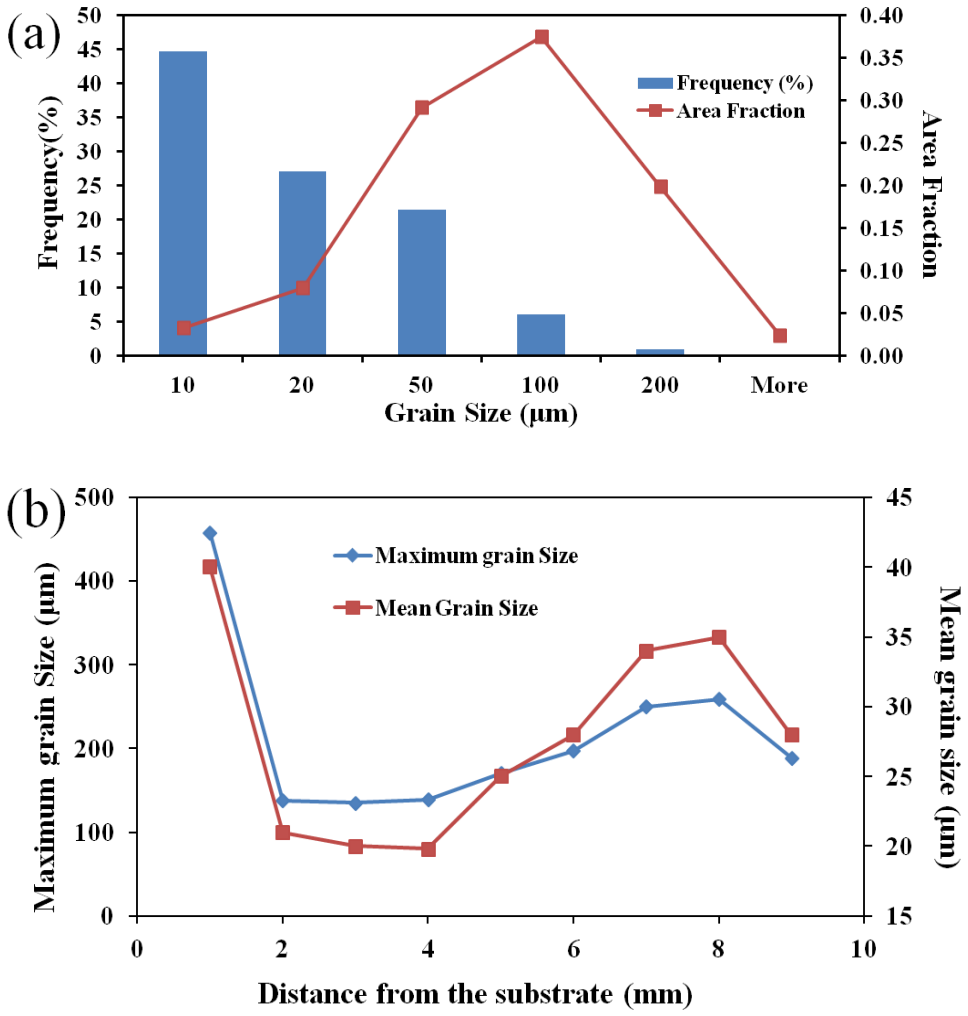

Figure 6-17: (a) Grain size distribution in a 1 mm × 1 mm area at the centre of the build, and (b) grain size variation from the bottom to the top of the build.

6.4.3 Grain Selection and Texture: Influence of substrate texture

In repair or hybrid manufacturing, it is important to understand the effect of the substrate condition (e.g. forged, cast, single crystal) on the build microstructure especially to see if the grain orientation in the build would follow the substrate orientation. In order to see this effect clearly, the build was deposited on a very large grained cast substrate. Figure 6-18 shows the EBSD map of the XZ plane of the build, showing 3 mm of the build from the substrate. The EBSD map showed a large grain at the bottom, which is the cast substrate, whereas the build itself shows a banded structure, with alternating bands showing the front (represented as X) and side (represented as Y) of the melt pool. This is due to the use of hatched type deposition path, where each layer is deposited perpendicular to the next layer. The build showed large non uniform beads at the bottom as observed in the optical micrograph (Figure 6-13.a). In the first few layers, the build is closer to the cold substrate and the melt pool would solidify rapidly producing non-uniform beads sizes whereas in the top layer of the build (image taken at 6 mm from the substrate, Figure 6-18, Xn) uniform beads are observed. This problem could be mitigated by increasing the laser power and scan speed, while decreasing the powder flow rate in the initial layers. After a few layers of deposition, when the build is away from the cold substrate, the porosity due to un-melted particles caused by limited heating of the melt pool would decrease.

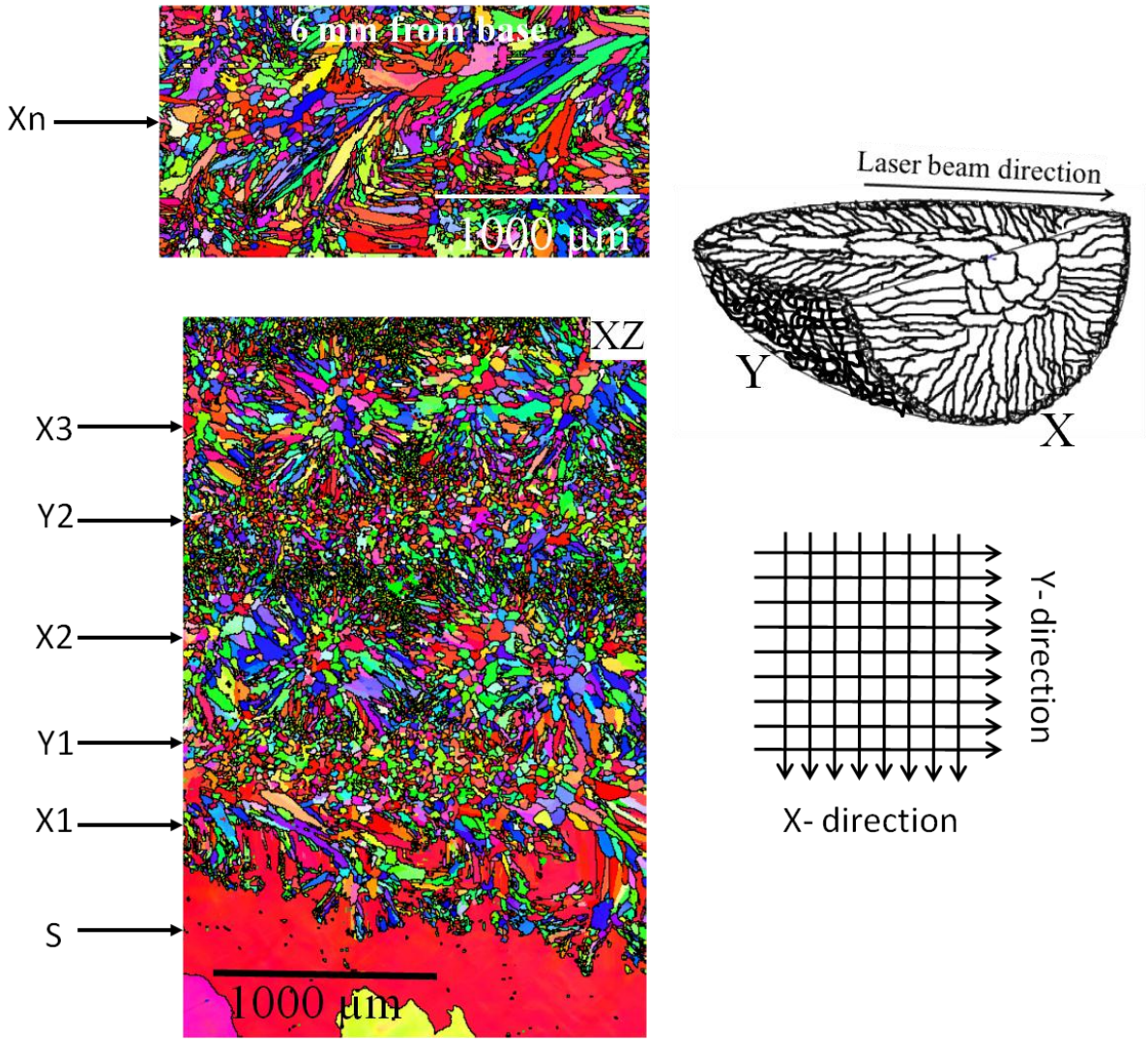

Figure 6-18: EBSD map from the bottom to the top of the XZ plane of the build.

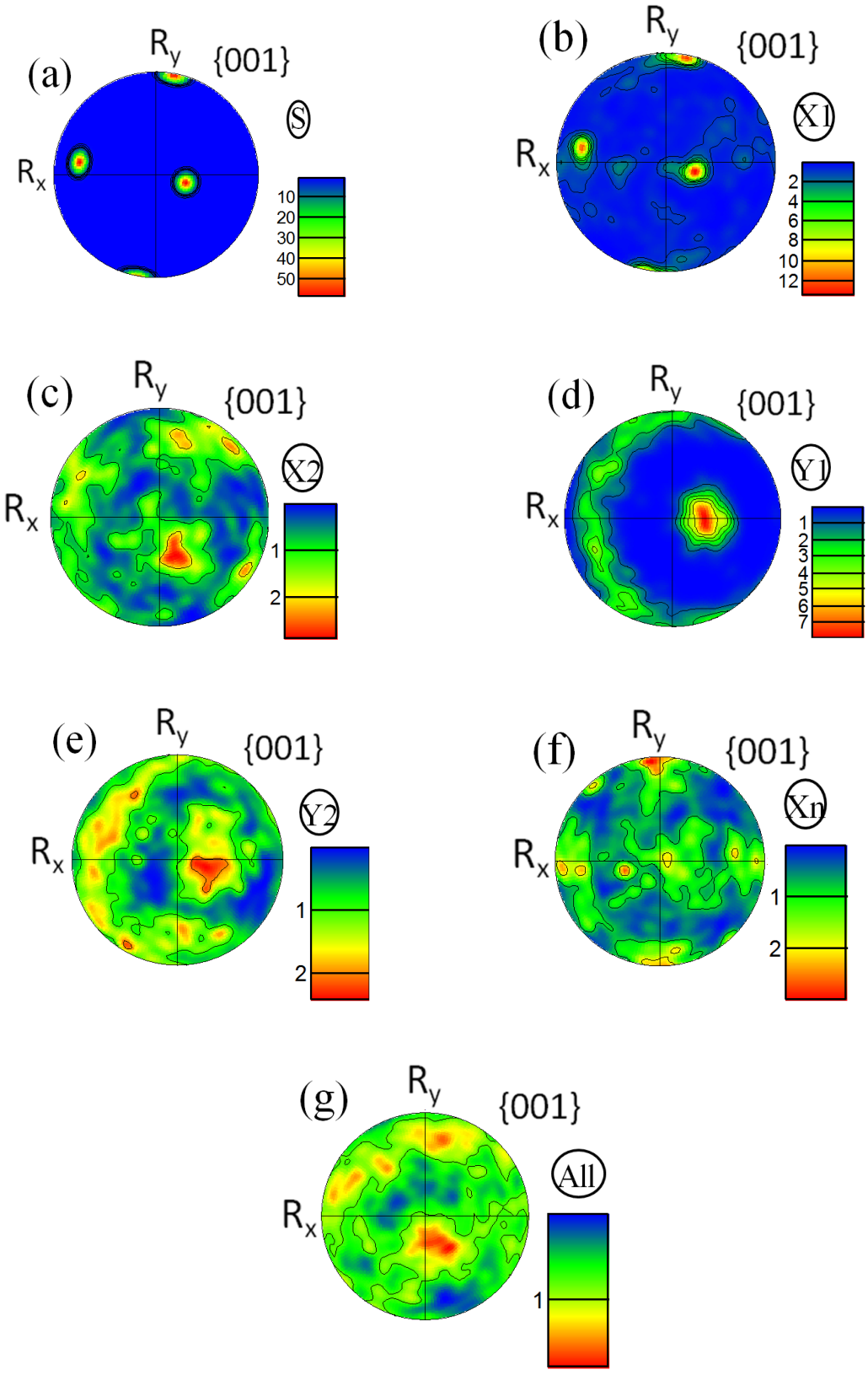

Figure 6-19: Pole figures plotted at different layers of the build as marked in Figure 6-18.

In order to trace the grain selection along the build height, pole figures were plotted at different locations of the build, Figure 6-19. Microtexture {100} pole figures were constructed from the different locations of EBSD data (marked in Figure 6-18), keeping the growth direction (GD) parallel to the deposition direction. Clearly, the substrate is a single coarse grain, with a strong orientation, Figure 6-19.a. Interestingly, the first layer (X1) of the build has almost the same texture as the base plate (Figure 6-19.b), but slightly weaker (14× random) and oriented towards the growth direction, which highlights the influence of the substrate grain structure and microtexture on the nucleation of the grain structure in the first layer. Generally, for a cubic crystal, <100> is the favourable growth direction during solidification [203].

The second layer (X2) showing the fine grains, which originate from the side of the melt pool, show a <100> fibre texture which is 9× random (Figure 6-19.d). In solidification, fibre textures are more common, whereby the grains tend to be oriented along the moving heat source meanwhile growing parallel to the <100> direction, giving a fibre texture. The fibre texture was previously observed by Moat *et al.* in laser fabricated Waspaloy [15] and by several authors in other alloys [3, 10, 204]. However, this fibre texture is seen at the edge of the melt pool, whereas as we move to the centre of the melt pool a cube texture is observed (as seen in Figure 6-19.a &c, where the texture on the centre of the melt pool is plotted). In the edge of the melt pool, the maximum thermal gradient occurs. As the melt pool cools down the edges of the melt-pool would try to orient themselves along the heat flux direction. Whereas at the centre of the melt-pool the melt-pool remains hot for little long time giving the grains sometime to orient themselves in a cube fashion (the favourable growth direction for FCC metals)

As the build progress, the texture is similar to the base material however, it has weakened substantially (2 × random at 2 mm from the base plate, Figure 6-19.c & e). Further up in the

build, the influence of the substrate texture slowly decreases to a random orientation. The layer, which is around 6 mm from the substrate, shows a weak cube texture (Figure 6-19.f), showing that the build has a similar orientation to the substrate only for the first few layers, and later no obvious influence of the base plate texture can be found. Figure 6-19.g shows that the macro-texture of the entire build is random. The reason for this is that there is a disruption in the texture from layer to layer because of the changing heat source direction in each pass. In other words, the grain orientation in layer n and n+1 are in opposite directions, forming a disruption in the macro-texture.

6.5 Precipitation in DLF of IN718

Figure 6-20 shows the optical micrographs of thin walled sample at the bottom, middle and side of the build. From the figure it is seen that the bottom and side of the build has a larger number of precipitates/dendrites than the middle. On examination with an SEM it is evident that the precipitation in the middle and the side of the build is similar, however the dendrites are slightly closer and oriented in a particular direction compared to the middle where the dendrites are random. The fine dendrites oriented in a certain direction compared to coarse random dendrites at the centre, could be due to very fast cooling rates present at the bottom as well as the sides of the build. Figure 6-22 shows the hardness contour for the entire build. From the figure we can observe that the hardness at the bottom and edge of the samples is slightly higher, which could be due to fine dendrites present here.

From Figure 6-20.a, it was found that the microstructure in the build had a dendritic morphology, with primary dendrite arm spacing (DAS) of ~ 5μm, which is comparable to other observations of laser deposited Ni-superalloys [199]. The hardness of the build was ~ 240VHN which is lower than wrought IN 718 (~ 440 VHN for a solution treated and aged condition [52]) but slightly better than cast IN718 (180-200VHN for 50μm dendrite arm

spacing [205]). From Figure 6-23 it can be seen that the hardness does not vary much with the deposition path, but an increase in hardness was observed with increase in laser power up to 40VHN.

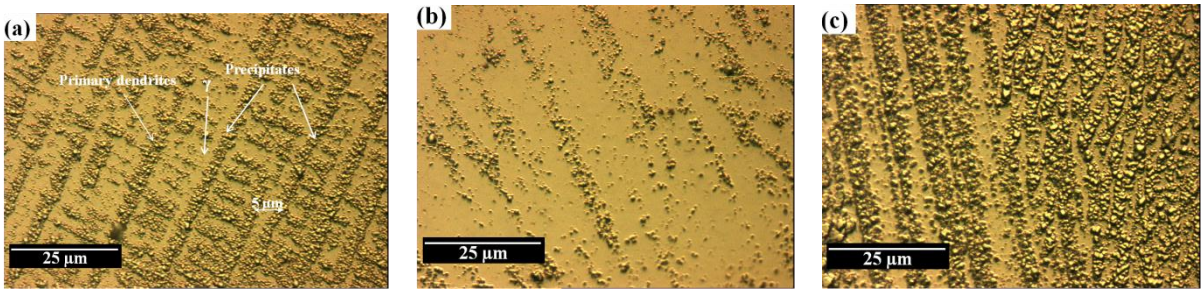

Figure 6-20: Optical micrograph of B1 sample etched with Kelling's reagent showing different regions of the build: a) bottom b) middle and c) side.

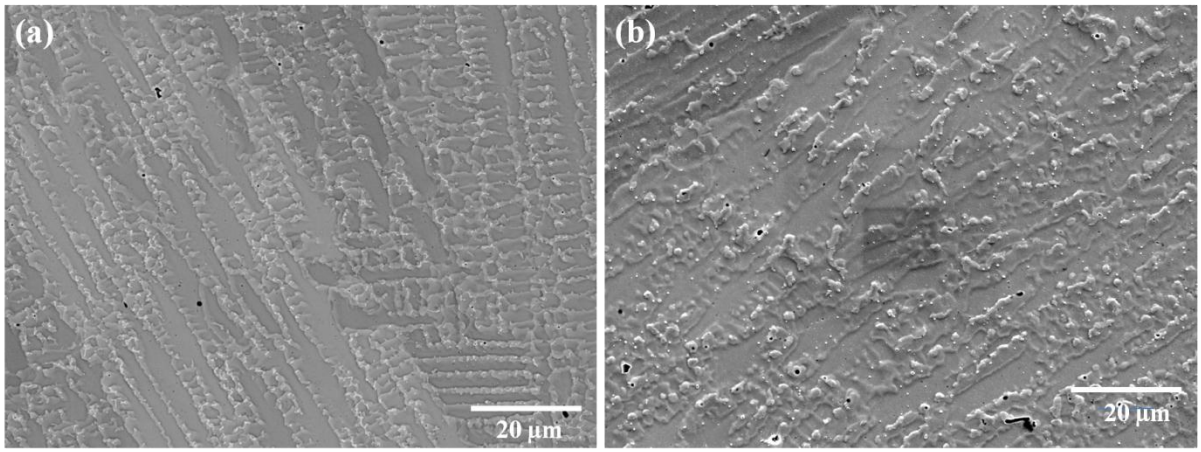

Figure 6-21: BSE micrographs showing the dendrite morphology at the a) bottom, and b) middle of the builds for the sample in Figure 6-20.

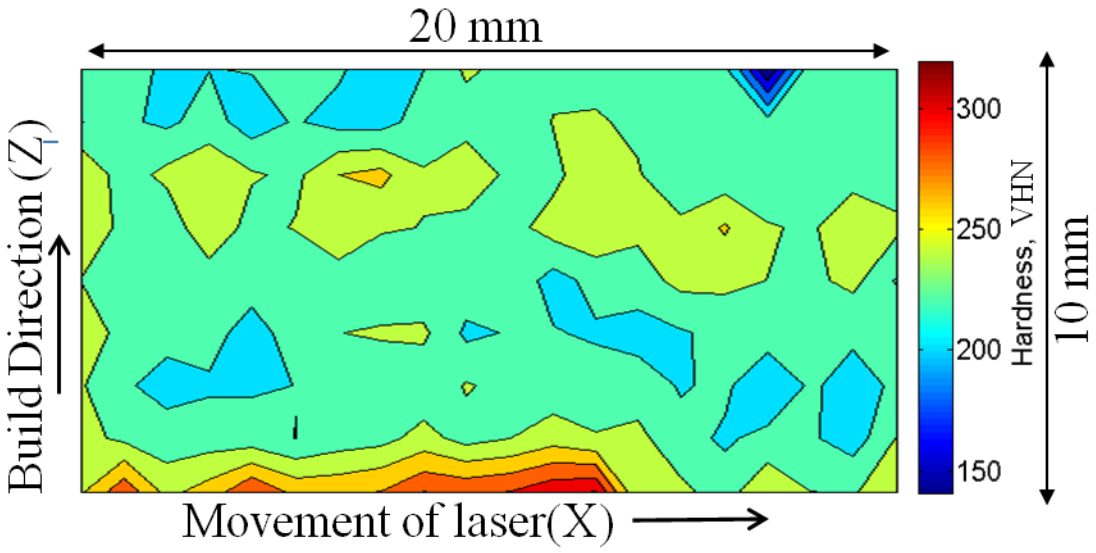

Figure 6-22: Hardness contours in the thin-walled samples (B2 sample).

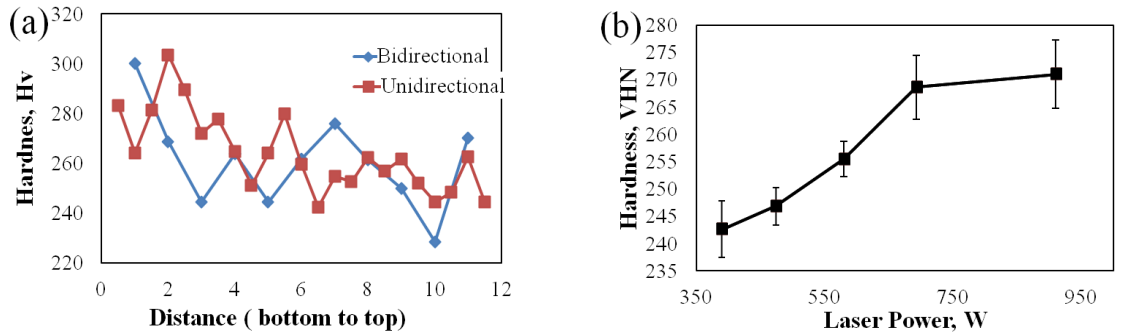

Figure 6-23: Hardness development due to DLF, showing: a) hardness traces (from bottom to top) in B1 and B2 samples b) Variation in hardness with laser power keeping the other process parameters constant (measures at the centre of the build taken from an average of 10 points).

Figure 6-24 shows high magnification micrographs for the precipitates for 390W (B2) and 910 W (B3) laser powers. As is evident, DLF generated a unique precipitate structure due to the rapid solidification associated in this process. Generally, both B2 and B3 builds showed a dendritic microstructure, with considerable segregation within the dendrites as is apparent from the contrast levels in the BSE images. White irregularly-shaped precipitates were observed in the inter-dendritic regions. Some differences in the precipitates structures were

observed between the two builds. The size of the precipitates was ~1-2μm in B2 whereas in B3 the precipitates are larger (high power builds), with less diffuse etch response around the precipitates, probably due to reduced segregation, in the low power deposits. The precipitates were oriented in the growth direction of dendrites (i.e. the solidification direction), and the size of these precipitates was around ~20-30μm (Figure 6-24.a), with a few precipitates as long as 100μm (Figure 6-24.b). EDS analysis showed that the precipitates are rich in Nb, Mo and Ti, which are the principal elements of the Laves phase (Figure 6-25).

Furthermore, the area around these precipitates was also Nb-rich (segregation), compared to the matrix but lower than the precipitate content. The Laves appears to form in the inter-dendritic regions due to solute rejection during solidification. Laves phase are irregularly-shaped precipitates which form due to Nb segregation, with the other alloying elements to form phases of a typical composition of $(Ni, Fe, Cr)_2(Mo, Nb, Ti)$, instead of γ" ($Ni_3Nb$). Qi *et al*. previously observed precipitates with similar morphology and composition in DLF IN718 builds, and this was also confirmed as being the Laves phase [22]. This phase is detrimental to the mechanical properties, and would affect the liquation crack sensitivity [206], but it can be dissolved into the matrix by certain heat treatments.

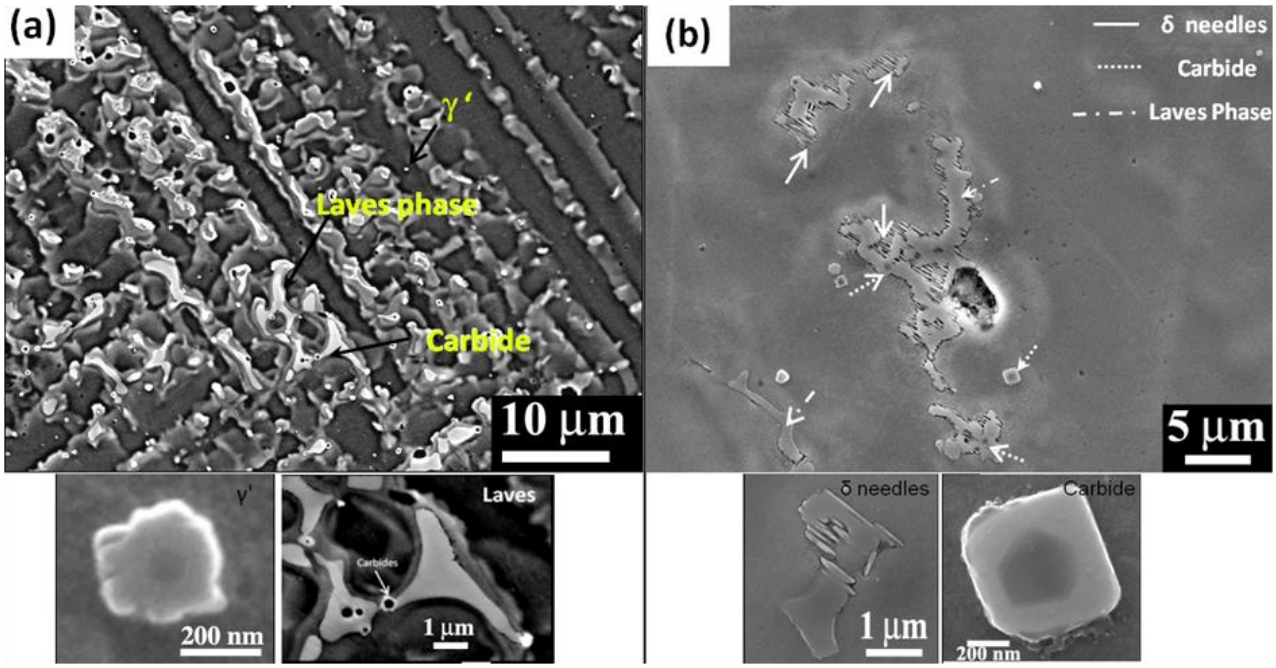

Figure 6-24: BSE SEM micrographs showing the intermetallic precipitates in (a) B2 (lower inset shows the γ′ and Laves phases at higher magnification) and (b) B3 (lower inset shows the δ needles at Laves phases and carbides at higher magnification).

Other than Laves, a few faceted precipitates (marked as carbides in Figure 6-24.a & b) were observed, which have been observed previously by Qi *et al.* [22], in laser deposited IN718 samples. The faceted carbides are generally primary MC-type carbides, with M being Ti, Nb and Zr [31]. EDS analysis showed that these carbides are rich in Ti and Nb (Figure 6-25). Very small globular precipitates (around 200-300 nm) were also observed, which have a disc shaped morphology and could thus be γ' precipitates. Line scan showed that the phase is rich in Ti, Nb and Al the principal elements of the γ' (Figure 6-25.b). The precipitates are too small to exactly measure the composition and confirm them to be γ'. TEM analysis needs to be carried out on these particles in the future to confirm these phases.

At high laser power, there were needle-like structures protruding from the precipitates, which resemble the δ phase morphology [207]. They were also observed by Clark *et al.* in MIG SMD processing of IN718 [208]. In general, precipitation of δ phase occurs following ageing for less than 100h at a temperature range of 750°C to 1000°C, with maximum precipitation

occurring at 900°C at the grain boundaries. Azadian *et al.* [207] stated that δ precipitation can start at lower temperatures at stacking faults in the γ" phase. δ phase has been also observed emanating from NbC particles, apparently providing the Nb required for its formation [63]. Because of the high laser power and the continuous heat input, the deposit layers could possibly stay at high temperatures for a considerable time [208], leading to the formation of δ needles at the stacking faults and also at the MC-type carbides. These δ needles can be seen protruding from the Laves phase, Figure 6-24.b, which could have provided the Nb for their formation. These needles were not observed in the low power builds due to the lower heat input, which was not enough for these needles to nucleate. Although δ phase is generally detrimental for the mechanical properties, proper morphology of these precipitates at grain boundaries could improve the creep property of these materials [59].

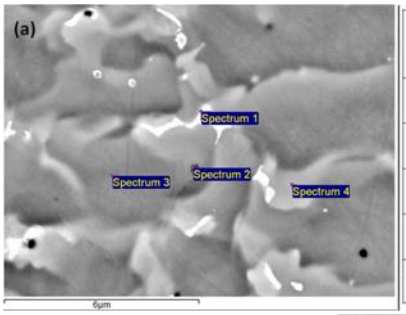

	Composition (Wt %) / Precipitates	Al	Si	Ti	Cr	Fe	Ni	Nb	Mo
Spectrum 1	Precipitate (Laves)	0.27	0.47	1.3	14.82	13.46	47	18.37	4.31
Spectrum 2	Carbide	1.33	0.11	9.19	16.8	14.97	43.35	11.45	2.8
Spectrum 3	Matrix	0.34	0.14	0.8	19.44	18.68	53.7	3.73	3.18
Spectrum 4	segregation	0.28	0.24	1.23	17.52	16.07	51.84	9.22	3.59
Powder composition	original	0.29	0.14	0.9	18.2	18.9	53.34	5.1	3.1

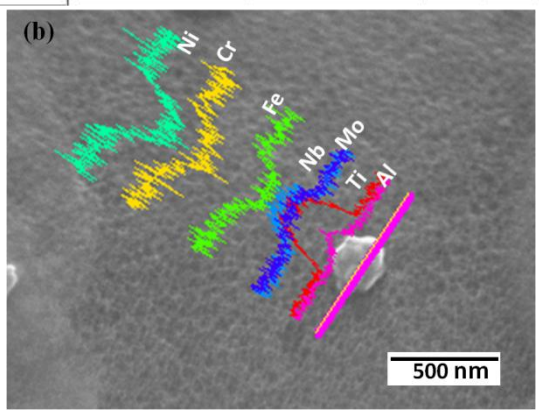

Figure 6-25: (a) BSE SEM micrograph of sample B2 showing a number of EDS point scans, and their respective chemical compositions of the various precipitates (b) EDS of sample B2 showing the composition of line scans of γ′ phase.

Figure 6-26 shows the SEM micrograph of the precipitates of solid blocks (stage III), which were found to have a similar microstructure, with segregation and Laves as in the thin-walled builds (stage I). However, the amount of segregation and the Laves phases are slightly less in solid blocks than in thin walls. This is due to the different cooling rates associated with the DLF of the solid blocks when compared to thin walls. From the literature, it is known that a welding processes with lower heat input and higher cooling rates produces less Laves phase [67]. In solid blocks, the laser would take a longer time to deposit the next layer, than in the thin walled builds, where the laser would come back immediately to reheat the materials. So, in thin walls the build would stay hotter for a longer time giving more Laves phases than in the solid blocks.

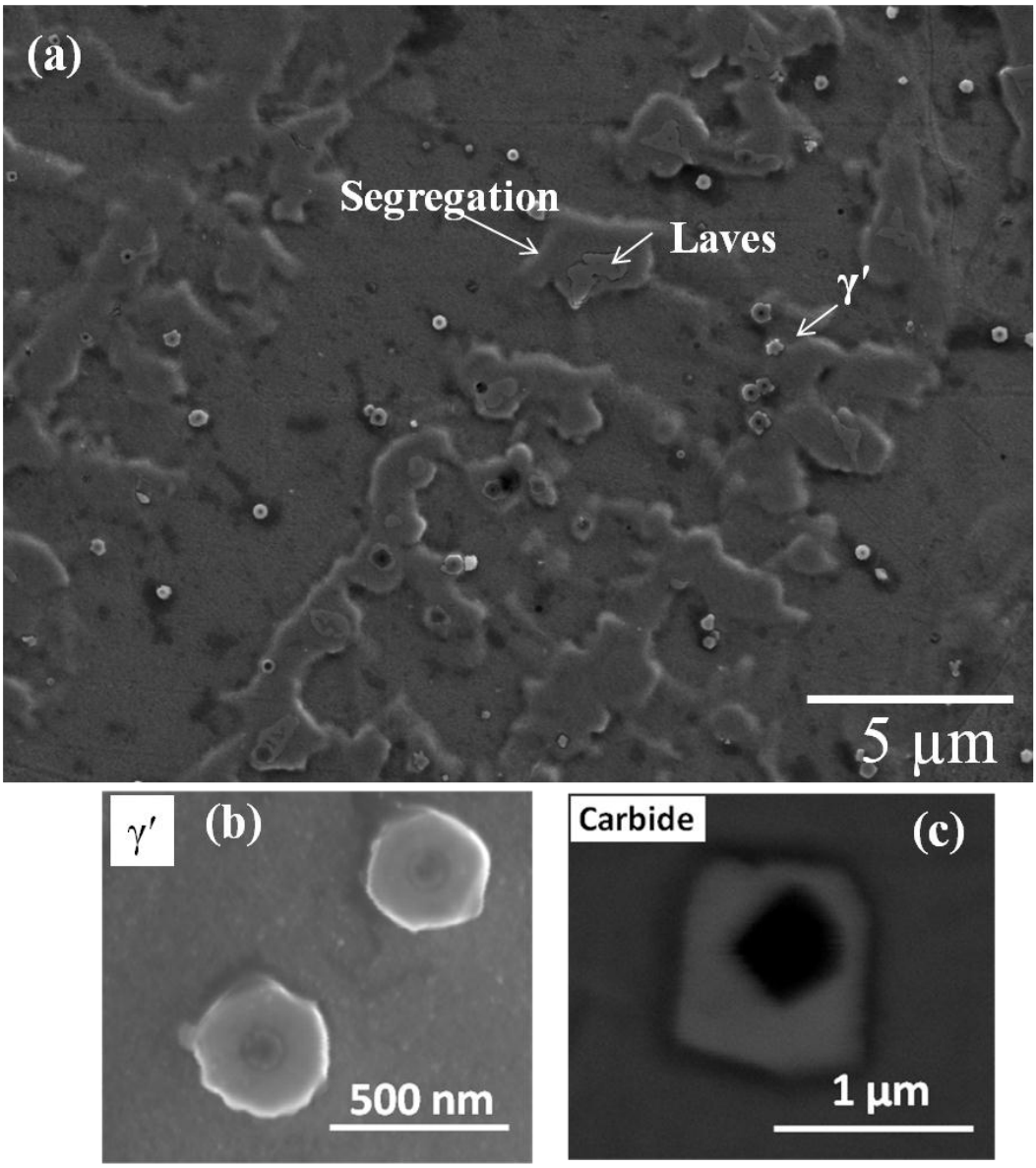

Figure 6-26: The precipitation in DLF solid blocks with inner figures showing carbides and γ′ phases.

As Laves phase is detrimental to the mechanical properties, a complete homogenisation treatment at 1093 °C was required to dissolve the Laves phase into the matrix [22]. Figure 6-27 shows the development in hardness across the build for thick wall samples, where the hardness of the as-deposited condition was around 270 VHN when compared to the substrate, which is from a rolled billet of hardness around 470 VHN. The reduction in the hardness was due to Nb segregation and Laves phases (Figure 6-27.b), retaining the alloying elements

required for the hardening phases (γ′ and γ″). The hardness in the substrate reduced gradually up to 1 mm below the build, due to depletion of precipitates in the HAZ region (as shown in the inner figure in the left hand corner in Figure 6-27).

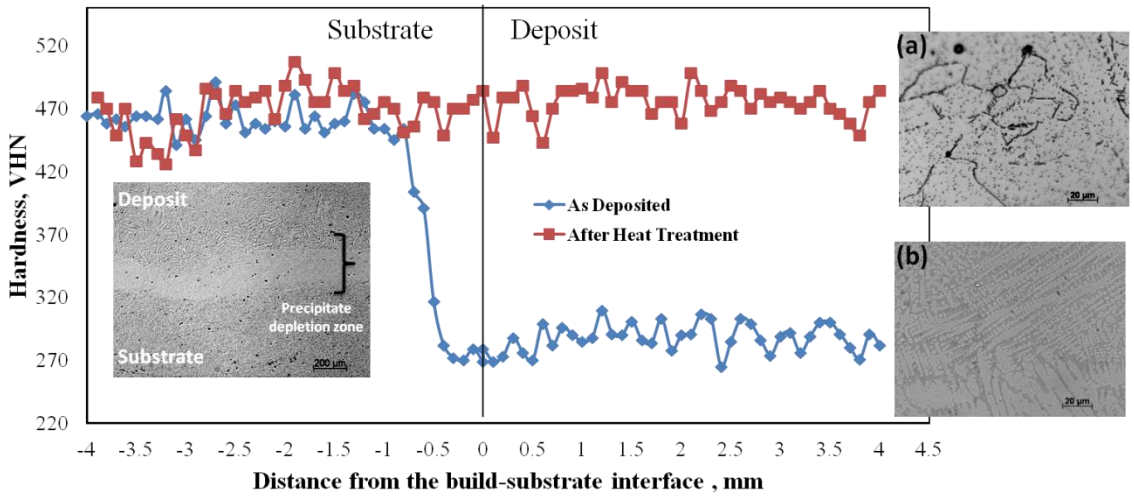

Figure 6-27: Variation in hardness in the deposition and substrate for thick walled samples before and after heat treatment.

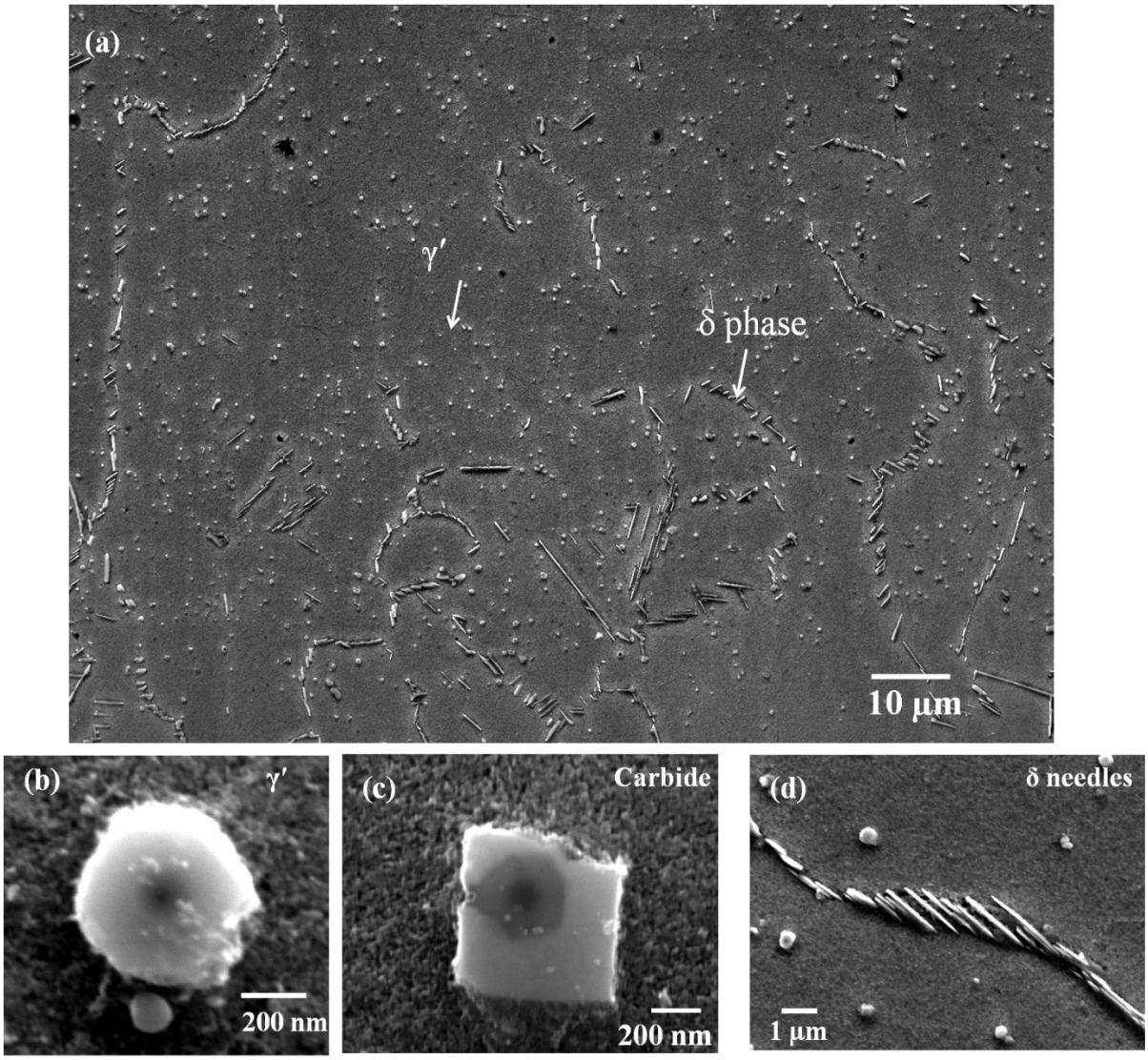

Figure 6-28: (a)Precipitates after solution and ageing heat treatment showing γ′ at the grain centre and δ and carbides at the grain boundaries (inner figures showing the enlarged images of the precipitates; (b) γ′ (c) carbide and (d) δ needles).

The hardness was restored to 470HV with solution + ageing treatment, where the Laves phases were completely dissolved into the matrix. During the ageing treatment the γ′ precipitates out in the matrix (Figure 6-28.b). The amount of γ′ is much higher and the size of this phase has doubled to 500nm after heat treatment, when compared to as-deposited condition (around 200nm). However γ″ is not observed under high magnification SEM. The solution heat treatment (1093°C) is not enough to dissolve the carbides at the grain boundaries, Figure 6-28.c, which could act as favourable sites for the incoherent δ needles,

Figure 6-28.d, to grow at the boundaries. Further analysis by TEM is required to see if the γ″ phase is present and also to confirm if the round 500nm precipitates are γ′.

Table 6-1: Composition of various phases in laser deposited IN718.

Predicted Phases (Wt %)	Al	Si	Ti	Cr	Fe	Ni	Nb	Mo
Matrix	0.2	0.1	0.4	18.9	18.6	55.1	3.6	3.1
δ	0.1	0.3	1.2	14.8	13.9	47.5	18.6	3.6
Carbide	0.5	0.1	2.34	17.7	14.8	46.3	15.6	2.8
γ′	3.3	0.0	31.8	1.8	2.4	40.5	17.8	2.3
Composition of powder	0.29	0.14	0.9	18.2	18.9	53.3	5.1	3.1

6.6 Effect of Heat Treatment on grain structure: Study on Thick Wall Samples (stage II)

After homogenisation, solutionising and ageing heat treatments (HSTA), recrystallisation was observed in the substrate. However, the build had the same columnar grain structure, Figure 6-29. The substrate was cut from a forged billet with a very fine microstructure of around 10-20μm grain size, with columnar grains in the build. As the heat treatment temperature was not sufficient for melting the carbides, which are potentially the grain boundary pinning phases, no significant changes occurred in the grain morphology after HSTA heat treatment. Also the standard heat treatment cycle would precipitate δ phase at the grain boundaries instead of γ″ phase. The presence of δ phase at the grain boundaries has been reported to be beneficial for enhanced ductility and toughness as this fine acicular δ phase at the grain boundaries provides an irregular morphology to the grain boundaries and thereby restricts grain boundary sliding and improves fracture ductility [22, 64]. However, the δ phase would pin the grain boundaries, limiting the extent of recrystallisation in the build. A heat treatment cycle has to be designed in the future to completely dissolve the Laves phases to precipitate γ″ and γ′ phases instead of δ phase. And also to completely dissolving the carbides, which pin

the grain growth and avoid recrystallisation to occur giving uniform grain morphology which could result in improved mechanical properties.

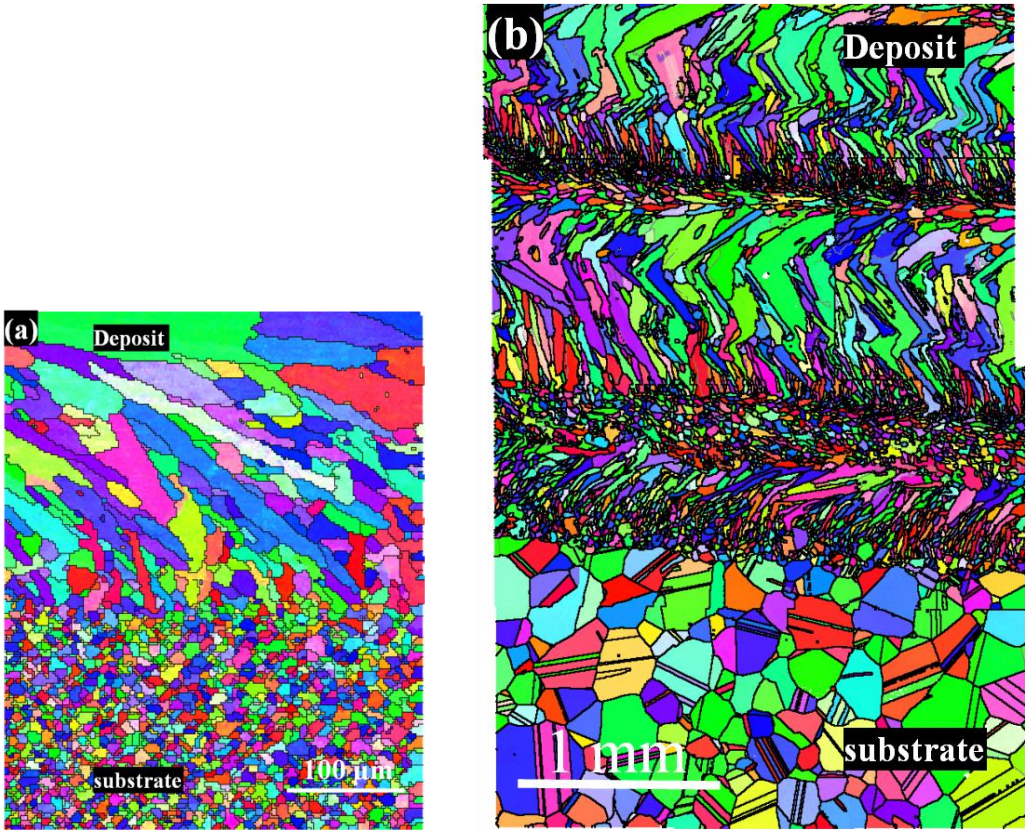

Figure 6-29:EBSD map showing the grain distribution of the build and the substrate in the (a) as deposited condition and (b) after solutionising and ageing heat treatment at 1093°C (with process parameters as in Figure 6-11.a).

6.7 Summary

The effect of various DLF parameters, in addition to post processing, on microstructural development can be summarised as follows:

Effect of deposition path:

The deposition path showed a significant difference in the dendrite orientation but only a slight variation in the grain size. However in unidirectional deposition path the first few layers showed more partially melted powder particles than in bidirectional deposition. The deposition paths did not show any variation in texture and precipitate morphology.

Effect of laser power:

Unlike the deposition path, the laser power showed a profound influence on the grain size, precipitate type and morphology, and texture. The grains grew bigger and more columnar with high laser power and showed more fibre texture than the lower power builds where small columnar grains with random texture were observed. The laser power also has an influence on the precipitate morphology, where increase in laser power increases the size of the Laves phases. Also some δ needles are formed at the Laves phases, which slightly increased the hardness of the build.

Effect of scan strategy:

A variation in scan strategy showed a significant variation in the grain size and morphology. A delay in deposition between two layers showed a more uniform small grain pattern than a normal build where the grains grew big as the build progressed. Thermal modeling suggested that during delay between the layers, the build would cool down substantially and promote independent nucleation between layers whereas with no delay a heat build-up is observed and the grains tend to nucleate from the previous layers. With a post scan between the layers, the grains grew completely columnar and showed a strong texture, as the build would stay hot twice as long as in deposition without a post scan which would allow the grains to grow bigger.

Effect of deposit geometry/size:

The build geometry did not show much variation in the overall grain morphology as both deposits showed a layered microstructure however the solid block showed slightly finer grains compared to thin and thick walls. Also at a given laser power solid blocks showed non uniform bead size at the layers near the substrate. The precipitate type is same in all the three

build geometries however the extent of segregation is less in solid blocks compared to thin and thick wall builds.

Heat treatment:

A standard homogenised STA heat treatment used for cast IN718 was not suitable for DLFed builds. The grain morphology did not change with HSTA treatment due to grain boundary pinning by carbides. As the homogenisation treatment is carried at 1093 C the carbides at grain boundaries, which would only dissolve at around 1280 °C as shown in the DSC curve (Figure 2-17) would have inhibited the grain growth. The heat treatment showed a significant variation in the precipitation where the Laves phases are completely dissolved and the γ′ precipitation is observed. The hardness of the material is regained to 470 VHN due to this. Also some δ needles are observed at the grain boundaries along with the carbides.

Chapter Seven

7 Distortion and Residual stress Development due to Hybrid Manufacturing using DLF (stage III)

7.1 Introduction

This section deals with the distortion and the corresponding residual stresses in curved substrates as a result of the deposition of solid blocks in stage III (dimensions of the substrate and deposition parameters are given in the experimental section 3.4.3).

Notation:

In this section, the distortion and residual stresses in the substrate were characterised along the X and Y directions, as represented in Figure 3-5 to Figure 3-8 (i.e. along the long and short sides), which will be referred to as X-axis and Y-axis.

For the build orientation with respect to the substrate, two orientations were studied, namely 'parallel' and 'perpendicular', with the build's longer axis being parallel and perpendicular to the substrate's X axis (as shown in Figure 3-5).

Three types of deposition paths were studied which are short (S), long (L) and hatched/mixed (H) type deposition path, as represented in Figure 3-6.

The residual stresses are represented as σ_x and σ_y for true stresses along the X and Y axes whereas σ_z represents stresses in the build-growth or Z direction.

The above notions are used in the entire chapter.

7.1.1 Distortion

The distortion in the substrate due to the deposition was assessed for the three parameters; the deposition strategy (S, H and L), laser power, and deposition orientation. The distortion was measured on the back of the substrate along the mid length of the plate using a CMM. From the results, shown in Figure 7-1 and Figure 7-2, it is evident that the distortion in the substrate is mainly concentrated at the region below the deposited block (location of deposition on the substrate is shown solid in black lines in, Figure 7-1) and extending 5 mm on each side along X direction and 15 mm along the Y direction from the deposition. It is understood that the effect of build on the substrate would be to a certain distance beyond which the substrate would no longer experience the high temperatures as well as the rapid cooling cycles which lead to distortion. Most of the work in the literature studied the effect of the build on distortion when the build size was almost equal to the substrate. However, work by Zhao *et al.* on single bead thick wall (2 mm) on a 120 mm large and 10 mm thick plate showed that the residual stresses are concentrated at around 5 - 10 mm on either side of the build [141].

The individual effects of the process parameters on the distortion are summarised below:

Effect of deposition path:

Figure 7-1.a shows the influence of the deposition path on the distortion along X axis. The S-path showed the highest distortion levels, whereas the L-path showed the least distortion. Finally, the H-path, with alternate layers of L ad S paths, showed similar distortion levels to the L-path.

In the S-path, the time taken for the laser head to build the subsequent passes is less than for the L-path. This leads to higher localised heat accumulation and to higher levels of distortion in the short deposition path in the X-direction. Vice-versa, in the Y-axis, the L-path should have higher distortion levels. Work by Fessler *et al.* [143] on DLF of stainless steel (builds of

size 100 mm × 15 mm on a 150 mm × 30 mm substrate) measured along Y axis, showed that the L-path showed higher distortion than the S-path. However, along Y-axis the different deposition paths showed similar distortion levels, Figure 7-1.b. Along the Y-axis; the substrate is around 60 mm, while the length of the deposition is 30 mm. This shows that the size of the substrate and the corresponding deposit length also play an important role in the magnitude of distortion.

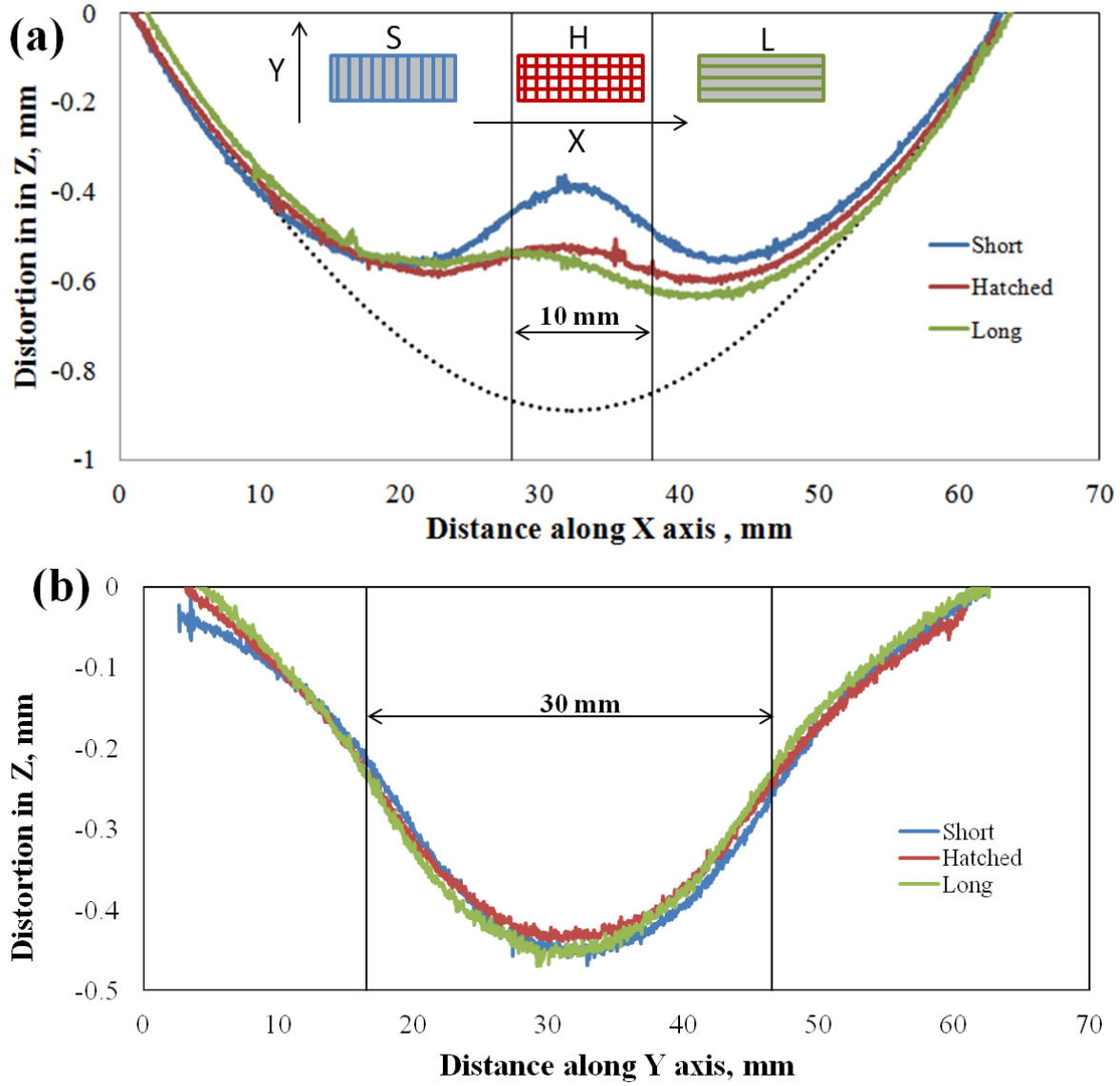

Figure 7-1: Effect of the deposition path on the distortion on a curved substrate (stage III): a) along the X-axis b) along the Y-axis. The vertical lines show the location of the build and the dotted curve shows the substrate profile before deposition.

Effect of Laser Power:

Figure 7-2.a shows the influence of the laser power on the distortion. It was found that by increasing the laser power by only 20%, the distortion levels increased in the substrate. At higher laser powers, the build would reach a higher maximum temperature than is reached for lower laser powers. This would result in a more rapid cooling, which is directly related to the temperature gradient, leading to larger distortion. It is recommended that lower laser power should be used for deposition or alternatively to pre-heat the substrate before deposition to raise the minimum temperature to reduce the distortion.

Effect of Build Orientation w.r.t the Substrate:

Figure 7-2.b shows the distortion in the deposits oriented parallel and perpendicular to the X-axis where the parallel deposition showed greater, but more uniform distortion than the perpendicular deposition. This shows that the orientation of the deposit also plays a significant role due to the variation in the cooling rates associated with the different deposition paths and directions.

From the above results, it is seen that the deposition path as well as the length of the build w.r.t the substrate play an important role in controlling the distortion levels. This is mainly due to the different thermal fields experienced by the substrate with various deposition paths based on the orientation of the build to the substrate. It is not straightforward to predict the cooling rates for different deposition paths. An investigation was performed to measure the thermal fields and cooling rates experienced by the substrate and the corresponding distortion, due to different deposition paths.

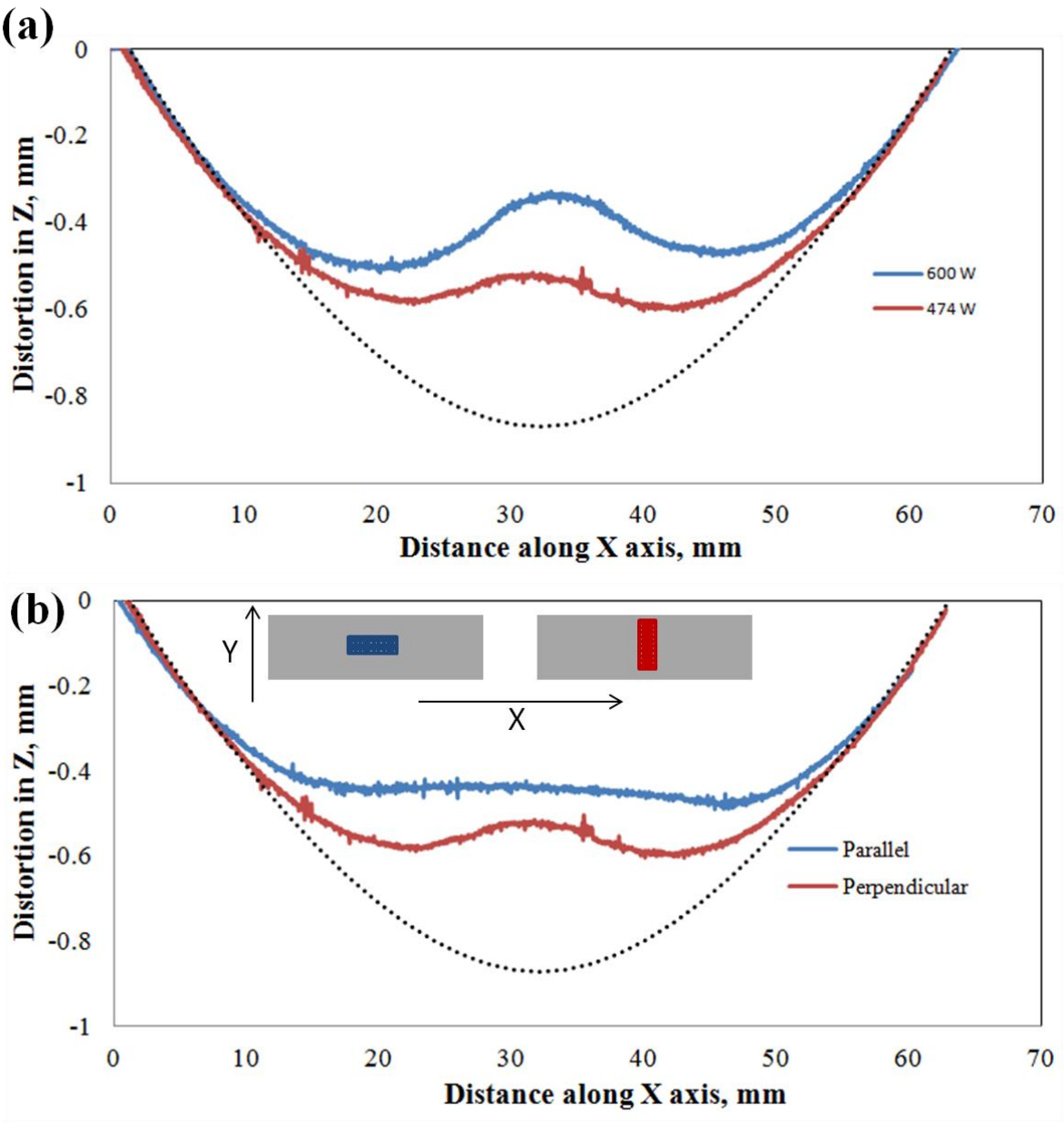

Figure 7-2: Distortion in the curved substrate along X-axis: a) showing the effect of laser power and b) showing the effect of the build orientation to the substrate on the distortion. The dotted curve shows the substrate profile before deposition. A hatched type deposition path is used.

7.1.2 Correlation of Distortion with Cooling Rates

A study was performed to understand the effect of the deposition path on the distortion, and correlate it with the corresponding cooling rates experienced by the substrate. For this, 3 depositions were made covering the entire substrate with three different deposition paths used in the previous study, i.e. long and short. A new deposition path, which is a combination of

long and short (i.e. a mixed type of deposition path), was also studied. The deposition strategy and dimensions of the build are shown in section 3.4.3 and Figure 3-7. The temperature measurement locations and other details are discussed in section 3.5.

Figure 7-3 shows the temperature profile for the three different deposition paths for the 8 thermocouple locations. The substrate attained a maximum temperature of around 40°C, at 3 mm from the build substrate interface, for all the deposition paths. However, the temperature profile was quite different for each deposition path. For the long deposition path (Figure 7-3.a), different thermocouple locations experienced varying peak and trough temperatures showing that different locations of the substrate experienced different temperatures at a given time. For short deposition path, Figure 7-3.b, all the thermocouples experienced similar peak and trough temperatures.

By performing laser scanning for the builds made using the three different deposition paths, it was possible to establish a correlation between the deposition path and the degree of distortion in the substrate caused by the thermal fields. In all three cases, the substrates become concave due to the action of laser beam, which was previously observed in the substrates during DLF [137, 143]. Comparing the distortion in long and short deposition paths (Figure 7-4.a &b), it becomes obvious that the amount of distortion is more in the longer path. The distortion in the X and Y axes for the long and short deposition paths, appears to be uniform in both orthogonal directions in the short deposition path.

To correlate the distortion with the corresponding cooling rates the distortion of the three builds at the thermocouple locations were plotted, Figure 7-5.a. The corresponding cooling rates obtained via the thermocouple measurements for the three deposition strategies were calculated as shown in Figure 7-5.b. It was found that the short deposition path resulted in the least distortion from the centre to the edge in the substrate among the three paths. By

correlating the cooling rates with the deposition path, it seemed that the short deposition path, which had the most uniform and lowest cooling rate (1˚C/s) distribution along the length of the substrate, was associated with the minimum distortion. Interestingly, the long deposition path, which led to a relatively uniform, yet higher cooling rate (~3˚C/s), was associated with the highest distortion levels obtained at the edge of the substrate. This large deformation at the edge of the substrate was previously observed by Ding on large rectangular Ti6AlV plates during WAAM process [137]. Although, not much work has been done in correlating the cooling rates with distortion in AM, previous studies showed that short inter-pass distance would give less distortion. FEM analysis of DLFed AISI 4140 steel on a rectangular plate (single layer 5 mm × 15 mm deposit on a 10 mm × 30 mm plate) also predicted least distortion in the plate with a short deposition path which was assumed to be due to the smaller temperature range than in other deposition strategies [145].

From this study it is possible to say that the deposition path influences the distortion, with lower and more uniform cooling rates producing less distortion. Deposition path plays a major role in the distortion; nonetheless the deposition direction and the length of the deposit with respect to substrate play an equal role. To get a uniform deformation the deposition should be designed in such a way that it gives a uniform cooling rate throughout the substrate during deposition which could be done either by pre-heating the substrate or by using laser beam to follow the actual deposition beam to avoid rapid cooling.

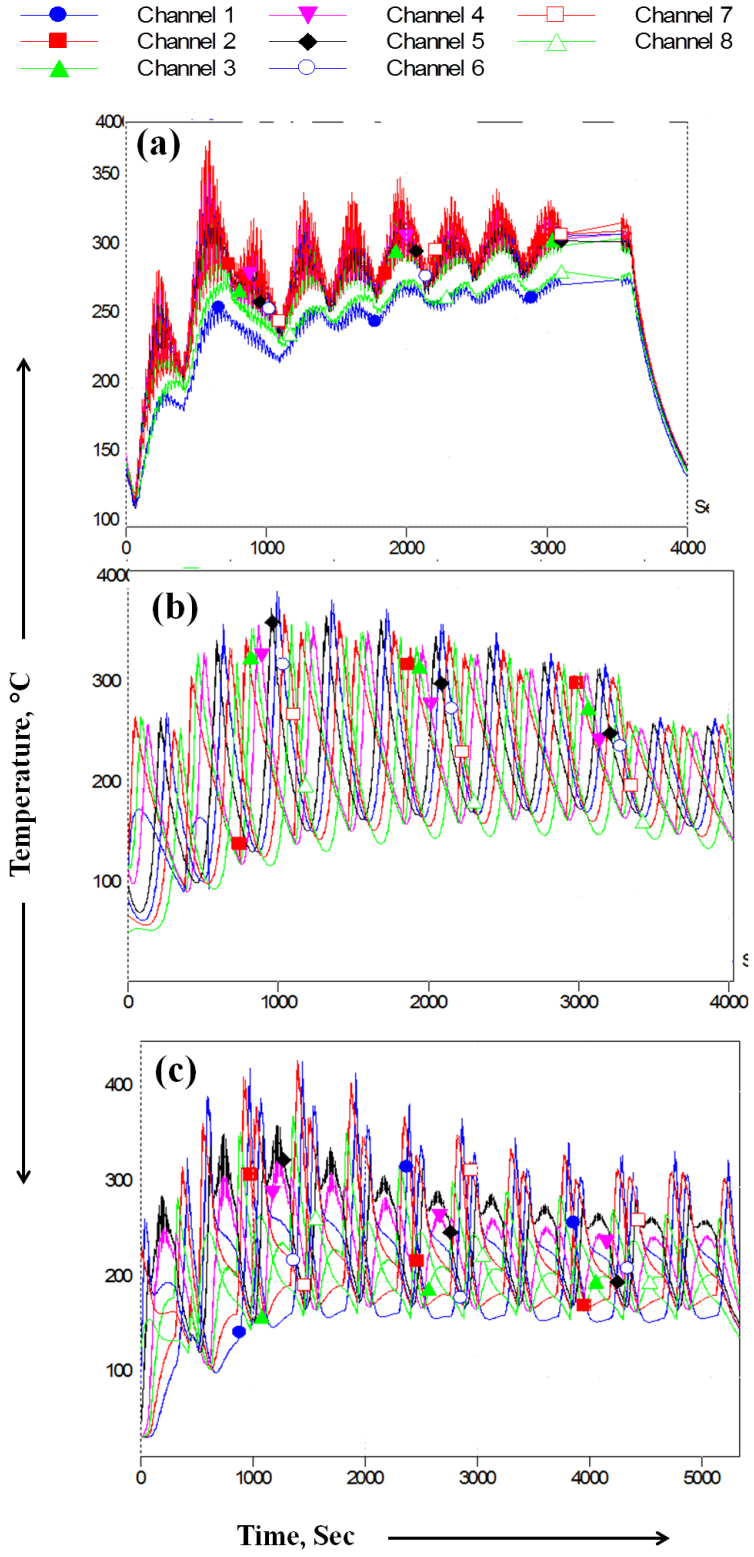

Figure 7-3: Thermal cycles at different thermocouple locations (see the location in Figure 3-10) for different deposition paths (stage III): a) long b) short and c) mixed. Thermocouple 1 and 8 are at the extreme ends of the substrate without deposition on the top.

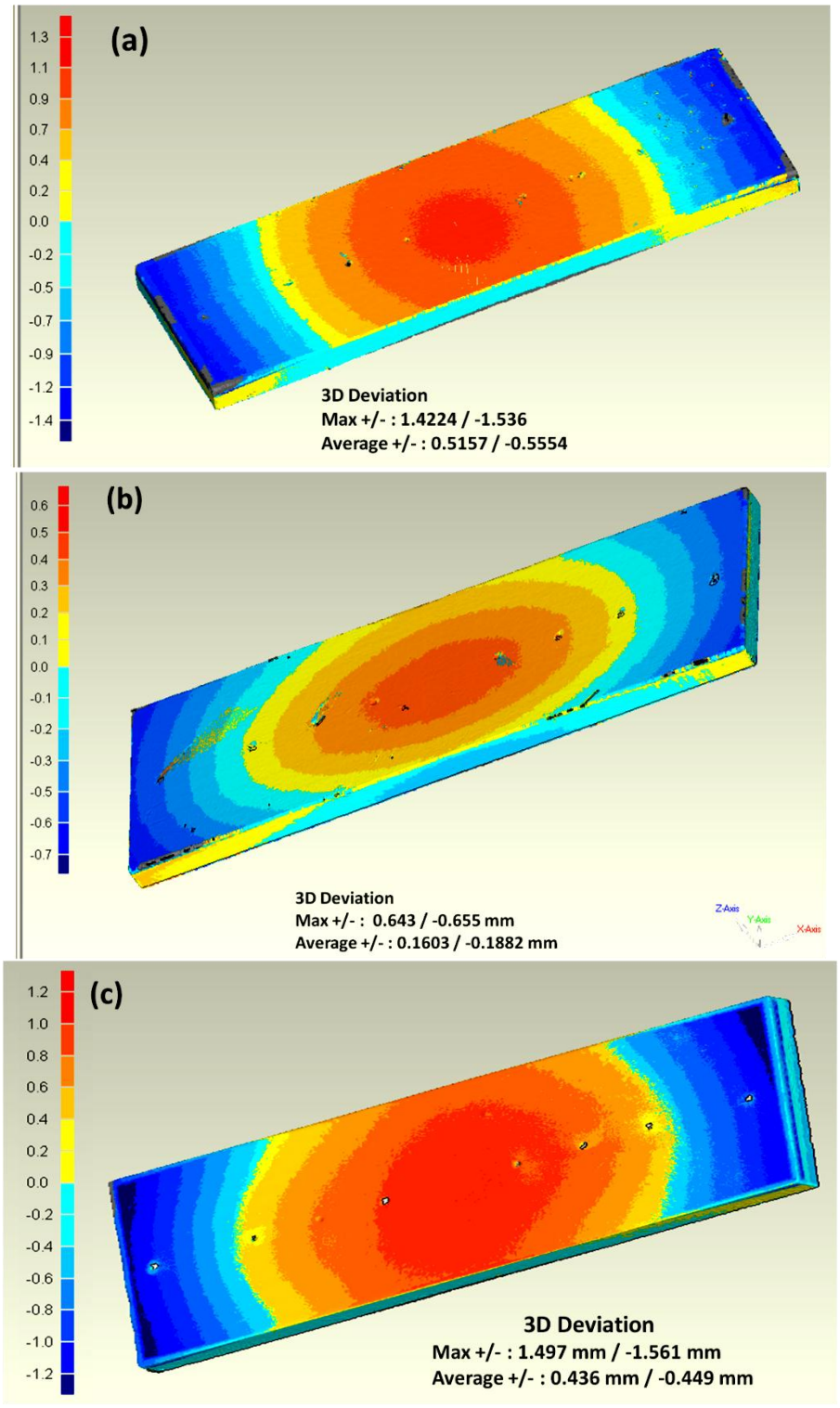

Figure 7-4: Distortion contours of the substrate in a) long b) short and c) mixed deposition paths (as represented in stage III).

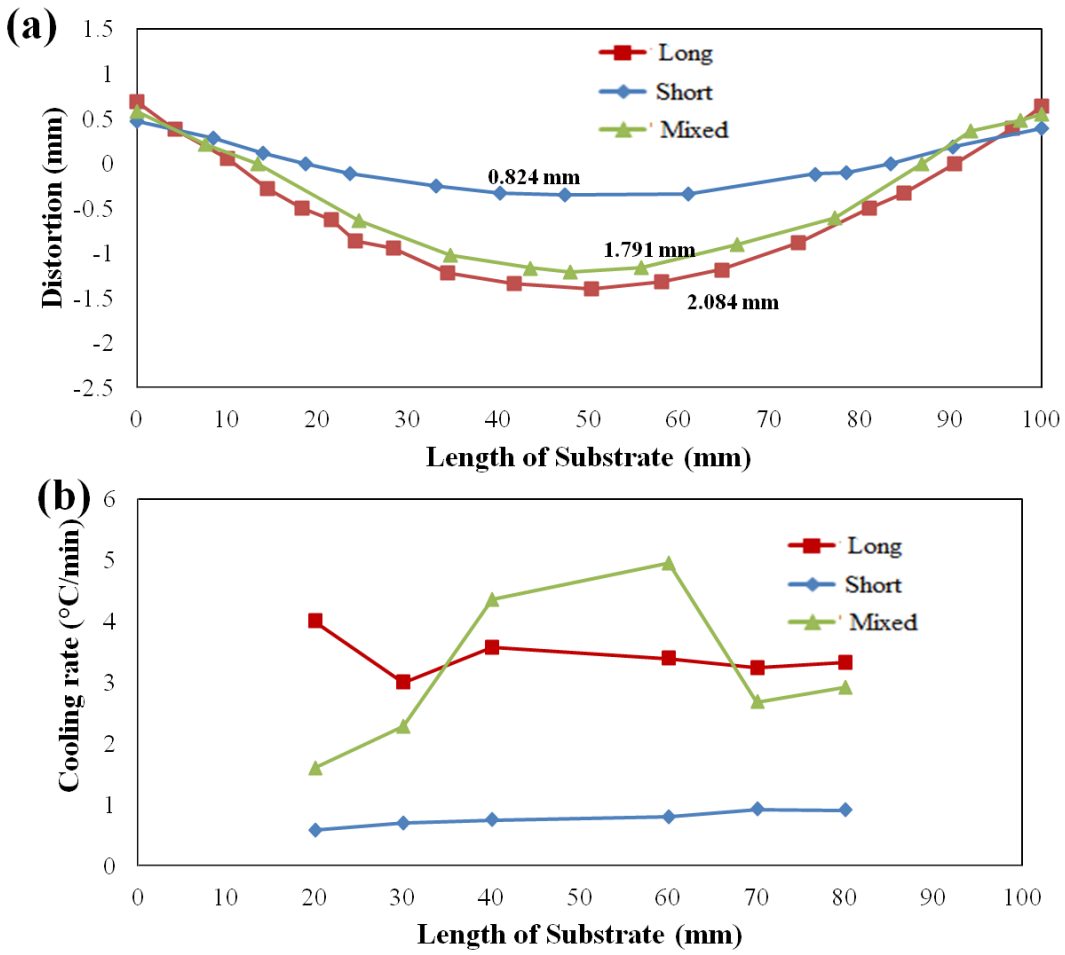

Figure 7-5: The correlation between a) distortion and b) the corresponding cooling rates in the substrate along the centre line near the 8 thermocouple locations.

7.2 Residual stress (stage III)

The effect of the process parameters (i.e. laser power, deposition direction and build orientation) on the residual stresses in the substrate, as well as in the build, are reported in this section. Neutron diffraction measurements were performed to characterise the residual stresses. The measurements were taken at mid-thickness of the substrate along the X and Y-axes (dotted lines in Figure 3-8). For characterising the stresses, the uncertainty lies in measuring stress-free d_0. Due to the small thickness of the substrate, the stress in the through-thickness (i.e. Z-direction) would be negligible [88]. Previous work showed that the stresses due to DLF in a 10 mm thick mild steel plate (modelled numerically and measured

experimentally by hole drilling) showed that they are negligible (~20 MPa) in the Z-direction, compared to the laser head moving directions (i.e. σ_x or σ_x stresses ~ 300 MPa) [141]. Residual stresses were calculated using the stress balance method, whereby the stress in the Z-direction was assumed to be zero [25] and the stress free d_0 values are back calculated. This d_0 value is used to calculate the stresses in the X direction (σ_x) and Y direction (σ_y).

Figure 7-6 to Figure 7-8 show the residual stress distribution (both σ_x and σ_y) along the X and Y-axes in the substrate. It is evident that the stress is mainly concentrated below the build, and the residual stress (especially the effect of the build on the substrate) is present up to ±10mm on either side of the build. This is similar to the distortion measurements where the distortion was found to be present up to 10 mm on either side of the build. This effect was previously observed by Zhao *et al.* on a single bead thick DLFed wall on a thin substrate [141]. For all the builds, the stresses were tensile in the σ_x direction, with compressive stresses in σ_y except at the build-substrate interface just below the build, where the stresses in both directions were tensile. This effect can be seen clearly in Figure 7-6.a & b. When a material expands in one direction, this should be compensated by contraction in another direction. This is the reason for the compressive stresses in σ_y, compensating the σ_x tensile stresses. However, the stresses at the build substrate interface, exactly below the build are tensile in both directions. Also, the magnitude of σ_x stress is higher than the σ_y. When the material experiences heating and cooling cycles, there should be enough material to compensate the expansion. At the build-substrate interface, the material would experience larger cooling rates, which would not have had sufficient time to accommodate these stresses, and would remain tensile in all the 3 principal stress directions. The tri-axial tensile stress state with higher stress σ_x direction was previously observed at the build substrate interface by Ding [137] and Zhao *et al.* [141] during multi-pass welding and DLF, respectively.

A sharp change from tensile to compressive stress was observed at the build substrate interface in σ_x and and vice versa in σ_y. When the laser beam passes on the substrate for deposition, the build as well as the substrate below would undergo tension along the deposition direction leaving a compressive field ahead to compensate this tension. This effect can be seen in the modelling chapter, Figure 5-13. This is the reason for the compressive field in the substrate immediately next to the deposition which was previously observed in welding as well as in DLF [137, 141]. The magnitude of stress in the substrate was ~180 to 250 MPa tensile and ~ -150 MPa compressive, which are below the tensile yield level in forged IN718 (~ 1040 MPa) [24]. The values are comparable with those obtained by Zhao *et al.* [141] during multi-pass welding on thin steel substrates, of around 250-300 MPa. This comparison can be made because the study by Rangaswamy *et al.* [24] showed similar stress profiles within 316 stainless steel and IN718, suggesting that the origin of stresses are thermal gradients and are independent of the materials used when the temperatures in the substrate do not lead to any phase transformations.

Effect of Process Parameters on Residual Stresses:

The input laser power has a strong influence on the residual stresses, whereby the tensile stresses increased by 50 MPa with a 20% increase in laser power, Figure 7-6. Studies by Colegrove *et al.* on welding of DH36 steel plate showed that techniques with a low heat input result in narrower tensile residual stress zone and lower stress magnitude [209].

Figure 7-7 shows the variation of σ_x due to the deposition path. An S-path showed maximum stress of ~181 MPa compared to H or L-paths which showed residual stresses of 150 MPa. The σ_y S- path generates a stress that is similar to or slightly less than the H or L-paths. This shows that the deposition path has an influence on the residual stresses although the variation is not very significant. FEM modelling of single layer rectangular AISI 4140 laser deposition

covering the entire substrate, showed that the S-path has a significantly lower residual stresses (~ 250 MPa) than the L- path [145]. Nonetheless, studies by Rangaswamy *et al.* [24] on square IN718 blocks, deposited on a large plate, did not show any significant effect of laser rastering direction on the magnitude of the residual stresses. However, in rectangular plates the rastering direction showed some effect even though not large enough to influence current processing methods. From this it is evident that the rastering pattern has a strong influence on residual stresses only if the build is large enough or covers the entire substrate.

Figure 7-8 shows the effect of the build orientation on the development of residual stress. The stress distribution in the X direction in a parallel oriented build is similar to the stress distribution in the Y direction for a perpendicular oriented build. This is because of the way in which the builds are orientated with the substrate, perpendicular to each other. However, the magnitude of stresses in the parallel build is less than in the perpendicular build, which can be explained by the more uniform distortion in this case as seen in Figure 7-2.b.

From the above results, it is evident that the residual stresses are not only dependent on the deposition path, but also on the direction of the build with respect to the substrate due to variation in thermal fields and cooling rates with respect to the substrate orientation. While depositing a square block, a hatched raster pattern would give uniform stresses in all directions given the length of the substrate below is the same in all directions.

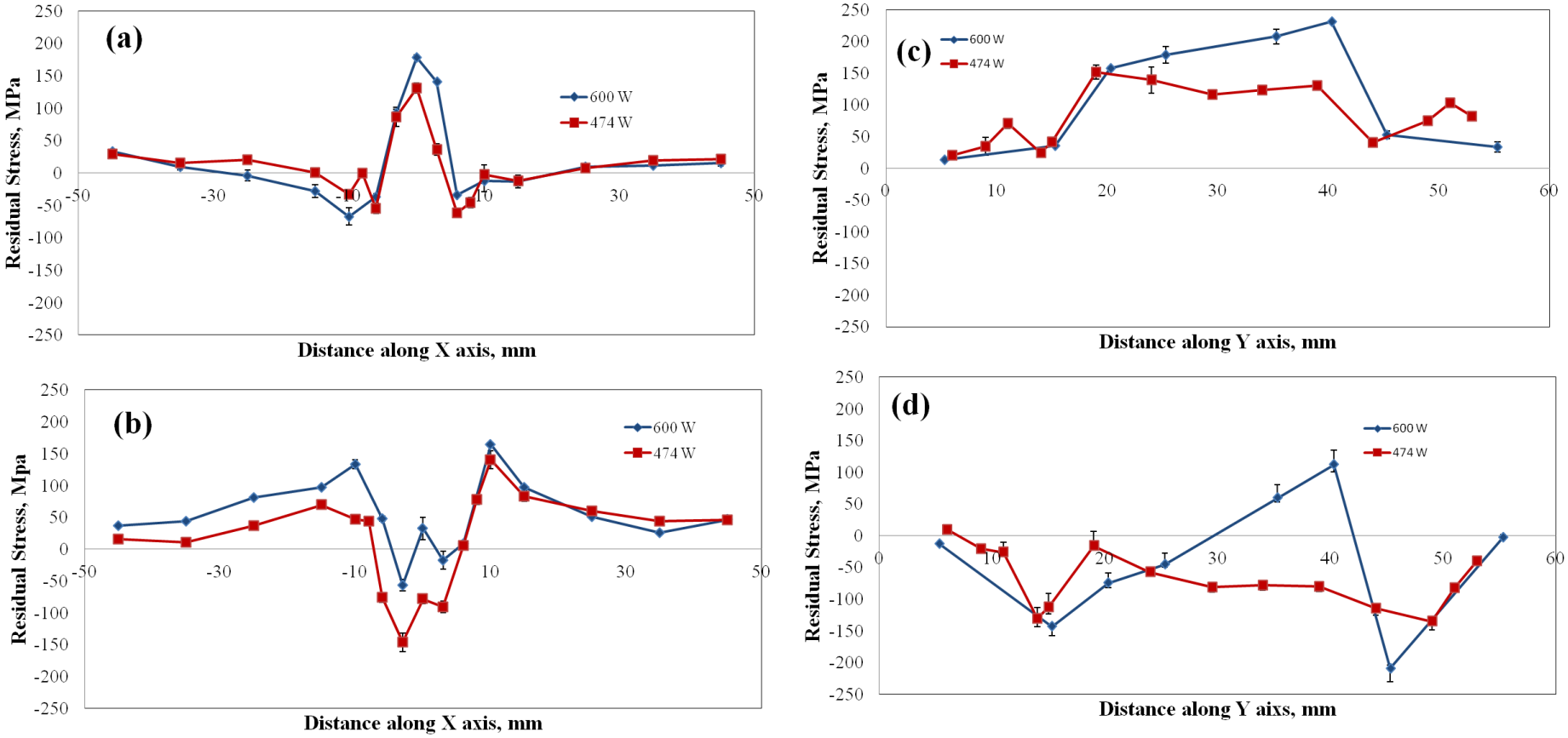

Figure 7-6: Effect of laser power on residual stress distribution in the substrate: a) σ_x stress along X axis, b) σ_y stress along X axis, c) σ_x stress along Y axis, and d) σ_y stress along Y axis.

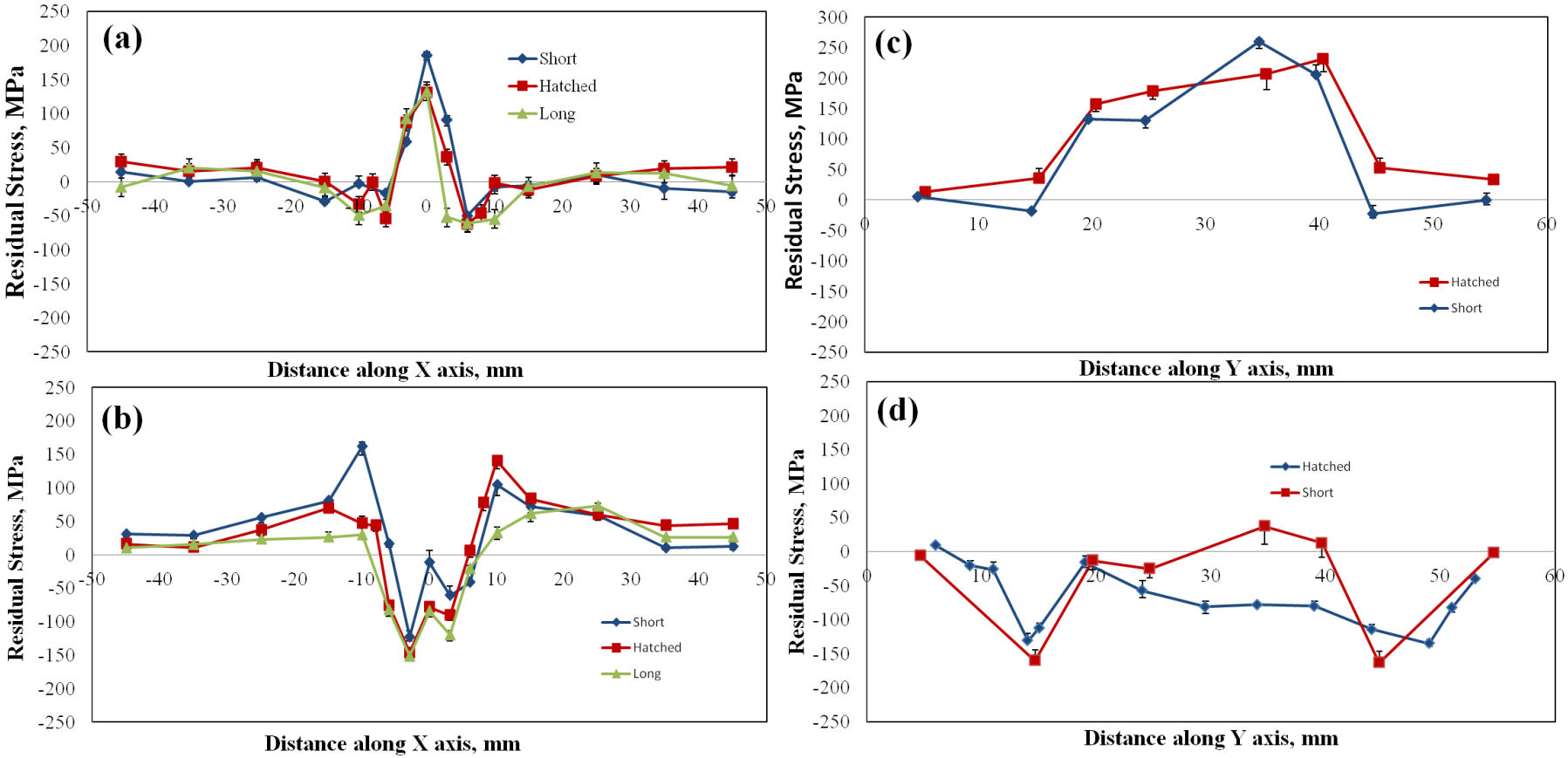

Figure 7-7: Effect of deposition path on residual stress distribution in the substrate: a) σ_x stress along X axis, b) σ_y stress along X axis, c) σ_x stress along Y axis, and d) σ_y stress along Y axis.

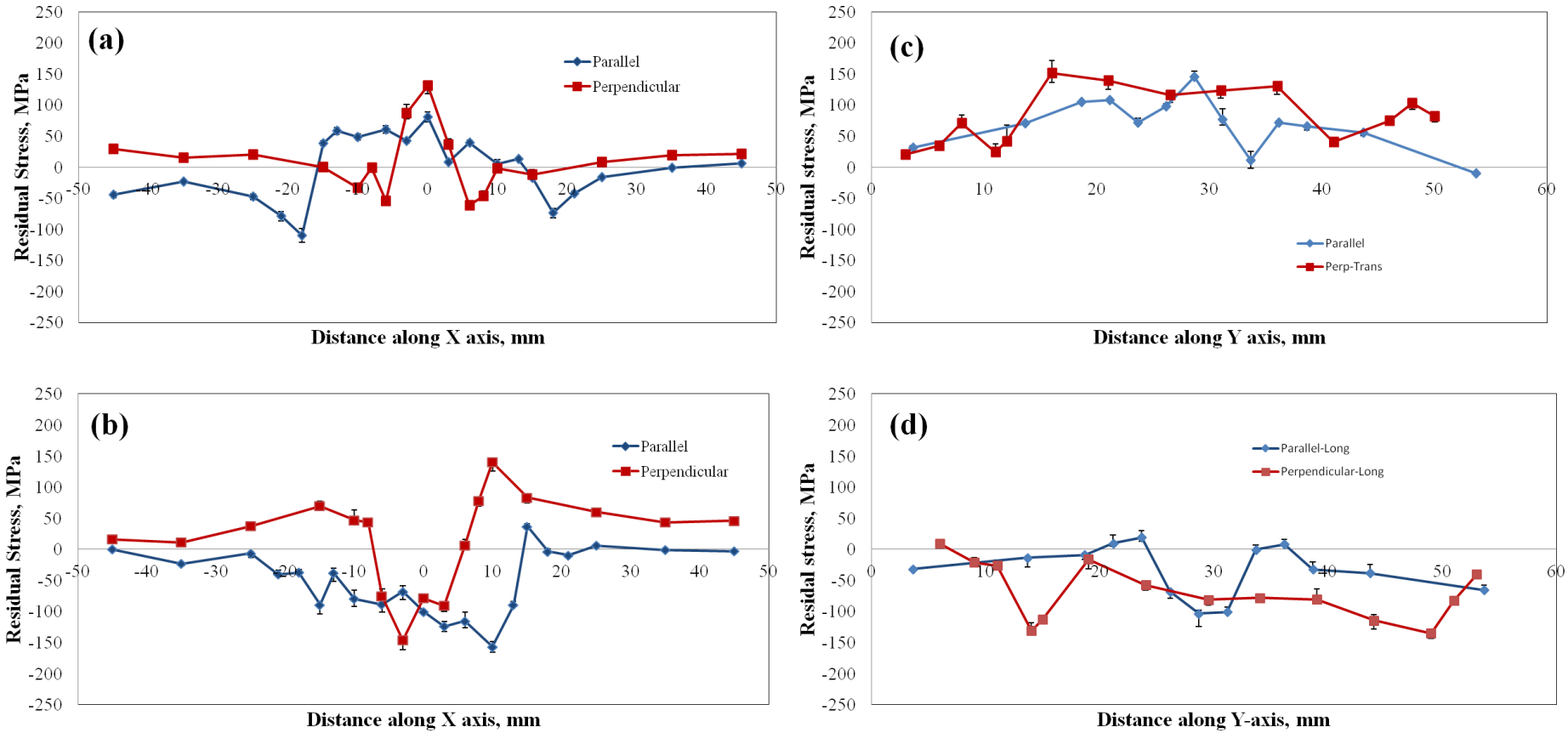

Figure 7-8: Effect of build orientation on residual stress distribution in the substrate: a) σ_x stress along X axis, b) σ_y stress along X axis, c) σ_x stress along Y axis, and d) σ_y stress along Y axis.

7.3 Final Scale-up of deposition with optimum process conditions

The deposition was scaled-up to a square block of 30 mm (X) × 30 mm(Y) × 10 mm (Z) using the optimum process parameters obtained from chapter 4 on the 2.5 mm thick substrate. A hatched type of deposition path was chosen to obtain uniform stress in both directions. Figure 7-9 shows the variation is stresses in the substrate (taken at the mid length of the substrate) along the X-axis, calculated using the stress balance method (making stress the in Z-direction zero). The magnitude of the tensile stresses in the substrate is slightly less than that seen in the rectangular blocks. While depositing a square block, the time required for the laser to return to do next pass is longer than doing a deposit which is $1/3^{rd}$ of its size, which would reduce the heat accumulation resulting in a lower residual stresses. Although, in a hatched deposition path, the laser would travel for same time in X and Y-directions, the magnitude σ_x and σ_y are different which is due to the smaller substrate size in the Y direction (60 mm) than in the X direction (120 mm) showing that the size of the substrate has a significant influence on the residual stresses in the substrate.

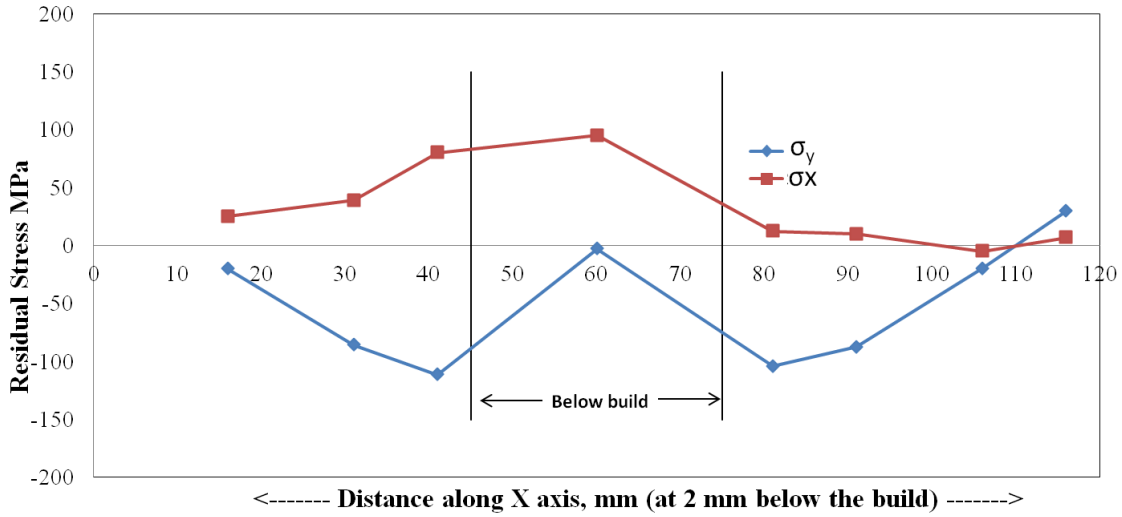

Figure 7-9: Stress distribution on the substrate due to DLF of solid block showing the variation of stress along the X axis.

Finally, the residual stresses have been characterised in the build in the XZ plane covering the build and the substrate. The stress contours were plotted, where the points were measured by neutron diffraction with a gauge volume of 2 × 2 × 2 mm at a distance of 2 mm between each point. The stress balance method cannot be used here due to a solid block. In order to obtain a stress-free d_0, 5 mm discs were cut from the build and substrate, and were used as reference for characterising the stress in the build and substrate, respectively [88].

Figure 7-10 shows the residual stress contours in the X-Z plane of the build. The build substrate interface has very high triaxial tensile stress (300 MPa) compared to the build. Studies by Ding on wire arc additive manufacturing showed tensile stresses in all the three directions at the build substrate interface with a magnitude of 350 MPa after 3 layers of deposition [137]. Immediately, compressive stresses are observed in the build compensating the tensile stresses at the build substrate interface. Slowly the stresses decrease to zero at the middle of the build. The stresses in the build in the σ_x and σy directions i.e. along the laser head moving direction are higher than in the $\sigma_{z\ direction}$ i.e perpendicular to laser head moving

direction or growth direction, which is almost negligible. At the top portion of the build in the final layers, again tensile stresses are observed. Previously, contour stress plots were made by Moat *et al.* on thin walled (5 mm thin) IN718 builds using DLF[25]. These stresses were measured by the stress balance method by taking the stresses in σ_y as zero. The stresses at the lower portion of the build showed a similar behaviour of compressive stresses reducing to zero as we move up the build. However, at the top portion of the build tensile stresses are observed in the σ_z with negligible stresses in the $\sigma_{x,}$ which is opposite to that observed in the current study. Also, contour maps of σ_z by Ranagasamy *et al.* [24] on the X-Y plane of a square pillar using the contour method showed compressive stresses in the core (-350 MPa) balanced by tensile stresses at the surface while depositing 316 steel and IN718 using DLF at a laser power of 390W and powder flow rate of 13g/min. High tensile residual stresses are expected to be present at the top portion of the build as the final layer of deposition would cool at a faster rate as the laser is switched off after that. Similar behaviour of tensile stresses at the top portion of the build in σ_x with negligible stresses in σ_z is observed in chapter 5 for thin walled IN718 samples. The variation in the size of the build does not show much variation in the magnitude of the residual stresses (thick walls in the current study compared to thin walls in chapter 5).

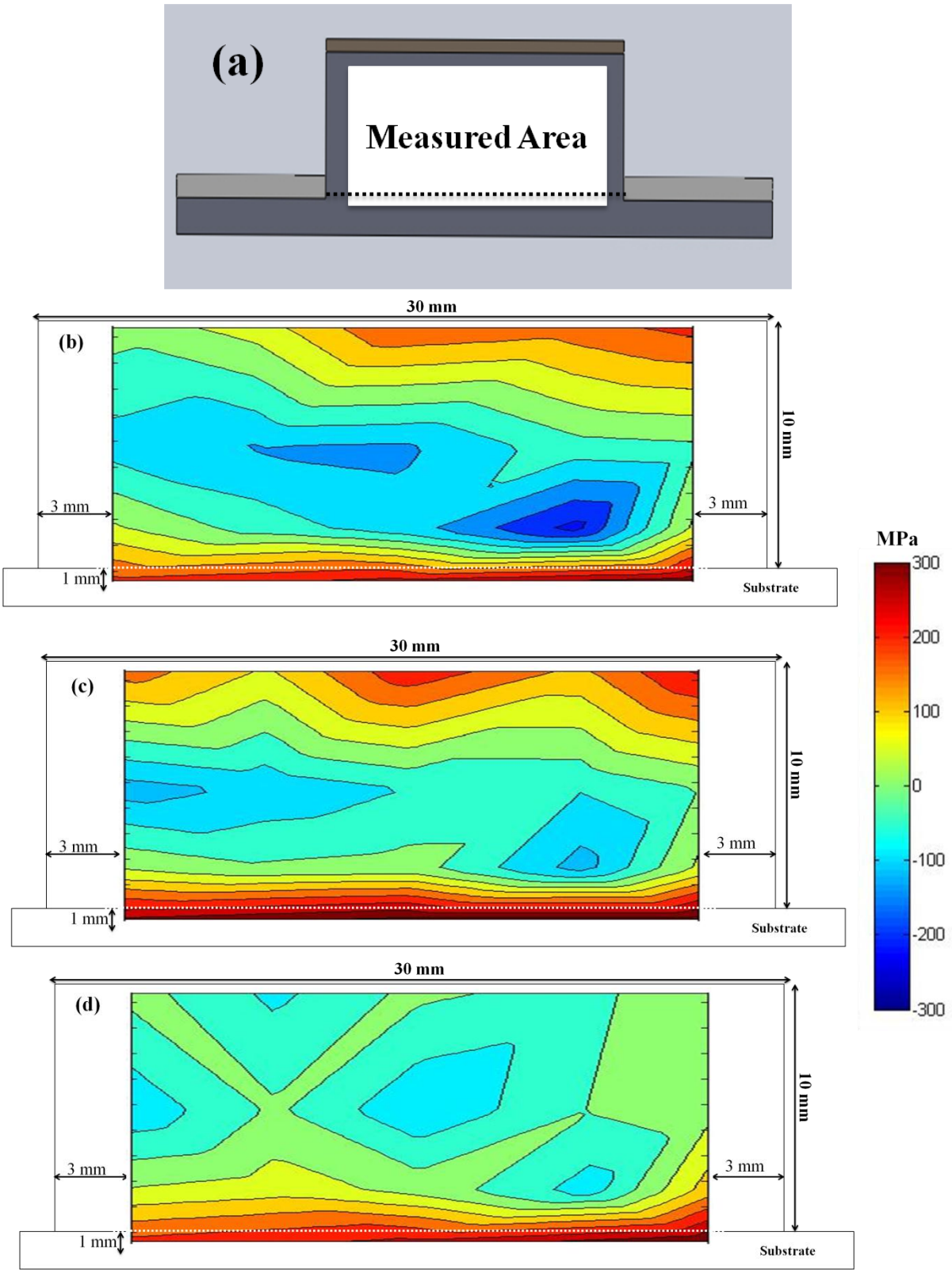

Figure 7-10: Contour maps for residual stress distribution in XZ plane of solid block on a thin substrate a) schematic showing the area where the stress contours were plotted b-d) residual stress contours in σx, σy and σz directions.

7.4 Summary

The key conclusions from the chapter, where the residual stresses during hybrid manufacturing application were studied, are summarised as below:

- The distortion and residual stresses are concentrated in the substrate at around 10 mm from the deposit.
- The stresses are tensile at the build substrate interface, due to high cooling rates associated at this location, with compensating compressive stresses in the substrate below the build.
- The longitudinal stresses, i.e. the stresses parallel to the moving heat source in the substrate are tensile and the transverse stresses perpendicular to the moving heat source are compressive.
- The deposition path has an influence on the distortion and the corresponding residual stresses
- When correlated with the cooling rates, short deposition paths with lower and uniform cooling rates resulted in less distortion and residual stresses.
- The laser power also played a significant role in distortion and stresses.
- Increase in the size of the build would result in lower and uniform stress distribution in the substrate.

In summary the maximum residual stresses are around 300 MPa concentrated at the build substrate interface. However, these stresses are well below the yield stress of a forged IN718 which makes the alloy process able without any solidification cracking. Residual stresses depend on the deposition path, build orientation and the size of the substrate used. Lower and uniform cooling rates would give smaller residual stresses. The deposition path should be carefully chosen depending on the size of the substrate. By varying the process parameters

the stresses can be reduced, but cannot be completely removed. Post deposition processes like HIPping or alternatively using preheated substrates may be considered in the future to completely avoid the stresses. In HIP, due to the high temperatures used, stress relaxation would occur during due to rearrangement of atoms by diffusion. Although the main advantage for the use of HIP treatment in AM would be to close the pores, due to plastic flow in the material at high temperature and Isostatic pressures, care should be taken in choosing this process. The prolonged high temperatures exposure as well as slow cooling rates involved in this process may produce Laves phases instead of the strengthening phases.

Chapter Eight

8 Overall Conclusion and Future Work

The main findings of the research are concluded in 4 sections:

8.1 Parametric study

Parametric studies were performed in chapter 4, to obtain builds with sound build quality and high geometrical accuracy to be used for repair as well as hybrid manufacturing application. The key conclusions are listed below:

- A statistically inspired empirical model has been developed which could successfully predict the thickness and height of the build.
- A process window has been identified which results in a porosity level of 0.2 ± 0.1 %
- The use of a statistical method to obtain sound builds was successful for thin and thick wall builds, but not for solid blocks.
- A combination of process parameters is recommended for a sound overall deposit in solid blocks.
- Higher laser power at the first few layers would improve the build quality, but increase in laser power at the lower layers would increase the residual stresses.
- The laser power has a strong influence on the porosity in the builds where higher gas entrapment is observed due to turbulence in the melt-pool with increase in laser power.

8.2 Development of the transient thermo-mechanical model and validation

A simple thermo-mechanical model has been developed in chapter 5 to simulate repair applications using DLF. The key conclusions drawn from the chapter are listed below:

- The transient thermal and thermo-mechanical models were successfully developed
- The maximum stresses were found at the build substrate interface, as well as the top portion of the build.
- The maximum stresses are typically observed along the melt-pool moving direction, whereas the minimum stresses are observed in the through -thickness direction.
- The first layer has high tensile stresses which decrease as the build progresses due to the annealing effect of the subsequent laser passes.
- The deposition path has less significant effect on residual stresses in thin walls. However the deposition path showed large variation in distortion when the build is deposited on a large plate.
- A delay and post scan reduces the tensile stresses in the build substrate interface.
- Although altering the deposition parameters results in changes in the stresses, but it is not possible to completely eliminate the stresses.

8.3 Microstructure and texture evolution in DLF

The microstructure and texture evolution in DLF for different process parameters and build geometries were studied in this chapter. The key conclusions are listed below:

- The DLFed builds showed a banded microstructure with fine grain zones in-between the layer which are identified as partially melted powder particles
- Deposition path did not show much effect on these partially melted powder particles whereas increase in laser power could rectify this problem.

- The build has non uniform grain structure with fine grains at the bottom layers and grain coarsening is observed during the build progress.
- Uniform grain size can be obtained in the build by adopting a delay in deposition between layers. However, a delay operation would increase the residual stresses in the build.
- Laser power has a strong influence on the grain size and texture where lower laser powers resulted in small grains with random texture and high laser powers produced builds with long columnar grains with fibre texture.
- The effect of substrate grain structure on the orientation of the build is observed only for the first few layers.
- The build showed Laves phases instead of strengthening γ′ and γ″ phases. Other than Laves few Ti and Nb rich carbides are also present.
- Laser power has a strong influence on the precipitate morphology and type, with an increase in laser power long elongated Laves phases are observed with δ needles protruding from them.
- The standard heat treatment routine used for cast IN718 is not good enough to give uniform grain size and precipitation.

8.4 Distortion and Residual stress Development due to Hybrid Manufacturing

This chapter studies the distortion and residual stress development during hybrid manufacturing. The effect of process parameters like laser power, deposition path and orientation of the build are studied in order to obtain a process parameter which gives minimum distortion and residual stresses. The key conclusions of the chapter as listed below:

- The distortion and stresses are observed in the substrate until a vicinity of 10 mm from the build.
- The deposition path showed an influence on the distortion of the substrate; which is seen prominently when the deposit covers the entire substrate.
- The short deposition path, where uniform and lower cooling rates are observed in the substrate, showed lower distortion than the long deposition paths which experience higher cooling rates.
- The residual stresses have increase with increase in the laser power.
- The residual stresses are mainly concentrated at the build substrate interface and at the top portion of the build; which are tensile in nature.
- The laser power and deposition path has lowered the residual stresses but did not eliminate them completely.

8.5 Recommendations for DLF of IN718

IN718 is a suitable alloy for DLF due to its high weldability. However due to the high cooling rates associated with the process, there are various associated problems which include non-uniform microstructure and residual stresses. The following procedures for the process are recommended to produce sound builds:

For single bead thin walls or thick walls, a single set of process parameter can be used for the entire build to obtain sound quality deposits. However for thick walls, with a large deposition area in a single layer, a variation in the process parameters is required as the build progresses. At the bottom layers of the build faster deposition speeds, low powder flow rate and higher laser power would give less porosity. However a high laser power would increase the residual stresses in the build substrate interface and consequently low powder flow rates or faster scan

speeds are recommended in this region. As low powder flow rate would affect the deposition rate (amount of deposition per unit time), after few layers when there is enough heat accumulation in the build, the powder flow rate can be increased to allow higher deposition rates. A thermal imaging camera with a feedback control system is recommended in the future to change the process parameters on the fly.

IN718 builds give rise to a non-uniform microstructure which can be mitigated by varying the process parameters. Of all the process parameters laser power showed the most influence on the grain size and texture. For epitaxial growth, suitable for creep applications, high laser power combined with a low powder flow rate is suitable while for fine grain sizes lower laser powers are recommended. Due to the non-uniform cooling rates associated with the process a non-uniform grain size distribution is observed in the builds which can be rectified by having a delay between each layer. However a delay between layers would increase the residual stresses in the build and although a post deposition scan can reduce these residual stresses this results in epitaxial growth.

Due to the fine dendritic microstructure with small laves phases observed in builds the deposited parts show better properties than a conventionally cast microstructure. If the part has to match any cast application then lower laser powers with a post deposition stress relief heat treatment are recommended to produce a fine microstructure. However if the part has to match a wrought application for fatigue performance then a low laser power with a complete solution heat treatment and age (SHTA) is advised due to the presence of the detrimental laves phases present in the as deposited condition. For creep applications high laser powers are recommended followed by a SHTA treatment. Also, to match wrought properties, a HIP treatment is required to close any gas pores resulting from the deposition, along with the SHTA treatment. The builds showed residual stresses of ~ 300 MPa and a stress relief heat treatment is recommended for deposition with any process given parameters. For deposits

with a small cross section area (thin and thick walls) the deposition path does not show any variation in residual stresses however a large cross sectional areas deposition path shows a huge variation in residual stresses. A thermal model or a temperature monitor is recommended to identify a path with uniform cooling rates when depositing large complex parts. Also, The stresses are mainly concentrated at the build substrate interface, due to very high cooling rates associated in this region, which may also lead to cracking in this region. To avoid this problem a pre-heated substrate is recommended to reduce the cooling rates. Also where possible the use of minimum amount of heat input would reduce the residual stresses.

8.6 Proposed Future Work

Based on the research conducted in this thesis DLF of IN718 has produced geometrically sound builds however, the microstructure and residual stresses in the build are not comparable with base material. Below are the potential issues that need to be solved for considering DLFed IN718 for practical industrial applications:

- The thesis was mainly focused on the microstructure, texture and residual stresses, however detailed mechanical testing needs to be carried out for various process parameters and with the microstructure in order to consider this process for practical applications.
- Even with the best process parameters chosen, the build still contains some entrapped pores, A critical assessment of the influence of these pores on properties should be undertaken including the influence of HIPping.
- TEM may be considered in the future to confirm the nature and distribution of precipitates present in the build and also design a heat treatment cycle for the DLF builds for a uniform microstructure and precipitation of strengthening phases.

- The thermo-mechanical transient model in this work has predicted the residual stresses, but is very slow to use for any complex and large geometries. A hybrid model may be considered in the future with a combination of steady state and transient approach to reduce computational time.
- A detailed microstructural model needs to be considered which could predict the microstructure with various process parameters as well as build geometries.
- Current mitigation methods employed for reducing the residual stresses has reduced but did not eliminate them. Alternative ways of pre-heating the substrate may be considered in the future that could reduce the high cooling rates.
- In the future, a feedback control system needs to be developed, with a thermal imaging camera, which would help in creating the thermal mass balance and thus achieving uniform microstructure and build quality.
- The major cost involved in the process is from the expensive powder. To reduce the cost of the final part alternative powder manufacturing routes may be employed which include manufacturing powder from machining swarf.

9 References:

[1]. Wu X., *A Review of Laser Fabrication of Metallic Components and of Materials*, Materials Science and Technology, 2007, **23**(6), pp. 631-640.

[2]. Hedges M. and Calder N., *Near Net Shape Rapid Manufacture & Repair by LENS*, in Cost Effective Manufacture via Net-Shape Processing. 2006, Meeting Proceedings RTO-MP-AVT-139: Neuilly-sur-Seine, France. p. 13-1 – 13-14.

[3]. Antonysamy A.A., *Microstructure, Texture and Mechanical Property Evolution During Additive Manufacturing of Ti6Al4V Alloy for Aerospace Applications*, in Materials Science. 2012, University of Manchester: Manchester. p. 315.

[4]. Wang F.,Williams S.,Colegrove P., and Antonysamy A.,*Microstructure and Mechanical Properties of Wire and Arc Additive Manufactured Ti-6Al-4V*, Metallurgical and Materials Transactions A, 2013, **44**(2), pp. 968-977.

[5]. Wang F.,Mei J., and Wu X.,*Microstructure Study of Direct Laser Fabricated Ti alloys Using Powder and Wire*, Applied Surface Science, 2006, **253**(3), pp. 1424-1430.

[6]. Mumtaz K. and Hopkinson N.,*Laser melting functionally graded composition of Waspaloy® and Zirconia powders*, Journal of Materials Science, 2007, **42**(18), pp. 7647-7656.

[7]. Taminger K.M. and Hafley R.A. *Electron Beam Freeform Fabrication for Cost Effective Near-Net Shape Manufacturing*.2006 1-19.

[8]. H. Qi,Azer M., and Singh P.,*Adaptive toolpath deposition method for laser net shape manufacturing and repair of turbine compressor airfoils*, The International Journal of Advanced Manufacturing Technology, 2010, **48**(1), pp. 121-131.

[9]. Kobryn P.A.,Moore E.H., and Semiatin S.L.,*The Effect of Laser Power and Traverse Speed on Microstructure, Porosity, and Build Height in Laser-Deposited Ti-6Al-4V*, Scripta Materialia, 2000, **43**(4), pp. 299-305.

[10]. Kobryn P.A. and Semiatin S.L.,*Microstructure and texture evolution during solidification processing of Ti–6Al–4V*, Journal of Materials Processing Technology, 2003, **135**(2–3), pp. 330-339.

[11]. I. Tabernero,Lamikiz A.,Martínez S.,Ukar E., and Figueras J.,*Evaluation of the mechanical properties of Inconel 718 components built by laser cladding*, International Journal of Machine Tools and Manufacture, 2011, **51**(6), pp. 465-470.

[12]. Zhao X.,Chen J.,Lin X., and Huang W.,*Study on microstructure and mechanical properties of laser rapid forming Inconel 718*, Materials Science and Engineering: A, 2008, **478**(1–2), pp. 119-124.

[13]. Kobryn P.A.,Perkins L.P., and Tiley J.S., *Additive Manufacturing of Aerospace Alloys for Aircraft Structures. in Cost Effective Manufacture*, in Net-Shape Processing Proceedings, France,2006.

[14]. Kelly S.M. and Kampe S.L.,*Microstructural evolution in laser-deposited multilayer Ti-6Al-4V builds: Part I. Microstructural characterization*, Metallurgical and Materials Transactions A, 2004, **35**(6), pp. 1861-1867.

[15]. Moat R.J.,Pinkerton A.J.,Li L.,Withers P.J., and Preuss M.,*Crystallographic texture and microstructure of pulsed diode laser-deposited Waspaloy*, acta materialia, 2009, **57**(4), pp. 1220-1229.

[16]. P. L. Blackwell,*The Mechanical and Microstructural Characteristics of Laser-deposited IN718*, Journal of Materials Processing Technology, 2005, **170**(1-2), pp. 240-246.

[17]. Dinda G.P.,Dasgupta A.K., and Mazumder J.,*Laser aided direct metal deposition of Inconel 625 superalloy: Microstructural evolution and thermal stability*, Materials Science and Engineering: A, 2009, **509**(1–2), pp. 98-104.

[18]. Dinda G.P.,Dasgupta A.K., and Mazumder J.,*Texture control during laser deposition of nickel-based superalloy*, Scripta Materialia, 2012, **67**(5), pp. 503-506.

[19]. Tabernero I.,Lamikiz A.,Martínez S.,Ukar E., and Figueras J.,*Evaluation of the mechanical properties of Inconel 718 components built by laser cladding*, International Journal of Machine Tools and Manufacture, 2011, **51**(6), pp. 465-470.

[20]. X. Wu and Mei J.,*Near Net Shape Manufacturing of Components Using Direct Laser Fabrication Technology*, Journal of Materials Processing Technology, 2003, **135**(2-3), pp. 266-270.

[21]. Liu F.,Lin X.,Leng H.,Cao J.,Liu Q.,Huang C., and Huang W.,*Microstructural changes in a laser solid forming Inconel 718 superalloy thin wall in the deposition direction*, Optics & Laser Technology, 2013, **45**(0), pp. 330-335.

[22]. H. Qi,Azer M., and Ritter A.,*Studies of Standard Heat Treatment Effects on Microstructure and Mechanical Properties of Laser Net Shape Manufactured INCONEL 718*, Metallurgical and Materials Transactions A, 2009, **40**(10), pp. 2410-2422.

[23]. F. Liu,Lin X.,Yang G.,Song M.,Chen J., and Huang W.,*Microstructure and Residual Stress of Laser Rapid Formed Inconel 718 nickel-base superalloy*, Optics & Laser Technology, 2011, **43**(1), pp. 208-213.

[24]. Rangaswamy P.,Griffith M.L.,Prime M.B.,Holden T.M.,Rogge R.B.,Edwards J.M., and Sebring R.J.,*Residual Stresses in LENS® Components using Neutron Diffraction and Contour Method*, Materials Science and Engineering: A, 2005, **399**(1-2), pp. 72-83.

[25]. Moat R.J.,Pinkerton A.J.,Li L.,Withers P.J., and Preuss M.,*Residual stresses in laser direct metal deposited Waspaloy*, Materials Science and Engineering: A, 2011, **528**(6), pp. 2288-2298.

[26]. M.J. Donachie and Donachie S.J., *Superalloys: a technical guide*. 2 ed, 2002, ASM International.

[27]. Roger R.C., *The superalloys: Fundamentals and Applications*, 2006, New York, Cambrindge University Press.

[28]. Donachie M.J. and Donachie S.J., *Superalloys: a technical guide*. 2 ed, 2002, ASM International.

[29]. Mankins W.L. and Lamb S., *Physical Metallurgy of Nickel and Nickel alloys*, Properties and selection: Nonferrous Alloys and special-Purpose Materials, **Vol**. 2, ASM International.

[30]. Rolls-Royce, *The Jet Engine*, 2005, Derby, Rolls-Royce plc.

[31]. Bhadeshia H.K.D.H. *Nickel Based Superalloys*. Available from: http://www.msm.cam.ac.uk/phase-trans/2003/Superalloys/superalloys.html.

[32]. Brown A.M. and Ashby M.F.,*Correlations for diffusion constants*, Acta Metallurgica, 1980, **28**(8), pp. 1085-1101.

[33]. Fost H.J. and Ashby M.F., *Deformation-mechanism maps: The plasticity and creep of metals and ceramics*, 1982, Oxford, Pergamon Press.

[34]. Reppich B.,Kühlein W.,Meyer G.,Puppel D.,Schulz M., and Schumann G.,*Duplex γ' particle hardening of the superalloy Nimonic PE 16*, Materials Science and Engineering, 1986, **83**(1), pp. 45-63.

[35]. Ochial S.,Oya Y., and Suzuki T.,*Alloying behaviour of Ni3Al, Ni3Ga, Ni3Si and Ni3Ge*, Acta Metallurgica, 1984, **32**(2), pp. 289-298.

[36]. Sundararaman M.,Mukhopadhyay P., and Banerjee S.,*Some Aspects Of The Precipitation Of Metastable Intermetallic Phases In INCONEL 718*, Metallurgical and Materials Transactions A, 1992, **23**(7), pp. 2015-2028.

[37]. Sundararaman M. and Mukhopadhyay P.,*Overlapping of γ " precipitate variants in Inconel 718*, Materials Characterization, 1993, **31**.

[38]. Baker H., *Alloy phase diagrams*, 1992, Materials Park, OH . ASM International

[39]. Cozar R. and Pineau A.,*Morphology Of γ' And γ" Precipitates And Thermal Stability Of Inconel 718 Type Alloys*, Metallurgical and Materials Transactions B, 1973, **4**(1), pp. 47-59.

[40]. Chang K.-M. and Nahm A.H., *Rene 220: 100°f Improvement Over Alloy 718*, in Superalloy 718--Metallurgy and Applications, E.A. Loria, Editor. 1989, TMS: warrendale. p. 631-646.

[41]. Oblack J.M.,Paulonis D.F., and Duvall D.S.,Met. Trans. A, 1974, **5**(1), pp. 143-153.

[42]. West S.L.,Baeslack Iii W.A., and Kelly T.J.,*Morphology Of Weld Heat-affected Zone Liquation Cracking In Ta-modified Cast Alloy 718*, Metallography, 1989, **23**(3), pp. 219-229.

[43]. Reed R.C.,Jackson M.P., and Na Y.S.,*Characterisation and modelling of the precipitation of the sigma phase in Udimet 720 and Udimet 720Li*,, Metallurgical and Materials Transactions, 19999, **30 A**, pp. 521-533.

[44]. R.C. Reed, *The Superalloys: Fundamentals and Applications*, 2006, USA, Cambridge University Press,NY, 327.

[45]. R.C. Roger, *The Superalloys: Fundamentals and Applications*, 2006, USA, Cambridge University Press,NY, 327.

[46]. Johnson J.,*Sigma phase formed in a nickel-base UDIMET 700*, Journal of the Institute of Metals, 1967, **95**, pp. 379.

[47]. Mihalisin J.R.,Bieber C.G., and Grant R.T.,*Sigma-Its Occurrence, Effect, and Control in Nickel-Base Superalloys*, Metallurgical Transactions, 1968, **242**, pp. 2399.

[48]. Youdelis W.V. and Kwon O.,*Carbide phases in nickel base superalloy: nucleation properties of MC type carbide.*, Metal Science, 1983, **17**(8), pp. 385-388.

[49]. Tin S.,Pollock T.M., and King W.T., *Carbon additions and grain defect formation in high refractory nickel-base single crystal superalloys*, in Superalloys 2000, Warrendale, PA, Minerals, Metals and Materials Society (TMS),2000.

[50]. Prager M. and Shira C.S., *Welding of Precipitation-Hardening Nickel-Base Alloys*, 1968, Welding Research Council.

[51]. Duvall D.S. and Owczarski W.A.,*Further heat affected zone studies in heat resistant nickel alloys*, Welding Journal 1967, **46**, pp. 423

[52]. Azadian S.,Wei L.-Y.,Niklasson F., and Warren R., *Precipitation in Spray-Formed IN 718*, in Superalloys 718, 625, 706, and Various Derivatives warrendale, TMS,2001.

[53]. J.F. Radavich, *The Physical Metallurgy of Cast and Wrought Alloy 718*, in Superalloy 718--Metallurgy and Applications Warrendale, TMS,1989.

[54]. Sundararaman M.,Mukhopadhyay P., and Banerjee S., *Precipitation and Room Temperature Deformation Behaviour of Inconel 718*, in Superalloys 718, 625, 706 and Various Derivatives E.A. Loria, Editor. 1994, TMS: warrendale. p. 419-440.

[55]. Li R.B.,Yao M.,Liu W.C., and He X.C.,*Isolation And Determination For δ, γ‘ and γ'' Phases In Inconel 718 Alloy*, Scripta Materialia, 2002, **46**(9), pp. 635-638.

[56]. Dahotre N.B.,McCay M.H.,McCay T.D.,Hubbard C.R.,Porter W.D., and Cavin O.B.,*Effect Of Grain Structure On Phase Transformation Events In The Inconel 718*, Scripta Metallurgica et Materialia, 1993, **28**(11), pp. 1359-1364.

[57]. Srinivasan D.,*Effect of long-time exposure on the evolution of minor phases in Alloy 718*, Materials Science and Engineering: A, 2004, **364**(1–2), pp. 27-34.

[58]. Desvalle´es Y.,Bouzidi M.,Bois F., and Beaude N., *Delta Phase In Inconel 718: Mechanical Properties And Forging Process Requirements*, in Superalloy 718—metallurgy and applications., warrendale, TMS,1994.

[59]. G. Sjfberg and Ingesten N., *Grain Boundary Y-phase Morphology, Carbides And Notch Rupture Sensitivities Of Cast Alloy 718*, in Superalloy 718—Metallurgy and Applications, warrendale, TMS,1991.

[60]. Schafrik R.E.,Douglas D.W., and Groh J.R., *Application of Alloy 718 in GE Aircraft Engines: Past, Present and Next Five Years*, in TMS (The Minerals, Metals and Materials Society), TMS,2001.

[61]. Stephen F., *Precipitation reactions in Inconel Alloy 718*, in Metallurgy and Materials. 1988, University of Birmingham: Birmingham.

[62]. Muzyka D.R. and Manier G.N.,Metals engineering quarterly, 1969, **9**(4).

[63]. Rizzo F.J. and Buzzanell J.D.,Journal of Metals, 1969, **21**(10), pp. 24-33.

[64]. Rao G.A.,Kumar M.,Srinivas M., and Sarma D.S.,*Effect of standard heat treatment on the microstructure and mechanical properties of hot isostatically pressed superalloy inconel 718*, Materials Science and Engineering: A, 2003, **355**(1–2), pp. 114-125.

[65]. Rao G.A.,Srinivas M., and Sarma D.S.,*Effect of oxygen content of powder on microstructure and mechanical properties of hot isostatically pressed superalloy Inconel 718*, Materials Science and Engineering: A, 2006, **435–436**(0), pp. 84-99.

[66]. Antonsson T. and Fredriksson H.,*The Effect of Cooling Rate on the Solidification of INCONEL 718*, Metallurgical and Materials Transactions B, 2005, **36B**, pp. 85.

[67]. Radhakrishna C.H. and Prasad Rao K.,*The Formation And Control Of Laves Phase In Superalloy 718 Welds*, Journal of Materials Science, 1997, **32**(8), pp. 1977-1984.

[68]. DuPont J.N.,Robino C.V., and Marder A.R.,*Solidification and weldability of Nb bearing superalloys*, Welding Journal, 1998, **77**, pp. 417.

[69]. Cieslak M.J.,Knorovsky G.A.,Headley T.J., and Rimig Jr. A.D., *Solidification metallurgy of alloy 718 and other Nb-containing superalloys*, in Superalloy 718 – Metallurgy and Applications, The Minerals, Metals & Materials Society,1989.

[70]. Bouse G.K., *Application of a modified phase diagram to the production of cast alloy 718 components*, in Superalloy 718-Metallurgy and Applications, The Minerals, Metals & Materials Society,1989.

[71]. Thompson R.G. and Genculu S., *Microstructure Evolution In The HAZ Of Inconel 718 And Correlation With The Hot Ductility Test*, in 64th annual AWS convention Philadelphia, Welding research supplimets,1983.

[72]. Schirra J.J.,Robert H. Caless, and Hatala R.W., *The Effect Of Laves Phase On The Mechanical Properties Of Wrought And Cast + Hip Inconel 718*, in Superalloys 718,625 and Various Derivatives, Warrendale, TMS,1991.

[73]. David S.A. and Vitek J.M.,*Correlation between solidification parameters and weld microstructure*, international Materials Reviews, 1989, **34**(5), pp. 213-245.

[74]. DuPont J.N.,Lippold J.C., and D.Kiser S., *Welding Metallurgy and Weldability of Nickel-based Alloys*, 2009, Hoboken, New Jersey, A John Wiley & Sons, Inc.

[75]. Kurz W. and Fisher D.J., *Fundamentals of Solidification*, 2005, Trans Tech Publications Ltd.

[76]. Porter D.A.,Easterling K.E., and Sherif M.Y., *Phase transformations in metals and alloys*. 3 ed, **Vol**. xix, 2009, Boca Raton, FL, CRC Press.

[77]. Mitchell A. and Wang T., *Solidification and Precipitation in IN 718*, in Superalloys 718, 625 , 706 and various derivatives, Warrendale, TMS,2001.

[78]. Kou S., *Welding metallurgy*. 2 ed, **Vol**. xiv, 2003, Hoboken, N.J, Wiley-Interscience, 461.

[79]. Nastac L.,Sundarraj S.,Yu K.-O., and Pang Y.,*The stochastic modeling of solidification structures in alloy 718 remelt ingots*, JOM Journal of the Minerals, Metals and Materials Society, 1998, **50**(3), pp. 30-35.

[80]. David S.,Vitek J.,Rappaz M., and Boatner L.,*Microstructure of stainless steel single-crystal electron beam welds*, Metallurgical and Materials Transactions A, 1990, **21**(6), pp. 1753-1766.

[81]. Kurz W. and Trivedi R.,*Rapid solidification processing and microstructure formation*, Materials Science and Engineering: A, 1994, **179–180, Part 1**(0), pp. 46-51.

[82]. Gäumann M.,Henry S.,Cléton F.,Wagnière J.D., and Kurz W.,*Epitaxial laser metal forming: analysis of microstructure formation*, Materials Science and Engineering: A, 1999, **271**(1–2), pp. 232-241.

[83]. Suutala N.,*Effect of solidification conditions on the solidification mode in austenitic stainless steels*, Metallurgical and Materials Transactions A, 1983, **14**(1), pp. 191-197.

[84]. Norman A.F.,Drazhner V., and Prangnell P.B.,*Effect of welding parameters on the solidification microstructure of autogenous TIG welds in an Al–Cu–Mg–Mn alloy*, Materials Science and Engineering: A, 1999, **259**(1), pp. 53-64.

[85]. Ganaha T.,Pearce B.P., and Kerr H.W.,*Grain Structures in aluminium alloy GTA welds*, Metallurgical and Materials Transactions A, 1980, **11**(8), pp. 1351.

[86]. Savage W.F.,Nippes E.F., and Erickson J.S.,Welding Journal, 1976, **55**, pp. 214s.

[87]. Withers P.J. and Bhadeshia H.K.D.H.,*Residual stress Part 2 –Nature and origins*, Materials Science and Technology, 2001, **17**, pp. 366.

[88]. Withers P.J. and Bhadeshia H.K.D.H.,*Residual stress Part 1 – Measurement techniques*, Materials Science and Technology, 2001, **17**, pp. 355.

[89]. Withers P.J.,Turski M.,Edwards L.,Bouchard P.J., and Buttle D.J.,*Recent advances in residual stress measurement*, International Journal of Pressure Vessels and Piping, 2008, **85**(3), pp. 118-127.

[90]. Sasaki K.,Kishida M., and Itoh T.,*The accuracy of residual stress measurement by the hole-drilling method*, Experimental Mechanics, 1997, **37**(3), pp. 250-257.

[91]. Rendler N.J. and Vigness I.,*Hole-drilling strain-gage method of measuring residual stresses*, Experimental Mechanics, 1966, **6**(12), pp. 577-586.

[92]. Schajer G.S.,Roy G.,Flaman M.T., and Lu J., *Handbook of measurement of residual stresses*, ed. J. Lu, 1996, Lilburn, GA, Society for Experimental Mechanics.

[93]. Price J.W.H.,Ziara-Paradowska A.,Joshi S.,Finlayson T.,Semetay C., and Nied H.,*Comparison of experimental and theoretical residual stresses in welds: The issue of gauge volume*, International Journal of Mechanical Sciences, 2008, **50**(3), pp. 513-521.

[94]. Withers P.J.,Preuss M.,Steuwer A., and Pang J.W.L.,*Methods for obtaining the strain-free lattice parameter when using diffraction to determine residual stress*, Journal of Applied Crystallography, 2007, **40**(5), pp. 891-904

[95]. Kröner E.,*Berechnung der elastischen Konstanten des Vielkristalls aus den Konstanten des Einkristalls*, Zeitschrift für Physik, 1958, **151**(4), pp. 504-518.

[96]. Repper J.,Hofmann M.,Krempaszky C.,Wimpory R.C.,Petry W., and Werner E. *Microstrain Accumulation in Multiphase Superalloys*.2009.

[97]. Prime M. *The Contour Method for Measuring Residual Stress*. Available from: http://www.lanl.gov/contour/.

[98]. Prime M., *The contour method; simple 2D mapping of residual stresses*, in 6th International conference on residual stress. 2000, Institute of Materials: Oxford.

[99]. Brown D.W.,Holden T.M.,Clausen B.,Prime M.B.,Sisneros T.A.,Swenson H., and Vaja J.,*Critical comparison of two independent measurements of residual stress in an electron-beam welded uranium cylinder: Neutron diffraction and the contour method*, acta materialia, 2011, **59**(3), pp. 864-873.

[100]. Atwood C.,Ensz M.,Greene D.,Griffith M.,Harwell L.,Reckaway D.,Romero T.,Schlienger E., and Smugeresky J., *Laser Engineered Net Shaping (LENS(TM)): A Tool for Direct Fabrication of Metal Parts*, 1998, Medium: ED.

[101]. Kong C.Y.,Scudamore R.J., and Allen J.,*High-rate laser metal deposition of Inconel 718 component using low heat-input approach*, Physics Procedia, 2010, **5, Part A**(0), pp. 379-386.

[102]. Clark D.,Bache M.R., and Whittaker M.T.,*Shaped metal deposition of a nickel alloy for aero engine applications*, Journal of Materials Processing Technology, 2008, **203**(1–3), pp. 439-448.

[103]. Susan D.F.,Puskar J.D.,Brooks J.A., and Robino C.V.,*Quantitative characterization of porosity in stainless steel LENS powders and deposits*, Materials Characterization, 2006, **57**(1), pp. 36-43.

[104]. Pinkerton A.J.,Wang W., and Li L.,*Component repair using laser direct metal deposition*, Journal of Engineering Manufacture Part B, 2008, **222**.

[105]. Bi G.,Ng G.K.L.,Teh K.M., and Jarfors A.E.W.,*Feasibility study on the Laser Aided Additive Manufacturing of die inserts for liquid forging*, Materials & Design, 2010, **31, Supplement 1**(0), pp. S112-S116.

[106]. Kruth J.P.,Froyen L.,Van Vaerenbergh J.,Mercelis P.,Rombouts M., and Lauwers B.,*Selective laser melting of iron-based powder*, Journal of Materials Processing Technology, 2004, **149**(1-3), pp. 616-622.

[107]. P.J. Andrew,Moat R.,Li L.,Preuss M., and Withers P.J., *Diode Laser Metal Deposition: The Effect of Pulsed Beam Parameters on Superalloy Microstructure and Deposit Morphology.*, in 25th International Congress on Applications of Lasers and Electro-optics (ICALEO), Scottsdale, AZ, USA,2006.

[108]. Choi J. and Chang Y.,*Characteristics of laser aided direct metal/material deposition process for tool steel*, International Journal of Machine Tools and Manufacture, 2005, **45**(4–5), pp. 597-607.

[109]. W. Hofmeister,Wert M.,Smugeresky J.,Philliber J.A.,Griffith M., and Ensz M.,*Investigating Solidification with the Laser-Engineered Net Shaping (LENSTM) Process*, JOM, 1999, **51**(7), pp. 1-6.

[110]. Xue L. and Islam M.-U., in Proc. 2002 Int. Conf. on Metal powder deposition for rapid manufacturing,MPIF., D.K.e. al., Editor. 2002: Princeton. p. 62-68.

[111]. Steen W.M., *Laser Material Processing*, 1991, London, Springer-Verlag London Limited.

[112]. Peng L.,Taiping Y.,Sheng L.,Dongsheng L.,Qianwu H.,Weihao X., and Xiaoyan Z.,*Direct laser fabrication of nickel alloy samples*, International Journal of Machine Tools and Manufacture, 2005, **45**(11), pp. 1288-1294.

[113]. Rombouts M.,Kruth J.P.,Froyen L., and Mercelis P.,*Fundamentals of Selective Laser Melting of alloyed steel powders*, CIRP Annals - Manufacturing Technology, 2006, **55**(1), pp. 187-192.

[114]. Gusarov A.V. and Yadroitsev I.e.a.,*Heat Transfer Modelling and Stability Analysis of Slelective Laser Melting*, journal of applied science, 2007, pp. 254.

[115]. Abioye T.E.,Folkes J., and Clare A.T.,*A parametric study of Inconel 625 wire laser deposition*, Journal of Materials Processing Technology, 2013, **213**(12), pp. 2145-2151.

[116]. Fearon E. and Watkins K.G., *optomization of layer height control in direct laser deposition*, in 23rd international congress on application of laser and electro-optics(ICALEO),2004.

[117]. Ravi G.A., *Direct Laser Fabrication at IRC: An Overview*. 2010, University of Birmingham: Birmingham.

[118]. Mazumder J.,Schifferer A., and Choi J.,*Direct materials deposition: designed macro and microstructure*, Materials Research Innovations, 1999, **3**, pp. 118–131.

[119]. Ravi G.A.,Hao X.J.,Wain N.,Wu X., and Attallah M.M.,*Direct laser fabrication of three dimensional components using SC420 stainless steel*, Materials & Design, 2013, **47**(0), pp. 731-736.

[120]. Bontha S.,Klingbeil N.W.,Kobryn P.A., and Fraser H.L.,*Thermal process maps for predicting solidification microstructure in laser fabrication of thin-wall structures*, Journal of Materials Processing Technology, 2006, **178**(1–3), pp. 135-142.

[121]. Qian L.,Mei J.,Liang J., and Wu X.,*Influence of position and laser power on thermal history and microstructure of direct laser fabricated Ti–6Al–4V samples* Materials Science and Technology, 2005, **21**, pp. 597-605.

[122]. Zhang Q.-l.,Yao J.-h., and Mazumder J.,*Laser Direct Metal Deposition Technology and Microstructure and Composition Segregation of Inconel 718 Superalloy*, Journal of Iron and Steel Research, International, 2011, **18**(4), pp. 73-78.

[123]. Wu X.,Sharman R.,Mei J., and Voice W.,*Direct laser fabrication and microstructure of a burn-resistant Ti alloy*, Materials & Design, 2002, **23**(3), pp. 239-247.

[124]. Liu F.,Lin X.,Yang G.,Song M.,Chen J., and Huang W.,*Microstructure and residual stress of laser rapid formed Inconel 718 nickel-base superalloy*, Optics & Laser Technology, 2011, **43**(1), pp. 208-213.

[125]. S.Mokadem,Bezençon C.,Drezet J.-M.,Jacot A.,Wagnière J.-D., and Kurz W., *Microstructure control during single crystal laser welding and deposition of ni-base superalloys.*, in Solidification Processes and Microstructures,2004.

[126]. R. J. Moat,Pinkerton A.J.,Li L.,Withers P.J., and Preuss M.,*Crystallographic Texture and Microstructure of Pulsed Diode Laser-Deposited Waspaloy*, Acta Materialia, 2009, **57**(4), pp. 1220-1229.

[127]. Xu F.J.,Lv Y.H.,Xu B.S.,Liu Y.X.,Shu F.Y., and He P.,*Effect of deposition strategy on the microstructure and mechanical properties of Inconel 625 superalloy fabricated by pulsed plasma arc deposition*, Materials & Design, 2013, **45**(0), pp. 446-455.

[128]. Majumdar J.D.,Pinkerton A.,Liu Z.,Manna I., and Li L.,*Microstructure characterisation and process optimization of laser assisted rapid fabrication of 316L stainless steel*, Applied Surface Science, 2005, **247**(1–4), pp. 320-327.

[129]. Gäumann M.,Bezençon C.,Canalis P., and Kurz W.,*Single-crystal laser deposition of superalloys: processing–microstructure maps*, acta materialia, 2001, **49**(6), pp. 1051-1062.

[130]. Pinkertona A.J.,Karadge M.,Syed W.U.H., and Li L.,*Thermal and microstructural aspects of the laser direct metal deposition of waspaloy*, Journal of Laser Applications, 2006, **18**(3), pp. 216.

[131]. Kobryn P.A. and Semiatin S.L.,*The laser additive manufacture of Ti-6Al-4V*, jom, 2001, **53**(9), pp. 40-42.

[132]. Xu F.,Lv Y.,Liu Y.,Shu F.,He P., and Xu B.,*Microstructural Evolution and Mechanical Properties of Inconel 625 Alloy during Pulsed Plasma Arc Deposition Process*, Journal of Materials Science & Technology, (0).

[133]. Wang Z.,Guan K.,Gao M.,Li X.,Chen X., and Zeng X.,*The microstructure and mechanical properties of deposited-IN718 by selective laser melting*, Journal of Alloys and Compounds, 2012, **513**(0), pp. 518-523.

[134]. Cao J.,Liu F.,Lin X.,Huang C.,Chen J., and Huang W.,*Effect of overlap rate on recrystallization behaviors of Laser Solid Formed Inconel 718 superalloy*, Optics & Laser Technology, 2013, **45**(0), pp. 228-235.

[135]. Baufeld B.,*Mechanical Properties of INCONEL 718 Parts Manufactured by Shaped Metal Deposition (SMD)*, Journal of Materials Engineering and Performance, 2012, **21**(7), pp. 1416-1421.

[136]. Klingbeil N.W.,Beuth J.L.,Chin R.K., and Amon C.H.,*Residual stress-induced warping in direct metal solid freeform fabrication*, International Journal of Mechanical Sciences, 2002, **44**(1), pp. 57-77.

[137]. Ding J., *Thermo-mechanical Analysis of Wire and Arc Additive Manufacturing Process*, in School of Applied Science Manufacturing and Material Department. 2012, Cranfield University: Cranfield.

[138]. Andrew J.P.,Li L.,Withers P.J.,Preuss M.,Allen J.,Hilton P., and Folwell R., *The effect of process parameters on residual stresses within an Inconel 718 part produced by the direct laser deposition process*, in 24th International Congress on Applications of Lasers and Electro-optics (ICALEO), Miami, FL, USA.,2005.

[139]. Wang L.,Felicelli S.D., and Pratt P.,*Residual Stresses in LENS-deposited AISI 410 Stainless steel plates*, Materials Science and Engineering: A, 2008, **496**(1-2), pp. 234-241.

[140]. Zhang C.,Li L., and Deceuster A.,*Thermomechanical analysis of multi-bead pulsed laser powder deposition of a nickel-based superalloy*, Journal of Materials Processing Technology, 2011, **211**(9), pp. 1478-1487.

[141]. Zhao H.,Zhang G.,Yin Z., and Wu L.,*Three-dimensional finite element analysis of thermal stress in single-pass multi-layer weld-based rapid prototyping*, Journal of Materials Processing Technology, 2012, **212**(1), pp. 276-285.

[142]. Nickel A.H.,Barnett D.M., and Prinz F.B.,*Thermal stresses and deposition patterns in layered manufacturing*, Materials Science and Engineering: A, 2001, **317**(1–2), pp. 59-64.

[143]. Fessler J.R.,Merz R.,Nickel A.H., and Prinz F.B., *Laser Deposition of Metals for Shape Deposition Manufacturing*, in Proceedings of the Solid Freeform Fabrication Symposium, University of Texas at Austin,August, 1996.

[144]. Finnie S.,Cheng W.,Finnie I.,Drezet J.-M., and Gremaud M.,*The Computation and Measurement of Residual Stresses in Laser Deposited Layers*, Journal of Engineering Materials and Technology, 2003 **125**(3), pp. 302.

[145]. Foroozmehr E.,Kong F., and Kovacevic R., *An Investigation On The Effect Of Path Planning On Residual Stress Distribution In The Laser Powder Deposition Process*, in ASME Early Career Technical Conference, Arlington, TX, ASME District E,2009.

[146]. Moat R.J.,Pinkerton A.J.,Hughes D.J.,Li L.,Withers P.J., and Preuss M., *Stress Distributions In Multilayer Laser Deposited Waspaloy Parts Measured Using Neutron Diffraction*, in Proceedings of the 25th International Congress on Applications of Lasers and Electro-optics (ICALEO), USA, Laser Institute of America,2007.

[147]. Vasinonta A.,Beuth J.L., and Griffith M.L.,*A Process Map for Consistent Build Conditions in the Solid Freeform Fabrication of Thin-Walled Structures* Journal of manufacturing science and engineering, 2001, **123**(4), pp. 615.

[148]. Griffith M.L.,Schlienger M.E.,Harwell L.D.,Oliver M.S.,Baldwin M.D.,Ensz M.T.,Essien M.,Brooks J.,Robino C.V.,Smugeresky J.E.,Hofmeister W.H.,Wert M.J., and Nelson D.V.,*Understanding thermal behavior in the LENS process*, Materials and Design, 1999, **20**(2-3), pp. 107-113.

[149]. Zhao H.,Zhang G.,Yin Z., and Wu L.,*A 3D dynamic analysis of thermal behavior during single-pass multi-layer weld-based rapid prototyping*, Journal of Materials Processing Technology, 2011, **211**(3), pp. 488-495.

[150]. Peyre P.,Aubry P.,Fabbro R.,Neveu R., and Longuet A.,*Analytical and numerical modelling of the direct metal deposition laser process*, Journal Of Physics D: Applied Physics, 2008, **41**, pp. 10.

[151]. Chiumenti M.,Cervera M.,Salmi A.,Agelet de Saracibar C.,Dialami N., and Matsui K.,*Finite element modeling of multi-pass welding and shaped metal deposition processes*, Computer Methods in Applied Mechanics and Engineering, 2010, **199**(37–40), pp. 2343-2359.

[152]. Han L.,Kaushik M.P., and Lioua F.W.,*Modeling of laser deposition and repair process*, Journal of Laser Applications, 2005, **17**(2), pp. 89.

[153]. Lundbäck A. and Lindgren L.-E.,*Modelling of metal deposition*, Finite Elements in Analysis and Design, 2011, **47**(10), pp. 1169-1177.

[154]. Alimardani M.,Toyserkani E., and Huissoon J.P.,*A 3D dynamic numerical approach for temperature and thermal stress distributions in multilayer laser solid freeform fabrication process*, Optics and Lasers in Engineering, 2007, **45**(12), pp. 1115-1130.

[155]. Dai K. and Shaw L.,*Thermal and stress modeling of multi-material laser processing*, acta materialia, 2001, **49**(20), pp. 4171-4181.

[156]. Eric Schlienger,Duane Dimos,Michelle Griffith,Joseph Michael,Mike Oliver,Tony Romero, and Smugeresky J., *Near Net Shape Production of Metal Components using LENS*. 1998, Sandia National Laboratories: Livemore, CA.

[157]. Ready J.F., *Handbook of laser Materials Processing*, 1995, The Laser Institute of America.

[158]. Pavelic V.,Tanbakuchi R.,Uyehara O.A., and Myers P.O.,*Experimental and Computed Temperature Histories in Gas Tungsten-Arc Welding of Thin Plates*, Welding Journal, 1969, **48**(7), pp. 295-305.

[159]. Labudovic M.,Hu D., and Kovacevic R.,*A three dimensional model for direct laser metal powder deposition and rapid prototyping*, Journal of Materials Science, 2003, **38**(1), pp. 35-49.

[160]. Picasso M.,Marsden C.F.,Wagniere J.D.,Frenk A., and Rappaz M.,*A simple but realistic model for laser cladding*, Metallurgical and Materials Transactions B, 1994, **25**(2), pp. 281-291.

[161]. Fu Y.,Loredo A.,Martin B., and Vannes A.B.,*A theoretical model for laser and powder particles interaction during laser cladding*, Journal of Materials Processing Technology, 2002, **128**(1–3), pp. 106-112.

[162]. Qi H.,Mazumder J., and Ki H., *Numerical simulation of heat transfer and fluid flow in coaxial laser cladding process for direct metal deposition*, Journal of Applied Physics, 2006, **100**(2).

[163]. Lindgren L.-E., *Computational welding mechanics*, 2007, Woodhead, Cambridhge.

[164]. Goldak J. and Akhlaghi M., *Computational Welding Mechanics*, 2005, Newyork, Springer, 333.

[165]. Mughal M.P.,Fawad H., and Mufti R.,*Finite element prediction of thermal stresses and deformations in layered manufacturing of metallic parts*, Acta Mechanica, 2006, **183**(1-2), pp. 61-79.

[166]. Shan X.Y.,Tan M.J., and O'Dowd N.P.,*Developing a realistic FE analysis method for the welding of a NET single-bead-on-plate test specimen*, Journal of Materials Processing Technology, 2007, **192–193**(0), pp. 497-503.

[167]. Mcdill J.M.,Goldak J.A., and Oddy A.S., *An adaptive mesh-management algorithm for three-dimensional automatic finite element analysis*, in Proceedings of the Twelfth Canadian Congress of Applied Mechanics,1989.

[168]. Lindgren L.E.,Häggblad H.A.,McDill J.M.J., and Oddy A.S.,*Automatic remeshing for three-dimensional finite element simulation of welding*, Computer Methods in Applied Mechanics and Engineering, 1997, **147**(3–4), pp. 401-409.

[169]. Hamide M.,Massoni E., and Bellet M.,*Adaptive mesh technique for thermal–metallurgical numerical simulation of arc welding processes*, International Journal for Numerical Methods in Engineering, 2008, **73**(5), pp. 624-641.

[170]. Zhu X.K. and Chao Y.J.,*Effects of temperature-dependent material properties on welding simulation*, Computers & Structures, 2002, **80**(11), pp. 967-976.

[171]. Souloumiac B.,Boitout F., and Bergheau I.-M.,*A new local global approach for the modelling of welded steel component distortions*, Mathematical Modelling of Weld Phenomena 2002, **6**, pp. 573-590.

[172]. Lindgren L.E.,*Numerical modelling of welding*, Computer Methods in Applied Mechanics and Engineering, 2006, **195**(48–49), pp. 6710-6736.

[173]. Chin R.K.,Beuth J.L., and Amon C.H.,*Successive deposition of metals in solid freeform fabrication process, part2: thermomechanical models of layer and droplet columns* Journal of manufacturing science and engineering, 2001, **123**, pp. 623-638.

[174]. Weerasinghe V. and Steen W., *Laser cladding by powder injection*, in Transport Phenomena in Materials Processing., J. Mazumder, M. Chen, and C. Tucker, Editors. 1983, ASME: New York. p. 15–23.

[175]. Weerasinghe V.M. and Steen W.M., *Laser cladding with pneumatic powder delivery*, in 4th International Conference on Lasers in Materials Processing. 1983: Los Angeles. p. 166-175.

[176]. Toyserkani E.,Khajepour A., and Corbin S.,*3-D finite element modeling of laser cladding by powder injection: effects of laser pulse shaping on the process,* Optics and Lasers in Engineering, 2004, **41**(6), pp. 849-867.

[177]. Voort G.F.V. and Manilova E.P., *Metallographhic techniques for superalloys*, in Microscopy & Microanalysis, Cambridge, England, Press Syndicate of the University of Cambridge, Cambridge, England, 2004.

[178]. Pirling T.,Bruno G., and Withers P.J.,*SALSA—A new instrument for strain imaging in engineering materials and components,* Materials Science and Engineering: A, 2006, **437**(1), pp. 139-144.

[179]. FRMII. *Stress-spec Instrument details*. Available from: http://www.frm2.tum.de/en/science/diffraction/stress-spec/index.html.

[180]. R.Gerling,*Porosities and gas concentrations in inert gas atomized titanium-aluminium alloy powders : R.Gerling et al. (GKSS Forschungzentrum, Geesthacht, Germany.),* Metal Powder Report, 1999, **54**(6), pp. 45-46.

[181]. IncoTest. *Chemical Analysis by Inert Gas Fusion for Hydrogen, Oxygen and Nitrogen*. Available from: http://www.incotest.co.uk/chemical_analysis/.

[182]. Design-ExpertSoftware. V7, Stat-Ease.

[183]. Montgomery D., *Design and Analysis of Experiments*. 4th Edition ed, 1997, New York, John Wiley & Sons.

[184]. Carter L.N., *Laser powderbed fabrication of nickel-based superalloys: Influence of parameters; characterisation,quantification and mitigation of cracking,* in Superalloys 2012, Warrendale, PA,USA, TMS,2012.

[185]. Lind D.A.,Marchal W.G., and Wathen S.A., *Statistical Techniques in Business and Economics.* 12 ed, 2005, Boston, McGraw Hill Irwin.

[186]. Liang Q., *The influence of direct laser fabrication variables on the microstructure of Ti-6Al-4V: Modelling and Observation*, in The school of engineering. 2006, University of Birmingham: Birmingham.

[187]. ABAQUS, *section 2.11.1*, in theory manual version 6.12.

[188]. Zienkiewicz O.C. and Taylor R.I., *The Finite ELement Method*. 4 ed, 1994, Newyork, McGraw-Hill Book Co.

[189]. Hutchinson J.W. and Neale K.W., *Finite strain J2 deformation theory*, in Proceedings of the IUTAM symposium of finite elasticity, Netherlands,1980.

[190]. Hutchinson J.,*Generalizing J 2 flow theory: Fundamental issues in strain gradient plasticity,* Acta Mechanica Sinica, 2012, **28**(4), pp. 1078-1086.

[191]. Fisk M. and Lundbäck A.,*Simulation and validation of repair welding and heat treatment of an alloy 718 plate*, Finite Elements in Analysis and Design, 2012, **58**(0), pp. 66-73.

[192]. Liu L.,Hirose A., and Kobayashi K.F.,*A numerical approach for predicting laser surface annealing process of Inconel 718*, acta materialia, 2002, **50**(6), pp. 1331-1347.

[193]. Zain-ul-Abdein M.,Nelias D.,Jullien J.-F., and Deloison D.,*Prediction of laser beam welding-induced distortions and residual stresses by numerical simulation for aeronautic application*, Journal of Materials Processing Technology, 2009, **209**(6), pp. 2907-2917.

[194]. Bontha S.,Klingbeil N.W.,Kobryn P.A., and Fraser H.L.,*Effects of process variables and size-scale on solidification microstructure in beam-based fabrication of bulky 3D structures*, Materials Science and Engineering: A, 2009, **513–514**(0), pp. 311-318.

[195]. Mills K.C., *Recommended values of thermophysical properties for selected commercial alloys*, 2002, Cambridge, Woodhead Publishing Ltd.

[196]. Grant B.M.B., *Finite element modelling of inertia friction welding advanced nickel-based superalloys using an energy balancing approach*, in School of Materials. 2009, University of Manchester Manchester p. 278.

[197]. Eshelby J.D.,*The Determination of the Elastic Field of an Ellipsoidal Inclusion, and Related Problems* Proceedings of the Royal Society A: Mathematical, Physical and Engineering Sciences. , 1957, **241** pp. 376-396

[198]. Flemings M.C., *Solidification Processing*, 1974, McGraw-Hill.

[199]. G. P. Dinda,Dasgupta A.K., and Mazumder J.,*Laser Aided Direct Metal Deposition Of Inconel 625 Superalloy: Microstructural Evolution And Thermal Stability*, Materials Science and Engineering: A, 2009, **509**(1-2), pp. 98-104.

[200]. Liu F.,Lin X.,Huang C.,Song M.,Yang G.,Chen J., and Huang C.,*The effect of laser scanning path on microstructures and mechanical properties of laser solid formed nickel-base superalloy Inconel 718*, Journal of Alloys and Compounds, 2011, **509**(13), pp. 4505-4509.

[201]. Blackwell P.L.,*The Mechanical and Microstructural Characteristics of Laser-deposited IN718*, Journal of Materials Processing Technology, 2005, **170**(1-2), pp. 240-246.

[202]. T.Ganaha,B.P.Pearce, and Kerr H.W.,*Grain Structures in aluminium alloy GTA welds*, Metallurgical and Materials Transactions A, 1980, **11**(8), pp. 1351.

[203]. K.E.Easterling, *Introduction to physical metallurgy of welding*, 1983, Butterworths,London.

[204]. Al-Bermani S.S.,Blackmore M.L.,Zhang W., and Todd I.,*The Origin of Microstructural Diversity, Texture, and Mechanical Properties in Electron Beam Melted Ti-6Al-4V*, Metallurgical and Materials Transactions A, 2010, **41**(13), pp. 3422-3434.

[205]. Ko Y.K. and Berry J.T., *Charectarisation of the different dendritic microstructure of investment cast alloy 718*, in Superalloys 718, 625, 706 and various derivatives, Pensilveniya, TMS,1994.

[206]. D. Dye,O. Hunziker, and Reed R.C.,*Numerical Analysis of the Weldability of Superalloys*, Acta Materialia, 2001, **49**, pp. 683-697.

[207]. S. Azadian,Wei L.-Y., and Warren R.,*Delta Phase Precipitation in Inconel 718*, Materials Characterization, 2004, **53**(1), pp. 7-16.

[208]. Clark D.,Bache M., and Whittaker M.,*Microstructural Characterization of a Polycrystalline Nickel-Based Superalloy Processed using Tungsten-Inert-Gas-Shaped Metal Deposition*, Metallurgical and Materials Transactions B, 2011, **42**(2), pp. 434-434.

[209]. Colegrove P.,Ikeagu C.,Thistlethwaite A.,Williams S.,Nagy T.,Suder W.,Steuwer A., and Pirling T.,*Welding process impact on residual stress and distortion*, Science and Technology of Welding and Joining, 2009, **14**(8), pp. 717-725.

Appendix A: Engineering Drawings for Various Deposits

In this appendix the engineering drawings for various depositions in experimental section are drawn showing the exact locations of the build on the substrate as well as the locations at which the distortion as well as the stress measurements were taken.

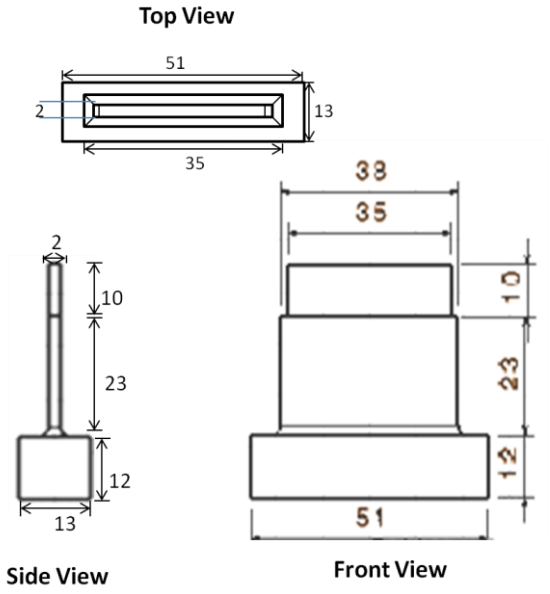

Figure A-I: Schematic showing thin wall in Figure 3-3.a build showing the dimensions.

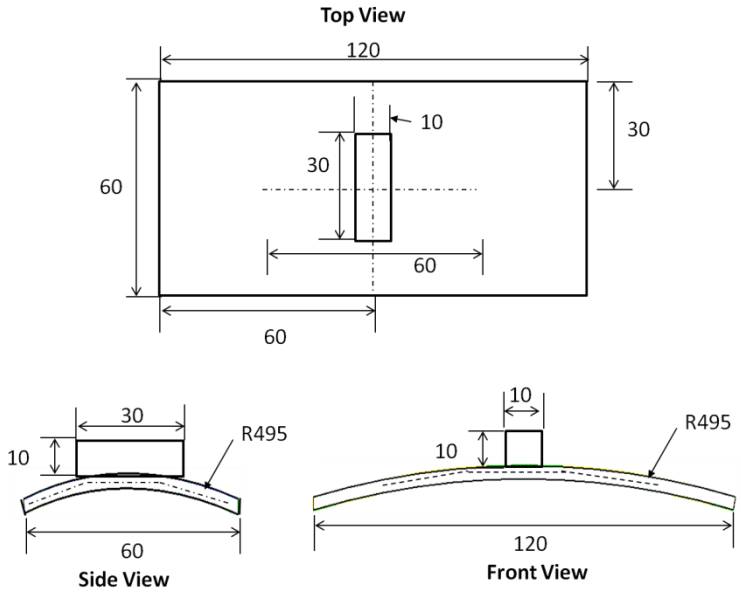

Figure A-II: schematic illustration of solid blocks deposited on the curved substrates (as shown in Figure 3-5.a), with dotted lines showing the location where the distortion and residual stress measurements were made.

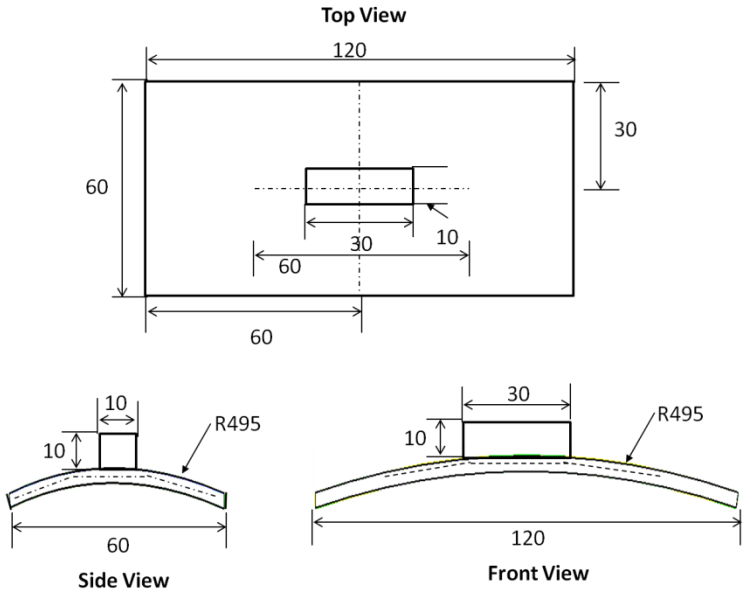

Figure A-III: Schematic illustration of solid blocks deposited on the curved substrates (as shown in Figure 3-5.b), with dotted lines showing the location where the distortion and residual stress measurements were made.

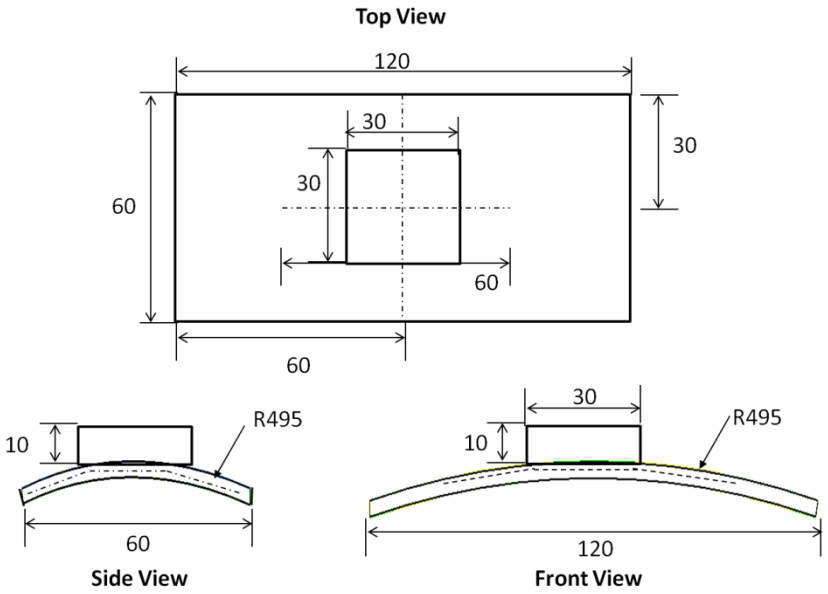

Figure A-IV: Schematic illustration of solid blocks deposited on the curved substrates (as shown in Figure 3-8), with dotted lines showing the location where the distortion and residual stress measurements were made.

Appendix B: Temperature dependent Thermo-Physical properties for IN718

The thermal expansion co-efficient of IN718, Figure B.I, as well as the high temperature stress strain values at different strain rates was taken from the literature and plotted in the Figure B.II.

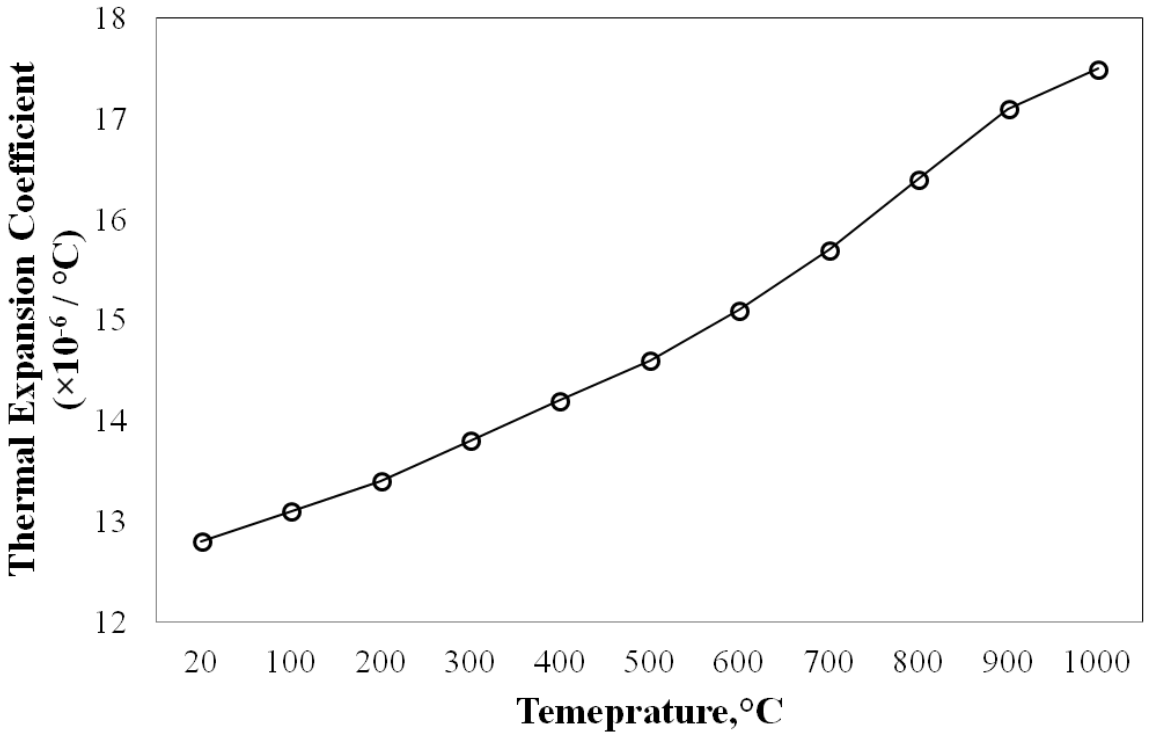

Figure B.I: Thermal expansion coefficient of IN718 as a function of temperature[196].

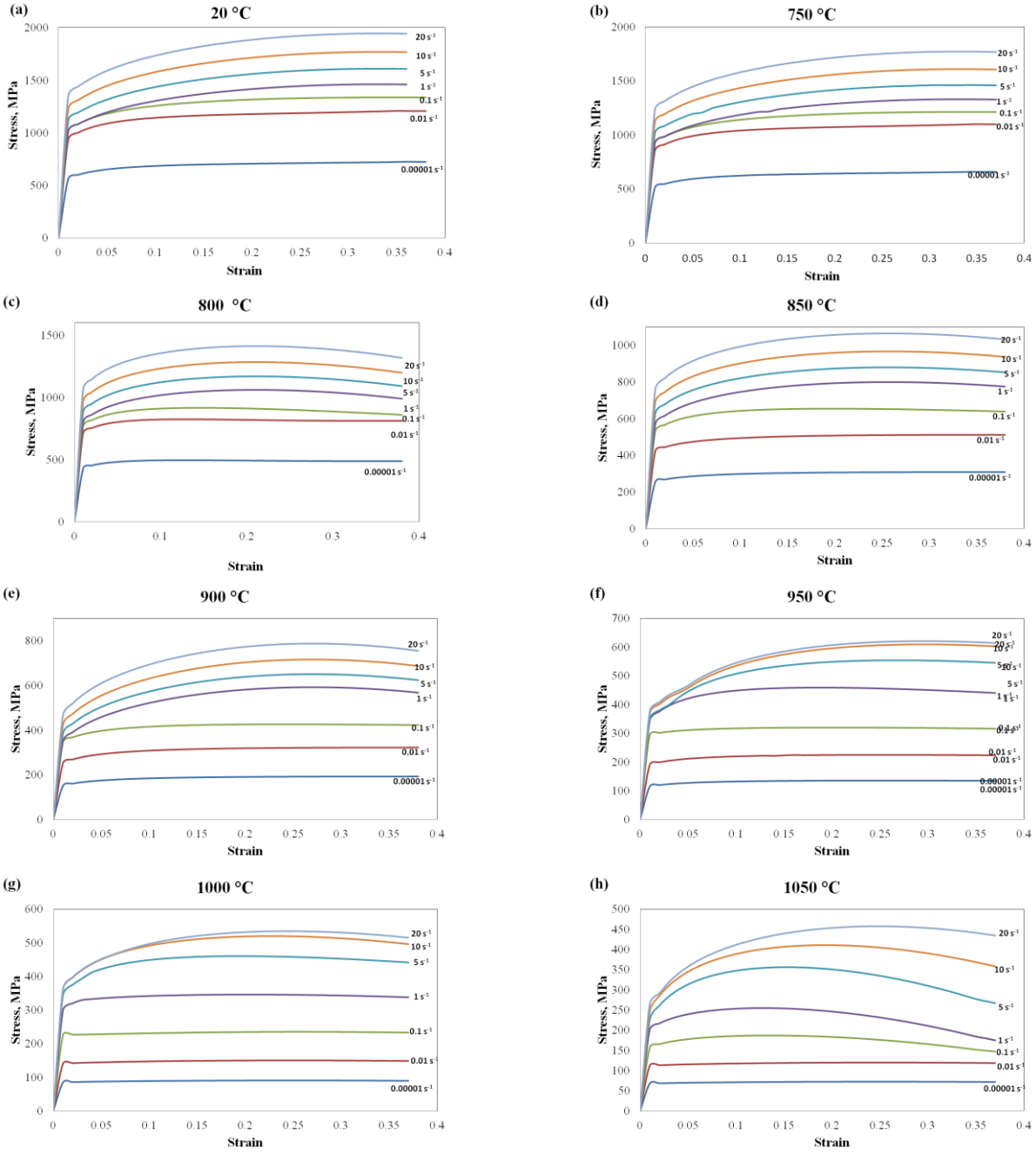
(a)
20 °C
(b)
750 °C
(c)
800 °C
(d)
850 °C
(e)
900 °C
(f)
950 °C
(g)
1000 °C
(h)
1050 °C
Stress, MPa
Strain
20 s-1
10 s-1
5 s-1
1 s-1
0.1 s-1
0.01 s-1
0.00001 s-1

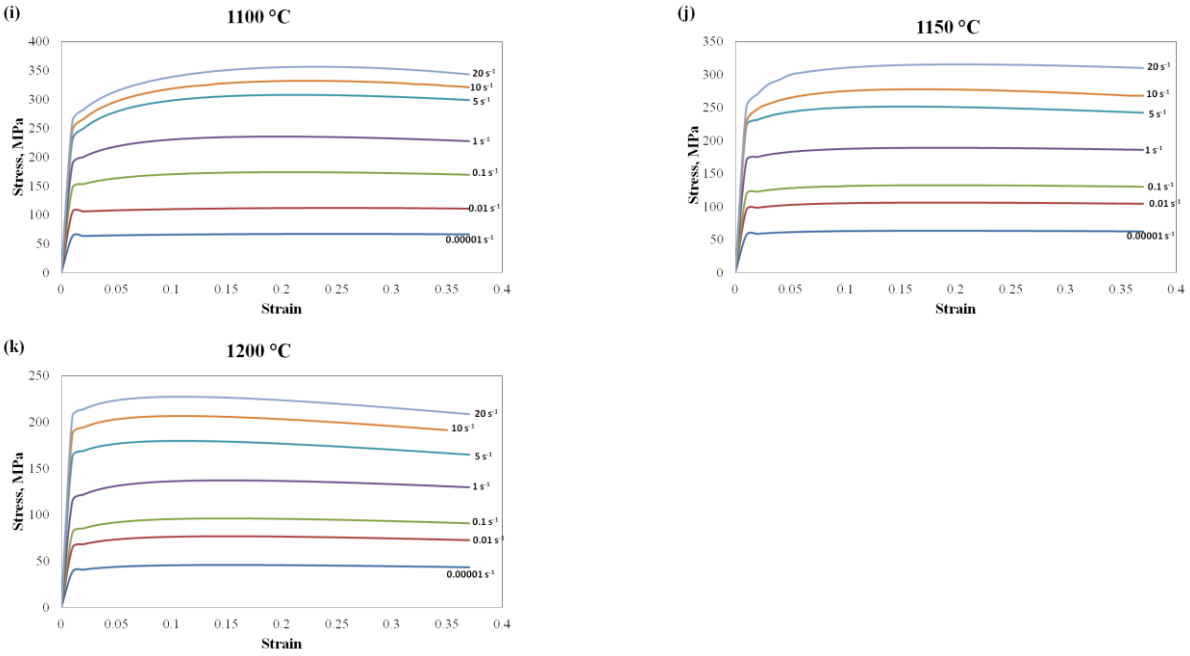

Figure B.II: Stress-strain curves at different strain rates and temperatures (Graphs plotted from data [196]).